EXPLORATION OF FORWARD AND INVERSE PROTOCOLS FOR PROPERTY OPTIMIZATION OF TI-6AL-4V

A Dissertation
Presented to
The Academic Faculty

by

Matthew W. Priddy

In Partial Fulfillment
of the Requirements for the Degree
Doctor of Philosophy in the
George W. Woodruff School of Mechanical Engineering

Georgia Institute of Technology
August 2016

EXPLORATION OF FORWARD AND INVERSE PROTOCOLS FOR PROPERTY OPTIMIZATION OF TI-6AL-4V

Approved by:

Dr. David L. McDowell, Advisor
George W. Woodruff School of
Mechanical Engineering
Georgia Institute of Technology

Dr. Donald S. Shih, Co-Advisor
Technical Fellow
Boeing Company

Dr. Surya R. Kalidindi
George W. Woodruff School of
Mechanical Engineering
Georgia Institute of Technology

Dr. Hamid Garmestani
School of Materials Science and
Engineering
Georgia Institute of Technology

Dr. Rick W. Neu
George W. Woodruff School of
Mechanical Engineering
Georgia Institute of Technology

Date Approved: July 1, 2016

I didn't know when I started running,

I'd be running my whole life.

– Bear's Den

ACKNOWLEDGEMENTS

The list of people that have had a positive influence on my academic pursuits, up to and including my time at Georgia Tech, is rather lengthy and thus there is little chance I will mention each and every one of them. However, I have attempted to properly acknowledge the many individuals who, through their love and support, have provided motivation to me during this quest.

First and foremost, I would like to acknowledge the endless support of my wife, Lauren. When we made the decision to enroll at Georgia Tech and move to Atlanta, I would never have believed how much we could each develop while also growing closer together. She has been a constant for me through this entire journey, something that I have needed more than I ever thought possible. She is a rock star and I am perfectly content to be on tour with her.

I am grateful for the love and guidance provided by my parents. My Mum, Anita Priddy, taught me that education was something to cherish and nurture, something that should be available to everyone. In doing so, I believe she also instilled in me a societal responsibility to aid in the education of others. My Dad, Richard Priddy, taught me (through his actions) that hard work should be implicit in everything we do and that if you have a goal, the sacrifices made to achieve that goal pale in comparison to the achievement.

I am also grateful for the love and support of my extended family. My older sister, Kirsti Wright, has always helped keep things in perspective for me and helped bring me out of my introverted shell. To my brother-in-law, Chris Wright, thank you for keeping us in constant laughter during our visits. His persistence to keep returning to nursing school for more advanced degrees was something that always motivated

me to keep moving forward as well. I also wish to thank my other brother-in-law, Grant Beatty, for enlightening us with his thought-provoking topics of conversation all while reminding us to pursue our passion and not lose sight of the things that make us happy. Lastly, I wish to thank my wife's parents, Hamp and Kim Beatty, for their constant encouragement and support. They haven't simply watched me grow over the years, they have helped in guiding my person into who I am today.

I wish to express my sincerest gratitude to my thesis advisor, Dr. David McDowell, for aiding in the development of my critical nature to couple with my enthusiasm for computational materials research. Dr. McDowell has constantly raised my level of understanding and communication, both of which will serve me well in the future. This work was supported by the National Science Foundation under Grant Number CMMI-1333083.

I extend a special thank you to Dr. Surya Kalidindi for his insightful advice related to spherical indentation and crystal plasticity modeling. And I also wish to thank my reading committee, Dr. Donald Shih, Dr. Rick Neu, and Dr. Hamid Garmestani for reading this dissertation and participating in my proposal and defense presentations.

The supportive environment of MRDC 3338 is one of the primary reasons for my success during my time at GT. The office has been home to quite a few students (and computers!) during my tenure, and every person that has come through that door has improved my research philosophy in some capacity. I hope the McDowell lab continues the tradition of being extremely supportive of one another, particularly towards newer students, because I know it results in a better collective of research.

In particular, I would like to thank Dr. Jeffrey Lloyd for his constantly critical thoughts, his expertise on Bunge Euler angles, and for his plethora of restaurant recommendations in Atlanta. I also wish to thank Dr. Brett Ellis for his general guidance on the balance of family life and academia, as well as providing me the opportunity to exercise my civil engineering background on his fabulously written

UHPC abstracts. I really appreciated having a fellow college sports fan in Dr. Bill Musinski in the office, in addition to his fantastic mentorship in generating beautiful pictures for publications and presentations.

I also wish to thank the trio of M.S. students for their friendship during their time in the McDowell group. Specifically, I would like to thank Ben Smith for teaching me much about fatigue experiments. I also wish to thank Conor Hennessey for aiding in diagnosing crystal plasticity error statements. And I also would like to thank Paul Kern for attempting to correct all of my ill-advised Python habits and for giving me one last college sports buddy in the lab.

I wish to thank Dr. Anirban Patra for his friendship and his tutelage regarding the Mo-Si-B material system. And of course Dr. Gustavo Castelluccio for his generous discussions about anything academic-related. Shuozhi Xu has been a good friend during my time at GT and I would like to thank him for setting the standard for work ethic and research publications. I also wish to thank Adrienne Muth for her stellar advice for the enhancement of the graphics in this thesis.

I would also like to thank my fellow NSF GOALI students. Particularly, I would like to thank Dr. Jordan Weaver for his enthusiasm regarding SNI simulation results, which most certainly aided in the construction of this dissertation. I also wish to thank Noah Paulson for his assistance in all things MKS. I have thoroughly enjoyed working closely with Noah and sharing our passion for connecting computational research to something closely tied to future industry needs.

I would especially like to thank Dr. Barrett Hardin for his friendship during our time at MSU and GT. Barrett was always ready with an answer when I had a question and he never shied away from a good sports-related conversation.

I wish to thank my original desk buddy, Jin Song, for his assistance during my first couple of years at GT. And to my newer desk buddy, Luke Costello, thanks for letting me take over the 1/2 that you never use. I also wish to thank Dr. Shreevant

Tiwari, Sam Britt, Aaron Tallman, and Joel Blumer for their friendship.

To Dr. Jason Mayeur, Dr. Ryan Austin, and Dr. Garritt Tucker, the senior group members that occupied the office on the 4th floor of MRDC, I wish to thank them for being role models to all of the less experienced McDowell group members. Your success after GT was nothing short of inspirational for all of us in MRDC 3338.

I wish to thank Dr. Mike Kirka for his assistance navigating CCMD meetings and his endless support during my preparation for ME quals. I also wish to thank Kyle Brindley for putting to use the knowledge I have gained at GT with his inquisitive questions related to crystal plasticity modeling and Python. I would also like to thank Dipen Patel for introducing me to spherical indentation simulations and his carefully crafted advice throughout my learning.

I would be remiss if I did not thank my GT-ASEE colleagues, particularly Dr. Scottie-Beth Fleming Lindsley, Dr. Wafa Soofi, Dr. Alex Coso, and Jason Wang. Being involved in such a wonderful and supportive organization constantly renewed my excitement for engineering education. And making friends outside of the MRDC building made my involvement that much more fulfilling. I cannot wait to put my event planning skills to work in the future, because thanks to you I know how to develop some killer workshops.

Although quite unusual, I would also like to thank GT and the City of Atlanta for providing such beautiful scenery for my afternoon/evening jogs. Whether its running the Pi Mile, traversing Piedmont Park, or a short run to Centennial Park, the pleasant surroundings always made it easier for me to get out of the office to get some exercise.

I also wish to thank Dr. Antonia Antoniou for allowing me to do my teaching practicum in her COE 3001 class. I am sure it was quite awkward to watch me deliver those few lectures, but her encouragement and feedback will stay with me for the duration of my academic career. She also gave me free reign to design the in-class activities, which I found to be simultaneously daunting and very rewarding. I hope

to someday reach the level at which she operates each and every day in the classroom with her students.

Lastly, I wish to acknowledge Dr. Tom Lacy, Dr. Phil Gullett, and Dr. Harry Cole for each inspiring me to pursue graduate school while I attended Mississippi State University. Dr. Lacy taught my Statics course (the foundation of so many engineering principles) as well as my first Finite Element course, and I can honestly say that I would not have the same passion for computational solid mechanics without having taken both of those courses with him. I wish to thank Dr. Gullett for taking a chance on me as a summer undergraduate, which then turned into my M.S. research. That was the perfect scenario for me to grow my academic curiosity; I still feel indebted to him for that. Finally, I wish to thank Dr. Harry Cole for being such a good friend/mentor during my time at MSU, and more importantly for demonstrating to me the responsibility of being a successful educator.

TABLE OF CONTENTS

LIST OF TABLES

LIST OF FIGURES

LIST OF SYMBOLS

3D	three-dimensional.
BCC	body-centered cubic.
BOR	Burgers orientation relation.
CP	crystal plasticity.
CPFEM	crystal plasticity finite element method.
CRSS	critical resolved shear stress.
EBSD	electron backscatter diffraction.
FCC	face-centered cubic.
FE	finite element.
FEM	finite element method.
FIP	fatigue indicator parameter.
HCF	high cycle fatigue.
HCP	hexagonal close-packed.
ICME	integrated computational materials engineering.
IDEM	inductive design exploration method.
ISS	indentation stress-strain.
LCF	low cycle fatigue.
MD	molecular dynamics.
MGI	materials genome initiative.
MKS	materials knowledge system.
MLC	mechanically long crack.
MSC	microstructurally small crack.
PSB	persistent slip band.
RVE	representative volume element.
SNI	spherical nanoindentation.

SVE	statistical volume element.
Ti-64	Ti-6Al-4V.
UMAT	user material subroutine.
α	HCP phase of titanium.
β	BCC phase of titanium.
$\boldsymbol{\sigma}$	Cauchy stress tensor.
$\boldsymbol{\sigma}^{\mathrm{PK2}}$	second Piola-Kirchhoff stress.
$\chi^{(\xi)}$	back stress for slip system (ξ).
$\dot{\gamma}^{\xi}$	shearing rate for slip system (ξ).
$\kappa^{(\xi)}$	threshold stress for slip system (ξ).
$\mathbb{C}_0$	fourth-order elastic stiffness tensor in intermediate configuration.
$\mathbf{E}^{\mathrm{e}}$	elastic Green strain.
$\mathbf{F}$	deformation gradient.
$\mathbf{F}^{\mathrm{e}}$	elastic portion of deformation gradient.
$\mathbf{F}^{\mathrm{p}}$	plastic portion of deformation gradient.
$\mathbf{I}$	identity tensor.
$\mathbf{L}$	velocity gradient.
$\mathbf{L}_0^{\mathrm{p}}$	plastic velocity gradient in intermediate configuration.
$\mathbf{R}$	rotation matrix.
$\mathbf{n}^{(\xi)}$	slip plane normal unit vector in current configuration.
$\mathbf{s}^{(\xi)}$	slip direction unit vector in current configuration.
ϕ_1, Φ, ϕ_2	Bunge-Euler angles.
$\tau^{(\xi)}$	resolved shear stress for slip system (ξ).
$\tau_{CRSS}^{(\xi)}$	critical resolved shear stress for slip system (ξ).
$D^{(\xi)}$	drag stress for slip system (ξ).
FIP_{FS}	Fatemi-Socie fatigue indicator parameter.

M	inverse strain-rate sensitivity exponent.
N_{FOR}	portion of fatigue life to form a crack.
N_{MLC}	portion of fatigue life due to mechanically long crack growth.
N_{MSC}	portion of fatigue life due to microstructurally small crack growth.
N_T	total fatigue life (in number of cycles).
$\mathbf{R}$	cyclic stress ratio; $\left(\frac{\sigma_{min}}{\sigma_{max}}\right)$.

SUMMARY

The modeling and simulation of advanced engineering materials undergoing mechanical loading requires accurate treatment of relevant microstructure features, such as grain size and crystallographic texture, to determine the heterogeneous response to deformation. However, many models constructed for this purpose are not being fully realized in their predictive capability. Additionally, physics-based models can be combined with bottom-up deductive mappings and top-down inductive decision paths to increase their utility in materials selection and optimization. However, connecting these types of models or algorithms with experiments, rapid inverse property/response estimates, and design decision-making via integrated workflows has yet to become well-established for materials design and/or development. One material system primed for this type of concurrent advancement is $\alpha + \beta$ titanium alloys, because its resultant microstructure and mechanical properties are highly dependent on material processing and composition.

This dissertation seeks to advance a materials design process for fatigue resistance, strength, and elastic stiffness of Ti-6Al-4V through the advancement of various computational tools, as well as the integration of simulation-based tools and high-throughput experimental datasets. The microstructure-sensitive crystal plasticity finite element method (CPFEM) is utilized to explicitly account for the grain structure and crystallographic texture of Ti-6Al-4V. To improve the predictive capability of the CPFEM model, high throughput spherical indentation experimental datasets are used for model calibration because of their ability to extract elastic and plastic individual phase and grain properties from multiphase materials such as titanium alloys. The CPFEM can be used to capture the microstructure heterogeneity on fatigue

crack driving forces, but these types of simulations are computationally expensive. Instead, an explicit integration of the relevant constitutive relations in the CPFEM model are combined with the materials knowledge system (MKS) approach for generating spatially local results of polycrystalline materials. These bottom-up simulation methods provide macroscopic properties from microstructure-level model inputs. For materials design, it is important to determine the inverse – microstructure-level information from the macroscopic response – which is referred to as top-down modeling. The Inductive Design Exploration Method (IDEM) offers a systematic approach to combining bottom-up simulations with top-down inductive design search. In this dissertation, a generalized framework of the IDEM is implemented to assess multi-objective design scenarios specific to the microstructure-sensitive datasets generated in this work.

The general approach presented in this dissertation integrates CPFEM simulations with experimental spherical indentation for model refinement and also combines CPFEM with the MKS for computational-efficient generation of local quantities. These advancements are the basis for accelerated decision-support for materials design exploration when merged with the IDEM. Although performed with $\alpha+\beta$ titanium, individual elements of the framework can be applied to a variety of engineering alloys for tasks such as extraction of model parameters from spherical indentation experiments, coupling MKS with crystal plasticity constitutive relations, and performing a top-down inductive design search with polycrystalline datasets.

CHAPTER 1

INTRODUCTION

1.1 Motivation

Throughout history, the advancement of technology has always been accompanied by the discovery of new materials or new ways of processing materials. In ancient times, the discovery of copper (8000 B.C.) signaled a transition from stone tools because of its durability and versatility. The Industrial Revolution would not have been possible without the development of Portland Cement (mid 18^{th} century) or the carburization of iron to yield carbon steel. In the modern era, advanced composites and specific shape memory metal alloys were necessitated by the extreme design parameters of NASA's Space Shuttle program.

In recent years, initiatives like the Materials Genome Initiative (MGI) [1] have increased enthusiasm for materials-based research because of the need for an increased rate of materials development. This need is derived from the interdependent nature of materials development and technological advances. It also originates from the requirement for new materials development to address some of the major engineering challenges facing future generations. The MGI discusses materials development from a historical approach, detailing it as a linear process as shown in Figure 1.1. Additionally, the historical approach has been characterized by trial-and-error inquiries in the discovery, development, and optimization phases. As such, the amount of time required to go from discovery to deployment in the historical process can be up to 20 years. To decrease this amount of time, the MGI recommends a concurrent approach that advances computational models, experimental tools, and digital data to aid in the speed-up of many of the steps shown in Figure 1.1.

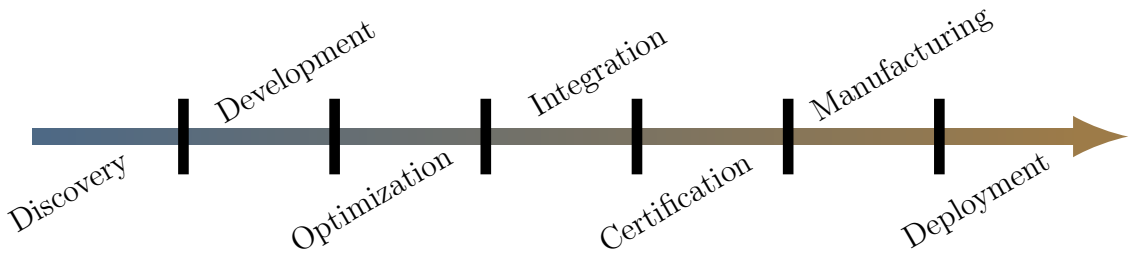

Figure 1.1: The historical materials development continuum (adapted from [1]).

Metal alloys are one class of materials that can greatly benefit from the concurrent approach proposed by the MGI. However, many properties of metals, including mechanical, magnetic, and electrical, are anisotropic. Polycrystalline metals exhibit anisotropic behavior in single grains (microscale) and aggregates of many grains (macroscale). Single crystals tend to deform under shear on preferred crystallographic slip systems. For polycrystalline metals, anisotropic deformation occurs because each grain will have a different orientation of its underlying crystal lattice. Additionally, grain boundaries act as barriers to dislocation motion, further contributing to the anisotropic behavior of polycrystalline metals. Therefore, any concurrent design approach specific to metals requires proper treatment of their anisotropic nature.

Crystal plasticity (CP) modeling is one example of a simulation-based tool that accounts for the anisotropic nature of metals and has the potential to increase the rate of materials development [2–13]. Single crystal plasticity provides a local description of plastic deformation that can include treatments for dislocation motion (slip) and deformation twinning. The slip directions and slip planes are explicitly defined for dislocation motion. The activation of dislocation motion is modeled with phenomenological or thermodynamically-based flow rules which relate the single crystal stress-state to a plastic shear strain rate for each slip system. The compilation of the plastic shear strain on all slip systems is directly related to the plastic strain for a given material point.

Development of the crystal plasticity finite element method (CPFEM) combined

the sophisticated deformation treatment of crystal plasticity with the finite element method (FEM), which allowed for the extension of crystal plasticity modeling from single crystal treatments to polycrystalline material representations. The CPFEM treats each integration point in the finite element model as a single material point with a specified orientation. The CP model dictates the stress-state of each element and the FEM ensures equilibrium in the model. This treatment allows for the modeling of polycrystalline metals with grains composed of many elements.

Another example of a simulation-based tool is the Materials Knowledge System (MKS) [14–20]. The MKS is a data-driven, meta-model that applies digital signal processing techniques to expedite the investigation of local connections between material response and microstructural topologies [14]. The MKS is an algebraic series capable of predicting response fields on the micro-scale given some macro-scale averaged loading or boundary conditions. For example, the MKS has been used to accurately predict components of the local strain tensor in a polycrystalline material given the digital microstructure and the applied boundary conditions [20] after calibration to a series of FEM simulation results. The MKS can be performed at a fraction of the computational cost of FEM once calibrated for a given material system.

CPFEM is a homogenization or bottom-up approach, wherein in provides macroscopic properties from microstructure-level model inputs. In contrast, the MKS is a localization or top-down approach, predicting the microstructure-level response from macroscopic model inputs. Both approaches are vital to materials design, but there is also a need to apply the generated datasets to achieve specific product performance requirements, some of which can require compromise between multiple objectives that are often in conflict or competition with one another. Optimal solutions may exist, but the uncertainties associated with model inputs and predictions motivate the desire for determining robust solutions [21–23] that are insensitive to uncertainty. The Inductive Design Exploration Method (IDEM) [23–26] offers a systematic approach

to combining bottom-up simulations with top-down inductive design search while accounting for model uncertainty.

Although the development of new materials would certainly be beneficial for specific applications, the optimization of current material systems could also improve performance or allow for their use in different applications. For example, $\alpha + \beta$ titanium alloys are commonly used in the aerospace industry for their high strength-to-weight ratio, fatigue resistance, and resistance to corrosion. They can result in a wide range of microstructures and mechanical properties depending on the heat treatment and thermomechanical processing routes, which make highly customizable depending on the specific application of use. However, $\alpha + \beta$ titanium has an anisotropic deformation response and many of the applications of titanium undergo fatigue loading, the number of cycles to failure of which can be difficult to predict because of the many possible microstructures of $\alpha + \beta$ titanium alloys.

1.2 Problem Definition

The design or optimization of alloys (i.e., new processes, structures, and properties) based on computational models is highly dependent on accurate model parameters, three-dimensional digital microstructure representation, and computationally efficient tools. One promising application of CPFEM simulations is their use in fatigue studies to explore mechanisms of fatigue crack initiation in specific material systems [27–31]. The high-cycle fatigue (HCF) regime is characterized by large variability in the number of cycles to failure because of the heterogeneous, localized response of plastic deformation from these loading conditions. The plastic deformation is spatially dependent because of the microstructure, which can very depending on grain morphology, texture, and the presence of discontinuities such inclusions, precipitates, or voids. To capture the variability, a significant number of microstructure features are needed to simulate the statistical variance in a specific material system.

However, one of the limiting factors of widespread implementation of physics-based models such as CPFEM for assessment of the variability of fatigue crack formation is the high computational cost associated with their implementation. Representative volume elements (RVEs) are intended to approximate the response of the overall material microstructure by encompassing a volume that is large enough to achieve statistical homogeneity in comparison with microstructure-specific features [32], but they are computationally prohibitive due to their size. Instead, statistical volume elements (SVEs) are commonly used, which are constructed such that their size is sufficient to sample microstructure features. While RVEs commonly provide accurate macroscopic responses (e.g., elastic stiffness, yield strength, etc.), SVEs can vary in their macroscopic response when compared to the true solution. It is therefore necessary to sample many SVEs to generate an ensemble average that mimics the RVE response. Each of the SVEs is then modeled with CPFEM and the results are sampled. This not only requires much computational time including number of processors, but the rate of generating results can also be limited by the number of software licenses available for a given software package.

Recent work in the field of statistical continuum mechanics [33–38] has established computationally efficient hierarchical structure-property evolution linkages for multi-scale modeling of materials. The MKS [14–20] utilizes localization relationships that capture accurately the microscale spatial distribution of a chosen response field (e.g., strain, concentration, etc.) for a selected macroscale boundary condition while also accounting for the spatial variability of the microstructure [14]. The advantage of the MKS or a similar localization technique is the ability to separate the microstructure-sensitive modeling from FEM simulations, thus improving the computational efficiency of the simulation workflow.

Another advantage of CPFEM simulations is the possibility of modeling multiple distinct phases in a specific material system via spatial distribution in the finite

element (FE) mesh. However, each phase requires unique model parameters to accurately represent the deformation response. The determination of phase-specific model parameters can be quite challenging for some material systems due to size limitations of features in their native state. In many CPFEM studies [39–44], the macroscopic stress-strain response is used to calibrate model parameters. Unfortunately, this can minimize the apparent effects of certain material systems or deformation phenomena, thus providing minimal quantitative information to support a thorough investigation of possible model treatment for a specific parameter.

Recent work in spherical nanoindentation (SNI) [45–47] has established a robust method for determining phase-specific properties such as indentation modulus, yield, and hardening. This method has the ability to provide single crystal-like responses individual grains in a polycrystalline material. These types of datasets could be extremely useful in gaining significant quantitative information about specific deformation phenomena, which would allow for incremental improvements in the calibration of crystal plasticity models.

Another deficiency of many crystal plasticity models is their lack of accounting for slip transfer through grain boundaries [48]. Commonly referred to as slip transfer, the transmission or restriction of dislocations motion across grain boundaries can have a significant effect on the overall strength of a material [49]. And although polycrystalline FE meshes can capture the distinct size and shape of grains, it is still extremely difficult to model slip transfer within the CP model due to the specifics of its deployment. CPFEM simulations have also been used, as they are in this research, to model homogenized multi-phase grains [39, 40, 42, 50] where the microstructure features are too small to explicitly be represented in the FE mesh. However, these homogenized regions could also benefit from more sophisticated treatment of quantifiable barriers to dislocation motion such as grain boundaries.

1.3 Research Directive

The research presented in this dissertation is part of a larger program directive that involves other researchers spanning multiple disciplines. The overall goal of the NSF GOALI research program is to couple material microstructure-level modeling and simulation with processing, characterization, and property measurement protocols to exploit recent advances in high throughput local property measurements and materials data analytics to realize accelerated search, evaluation, and design exploration of $\alpha + \beta$ Ti alloys. This research goal focuses on three key underdeveloped technologies:

(i) Developing cost-effective protocols for acquiring key 3D microstructure information in $\alpha + \beta$ Ti alloys, performing necessary statistical analyses on the data to objectively identify the salient microstructural features and their spatial distributions, and reconstructing an ensemble of instantiations representing the material microstructure for evaluation of properties using multiscale modeling techniques.

(ii) Developing strategies for coupling modeling and simulation (CP) with spherical nanoindentation experiments within individual phases (α and β) and in the vicinity of α/β interfaces to quantify local threshold strength for dislocation plasticity and slip transfer across interfaces.

(iii) Developing a rapid throughput scheme to estimate key structural design variables such as elastic stiffness, yield strength, and minimum fatigue life for a broad range of polycrystalline low symmetry $\alpha + \beta$ Ti alloys using reduced-order representations of structure-property-processing linkages mined from sophisticated multiscale material models using modern data science approaches.

Towards these goals, this work is configured into four tasks:

1. Characterization and quantification of microstructure with extraction and validation of weighted statistical volume elements (WSVEs).

2. Development and validation of new data analyses protocols for estimating grain-scale mechanical properties from spherical indentation on $\alpha + \beta$ Ti alloys to inform microstructure-sensitive crystal plasticity models.

3. Implementation of the MKS model for computationally efficient microstructure-response estimates of polycrystals, informed by polycrystal plasticity simulations.

4. The utilization of the IDEM for various competing property objectives.

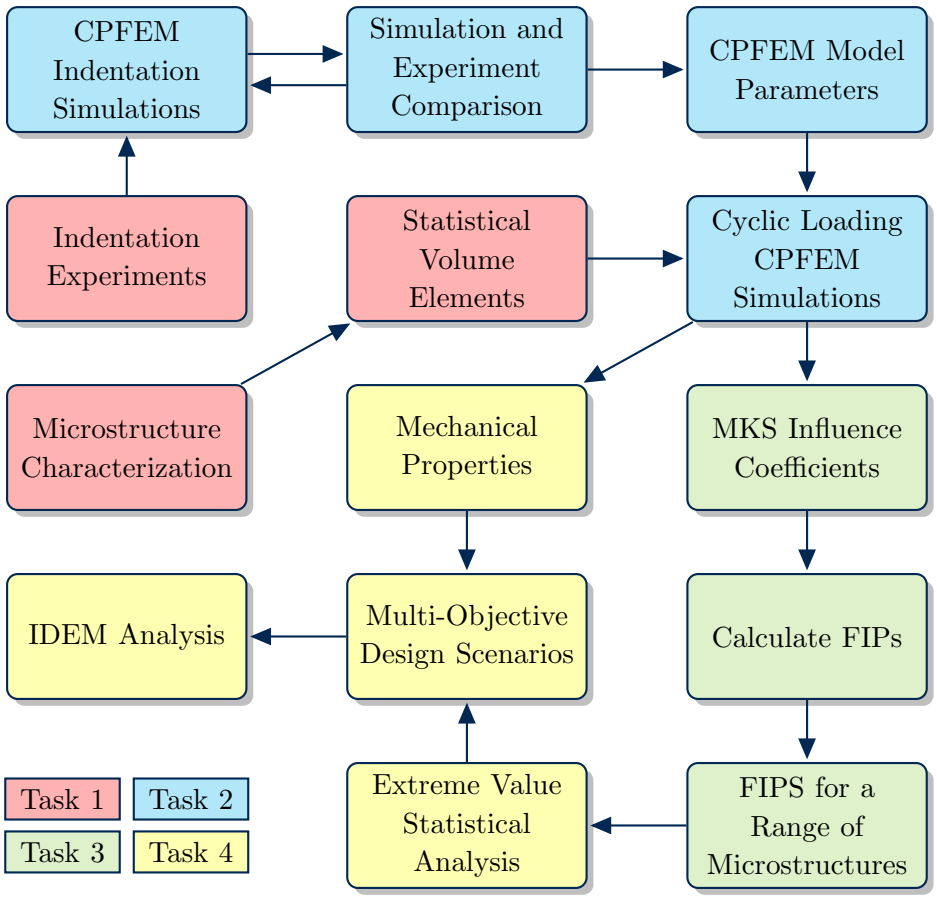

Figure 1.2: NSF GOALI project flowchart with items broken down into four key tasks.

Figure 1.2 presents the major components of each task and the connections among those tasks. Task 1 encompasses the two main experimental components (microstructure characterization and indentation experiments) and the development of digital microstructures classified as SVEs. Microstructure characterization includes the use of EBSD to quantify grain morphology and texture information, both of which are inputs for the generation of SVEs. Indentation experiments are performed for multiple indenter sizes (16 µm, 100 µm, and 6.35 mm) and multiple $\alpha + \beta$ titanium alloy microstructure features (α-grain, colony grains, and multiple grains) to provide datasets for multiple length scales. Task 2 is the calibration of the CPFEM model with indentation experimental datasets and employing the refined model parameters in CPFEM cyclic loading simulations of the SVEs developed in Task 1. Task 3 is the use of the MKS to generate extreme value distributions of fatigue indicator parameters (FIPs). The MKS uses the cyclic CPFEM simulations from Task 2 as an input dataset to determine the influence coefficients. Task 4 uses the datasets generated in Task 2 and Task 3 to assess multi-objective design scenarios with the IDEM. This project combines experimental, computational, and data science approaches in the advancement of materials research specific to $\alpha + \beta$ titanium alloys.

1.4 Basic Scientific Questions to Answer

In this dissertation, multiple computational tools (e.g., CPFEM and IDEM) will be employed to address various scientific aspects of the research directive presented in Section 1.3. The specific questions addressed in this dissertation include:

- What $\alpha + \beta$ titanium alloy material parameters can be extracted from spherical indentation experimental datasets when compared with simulation results? What are the important factors of constructing a FEM model sufficient for modeling spherical indentation? Do these factors differ for elastic deformation versus elastic-plastic deformation?

- ◇ How can local quantities be calculated from CP constitutive relations without CPFEM? Is it possible to replace CPFEM with MKS? How accurate are these methods and is this accuracy sufficient for CPFEM replacement? Are the methods general in nature or are the applications problem-specific?

- ◇ What types of datasets are required for utilizing microstructure-sensitive simulations with IDEM? How is uncertainty estimated for these types of datasets and represented in IDEM?

- ◇ What types of challenges are presented by attempting to explicitly model α/β interfaces in $\alpha + \beta$ titanium alloys? Are previously determined slip transfer relations sufficient in capturing the potential for slip transfer among α and β phases? What types of experimental information are needed to advance CPFEM models in regard to slip transfer?

1.5 Thesis Objectives

To develop basic scientific aspects of and in addition to aid the success of the larger research project, this dissertation has four primary objectives:

(i) Develop FEM models of the SNI process to explore the coupling of CPFEM simulations with similar experimental data for the α and $\alpha + \beta$ phases of Ti-64 primarily for model parameter extraction, but additionally for model validity.

(ii) Extend CPFEM modeling and local deformation fatigue simulations results for the MKS model calibration.

(iii) Utilize the IDEM with microstructure-sensitive simulation data for local (grain level) and global (polycrystalline) properties/response to pursue robust material designs for ranged sets of specified performance objectives.

(iv) Explore the viability of concepts from existing slip transfer correlations with regard to formulation of constitutive relations to address the behavior of slip transfer across grain and phase boundaries in $\alpha + \beta$ titanium alloys.

The CPFEM model used in this dissertation has been developed in previous works [39, 40, 42–44, 50–57] for analyzing the various aspects of high-cycle fatigue of Ti-64, but the model has always been calibrated to the macroscopic stress-strain response of polycrystalline specimens. This dissertation explores the assumptions made when calibrating to macroscopic datasets and attempts to refine the model parameters with individual phase/grain spherical indentation experimental data. Indentation experiments typically display results in force-displacement, but the use of spherical indentation allows for the determination of indentation stress-strain (ISS) plots. It is imperative to develop a FEM model that demonstrates convergence when calculating indentation stress and strain from simulations.

Second, CPFEM simulations and the current fatigue modeling scheme is extended to use the computationally efficient MKS for the examination of multiple textures and loading directions. The MKS is used to extract the total strain tensor from anisotropic elastic FEM simulations and an explicit integration scheme of the relevant constitutive relations from CPFEM was formulated to determine the local plastic strain fields from the local strain fields provided by the MKS. Extreme value distributions of FIPs are constructed for each texture and loading direction, in addition to directional elastic stiffness and yield strength values.

Third, the primary reason for updating the current constitutive relations, obtaining refined model parameters, and developing computationally-efficient methods of data generation is to demonstrate the exploration of various Ti-64 textures and inform material selection/optimization procedures for given design scenarios. The microstructure-sensitive FIP, directional elastic stiffness, and yield strength datasets are used as input for the IDEM. Various design scenarios are presented and robust

solutions are determined for given textures and loading directions.

Finally, correctly accounting for dislocation motion across grain and phase boundaries is of high importance for microstructure-sensitive modeling. Studies into slip transfer [58, 59] have demonstrated the difficulty of incorporating such phenomena into computational models, but there is still room for improvement to the first-order estimations currently employed in the CPFEM model. This objective applies various slip transfer relations to the α/β interface specific to $\alpha+\beta$ titanium alloys to perform an analysis of the boundary and the relationship between the available slip systems. Additionally, updated constitutive relations are presented that account for the α/β and are discussed in the context of the current CPFEM implementation.

1.6 Significance of Research

Enhancing or even supplanting experimental techniques with computational tools requires not only confidence in model outputs, but also an exemplary understanding of model assumptions and limitations. More importantly, computational efficiency must move to the forefront in priority for research codes to shift towards being design codes. But, their robust nature must be kept intact during this evolution.

The significance of this research spans multiple domains, with the common focus of improving computational tools for extension to rapid decision making in material design and optimization. The significance of this research includes:

- ◇ The coupling of CPFEM simulations of the SNI process with experiments (conducted by a collaborator) for parameter extraction and evaluation of model validity and form for individual phase and interface properties/responses.
- ◇ The development of constitutive relations that account for the slip resistance associated with the presence of the α/β interface.
- ◇ The extension of the CPFEM model and fatigue simulation results for MKS

model calibration.

- ◇ The application of IDEM to CPFEM and accelerated MKS-generated datasets for both local (grain level) and global (polycrystalline) properties/responses to pursue robust material designs for ranged sets of specified performance objectives.

1.7 Thesis Structure

This dissertation is organized as follows. Chapter 2 provides background information for Ti-64, crystal plasticity finite element method, spherical indentation theory, fatigue indicator parameters, and the inductive design exploration method (IDEM).

The research results in this thesis are subdivided into four categories: FEM simulations of spherical indentation (Chapter 3), CPFEM simulations of spherical indentation (Chapter 4), CPFEM extension to fatigue simulations (Chapter 5), the inductive design exploration method applied to Ti-64 (Chapter 6), and CPFEM slip transfer criteria specific to $\alpha + \beta$ titanium alloys (Chapter 7). Each of these chapters is organized with an introduction, methodology, discussion/results, and summary sections. They are organized in this manner because each chapter represents a submitted journal article or manuscript in preparation.

Finally, Chapter 8 summarizes the significant findings of this dissertation and the overall contributions of this research as a whole. Important conclusions and a short summary of each chapter is provided along with potential future work extensions for each chapter. Last, there is a brief discussion about future research directions that may build upon the findings of this dissertation.

CHAPTER 2

BACKGROUND AND METHODOLOGY

2.1 Introduction

Chapter 2 reviews multiple topics that are prevalent throughout this dissertation, including titanium alloys and specifically Ti-6Al-4V (Section 2.2), crystal plasticity and its extension to Ti-6Al-4V (Section 2.3), the fatigue of metals with an emphasis on fatigue crack nucleation in Ti-6Al-4V (Section 2.4), indentation with an emphasis on spherical indentation (Section 2.5), slip transfer across grain boundaries (Section 2.6), and finally the inductive design exploration method (Section 2.7).

2.2 Titanium and its Alloys

Titanium alloys play an integral role in the aerospace industry for applications such as airframes and aeroengines because of their high strength-to-weight ratio, fatigue resistance, and resistance to corrosion. Titanium alloys have also been widely used in biomedical applications (e.g. fabrication of implants) because of their biocompatibility, while the automotive industry has employed titanium for weight savings in higher-end vehicles.

At 882°C, pure titanium undergoes an allotropic phase transformation from hexagonal close-packed (HCP) crystal structure to body-centered cubic (BCC) crystal structure [60]. Some alloying elements (e.g. Al, O) added to pure titanium cause the transformation temperature of the resultant alloy to increase; these elements are known as α stabilizers. Other alloying elements (e.g. V, Mo) decrease the transformation temperature and they are known as β stabilizers. There are also a few alloying elements (Sn, Zr) that have very little effect on the transformation temperature of

the resultant alloy and are thought of as α stabilizers as well. The use of α and β also extends to the naming convention of titanium alloys.

In general, titanium alloys can be categorized as α or near α, $\alpha+\beta$, or β alloys [61]. The $\alpha + \beta$ titanium alloys, such as Ti-6Al-4V, contain a combination of α- and β-phases, which result in a wide range of microstructures and mechanical properties depending on the heat treatment and thermomechanical processing routes. Specifically, the microstructure can range from bimodal, meaning a combination of α-grains and β-grains with embedded α-laths, to fully lamellar.

The c/a ratio of α-titanium is 1.587 and the room temperature lattice parameters a and c for the HCP unit cell are 0.295 nm and 0.468 nm, respectively. This c/a ratio is less than the ideal ratio of 1.633 for the HCP crystal structure, which can have an effect on the types of active slip systems if the material is undergoing deformation twinning. The unit cell of the BCC β phase has has side length of 0.332 nm at 900°C. The elastic properties of α-titanium are anisotropic due to the nature of the HCP crystal structure. The elastic modulus of α-titanium is largest when loaded parallel to the c-axis and lowest when loaded perpendicular to the c-axis.

Titanium has a density of 4.50 g/cm^3, which makes it less dense than iron (7.9 g/cm^3), but more dense than aluminum (2.7 g/cm^3) and magnesium (1.7 g/cm^3). However, titanium has a much higher yield strength than aluminum and magnesium and a similar yield strength as iron [60]. Titanium has the second highest strength-to-weight ratio (Mg is higher), which is one of the reasons it is quite advantageous for applications that place a high priority on weight-savings.

2.2.1 Phases of Ti-6Al-4V

Ti-6Al-4V (Ti-64) is one of the more commonly used titanium alloys because of its balance of strength, ductility, fatigue, and fracture properties [60], which is mainly due to its balance of α and β stabilizers (Al and V, respectively). Ti-64 made up

approximately 56% of the titanium market in the United States in 1998 [60]. A representative chemical composition for Ti-64 is shown in Table 2.1 [62].

Table 2.1: Chemical composition of Ti-6Al-4V, wt.% [62]

Al	V	Fe	O	C	N	H	Other	Ti
5.5-6.75	3.5-4.5	0.40	0.20	0.080	0.030	0.15	0.30	Bal

In terms of deformation modes, HCP crystal structures are made up of four types of slip families: are basal slip $\{0001\}\langle 11\bar{2}0\rangle$, prismatic slip $\{10\bar{1}0\}\langle 11\bar{2}0\rangle$, $\langle \mathrm{a}\rangle$ pyramidal slip $\{10\bar{1}1\}\langle 11\bar{2}0\rangle$, and $\langle \mathrm{a}+\mathrm{c}\rangle$ pyramidal slip $\{10\bar{1}0\}\langle 11\bar{2}3\rangle$. These slip planes and their associated slip directions are depicted in Figure 5.1.

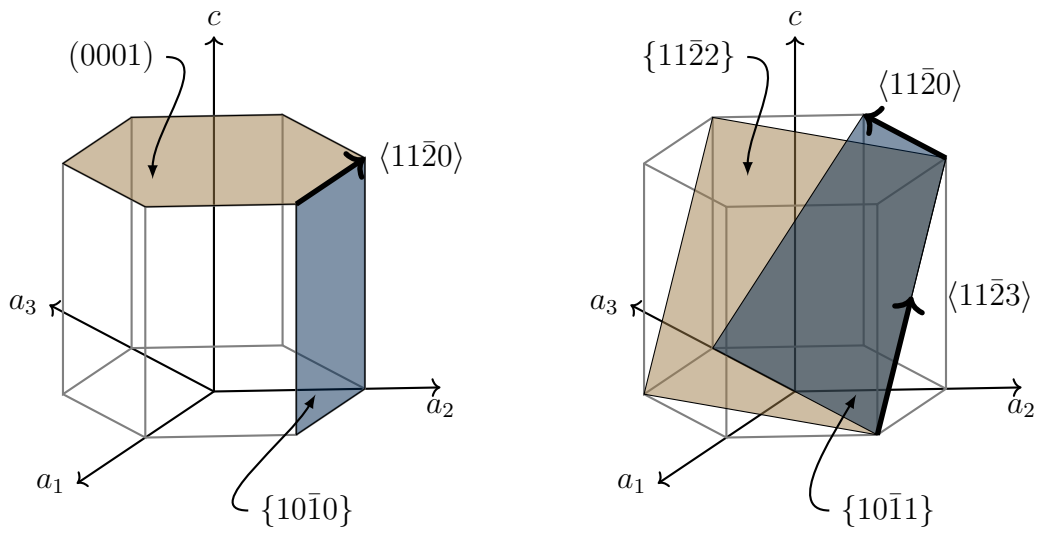

(a) Basal and Prismatic Slip **(b)** Pyramidal Slip

Figure 2.1: Schematic of (a) basal and prismatic slip plane and associated slip directions along with (b) $\langle \mathrm{a}\rangle$ pyramidal and $\langle \mathrm{a}+\mathrm{c}\rangle$ pyramidal slip plane and associated slip directions.

In titanium and its alloys, prismatic slip has the smallest critical resolved shear stress (CRSS), followed by basal slip and then the pyramidal slip families. Deformation twinning can also be present in Ti alloys, but their presence is severely diminished at room temperature with an Al content above 6% [63]. In general, the BCC crystal structure has up to 48 slip systems, but it is common to only consider the twelve

$\{110\}\langle 111\rangle$ and twelve $\{112\}\langle 111\rangle$ slip systems. BCC crystal structures also have twenty-four $\{123\}\langle 111\rangle$ slip systems, but they can be very difficult to activate.

Ti-64 is made up of an α matrix that is combined with β grains [64]. The lamellar colonies are formed during cooling and are also related to the -matrix, meaning there is a Burgers orientation relation (BOR) that relates the HCP and BCC crystal orientations. The BOR follows:

$$(110)_\beta \parallel (0001)_\alpha \,\&\, [1\bar{1}1]_\beta \parallel [11\bar{2}0]_\alpha\,, \tag{2.1}$$

which was originally determined for zirconium [65] and then later confirmed for titanium [66]. In general, there are 12 possible HCP variants for a single BCC crystal [60], but typically only one of them is present in the duplex microstructure. A graphical representation of α and β relationship in a colony grain is shown in Figure 2.2.

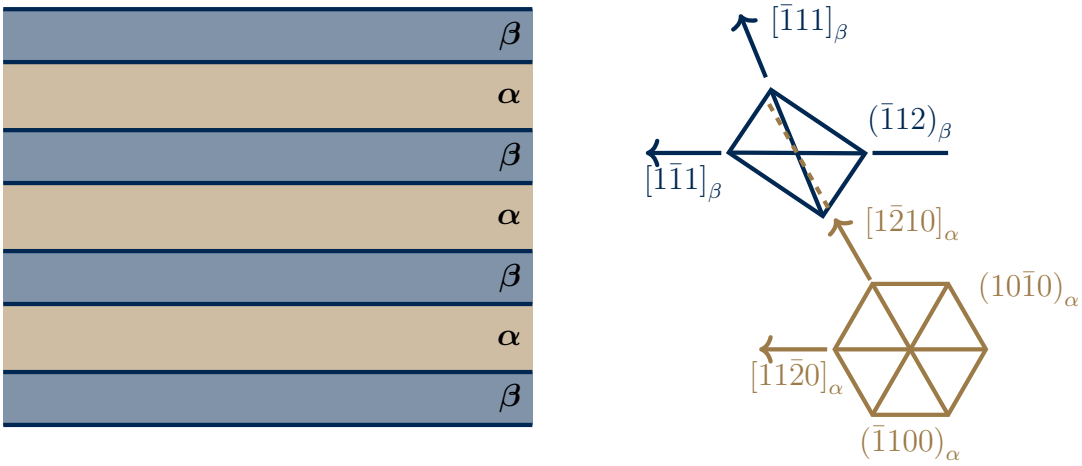

Figure 2.2: Schematic representation of the crystallographic relationship between α and β phase in colony grains (adapted from [60]).

In addition to $\alpha+\beta$ colonies, which can affect the material response due to boundary hardening and strengthening because of a high dislocation density, the β phase can also be hardened by secondary α which forms as precipitates inside the β lamellae [60]. This feature is not considered in this work.

2.3 Crystal Plasticity Finite Element Model for Ti-6Al-4V

To model the complex behavior of the $\alpha + \beta$ Ti-64, a fully three-dimensional computational crystal plasticity finite element method (CPFEM) model is used in this work. The crystal plasticity model follows from previous titanium-specific work [39, 40, 42–44, 50–57], starting with computational fatigue studies for bi-modal $\alpha + \beta$ titanium that employed a two-dimensional CPFEM model [51, 52]. This model was extended to a three-dimensional CPFEM formulation [39, 53, 54] and subsequently modified to capture strain rate sensitivity in the model for complex loading histories [40, 56], to examine slip band evolution in HCF [41], to determine extreme value distributions related to FIPs [42, 67], and to explore the impact of various $\alpha + \beta$ textures on the resultant FIP distributions [43, 44, 50]. The Ti-64 constitutive model is a rate-dependent, microstructure-sensitive model used to capture the first order effects on the macroscopic stress-strain response due to primary-α grains and $\alpha + \beta$ colony grains. As discussed in the previous section, the microstructure has a significant effect on the fatigue response of titanium and its alloys.

The development of the crystal plasticity theory has occurred over the last 50 years, with significant work being done by many authors [2–13]. However, simulations have only been mainstream for approximately the last 25 years, enabled by the increase in computational power. The first crystal plasticity simulation included two slip systems and was performed in 1982 [68] while the first three-dimensional simulations were performed in 1991 [69, 70].

For the introduction of crystal plasticity theory, it is important to start with the kinematic description of the elastic-plastic deformation of single crystals based on large strain theory to connect dislocation slip along crystallographic slip planes to the micromechanical behavior of a deforming single crystal or an aggregate of crystals [67].

2.3.1 Kinematics of Crystalline Deformation

Consider a body composed of material points, each with an initial (reference) position $\mathbf{x}$ at time t_0. At a time $t > t_0$, the current position of the material point is $\mathbf{X}$. The deformation gradient, $\mathbf{F}$, is defined as the a differential line segment mapping the reference configuration to the current configuration, i.e.

$$\mathrm{d}\mathbf{x} = \mathbf{F} \cdot \mathrm{d}\mathbf{X} \, . \tag{2.2}$$

For large strain based crystal plasticity, the total deformation gradient can be decomposed into elastic ($\mathbf{F}^{\mathrm{e}}$) and plastic parts ($\mathbf{F}^{\mathrm{p}}$). The total deformation gradient is then written as a multiplicative elastic-plastic decomposition of the form

$$\mathbf{F} = \mathbf{F}^{\mathrm{e}} \cdot \mathbf{F}^{\mathrm{p}} \, . \tag{2.3}$$

The mathematical decomposition of the total deformation gradient separates the specific mechanisms of deformation into two separate categories. The rigid body rotation and elastic stretching of the lattice is described with $\mathbf{F}^{\mathrm{e}}$, while the dislocation motion through the lattice along the various slip planes is captured with $\mathbf{F}^{\mathrm{p}}$. This decomposition is a mathematical construct proposed by [71] for dislocated crystals and [3] for macroscale plasticity models. Note that $\det\left(\mathbf{F}^{\mathrm{p}}\right) = 1$ due to plastic incompressibility. In reality, all deformation modes occur simultaneously. This decomposition is shown schematically in Figure 2.3. The slip direction unit vector, $\mathbf{s}^{(\xi)}$, for the ξ^{th} slip system is mapped from the intermediate to the current configuration by

$$\mathbf{s}^{(\xi)} = \mathbf{F}^{\mathrm{e}} \cdot \mathbf{s}_0^{(\xi)}, \tag{2.4}$$

and the slip plane normal unit vector, $\mathbf{n}^{(\xi)}$, in the current configuration is mapped from the intermediate configuration by

$$\mathbf{n}^{(\xi)} = \mathbf{n}_0^{(\xi)} \cdot (\mathbf{F}^{\mathrm{e}})^{-1} \,. \tag{2.5}$$

This mapping ensures orthogonality between the slip plane normal and slip direction unit vectors, which can be shown by

$$\mathbf{n}^{(\xi)} \cdot \mathbf{s}^{(\xi)} = \mathbf{n}_0^{(\xi)} \cdot (\mathbf{F}^{\mathrm{e}})^{-1} \cdot \mathbf{F}^{\mathrm{e}} \cdot \mathbf{s}_0^{(\xi)} = \mathbf{n}_0^{(\xi)} \cdot \mathbf{s}_0^{(\xi)} = 0 \tag{2.6}$$

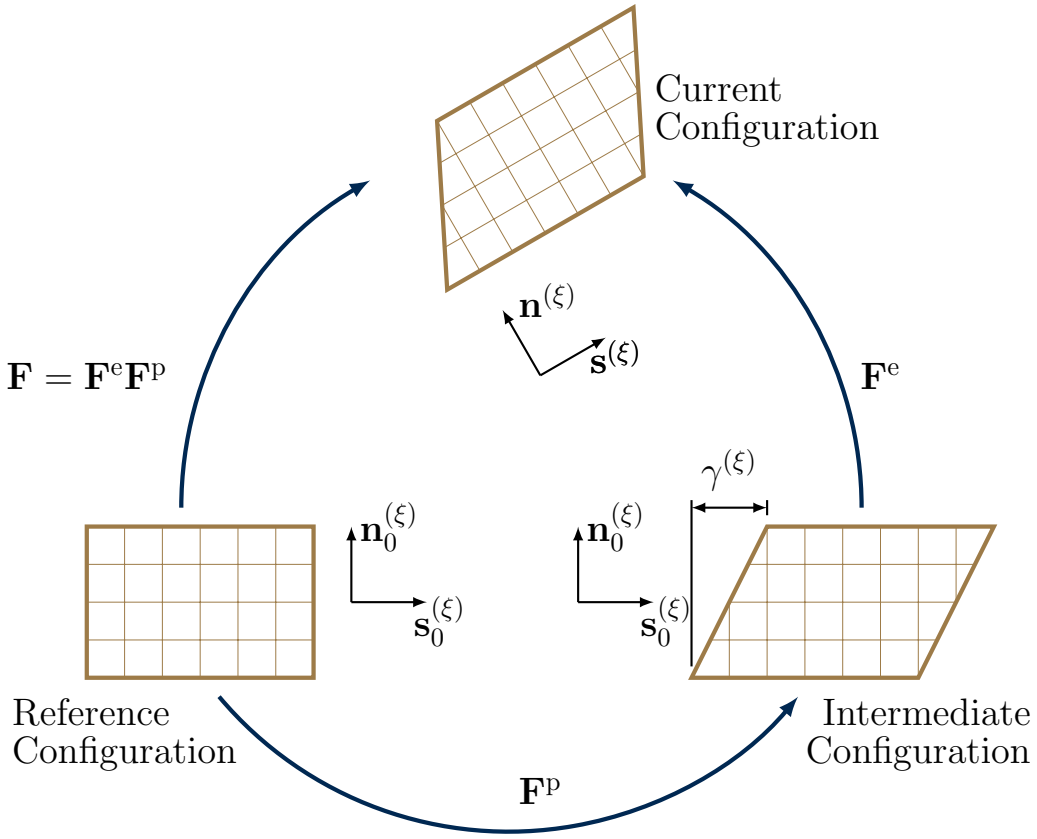

Figure 2.3: Schematic representation of the elastic and plastic deformation gradients in a crystalline solid [3, 71].

The velocity gradient in the current configuration, $\mathbf{L}$, is defined as

$$\mathbf{L} = \dot{\mathbf{F}} \cdot (\mathbf{F})^{-1} \tag{2.7}$$

and can be decomposed into elastic and plastic portions by

$$\mathbf{L} = \dot{\mathbf{F}} \cdot (\mathbf{F})^{-1} = \dot{\mathbf{F}}^{\mathrm{e}} \cdot \mathbf{F}^{\mathrm{e}} + \mathbf{F}^{\mathrm{e}} \cdot \dot{\mathbf{F}}^{\mathrm{p}} \cdot (\mathbf{F}^{\mathrm{p}})^{-1} \cdot (\mathbf{F}^{\mathrm{e}})^{-1} \ . \tag{2.8}$$

The velocity gradient can also be written as

$$\mathbf{L} = \mathbf{D} + \mathbf{W} \ , \tag{2.9}$$

where $\mathbf{D}$ is the symmetric rate of deformation tensor and $\mathbf{W}$ is the anti-symmetric rate of spin tensor. The rate of deformation and rate of spin tensors can also be decomposed into elastic and plastic portions, i.e.

$$\mathbf{D} = \mathbf{D}^{\mathrm{e}} + \mathbf{D}^{\mathrm{p}} \ , \mathbf{W} = \mathbf{W}^{\mathrm{e}} + \mathbf{W}^{\mathrm{p}} \ . \tag{2.10}$$

The shearing rate, $\dot{\gamma}^{\xi}$, is related to the plastic velocity gradient through

$$\mathbf{L}_0^{\mathrm{p}} = \sum_{\xi=1}^{\mathrm{N}} \dot{\gamma}^{(\xi)} \left(\mathbf{s}_0^{(\xi)} \otimes \mathbf{n}_0^{(\xi)} \right) = \dot{\mathbf{F}}^{\mathrm{p}} \cdot (\mathbf{F}^{\mathrm{p}})^{-1} \tag{2.11}$$

where $\mathbf{L}_0^{\mathrm{p}}$ is the plastic velocity gradient in the intermediate configuration. The elastic deformation gradient can also be found given the total and plastic deformation gradient, i.e.

$$\mathbf{F}^{\mathrm{e}} = \mathbf{F}^{\mathrm{p}} \cdot \mathbf{F}^{-1} \ . \tag{2.12}$$

The elastic Green strain tensor, $\mathbf{E}^{\mathrm{e}}$, is defined as

$$\mathbf{E}^{\mathrm{e}} = \frac{1}{2} \left[(\mathbf{F}^{\mathrm{e}})^{\mathrm{T}} \cdot \ \mathbf{F}^{\mathrm{e}} - \mathbf{I} \right] \ . \tag{2.13}$$

where $\mathbf{I}$ is the second order identity tensor. The symmetric second Piola-Kirchhoff stress tensor is

$$\boldsymbol{\sigma}^{\mathrm{PK2}} = \mathbb{C}_0 : \mathbf{E}^{\mathrm{e}} \tag{2.14}$$

where $\mathbb{C}_0$ is the fourth-order elastic stiffness tensor in the intermediate configuration. Note that $\mathbf{E}^{\mathrm{e}}$ and $\boldsymbol{\sigma}^{\mathrm{PK2}}$ are also defined in terms of the intermediate configuration. The Cauchy stress, $\boldsymbol{\sigma}$, can be found by mapping the second Piola-Kirchhoff stress to the current configuration, as defined by

$$\boldsymbol{\sigma} = \frac{1}{\det\left(\mathbf{F}^{\mathrm{e}}\right)} \left[\mathbf{F}^{\mathrm{e}} \cdot \boldsymbol{\sigma}^{\mathrm{PK2}} \cdot \left(\mathbf{F}^{\mathrm{e}}\right)^{\mathrm{T}}\right] \tag{2.15}$$

The resolved shear stress, $\boldsymbol{\tau}$, resides in the intermediate configuration and is therefore calculated from the second Piola-Kirchhoff. The resolved shear stress on each slip system, $\tau^{(\xi)}$, is

$$\tau^{(\xi)} = \boldsymbol{\sigma}^{\mathrm{PK2}} : \left(\mathbf{s}_0^{(\xi)} \otimes \mathbf{n}_0^{(\xi)}\right) \ . \tag{2.16}$$

The fourth-order elastic stiffness tensor in the crystal coordinate system can be related to the fourth-order elastic stiffness tensor in the sample coordinate system according to

$$\mathbb{C}^s = \mathbf{R} \otimes \mathbf{R} : \mathbb{C}^c : \mathbf{R}^{\mathrm{T}} \otimes \mathbf{R}^{\mathrm{T}} \tag{2.17}$$

where $\mathbf{R}$ is an orthonormal rotation matrix that takes the base vectors from the crystal coordinate system to the sample reference coordinate system. It is common practice to define rotation matrices in terms of multiple angles. In this case, the Euler angles are three successive rotations performed to transform the sample orientation to the crystal orientation. There are many different conventions for Euler angles, with the most common convention formulated by Bunge [72, 73]. The Bunge rotations are shown in Figure 2.4, and are described as:

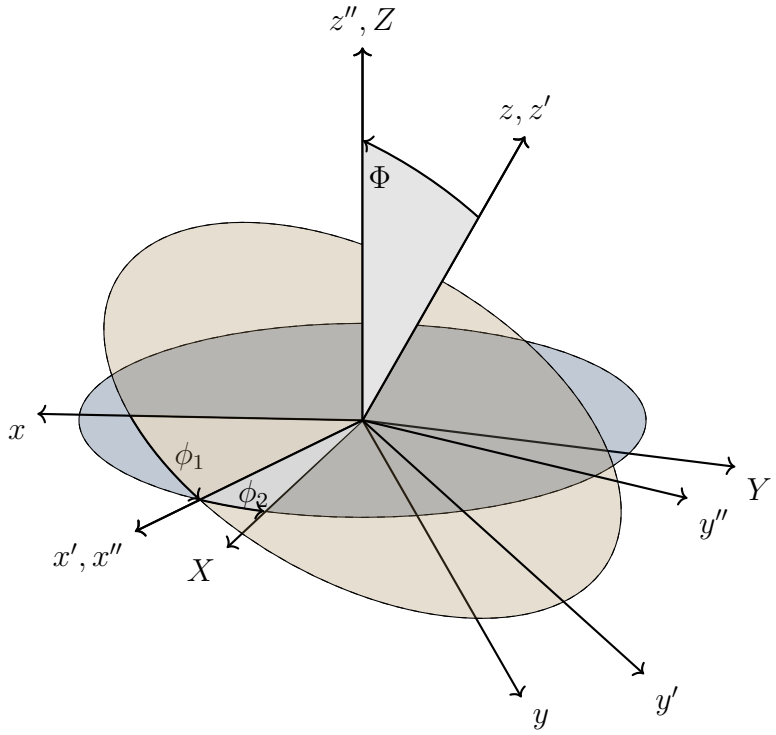

Figure 2.4: The rotation of the Euler angles in order ϕ_1, Φ, ϕ_2 as shown, describes the rotation between the sample and crystal axes (adapted from [74]).

1. Rotate about the z-axis by angle ϕ_1, transforming the x-direction into x' and the y-direction into y'.

2. Rotate about the x'-axis by angle Φ, transforming the z-direction into Z and the y'-direction into y''.

3. Rotate about the Z-axis by angle ϕ_2, transforming the x'-direction into X and the y''-direction into Y.

The angles ϕ_1, Φ, ϕ_2 are Euler angles in Bunge notation. Analytically, the three rotations are expressed by individual rotation matrices. The rotations are:

$$g_{\phi 1} = \begin{pmatrix} \cos(\phi_1) & \sin(\phi_1) & 0 \\ -\sin(\phi_1) & \cos(\phi_1) & 0 \\ 0 & 0 & 1 \end{pmatrix} \tag{2.18}$$

$$g_{\Phi} = \begin{pmatrix} 1 & 0 & 0 \\ 0 & \cos(\Phi) & \sin(\Phi) \\ 0 & -\sin(\Phi) & \cos(\Phi) \end{pmatrix} \tag{2.19}$$

$$g_{\phi 2} = \begin{pmatrix} \cos(\phi_2) & \sin(\phi_2) & 0 \\ -\sin(\phi_2) & \cos(\phi_2) & 0 \\ 0 & 0 & 1 \end{pmatrix} \tag{2.20}$$

The three rotation matrices are combined for the complete rotation matrix, expressed as

$$g = \begin{pmatrix} g_{11} & g_{12} & g_{13} \\ g_{21} & g_{22} & g_{23} \\ g_{31} & g_{32} & g_{33} \end{pmatrix} = g_{\phi 2} \cdot g_{\Phi} \cdot g_{\phi 1} \tag{2.21}$$

where the elements of g are

$$\begin{aligned} g_{11} &= \cos(\phi_1)\cos(\phi_2) - \sin(\phi_1)\sin(\phi_2)\cos(\Phi) \\ g_{12} &= \sin(\phi_1)\cos(\phi_2) + \cos(\phi_1)\sin(\phi_2)\cos(\Phi) \\ g_{13} &= \sin(\phi_2)\sin(\Phi) \\ g_{21} &= -\cos(\phi_1)\sin(\phi_2) - \sin(\phi_1)\cos(\phi_2)\cos(\Phi) \\ g_{22} &= -\sin(\phi_1)\sin(\phi_2) + \cos(\phi_1)\cos(\phi_2)\cos(\Phi) \\ g_{23} &= \cos(\phi_2)\sin(\Phi) \\ g_{31} &= \sin(\phi_1)\sin(\Phi) \\ g_{32} &= -\cos(\phi_1)\sin(\Phi) \\ g_{33} &= \cos(\Phi) \end{aligned} \tag{2.22}$$

Note that this definition above transforms from sample orientation to crystal orientation, therefore g^{T} would transform from crystal to sample orientation.

2.3.2 Kinetics of Crystalline Deformation

2.3.2.1 Introduction to Flow Rules

Two types of flow rules [50] have been used previously for crystal plasticity modeling of titanium and its alloys: (i) the Power Law Flow Rule and (ii) the Kocks Activation Enthalpy Flow Rule. The advancement of crystal plasticity has occurred mainly with the study of face-centered cubic (FCC) materials with the Power Law flow rule, which has the form

$$\dot{\gamma}^{(\xi)} = \dot{\gamma}_0 \left| \frac{\tau^{(\xi)}}{\tau^{(\xi)}_{CRSS}} \right|^n \operatorname{sgn}\left(\tau^{(\xi)}\right) \quad , \tag{2.23}$$

where $\dot{\gamma}^{(\xi)}$ is the shearing rate on the ξ slip system, $\dot{\gamma}_0$ is the reference rate of shearing, $\tau^{(\xi)}$ is the resolved shear stress, $\tau^{(\xi)}_{CRSS}$ is the slip system deformation resistance, and n is the rate sensitivity parameter. The rate independent limit occurs as $n \to \infty$. With this formulation, every slip system is defined as active unless the resolved shear stress is exactly zero. This category of flow rule is defined as visco-plastic. The sgn (signum) function extracts the sign of a real number and is defined as

$$\operatorname{sgn}(x) = \begin{cases} -1 & \text{if } x < 0 \\ 0 & \text{if } x = 0 \\ 1 & \text{if } x > 0 \end{cases} \quad . \tag{2.24}$$

Advances in constitutive modeling led to a physically motivated constitutive function based on the thermally activated theory for plastic flow [75–78], commonly referred to as the Kocks Activation Enthalpy Flow Rule [76]. The kinetic equation for the shearing rates of each slip system allows them to not be active unless the effective shear stress is larger than some critical value. This category of flow rule is defined as elastic visco-plastic, and represents plastic flow in the thermally activated regime.

Although the ideal shear strength (displacement of one plane of atoms relevant to another) of a material can be quite high (> 1 GPa), a stress which is typically a

fraction of the ideal shear strength is required to initiate plastic deformation. The motion of dislocations is limited by obstacles in the surrounding material; dislocation motion is a kinetic process, described by the Orowan equation [79], which states, for the ξ^{th} slip system,

$$\dot{\gamma}^{(\xi)} = \rho_m^{(\xi)} b \overline{\nu}^{(\xi)} \quad , \tag{2.25}$$

where ρ_m is the mobile dislocation density, b is the magnitude of the Burger's vector, and $\overline{\nu}$ is the average dislocation glide velocity. Obstacles for dislocations fall into two categories: (i) discrete obstacles which are bypassed individually by a moving dislocation or cut by it and (ii) extended, diffuse barriers to dislocation motion which are overcome collectively [77]. The average dislocation glide velocity is given by the kinetic equation,

$$\overline{\nu}^{(\xi)} = \beta b \nu_0 \exp\left\{-\frac{\Delta G^{(\xi)}}{kT}\right\} \quad , \tag{2.26}$$

where ν_0 is the jump frequency, ΔG is the change in Gibbs free energy of activation for the cutting or bypassing of an obstacle, k is the Boltzmann constant, T is the temperature, and β is a dimensionless constant. The relation for the change in Gibbs free energy is dependent on the distribution of obstacles and the corresponding pattern of internal stress, with the general relation for the ξ^{th} slip system given by

$$\Delta G^{(\xi)} = \Delta F \left[1 - \left(\frac{\left|\tau^{(\xi)} - \chi^{(\xi)}\right| - \kappa^{(\xi)}}{D^{(\xi)}}\right)^p\right]^q \tag{2.27}$$

where τ is the resolved shear stress (commonly referred to as the applied stress), χ is the back stress, κ is the threshold stress, D is the drag stress, ΔF is the activation energy required to overcome the obstacles to slip without the aid of an applied shear stress, and p and q are model parameters that attempt to reflect the "shape" of the many-body obstacle bypass process [75, 76]. The Kocks Activation Enthalpy Flow Rule for the ξ^{th} slip system has the form

$$\dot{\gamma}^{(\xi)} = \dot{\gamma}_0 \exp\left\{-\frac{\Delta F}{kT}\left[1 - \left(\frac{\left|\tau^{(\xi)} - \chi^{(\xi)}\right| - \kappa^{(\xi)}}{D^{(\xi)}}\right)^p\right]^q\right\} \operatorname{sgn}\left(\tau^{(\xi)} - \chi^{(\xi)}\right) \tag{2.28}$$

A slip system is considered 'active' when the numerator of the flow rule is greater than zero, i.e.,

$$\dot{\gamma}^{(\xi)} = \begin{cases} 0 & \text{if } \left|\tau^{(\xi)} - \chi^{(\xi)}\right| - \kappa^{(\xi)} \leq 0 \\ \dot{\gamma}^{(\xi)} & \text{if } \left|\tau^{(\xi)} - \chi^{(\xi)}\right| - \kappa^{(\xi)} > 0 \end{cases} . \tag{2.29}$$

As an example of typical values for this particular flow rule, $\dot{\gamma}_0$ can range between 10^6 to 10^{10} (1×10^7 s^{-1} for Mg [80]), p from 0 to 1 [76], and q from 1 to 2 [76]. Representative values for ΔF and possible sources are in Table 2.2 [78], in addition to the general range of $0.05\mu b^3 \leq \Delta F \leq 2.0\mu b^3$ [81].

Table 2.2: Characteristics of Obstacles [78]

Obstacle Strength	ΔF	Example
Strong	$2.0Gb^3$	Dispersions; large/strong precipitates
Medium	$0.2Gb^3 - 1.0Gb^3$	Forest dislocations; small/weak precipitates
Weak	$< 0.2Gb^3$	Lattice resistance; solution hardening

The introduction of both of the flow rules (Equations (2.23) and (2.29)) is helpful in displaying the types of information needed to define dislocation motion for various slip systems and crystal structures. For example, the resolved shear stress value in Equation (2.23) might be a single value for FCC material where all of the slip systems are of the same family (i.e.$\{111\}\langle\bar{1}10\rangle$), but this is not the case for BCC or HCP materials, which have multiple slip families that each have a distinct critical resolved shear stress. In later chapters, more detail will be provided about the flow rule used in this work as well as each of the constitutive relations.

2.3.2.2 Flow Rule and Evolution Equations for Ti-6Al-4V

The flow rule used for Ti-6Al-4V is an expanded power law flow rule, i.e.

$$\dot{\gamma}^{(\xi)} = \dot{\gamma}_0 \left\langle \frac{\left|\tau^{(\xi)} - \chi^{(\xi)}\right| - \kappa^{(\xi)}}{D^{(\xi)}} \right\rangle^{M} \operatorname{sgn}\left(\tau^{(\xi)} - \chi^{(\xi)}\right), \tag{2.30}$$

where $\dot{\gamma}_0$ is the reference shearing rate, $\tau^{(\xi)}$ is the resolved shear stress, $\chi^{(\xi)}$ is the back stress, $\kappa^{(\xi)}$ is the threshold stress, $D^{(\xi)}$ is the drag stress, and M is the inverse strain-rate sensitivity exponent. The back stress represents the kinematic hardening of the ξ^{th} slip system. As defined by Prager [82], the back stress accounts for the translation of the yield surface during the process of plastic loading. These effects lead to a dependence of reverse yielding on pre-strain in the forward direction. McDowell [83] offers several physical origins of back stress in polycrystalline metals: (i) differential yielding among grains with hard and soft orientations, (ii) pile-ups of dislocations against hard boundaries (e.g. grain boundaries), (iii) differential resistance to slip in forward or reverse directions in certain systems by virtue of irreversible pinning mechanisms in the presence of planar dislocation structures in second phases (or Taylor lattices), and (iv) distribution of short range barriers to thermally activated dislocation motion and anelastic bowing of dislocations. The back stress term is represented by a self-hardening form of the Armstrong-Frederick direct hardening/dynamic recovery relation and takes the form

$$\dot{\chi}^{(\xi)} = h\dot{\gamma}^{(\xi)} - h_D \chi^{(\xi)} \left|\dot{\gamma}^{(\xi)}\right| \quad , \tag{2.31}$$

where h and h_D are the direct hardening and dynamic recovery coefficients, respectively. The back stress values for α-titanium are generally very low, on the order of 5-10 MPa. Clear and concise definitions for the threshold stress and drag stress can be found in the literature [81, 84]. In some models, the threshold stress represents the long range (non-thermally activated) obstacles and the drag stress represents the short range (thermally activated) obstacles. However, due to the construction of the constitutive model, the threshold stress (located in the numerator) is an evolving term while the drag stress is held constant throughout deformation. Therefore, for

the purposes of this constitutive model, the drag stress represents the Peierls resistance and the threshold stress represents all other remaining obstacles to dislocation motion.

The threshold stress represents the isotropic hardening of the ξ^{th} slip system. Isotropic hardening grows the yield surface (in all directions) when the material is plastically deformed. In this model, the threshold stress accounts for a Hall-Petch strength term and a softening term due to breakdown of short-range order. The threshold stress takes the form

$$\kappa^{(\xi)} = \frac{\kappa_y}{\sqrt{d}} + \kappa_s^{(\xi)} \quad , \tag{2.32}$$

where, κ_y is the Hall-Petch slope, d is the man slip distance in the α-phase (primary or secondary), and $\kappa_s^{(\xi)}$ is a softening parameter. The evolution of the threshold stress is governed solely by the softening term (μ is the softening rate coefficient), which follows a dynamic recovery law and takes the form

$$\dot{\kappa}^{(\xi)} = \dot{\kappa}_s^{(\xi)} = -\mu\kappa_s \left|\dot{\gamma}^{(\xi)}\right| \quad . \tag{2.33}$$

The drag stress also represents the isotropic hardening of the ξ^{th} slip system, but does not evolve (i.e., $\dot{D}^{(\xi)} = 0$) and represents just the Peierls resistance, which can be approximated as the difference in between the CRSS (τ_{CRSS}) and the initial threshold stress [41], i.e.

$$D^{(\xi)} = \tau_{CRSS}^{(\xi)} - \kappa^{(\xi)}\big|_{t=0} \, . \tag{2.34}$$

It is a common assumption in the literature that $\alpha + \beta$ titanium is stronger than α titanium and the α/β interface is one of the main contributors to the increase in strength [85]. Currently, the constitutive relations assume an increase in basal and prismatic slip system CRSS values for colony grains, $\tau_{CRSS}^{(\xi)}(\alpha+\beta) = 1.25\tau_{CRSS}^{(\xi)}(\alpha)$

[41]. Additionally, the diameter used in the threshold stress (Equation (4.8)) is assumed to be the α-lath spacing for the hard orientations in the colony grains. Finally, the CPFEM model does not differentiate between the primary-α and $\alpha + \beta$ colony grains in terms of elastic stiffness. This coarse assumption is based on comparing with experimental information on cyclic stress-strain response at the macroscale rather than at the scale of individual phases. However, the elastic constants for $\alpha + \beta$ Ti-6242 have been found to be extremely close to the elastic constants for the α-phase of the same material [86].

Single crystal elastic constants for α-titanium are assigned to all grains in the polycrystal [43]; the $\alpha+\beta$ colonies are predominantly composed of α laths. The crystal plasticity formulation is coded into an Abaqus/Standard [87] via a User MATerial subroutine (UMAT) [88]; the numerical integration scheme is similar to that of fully implicit method [89].

2.3.3 Implementation of CPFEM

Given the kinematics and kinetics of crystal plasticity provided in Sections 2.3.1 and 2.3.2, respectively, there are also some necessary details to understand for the proper implementation of CPFEM. In this work, Abaqus/Standard is used in conjunction with a User Material Subroutine (UMAT) to deploy CPFEM.

This interplay between Abaqus at the UMAT is shown in Figure 2.5. The finite element solver applies the loading conditions and boundary conditions for the digital specimen which are then determined for each integration point. Abaqus/Standard then passes the total deformation gradient for an updated time increment to the UMAT. The UMAT performs an implicit integration scheme to determine the stress and the Jacobian matrix (tangent stiffness matrix). The UMAT also updates the internal state variables needed to track the deformation history at a given integration point. Then the UMAT passes this information back to Abaqus and the process is

repeated for each integration point.

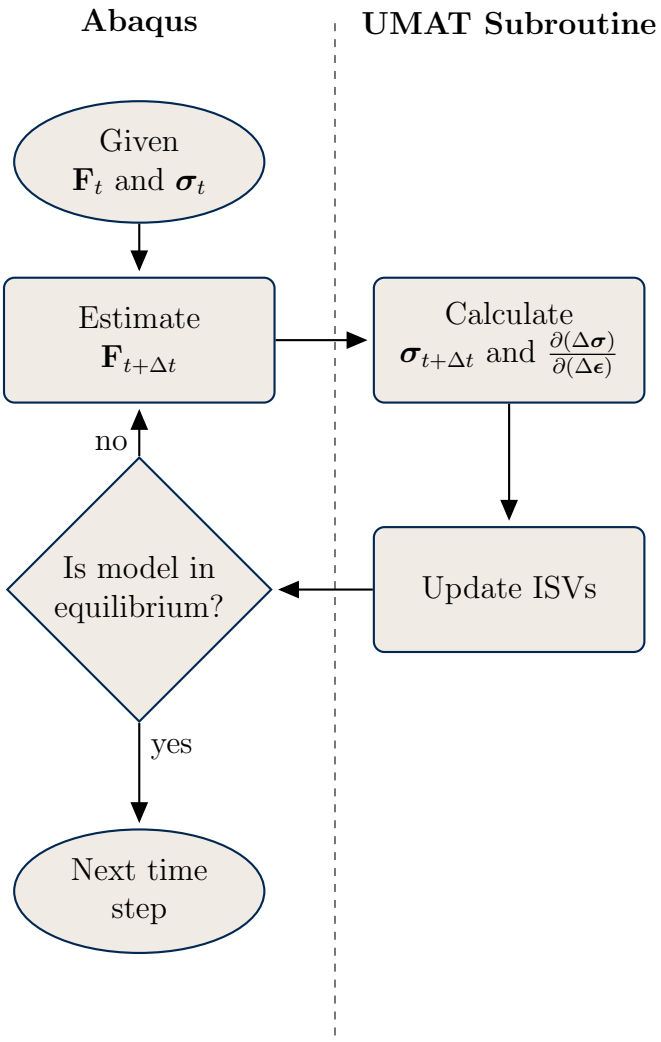

Figure 2.5: The interaction of Abaqus and the UMAT (adapted from [90])

When all of the updated local stresses and Jacobian matrices have been estimated, the finite element solver then determines if the model is in equilibrium. If the equilibrium criteria have been met, the solution is accepted for that specific time increment and the time is further increased and the process repeated. If the equilibrium criteria are not met, typically the finite element solver will reduce the time step and recalculate the stress and Jacobian matrix for each integration point.

As previously stated, this CPFEM UMAT performs an implicit integration scheme [90] that is similar to that of Cuitino and Ortiz [89]. The semi-implicit integration

scheme is detailed in Appendix A of Przybyla's Ph.D. thesis [67], but it might aid the reader to gain some perspective on the connection between the kinematics and kinetics discussed in previous sections.

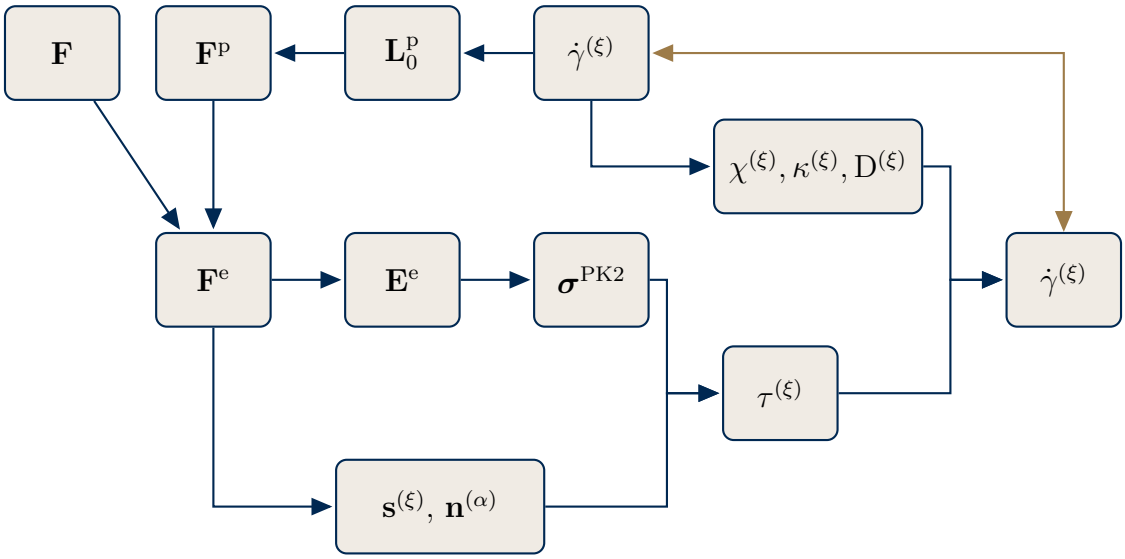

Figure 2.6: Flowchart for the modified implicit integration algorithm based on Cuitino and Ortiz [89] and altered by McGinty [90] (adapted from [91]).

The objective of the semi-implicit integration scheme is to determine values for the independent variables at the end of the time step. Therefore, the current value of the slip rates are estimated with a Newton-Raphson iterative technique and the other independent variables are estimated from the updated slip rates. The Newton-Raphson iterative technique set the flow rule equal to zero and approximates the value of $\dot{\gamma}^{(\xi)}$ as a Taylor series expansion about the slip rates from the previous estimate. This procedure is shown in flowchart form in Figure 2.6. The main feature is the comparison of slip rates values and iterative updating until their difference is within an acceptable tolerance value.

2.4 Fatigue of Metals

Fatigue crack nucleation and fatigue crack growth are governed by different damage processes and have been described by various classification schemes. One classification scheme commonly referenced in the literature defines two regimes of crack formation and early growth, Stage I and Stage II [92]. Stage I is the combination of crystallographic crack nucleation and microstructurally small crack growth and is governed by the activity of localized crystallographic slip, particularly on a single slip system. Stage II cracks growth is characterized by dislocation slip along multiple crystallographic slip planes, therefore the crack grows in a direction that does not necessarily coincide with a specific crystallographic direction. Similar to this classification system, the total fatigue life (N_T) can be expressed as the summation of three distinct stages [29, 56, 67],

$$N_T = N_{FOR} + N_{MSC} + N_{MLC}, \tag{2.35}$$

where N_{FOR},N_{MSC}, and N_{MLC} correspond to the number of cycles required for fatigue formation, microstructurally small crack (MSC) growth, and mechanically long crack (MLC) growth, respectively.

Fatigue crack nucleation and early growth in the nucleating phase are commonly combined and denoted as fatigue crack formation. Damage accumulation as a result of irreversible dislocation migration from cycle loading leads to the formation of cracks within a given microstructure. Strain localization can occur when the macroscopic stress state is well below yield strength of the material. Strain localization commonly due to the heterogeneity of the microstructure, including in grains that are favorably oriented for plastic flow as well as in grains that are neighbored by harder grains, harder particles, or inclusions. Also, defects intrinsic to the bulk material due to processing (e.g., voids, vacancies, etc.) can also be likely sites for strain localization. The formation of persistent slip bands (PSBs) is a common source of fatigue crack

nucleation, which can occur either within PSBs or at interfaces such as grain or phase boundaries [93]. PSBs are especially likely to occur on the surface of a material. However, subsurface cyclic plastic strain accumulation can also lead to the formation at cracks, particularly at grain or phase boundaries. The primary focus of the work in this dissertation is on fatigue crack formation.

MSCs are defined as cracks having size and/or crack tip cyclic plastic and damage process zone sizes on the scale of the dominant microstructure barriers such as grain or phase size [94,95]. Because of MSCs limited size, local microstructure features can also have a significant impact on their growth rates. The typical length of MSCs is 3 to 10 grain diameters [94,95]. Once they reach a length of larger than approximately 5 grain diameters, the effect of the local microstructure diminishes as compared to the macroscopic loading conditions. In contrast to MSCs, MLCs are sufficiently large cracks relative to the size of the dominant microstructural features and the crack tip plastic zone size encompasses multiple grains. Therefore, MLCs are typically governed by linear elastic fracture mechanics (LEFM).

2.4.1 Classification of Fatigue Regimes

The classification of fatigue regimes primarily depends on the stress amplitude relative to the material yield strength. Under completely reversed loading, low cycle fatigue (LCF) is characterized by cyclic stress well above the yield strength while high cycle fatigue (HCF) is characterized by cyclic stress well below the yield strength of the material. Because of widespread plastic deformation, small fatigue cracks are quickly distributed throughout the material in LCF, therefore the fatigue life is dominated by crack propagation and coalescence. In contrast, the response in HCF is dominantly elastic with highly heterogeneous plasticity, resulting in the fatigue life being dominated by fatigue crack formation and MSC growth. The primary focus of this dissertation is fatigue crack formation, meaning the cyclic loading work presented

later will focus on the HCF regime.

2.4.2 Fatigue Crack Formation in $\alpha + \beta$ Titanium Alloys

Experimental observations for Ti-6Al-4V have demonstrated that fatigue crack formation is most likely slip dominated [96], but there is not agreement as to the relative importance of various microstructure features in regards to fatigue crack formation. Previous work detailed by Przybyla [67] has illustrated that several different microstructure features, including grain orientation/misorientation and grain size have been identified as possible indicators of fatigue crack formation in $\alpha + \beta$ titanium alloys.

The high cycle fatigue failure of Ti-64 is characterized by more than 85% of the fatigue life spent propagating a crack [97] up to the length of 0.5 mm, as illustrated in Figure 2.7. Ti-64 specimens were cyclically loaded (R=0.1) for a range of strain amplitudes that reside in the HCF regime. There are five different heat treatments shown in Figure 2.7, with no real discernible difference found among them for percent of fatigue life spent propagating a crack from 0.5 mm to failure [97].

As stated earlier, the prismatic and basal slip systems are much easier to activate than any of the pyramidal slip systems. Following with that trend, previous studies have found fatigue crack formation associated with basal planes in Ti-6Al-4V either favorably [55, 98] or unfavorably [99, 100] oriented for slip on the basal plane. Additionally, the size of the primary-α grains is one microstructure feature that might have an effect in fatigue crack formation in $\alpha + \beta$ titanium alloys. For example, it has been found that larger fatigue cracks formed more readily in primary-α grains with longer paths for slip [101] and other studies, specifically for Ti-6246, have noted that the larger primary-α grains contain facets [102, 103].

In the HCF regime, significant scatter is also observed in the overall fatigue lives for titanium alloys. Much of this scatter can be directly related to the distribution

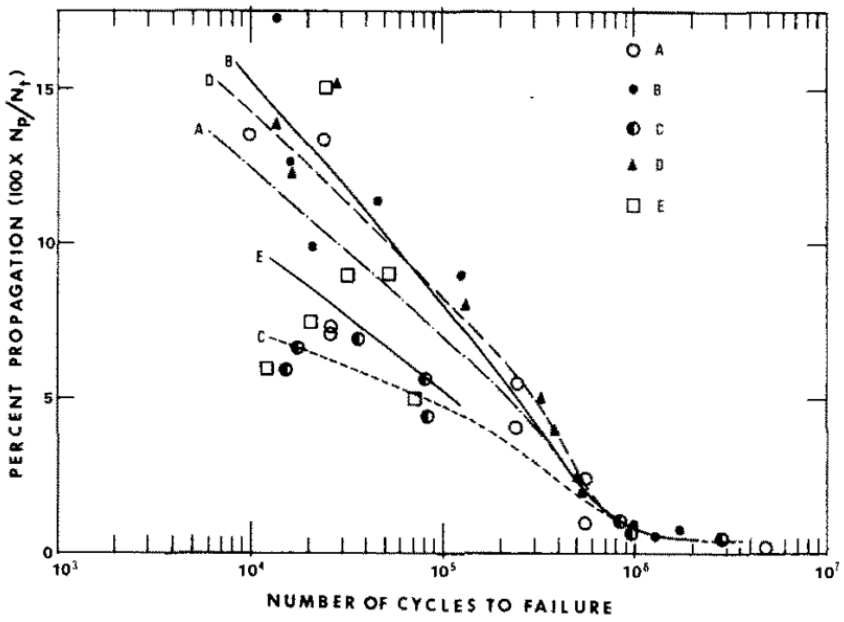

Figure 2.7: Percent of fatigue life spent propagating a crack from 0.5mm to fracture versus number of cycles to failure [97].

of microstructure features and their influence on the local stress-state. For example, previous work has observed a significant increase in the scatter of fatigue life in Ti-6246 as the maximum applied stress was decreased, thus shifting from LCF to HCF [104]. The data from this study is shown in Figure 2.8.

The desired microstructure for fatigue crack formation and early growth resistance in $\alpha + \beta$ titanium alloys is a small grain structure, with short interfaces, and without texture on a micro- or a macroscale [105]. In this work, fatigue crack formation is considered in the HCF regimes, therefore this work will focus on fatigue crack nucleation and MSC growth. MSC and MLC regimes typically comprise a very small fraction of component life, particularly in the HCF regime. As the focus here will be on on HCF, this work will emphasize crack formation and will not consider MSC and MLC growth.

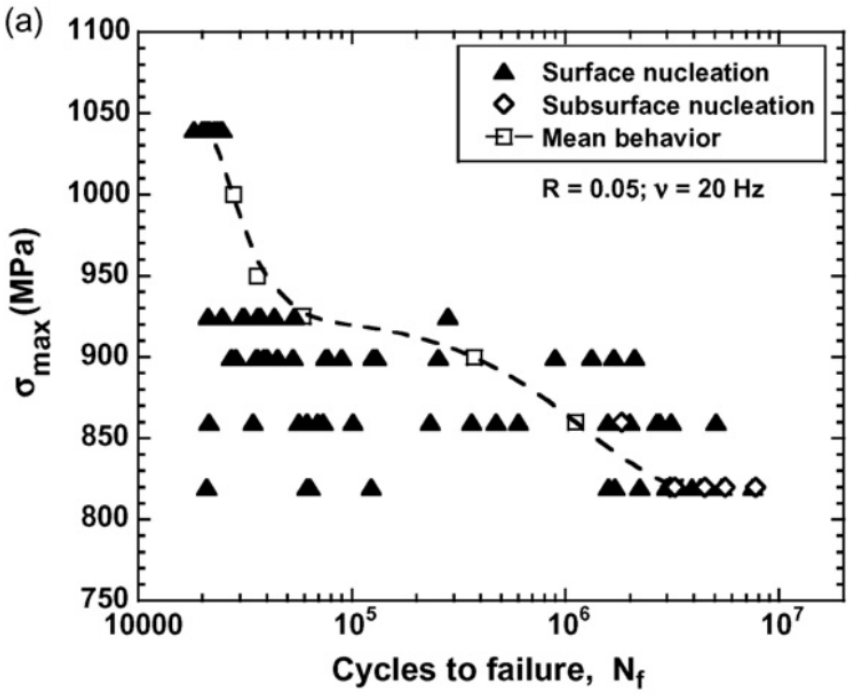

Figure 2.8: The maximum applied stress versus number of cycles to failure for Ti-6246, capturing fatigue variability of Ti-6246 for repeated tests [104].

2.4.3 Fatigue Indicator Parameters

With the consideration of HCF and fatigue crack formation, the driving force for crack nucleation and early growth is highly dependent on the local driving force, which in turn is directly linked to various microstructure features of the material [106]. One such method for quantifying these local driving forces is the use of fatigue indicator parameters (FIPs) [30]. The premise of multiaxial FIPs is to combine the effects of resolved shear and normal stresses for a given plane. In theory, the resolved shear stresses lead to dislocation motion and normal stresses result in the opening of a crack while also reducing the friction between crack surfaces.

FIPs were introduced [27–29] to reflect, in a more explicit manner, the relative roles of reversed and cumulative directional slip at the scale of individual grains or crystalline regions in polycrystalline materials [31]. The selection of a particular FIP is extremely important to accurately capture the deformation mechanism that leads

to fatigue crack formation and early growth. For example, the Fatemi-Socie [107,108] shear-based parameter (FIP_{FS}) originally determined from macroscopic loading has been shown to correlate well in the LCF and HCF regimes for multiaxial fatigue crack initiation [30] in FEM simulations and is defined by

$$FIP_{FS} = \frac{\Delta\bar{\gamma}^p_{max}}{2}\left[1 + k\frac{\bar{\sigma}^n_{max}}{\sigma_y}\right], \tag{2.36}$$

where $\Delta\gamma^p_{max}$ is the maximum cyclic plastic shear strain range, σ^n_{max} is the maximum normal stress acting on the plane of maximum cyclic plastic shear strain, σ_y is the macroscopic yield strength of the material, and k is a constant with typical values between 0.5 and 1. The overbar ($\Delta\bar{\gamma}^p_{max}$, $\bar{\sigma}^n_{max}$) indicates that volumetric averaging should be performed [42] to include averaging over a damage process zone. In FEM simulations, this is performed by averaging neighboring elemental values in some specified manner. The Fatemi-Socie FIP correlates well with the early fatigue behavior of metals that exhibit planar slip [41]. Additionally, FIP values can also be extended to assist in the calculation of life estimates [109–111].

2.4.4 Extreme Value Statistics in Fatigue

As discussed in the previous section, there resides a significant amount of scatter in HCF life curves due to the local microstructure dependence of fatigue crack formation. This variability is primarily due to the extreme value probabilities of microstructure features that lead to fatigue crack formation. Multiple probabilistic approaches have been developed to account for this variability; most of these approaches are based on weakest link theory as well as extreme values (i.e., largest and/or smallest) and use probability distributions to represent the likelihood of fatigue failure given n specimens. For single variable distributions, there exist three types of non-degenerate distributions to which the extreme value distributions can converge for large n [112]. The three possible asymptotic distributions are the Gumbel (Type I), Fréchet (Type

II), and Weibull (Type III) [113]. The expression for each of these distributions is as follows:

$$F_{Y_n}^{I}(y) = \exp\left[-e^{-\alpha_n(y-u_n)}\right], \tag{2.37}$$

$$F_{Y_n}^{II}(y) = \exp\left[-\left(\frac{v_n}{y}\right)^k\right], \tag{2.38}$$

$$F_{Y_n}^{III}(y) = \exp\left[-\left(\frac{\omega - y}{\omega - w_n}\right)^k\right]. \tag{2.39}$$

In the Gumbel distribution, u_n is the characteristic largest value of the initial variate X and α_n is an inverse measure of dispersion of Y_n. The number of samples of the initial variate X in the set of distributions of X from which Y_n is sampled is n. For the Fréchet distribution, v_n is the characteristic largest value of the underlying variable X and k is a shape parameter or inverse measure of the dispersion. In the Weibull distribution, ω is the upper bound of the initial variate X (i.e. $F(\omega) = 1$), w_n is the characteristic largest value and k is the shape parameter. The purpose of comparing these extreme value distributions to fatigue datasets is to determine that one of the distributions models the data in a satisfactory fashion so that its mathematical properties can be used to better understand the data. In previous studies [67], it has been found that the Gumbel distribution more accurately captured the tails of the data distribution when compared to the Weibull or Fréchet distributions.

2.5 Spherical Indentation

Many CPFEM studies [39–44] have used macroscopic stress-strain experimental results for the determination of CPFEM model parameters. There are particular advantages to this strategy, including: well defined experimental procedures and standards, the relative ease of performing specific experiments, and the availability of experimental datasets in the literature. However, there are also limitations to this

method when applying it to multi-phase materials and/or materials of low-symmetry, such as the inability to determine the relative activity of each slip family and/or the lack of microstructural information (e.g., texture, grain size, volume fraction, etc.) needed to accurately generate a digital microstructure. Therefore, the introduction of testing procedures that occur on a length-scale similar to the size of microstructure features are important for determining properties of individual phases and/or features of a given material. One example is indentation testing, which was introduced in the early 20$^{\text{th}}$ Century [114–116]. An advantage of indentation testing over similar micron length scale testing is the relative ease of sample preparation, which leads to a reduced amount of time needed for the implementation of the experimental procedure. In contrast, micron length scale tension or bending specimens require a significant amount of time for specimen preparation [117]. Indentation is compared with other micron scale testing procedures in Figure 2.9.

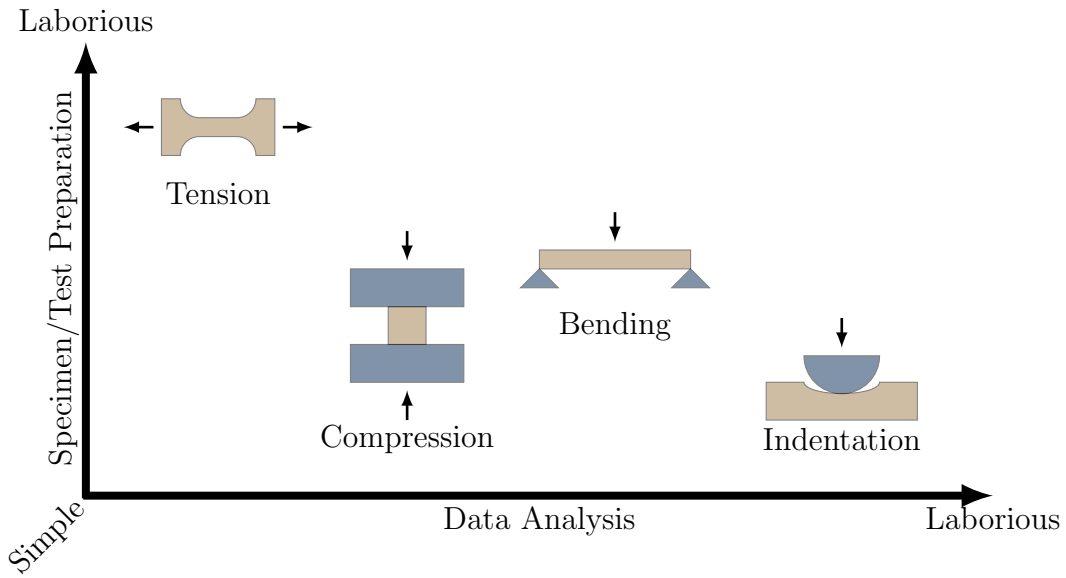

Figure 2.9: Various mechanical testing methods for micron to sub-micron length scales (adapted from [117]).

Indentation testing can be divided into two main types of systems and analyses [47]: (i) traditional hardness measurements obtained by applying a specific force and

measuring the geometry of the impression [118, 119] and (ii) property measurements from the continuous recording of force and displacement during loading and unloading [120]. There are also a number of geometry tip geometries, including flat punch, spherical, Berkovich (three-sides pyramid), and Vickers (four-sided pyramid). The focus of this work is the application of spherical indenters, but other types of indenters will be discussed when referencing specific studies in the literature.

Indentation experiments were initially used to determine the hardness of materials [116]. These tests were appealing because of their versatility for exploring a range of material classes, but the indenter size was initially too large to isolate properties from thin films or single crystals. Therefore, nanoindentation [121] was introduced to perform indents with a minimum depth of a few nanometers to measure elastic modulus in addition to hardness [120]. However, experiments were not able to ascertain the specifics of the material deformation directly beneath the indenter, so FEM simulations were first performed to model the elastic-plastic deformation during the indentation of FCC materials [122]. Early FEM analysis showed that indentation testing could be used to determine the material hardness and stiffness [123]. Additionally, early FEM analysis also showed there was a general correlation between load and indentation depth with mechanical properties such as elastic modulus, yield strength, and strain hardening [122, 123].

More recently, CPFEM studies have been able to estimate CRSS and hardening values for HCP materials from load-displacement curves [124] and analyze the size/shape of the plastic region attributed to indentation in bulk single crystals and thin films [125]. CPFEM results have also produced good agreement when comparing plastic zone sizes with plastic slip traces from nanoindentation experiments [126]. However, these studies have primarily utilized certain specimen symmetry in order to employ reduced portions of the crystal sample while applying pertinent boundary conditions on symmetry planes. This limits the range of orientations and responses

that can be studied with these schemes.

Computational nanoindentation studies are not limited to CPFEM; they have also been explored with molecular dynamics (MD). Small indenter radii (100 nm) are more likely to lead to a defect-free volume under the indenter, while larger indenter radii (1.3 μm) reveal the effects of defects on the load-displacement curve [127]. Nanoindentation MD simulations have also been used to explain grain growth in nanocrystallline nickel as a function of indentation rate [128], while MD nanoindentation simulations of α-Fe have also demonstrated that all previously observed slip plane families were active during deformation [129]. Nanoindentation MD simulations of titanium have found a difference in hardness and elastic modulus based on the shape of the indenter [130]. Finally, nanoindentation simulations performed with the concurrent atomistic-continuum method for FCC crystals have demonstrated that a fully atomistic surface is needed to reproduce the local lattice deformation [131].

One of the common themes among these indentation studies is their use of the load-displacement curve for model calibration/validation. The theory of Hertz [132–135] is the basis for the mathematical formulation used for spherical indentation. Hertz theory assumes the contact between two isotropic surfaces is frictionless and isotropic. From this theory, the relationship between the force and indenter displacement can be represented as

$$P = \frac{4}{3} E_{eff} \left(R_{eff}\right)^{\frac{1}{2}} \left(h_e\right)^{\frac{3}{2}} \tag{2.40}$$

where P is the indentation force, E_{eff} is the effective indentation modulus, R_{eff} is the effective radius, and h_e is the elastic penetration depth. By utilizing Hertz theory for isotropic materials, the effective indentation modulus can be related to the orientation dependent indentation modulus (E_{ind}) via

$$\frac{1}{E_{eff}} = \frac{1}{E_{ind}} + \frac{1 - \nu_i^2}{E_i}. \tag{2.41}$$

The spherical indentation protocols of Kalidindi and Pathak [117,136] have emerged as a high-throughput experimental procedure for quantifying orientation, composition, and processing effects on the elastic and plastic mechanical response of individual phases and constituents [45–47]. The result of this protocol allows for consistent measures for indentation stress and indentation strain, i.e.

$$\epsilon_{ind} = \frac{3}{4\pi}\frac{h}{a} \tag{2.42}$$

$$\sigma_{ind} = \frac{P}{\pi a^2} \tag{2.43}$$

where h is the depth of the indenter and a is the contact radius. Indentation stress and strain are true measures because the contact radius is changing with the deformation, along with the indenter force and displacement. These relationships were evaluated with an isotropic elastic, perfectly plastic material in an FEM model [137] and it was demonstrated that Equations (2.42) and (2.43) provide a description of strain hardening behaviors that closely match the expected response.

2.6 Slip Transfer across Phase and Grain Boundaries

The α/β interface has a large effect on the overall deformation response of titanium due to an increase in hardening. However, the understanding of slip transfer criteria across interphase boundaries is far less understood and developed than that of large-grained metals [58]. According to previous studies, there is quite a variance in the slip activity across the α/β interface, from zero slip activity and restricted basal slip [138] to selective slip system transmission with residual dislocations [139]. In addition, slip transfer is reduced as the coherence of the α/β interface decreases, which occurs because of an increase in boundary energy with deformation [140, 141]. Seal et al. [142] examined the α/β interface of Ti-5Al-2.5Sn with conical indentation and found that as the indenter approached the α/β interface, the dislocation pile-up

around the indenter changes from symmetric to non-symmetric. This is, quite simply, an indication of a lack of dislocation penetration from α to β. Alternatively, TEM in-situ tensile tests performed on Ti-6Al-4V at room temperature have shown there is a stress gradient at the α/β interface, which is caused by dislocations that are present at the boundary [143]. Those dislocations may be present at the boundary because the boundary is an initial source of dislocations [143]. Another study found that α/β interfaces do not hinder slip transfer and the major component to an increase in strength comes from the boundaries between α phase grains and lamellar colony grains [144]. Additionally, for a near-α titanium alloy (Ti-6Al-2Zr-1Mo-1V), the retained β lamellae had a significant influence on slip transmission [145]. Slip transmission from β to α commonly occurred when the BOR was closely followed. Additionally, when the misalignment angles of two α lamellae, separated by β, deviate from the BOR, then slip transmission terminates at the α/β interface. However, this study also showed that this misalignment can be overcome through a cross slip mechanism.

2.6.1 Slip Transfer Models

When a dislocation approaches a grain/phase boundary, the grain boundary can act as (i) an impenetrable barrier to dislocation transfer, (ii) a barrier to dislocation transfer where the dislocation can cross the barrier but might be altered, and (iii) a bridge connecting two grains/phases where the dislocation crosses the bridge without incident [49]. Option (iii) is commonly associated with low Σ boundaries or low-angle boundaries which provide little or no resistance to dislocation transmission across the boundary. Therefore, options (i) and (ii) will be the focus of this dissertation. Previous studies have led to the development of multiple slip transfer criteria; there is an extensive list in the literature [58, 59].

Figure 2.10 describes the relationship of two neighboring slip systems in neighboring grains, denoted Grain A (incoming) and Grain B (outgoing). The grain boundary

plane separates the two grains; it can be defined by the normal vector to the grain boundary plane. the neighboring slip systems are defined by slip direction and slip plane normal directions.

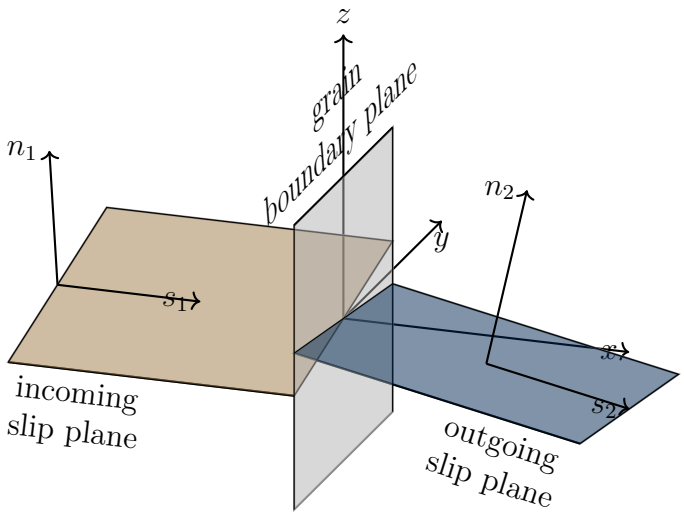

Figure 2.10: Depiction of the intersection of grain A (navy) and grain B (gold). The three angles related to the grain boundary (gray) are between the slip directions, between the slip plane normal directions, and the angle between the traces of the slip planes on the grain boundary plane.

There have been a wide variety of slip transmission factors between neighboring grains proposed in the literature [142, 146–150]. One of the more promising slip transmission factors for the α/β interface of Ti is the Luster parameter [150], defined by

$$\mathrm{M_{Luster}} = (\mathbf{s}_\mathrm{A} \cdot \mathbf{s}_\mathrm{B}) \cdot (\mathbf{n}_\mathrm{A} \cdot \mathbf{n}_\mathrm{B}) \,, \tag{2.44}$$

where $\mathbf{s}$ and $\mathbf{n}$ are the slip direction and slip plane normal vectors for the incoming (A) and outgoing (B) grains, respectively. The Luster parameter varies between 0.0 and 1.0 and can be calculated for each of the incoming-outgoing slip system pairs among neighboring grains. The theory suggests that the slip system pair with the highest Luster parameter value also are the most likely to allow for slip transfer across the grain boundary. Similarly, slip system pairs with low Luster parameter

values are thought to have a lower likelihood for slip transfer across the boundary. Other slip transfer parameters include the use of the twist angle of the incoming and outgoing slip planes with grain boundary [147], the force acting on a particular dislocation [147, 148], residual Burgers vectors [149], and the Schmid factors on the outgoing slip plane [142]. The latest studies of grain and phase boundaries indicate that slip direction and slip plane normal are important for Ti alloys, but there is little evidence to suggest the angle of intersection of the slip planes on the grain boundary plane ($\cos(\theta)$) play a large role [48]. However, it is important to determine which slip systems are active on either side of the boundary.

The challenge of incorporating even the current level of detail into the constitutive relations is the combination of the low symmetry systems in $\alpha + \beta$ titanium alloys combined with a lack of experimental data for model calibration/validation. With a minimum of three different slip families required for arbitrary shape changes, it is extremely difficult to estimate model parameters that provide predictive capabilities when applying them to validation datasets.

It is a common conclusion in the literature that $\alpha + \beta$ titanium is stronger than α titanium and the α/β interface is one of the main contributors to the increase in strength. Currently, the constitutive relations (in the presented model) assume an increase in basal and prismatic slip system CRSS values if the grains are colony grains, $\tau^{(\xi)}_{CRSS}(\alpha + \beta) = 1.25\tau^{(\xi)}_{CRSS}(\alpha)$ [41]. Additionally, the diameter used in the threshold stress relation (Equation 4.8) is changed to be the α-lath spacing for the hard orientations in the colony grains. Finally, the CPFEM model does not differentiate between the primary-α and $\alpha + \beta$ colony grains for elastic stiffness. This relationship is empirical and based on comparing with experimental information on cyclic stress-strain response at the macroscale rather than at the scale of individual phases. However, the elastic constants for $\alpha + \beta$ Ti-6242 have been found to be extremely close to the elastic constants for the α-phase of the same material [86].

Besides the constitutive relations, other methods have been proposed in the literature to account for the $\alpha + \beta$ colonies. For example, an increase in strength of one prismatic slip system due to difficulty of transmission across the α/β interface [138]. Many studies have also altered the diameter in the Hall-Petch style equation to account for different mean-free slip paths. However, most of these studies have assumed an homogenized response of $\alpha + \beta$ colonies as defined earlier, meaning no explicit treatment of alpha and beta regions.

In general grain boundary studies, multiple treatments have been used to discern the role of grain boundary in a polycrystalline structure. One of the earliest studies involved a CPFEM framework with grain and boundary elements to study the interfacial interaction with dislocations [151]. Some more recent work employs CPFEM for a general polycrystal, but also introduces a mesoscale model that can redistribute mobile dislocations based on certain conditions [152]. Previous work has also introduced cohesive elements between grains [153] and analyze the treatment of smooth versus stepped grain boundaries [154]. However, Bieler *et al.* [48] point out that this level of detail is not required for a specific model to capture spatial accuracy of local driving forces for slip activity [155].

2.7 Inductive Design Exploration Method

As earlier stated, the overall goal of this dissertation is to implement a simulation-based workflow that aids the materials design exploration process. As outlined by the Materials Genome Initiative (MGI) [1], new and improved material deployment can take 20 years or more from discovery to commercial production. Materials development typically employs trial-and-error strategies, along with empirical relationships, and a simple, sequential design and deployment protocol with limited iteration due to a reliance on experimental findings. Olson proposed the simultaneous use of inductive and deductive decision paths commonly employed in materials development [156].

The deductive path is referred to as a cause-and-effect path (bottom-up experiments and/or models) and the inductive path is the goals-means (top-down) path. Whereas scientific modeling seeks to determine accurate deductive paths, materials designers seek to efficiently search inductive decision paths for process-structure and structure-property relationships that satisfy several performance requirements.

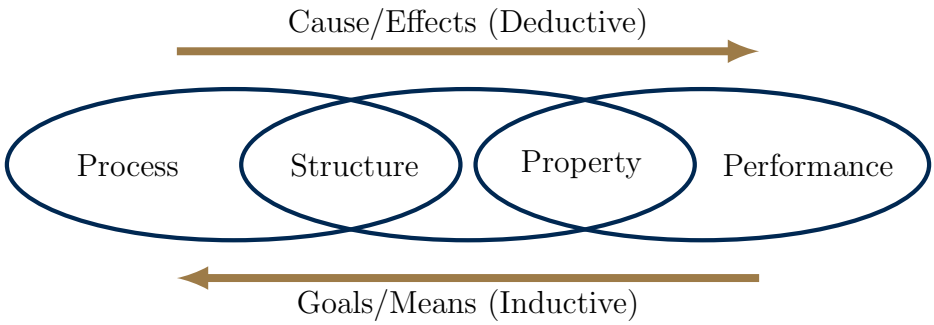

Figure 2.11: Olson's hierarchical concept of materials by design (adapted from [156]).

The deductive path is simply too hit and miss to offer utility for accelerating materials development, and hence much effort within ICME at the MGI is devoted to inverse methods in inductive design. With the ever increasing capabilities and efficiency of computational resources, the materials design and deployment process can become more concurrent and iterative in nature by exploiting computational tools and design strategies. Figure 2.12 presents a schematic that compares the present materials development continuum (referred to as the historical materials development continuum in Figure 1.1) with the future materials development continuum proposed by the MGI [1]. The linear process of the historical continuum will be improved through the overlapping and interaction of various components of materials development, while also decreasing the reliance on physical experimentation and increasing the use of computational tools [1]. This would allow for improved data sharing and simultaneous advancement of many of the materials design components.

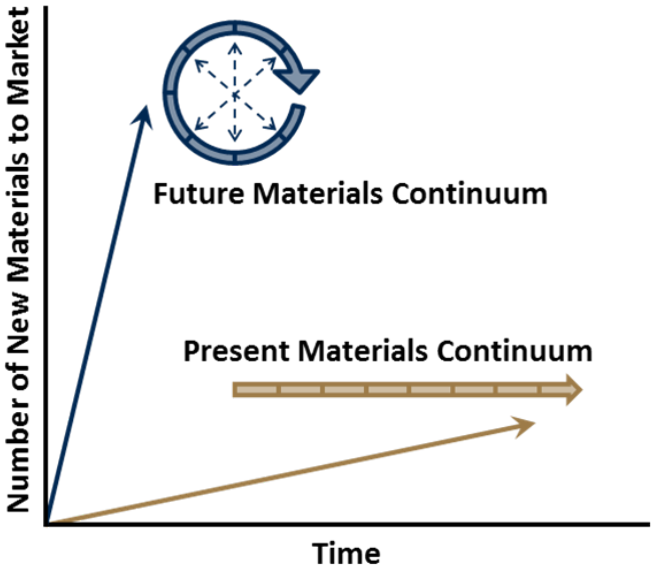

Figure 2.12: Comparison of present (historical) and future materials continuum design proposed by the MGI (adapted from [1]).

From a materials design perspective, achieving specific product performance requirements can require compromise between multiple objectives that are often in conflict or competition with one another. Although optimal solutions may exist, the uncertainties associated with values of design variables, the response of analytic and numeric models, and propagation across multiple levels motivate the desire for robust regions rather than single point, optimal solutions. To account for uncertainty and its propagation, Pareto optimal solutions are recommended [25], subject to designer preference.

There are three robust solution schemes that seek to achieve desired performance by minimizing variation of different elements of the solution space: (i) Type I robust solutions [21] seek minimization of variation due to noise factors, (ii) Type II robust solutions [22] seek minimization of variation due to control factors, and (iii) Type III robust solutions [23] seek minimization of variation due to the uncertainty inherent to the model. Each of these types of uncertainties can occur in realistic systems and are inherent to the surrogate models being used, but they should also be addressed

when being applied to robust design decisions.

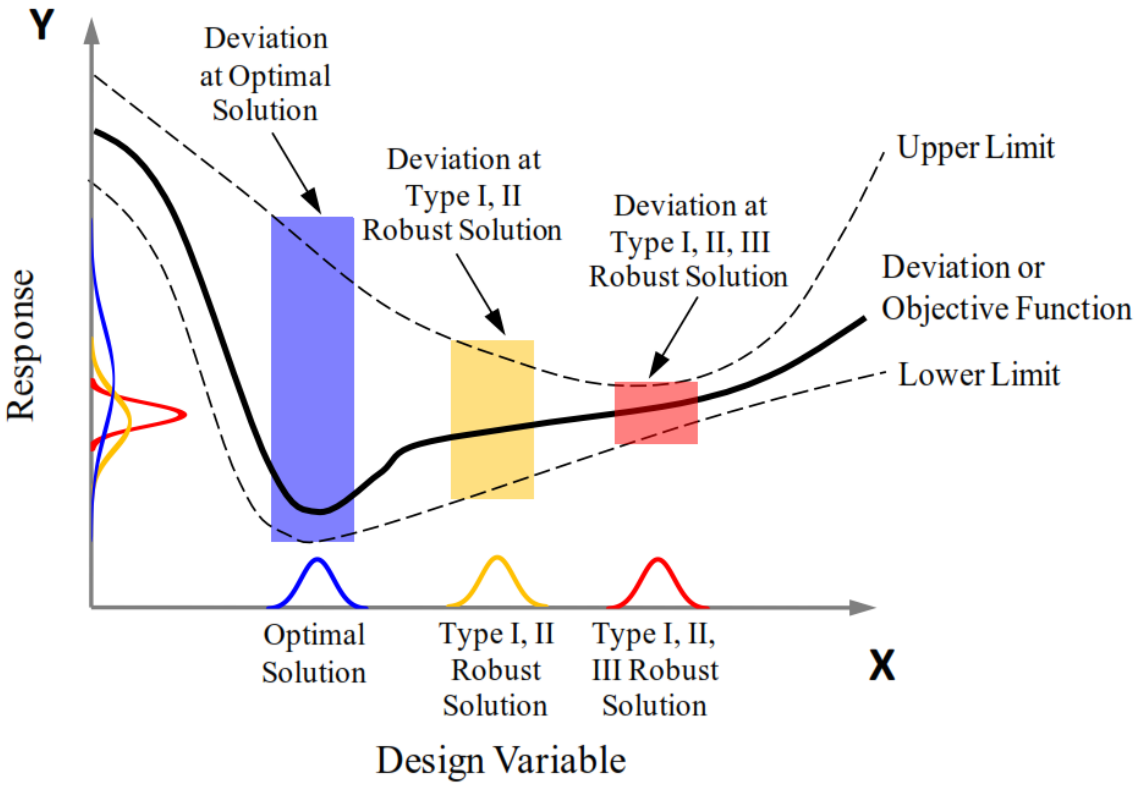

Figure 2.13: Comparison of optimal and robust solutions (adapted from [25]) [26].

A multi-level model chain is even more sensitive to uncertainty due to its propagation through the levels. One multi-level robust design method that allows for the user to account for uncertainty is the Inductive Design Exploration Method (IDEM) [24]. Given design variables (input space) and performance requirements, IDEM discretizes the input variables, projects each set of discretized input values to a range in the output space, and then determines which set of discrete input values satisfy the output space [24,29,157,158]. The IDEM is an inherently recursive process that links multiple levels of performance requirements.

The IDEM requires functions and/or discrete data to relate the input and response variables. Additionally, design criteria are required for each of the response variables, as well as extents for the input variables. The IDEM iterates (or samples, depending

on the size of the input space) over the entire input space to determine if a specific input values produce the required response variable such that the design criteria are met. The set of input values that produce satisfactory response values are referred to as feasible points. The points that do not meet the design criteria are referred to as infeasible points. The IDEM can also determine the boundary points between the feasible and infeasible points to provide an exact input range for the designer that satisfies the design criteria.

One advantage of IDEM over similar methods is the ability to account for uncertainty associated with the input and response variables. Uncertainty is associated with each input and response variable such that each input value can be thought of as a vector that contains the original input value and the extents of input values that encompass the uncertainty associated with the original value. Similarly, the functions that provide the relation between the input and response variables can return multiple values, which include the original response value and the upper and lower bound of the response value related to the level of uncertainty selected by the designer. For an input value to be deemed a feasible point, all of the response values must be satisfactory for the specified design criteria. Finally, the IDEM can also be multi-level where the response values from one level are then the input values for the next level. In this manner, the uncertainty can be explicitly accounted for between each level.

CHAPTER 3

EXTRACTION OF ELASTIC CONSTANTS FROM SPHERICAL INDENTATION DATASETS

3.1 Introduction

Microstructure-sensitive modeling schemes are used to capture the anisotropic elastic and plastic deformation response of metals [40,42,50,53]. The accuracy of these modeling schemes is highly dependent on all input parameters, including elastic constants. Previously, the measurement of elastic constants has been performed mainly using wave propagation and ultrasonic pulse techniques for single-crystal metals [159–163], composites [164], and bone [165].

More recently, acoustic microscopy [166], which has the capability of discerning the acoustic anisotropy of materials, has been used to determine elastic constants for multi-layered materials like $\alpha + \beta$ titanium [86]. Indentation results have also been compared to acoustic microscopy findings with good agreement [167]. However, the determination of elastic constants for individual phases in a multiphase material is still very difficult to ascertain. This is an important problem for many material systems for which traditional analyses cannot be applied. It is very challenging to produce single crystal samples of sufficient size for wave propagation and ultrasonic pulse techniques that have a consistent composition (e.g., % wt, distribution, etc. of alloying elements) and structure (e.g., different defect structures) as compared with the native phase. For example, martensite in dual-phase steels can have a grain size of less than 10 µm [168] and β-phase lath thickness in Ti-6Al-4V can be less than 5 µm.

Nanoindentation [169] is an approach which allows for the testing of individual phases and constituents in a multiphase and/or polycrystalline sample. Sample preparation is similar to procedures used in metallography (sectioning, grinding, and polishing), resulting in prepared surfaces sufficiently large for many indents [47]. For example, single grain measurements in polycrystalline metals [45–47] can be considered single crystal measurements of different crystal orientations. While there are size effects due to the very small (sub-micron) volumes of material being probed during nanoindentation [170–173], there have not been any reports of a size effect on elastic properties in metals and the indentation stress-strain protocols [117, 136] typically mitigate any size effects on the mechanical response between different indenter sizes [174–177].

The elastic anisotropy of the material must be properly considered when analyzing the indentation response. There have been numerous studies with different indenter shapes, both experimental and theoretical, which have shown that the response from indentation can be correlated to the elastic anisotropy of the probed material [178–185]. From these previous studies, there are two important conclusions relevant to the current work: (i) the linear relationship between the indentation force and depth $\left(\text{i.e. } h/P^{2/3} = const\right)$ from Hertz's isotropic theories [132, 133] also holds for anisotropic elasticity, but (ii) the measured indentation modulus cannot be simply converted to the Young's modulus using Hertz's original equation for the effective modulus. This second point is discussed in more detail later.

The recovery of reliable indentation modulus data from experiments is difficult with traditional Berkovich type indentation or similar procedures, which measure stiffness from the unloading response after significant plastic deformation has occurred at the site of indentation. Berkovich (sharp) tip indentation plastically deforms the material almost immediately and causes significant deformation with increased indentation depth, leading to possible crystal rotation, thus altering the elastic response

during the unloading portion [47]. This is most evident in the varied values and orientation trends of single grain indentation measurements of α-titanium [47, 186]. The range in values is likely from two sources: (i) the estimation of tip contact area and (ii) the plastic deformation of the material at the indentation site. The latter is most troubling because the modulus measurement is no longer related to the virgin material, but rather a heavily deformed volume. Even with minimal loading and a sharp indenter, there is significant plastic deformation at the indentation site. In contrast, spherical indenters (blunt compared to Berkovich) allow for the material to be loaded elastically to higher indenter displacements (as compared with comparatively sized sharp indenters), thus collecting additional data from the initial elastic response [136, 187–190]. The zero-point correction [136] is critical to establishing the correct modulus and a meaningful indentation stress-strain response, particularly for the elastic-plastic transition.

This work combines a titanium-specific indentation experimental dataset collected using spherical indentation protocols [186] with an anisotropic elastic FEM simulation procedure to develop forward and inverse procedures to estimate the indentation moduli and anisotropic elastic constants, respectively. The primary application of the forward procedure is to determine estimates of the indentation moduli to aid the generation of the experimental indentation stress-strain (ISS) curves. For example, if the elastic constants of a material are well known, then the experimentalist has an expected indentation modulus for a grain with a given orientation. In some cases, knowing the indentation modulus can reduce the analysis time significantly and provide validation of the experimental result. The calculation of the indentation modulus for any given orientation for HCP crystals is a challenging task.

3.1.1 Titanium

Titanium and its alloys have a wide variety of mechanical properties that are advantageous in engineering applications, including a relatively high elastic stiffness. The elastic stress-strain relationship for hexagonal close-packed (HCP) metals (including α-titanium and its alloys) is transversely isotropic and takes the form (in Voigt notation)

$$\begin{pmatrix} \sigma_{11} \\ \sigma_{22} \\ \sigma_{33} \\ \sigma_{13} \\ \sigma_{23} \\ \sigma_{12} \end{pmatrix} = \begin{pmatrix} c_{11} & c_{12} & c_{13} & 0 & 0 & 0 \\ c_{12} & c_{11} & c_{13} & 0 & 0 & 0 \\ c_{13} & c_{13} & c_{33} & 0 & 0 & 0 \\ 0 & 0 & 0 & c_{44} & 0 & 0 \\ 0 & 0 & 0 & 0 & c_{44} & 0 \\ 0 & 0 & 0 & 0 & 0 & \frac{1}{2}(c_{11} - c_{12}) \end{pmatrix} \begin{pmatrix} \epsilon_{11} \\ \epsilon_{22} \\ \epsilon_{33} \\ \gamma_{13} \\ \gamma_{23} \\ \gamma_{12} \end{pmatrix} \tag{3.1}$$

with five independent elastic constants $(c_{11}, c_{33}, c_{44}, c_{12}, c_{13})$. Elastic constants for α-titanium and its alloys (different chemical compositions of α-Ti) have been previously determined in the literature; a compilation of the relevant sets is shown in Table 3.1.

Table 3.1: Titanium elastic constants determined in previous work

Bulk Composition	Elastic Constants (GPa)					Ref
	c_{11}	c_{33}	c_{44}	c_{12}	c_{13}	
CP Ti	162.4	180.7	46.7	92.0	69.0	[191]$^{\clubsuit}$
α-Ti	154.0	183.0	46.7	86.0	67.3	[162]$^{\diamondsuit}$
α-Ti(Ti-6Al)	136.0	163.0	40.6	78.0	68.5	[86]
α-Ti(Ti-6242)	141.0	163.0	48.7	76.9	57.9	[86]
Ti-64	172.8	192.3	49.7	97.9	73.4	[50]$^{\spadesuit}$

$^{\clubsuit}$also cited in [192]
$^{\diamondsuit}$also cited in [193]
$^{\spadesuit}$estimated from macroscopic stress-strain response

3.1.2 Spherical Indentation

Recently developed spherical indentation protocols [117,136] have emerged as a high-throughput experimental procedure for quantifying orientation, composition, and processing effects on the elastic and plastic mechanical response of individual phases and constituents [45–47]. According to Hertz's theory [132–135], for isotropic materials, the effective indentation modulus (E_{eff}) can be related to the Young's modulus (E_s) and Poisson's ratio (ν_s) of the specimen material via

$$\frac{1}{E_{\mathit{eff}}} = \frac{1-\nu_s^2}{E_s} + \frac{1-\nu_i^2}{E_i} \tag{3.2}$$

where E_i and ν_i are the Young's modulus and Poisson's ratio of the spherical indenter, respectively. Vlassak and Nix [179, 180] showed that for anisotropic materials, the effective modulus can be determined as

$$\frac{1}{E_{\mathit{eff}}} = \left(\frac{1}{\beta_{dir}}\right)\frac{1-\bar{\nu}_{avg}^2}{\bar{E}_{avg}} + \frac{1-\nu_i^2}{E_i} \tag{3.3}$$

where the sample modulus and Poisson's ratio are the polycrystalline averages (e.g., Voigt-Ruess-Hill values for a random polycrystalline sample) and the β_{dir} term holds the crystal orientation dependence. Vlassak and Nix provide a regression analysis of many different simulations from which β can be estimated for cubic materials [180]. An alternative representation is

$$\frac{1}{E_{\mathit{eff}}} = \frac{1}{E_{ind}} + \frac{1-\nu_i^2}{E_i} \tag{3.4}$$

where E_{ind} is orientation dependent. Equations (3.2) and (3.4) are equivalent; however, Equation (3.4) requires no prior knowledge of the material's elastic constants. It is tempting to simply use Equation (3.2) with a constant Poisson's ratio (e.g., $\nu_s = 0.3$) to determine the crystal Young's modulus for any given orientation. However, this is incorrect since Equation (3.2) assumes an isotropic material. In other

words, the sample modulus from Equation (3.2) and the crystal Young's modulus are not equivalent in any sense since the stiffness response from indentation depends on the full elastic stiffness tensor. Hence the justification for Equations (3.3) and (3.4) to properly account for anisotropic elasticity.

The determination of elastic constants from indentation modulus is quite a difficult proposition. Previous work [185] performed a series of anisotropic elastic spherical indentation finite element simulations for a range of face-centered cubic elastic constants to determine a numerical function for estimating the elastic constants given indentation moduli for multiple indentation orientations. This work looks to build on that practice by building a database specific for titanium alloys (α and $\alpha + \beta$). Specifically it will focus on HCP crystal symmetry for a range of elastic constants relevant to titanium.

3.1.3 Finite Element Modeling of Indentation

Multiple finite element studies [124,194–200] have been performed with a focus of analyzing the response of materials under the deformation of various shaped indenters. These studies have employed various methods of comparing simulation results with experimental data, but the primary focus is almost exclusively a function of plastic deformation. Experimental values of interest for comparison include hardness measurements [201] and force-displacement plots [124,125,196,197,202,203]. Additionally, FEM simulation results focus on surface topology (e.g., pile-up patterns) [204] and dislocation activity beneath the indenter [126] for model comparison with experiments. The majority of these studies have been more concerned with characterizing plastic deformation by measuring specific slip system activity or critical resolved shear stress values. However, the studies that have also reported elastic modulus values from indentation simulations [201, 205, 206] have captured similar trends, but the reported modulus values have been highly varied. Additionally, many of the FEM studies have

performed axisymmetric simulations and, while these two-dimensional simulations can be quite computationally efficient, they are limited to materials of high symmetry or select planes of symmetry for HCP crystal structures [125]. Finally, Previous indentation studies have also looked specifically at titanium and its alloys, including CP Ti [201, 206, 207], α-Ti [204, 205], and other titanium alloys [208], but they also suffer from the same deficiencies previously mentioned.

Studies that utilize three-dimensional FEM meshes need a great deal of elements to ensure solution accuracy beneath the indenter. While plastic properties, such as critical resolved shear stress values and dislocation activity estimates, are extremely important in advancing the current microstructure-sensitive modeling schemes, the accuracy of these measures is limited without a high confidence in the representation of a specific material system's elastic response. All of this background supports the need for an accurate and computationally-efficient method for estimating microstructure-scale specific properties, such as elastic constants, for α phase and $\alpha + \beta$ colonies.

3.2 Methods

3.2.1 FEM Model

The FEM model of the indenter specimen presented in this work is unique relative to previous studies because it utilizes infinite elements in the outer region of the three-dimensional mesh. To minimize the influence of boundaries and free surfaces on the area of interest (e.g., finite volume beneath the indenter), infinite elements [87] have been introduced in the outer region of the three-dimension mesh. The first-order infinite elements are defined over semi-infinite domains and are prescribed decay functions [87]. Infinite elements were originally introduced for the field of fluid mechanics [209]. They have been implemented via infinite domain elements [210] and mapped

infinite elements [211]; the latter is used in this work. The mapping elements are defined for a finite domain and mapped onto an infinite domain with the aid of a pole location (e.g., point of contact of indenter in this case) and polynomial decay functions that project boundary nodes at infinite distances in the specified direction [212]. In the three-dimensional case, the infinite element has four nodes that share a face with a traditional finite element and those shared nodes are precisely midway between the pole location and the boundary nodes. The shape functions corresponding to the boundary nodes are set equal to zero, therefore implicitly imposing the boundary conditions of the infinite domain [211]. For additional information, please refer to the following references [211–213].

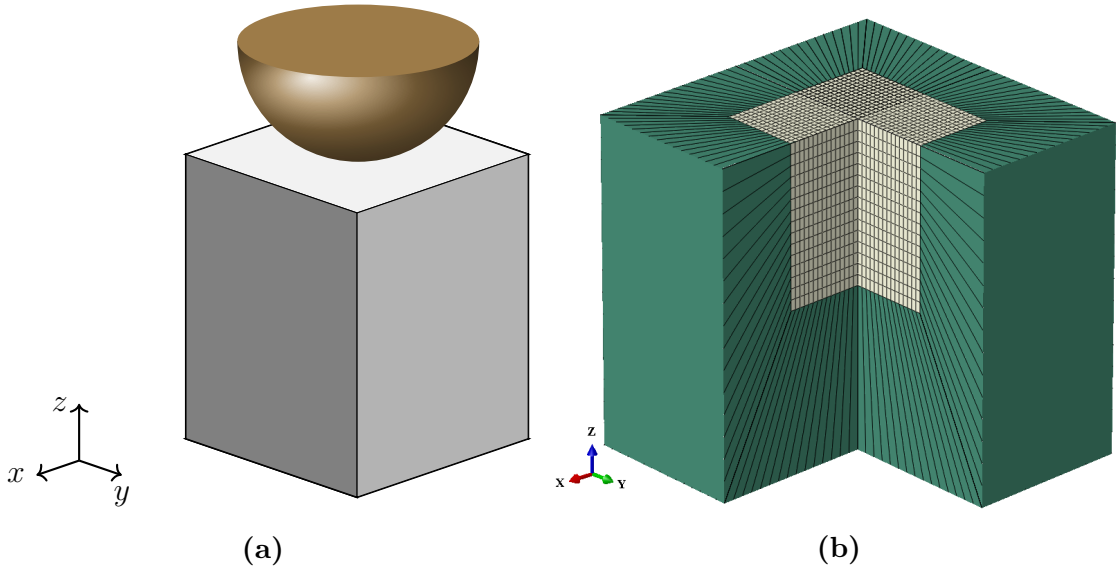

Figure 3.1: Images of the (a) indenter on on the surface of the three-dimensional specimen and (b) the mesh used in this study with the finite (tan) and infinite (green) elements.

The indentation specimen is three-dimensional and composed of an inner and outer region. The inner region consists of hexahedral elements (type C3D8) with eight integration points and is designed for direct contact with the indenter. The outer region is comprised of infinite elements (type CIN3D8) that require the sharing of at least one face with a hexahedral elements. The indenter is defined as a rigid sphere

with a radius of 10 µm. The contact surface between the indenter and indentation specimen is modeled as frictionless, an estimate that has been proven valid in previous studies for relatively flat indentation surfaces [116,122,194–196] but that contact with sharp indenters might need to account for friction [197, 198].

For loading conditions, the indenter is displaced in the negative and positive z-direction for loading and unloading the indentation specimen, respectively. The boundary conditions of the indentation specimen are dictated by the infinite elements; the negative z-face as well as the positive and negative x- and y-faces (Figure 3.1b) are fixed in all directions. The FEM mesh is constructed with a Python [214] script that generates a three-dimensional elemental structure for the indentation specimen, defines the finite and infinite element sets, constructs the rigid spherical indenter, defines the corresponding contact surfaces on the indenter and indentation specimen, defines the material properties to the indentation specimen, and defines the loading and boundary (if applicable) conditions. The advantage to constructing a Python script for the generation of these Abaqus [87] input files is the flexibility provided once created. For example, model characteristics such as dimensions, number of elements, indenter size, material properties, and loading conditions can be treated as variables and iterated over the create multiple input files.

The indentation modulus is determined from a single load-unload sequence of 1.0 nm and 0.1 nm, respectively, to reduce the computational expense of these simulations. Many of the results in this work are expressed as a function of the second Bunge Euler angle, Φ. The elastic stiffness of titanium and its alloys is highest with uniaxial loading parallel to the c-axis and lowest with uniaxial loading perpendicular to the c-axis. The elastic stiffness does not have any dependence on the other two angles (ϕ_1, ϕ_2). The Φ angle relative to the c-axis of the HCP unit cell and specimen coordinate systems is shown in Figure 3.2. Note that Φ is sometimes defined as the declination angle in other works.

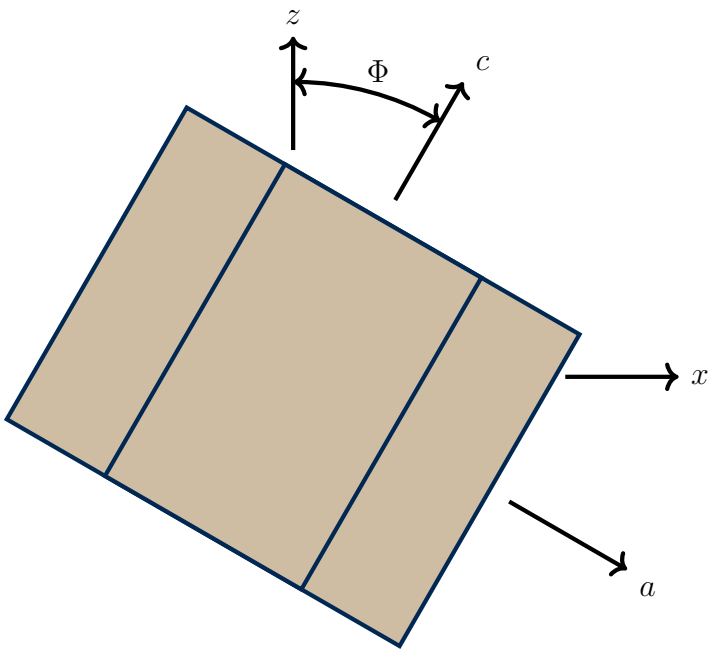

Figure 3.2: The Φ angle as it relates to the c-axis of the HCP unit cell and the coordinate system of this study.

The slope of the unload curve is used to estimate the indentation modulus. The indenter radius is equal to the effective radius since the deformation is fully elastic. Hertz theory assumes the contact between two axisymmetric surfaces is frictionless and isotropic. For this theory, the relationship between the indenter force and displacement can be represented as

$$P = \frac{4}{3} E_{eff} \left(R_{eff}\right)^{\frac{1}{2}} \left(h_e\right)^{\frac{3}{2}} \tag{3.5}$$

where P is the indentation force, E_{eff} is the effective indentation modulus, R_{eff} is the effective radius, and h_e is the elastic penetration depth. The contact radius (a_i) of the spherical indenter is defined as $a_i = \left(R_{eff}\right)^{\frac{1}{2}} \left(h_e\right)^{\frac{1}{2}}$. The indentation force and displacement can be used to define equations for true indentation stress (σ_{ind}) and strain (ϵ_{ind}) via

$$\epsilon_{ind} = \frac{3}{4\pi} \frac{h_i}{a_i} \quad \& \quad \sigma_{ind} = \frac{P_i}{\pi a_i^2} \tag{3.6}$$

The hexahedral elements have an aspect ratio (height-to-width) of 2:1, which has been found to sufficiently capture the gradients beneath the indenter and allow for fewer elements in the mesh. The size of the inner region was defined such that the stress and strain in the loading direction are minimal at the transition from hexahedral to infinite elements. The relative error between the 1:1 and 2:1 aspect ratio element sets is between 0.2% and 0.4% depending on the Φ angle. The results for varying the aspect ratio are given in Figure 3.3. There is an obvious deviation from the ideal ratio (1:1) solution as the ratio increases beyond 2:1.

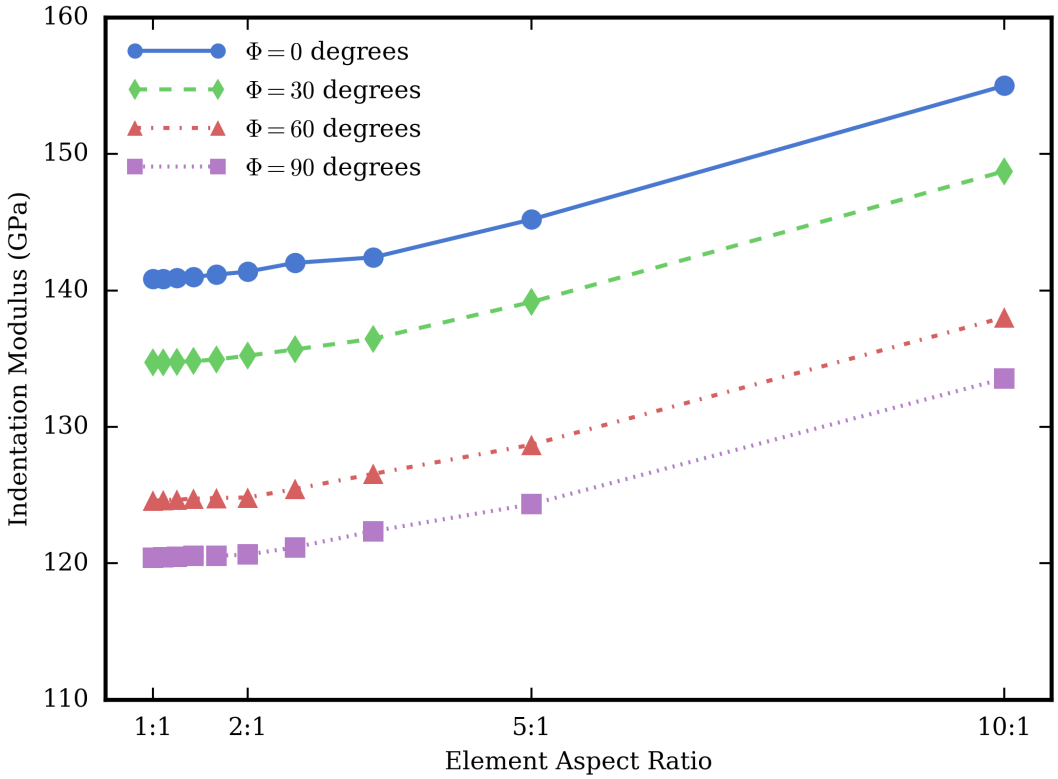

Figure 3.3: The indentation modulus is plotted versus inner region element height-to-width ratio.

One advantage of employing infinite elements is the ability to obtain converged indentation modulus values with a relatively course mesh. A mesh convergence study was performed to determine the effect of mesh refinement; the element sizes tested are detailed in Table 3.2. Although the number of processors increases with the number

of elements, it is important to note that linear scaling is not achieved partially because of the infinite elements. The infinite elements in Abaqus 6.10-1 [87] do not allow for parallel element computations, severely diminishing the scalability of these particular simulations.

Table 3.2: Mesh Convergence Study

Element Size (nm)		Number of	Number of	Simulation
x and y	z	Elements	Processors	Time (min)
50.0	100.0	800	1	2
25.0	50.0	5,200	4	2
12.5	25.0	36,800	16	25
10.0	20.0	70,000	24	60
5.00	10.0	530,000	64	270
3.33	6.67	1,755,000	256	660

The results from the mesh convergence study are shown in Fig. 3.4 where indentation moduli are displayed versus number of elements for Φ angles of 0°, 30°, 60°, and 90° for pure Ti. The indentation moduli reach converged values for the 5,200 element simulation configuration. The width-to-height ratio was also varied from 1.0 to 10.0 in the mesh convergence study and it was found that the results became less dependent on the width-to-height ratio as the mesh was refined.

For additional validation of the three-dimension mesh introduced in this work, it was also compared with theoretical values for the indentation modulus of zinc determined previously in the literature [180]. The elastic constants for zinc (c_{11} = 161.1, c_{33} = 61.0, c_{44} = 38.3, c_{12} = 34.3, and c_{13} = 50.3 (GPa)) were obtained from the study [180] and the indentation modulus calculated for simulations with varying Φ angles; the comparison of the theoretical and simulation results can be found in Figure 3.5. The current meshing scheme shows excellent agreement with the theoretical values, providing additional confidence in the proposed methodology. An inner region element sidelengths of 25 nm and a 2:1 ratio of width-to-height were used

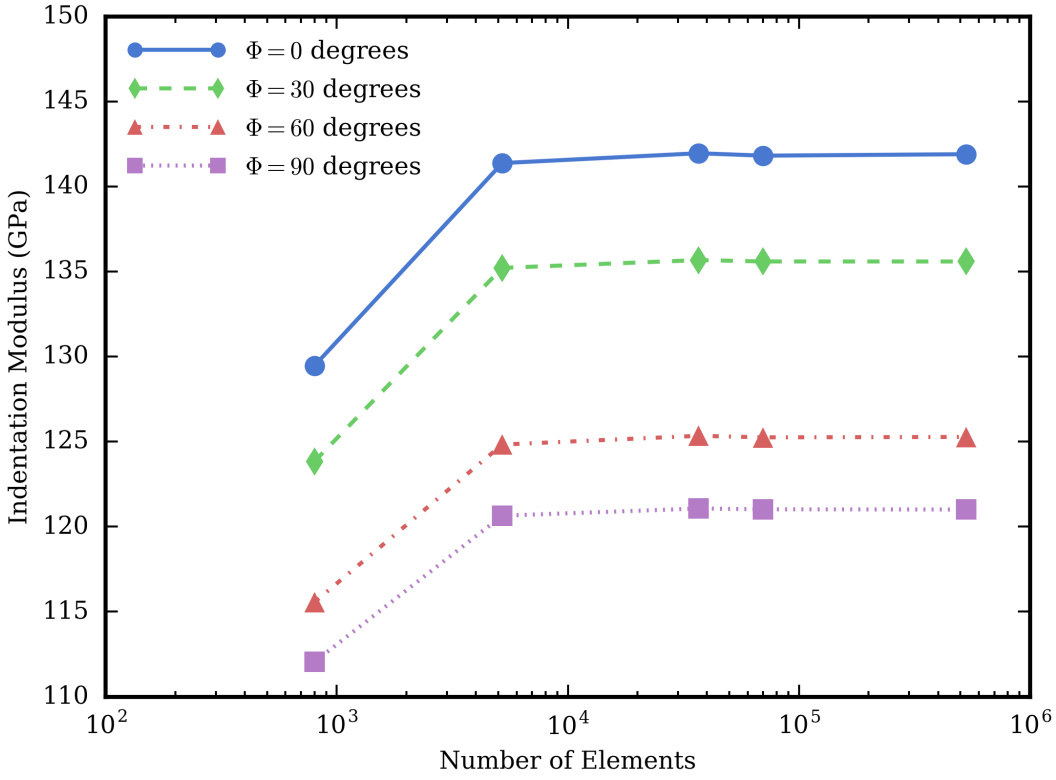

Figure 3.4: The indentation modulus is plotted versus number of elements for Φ angles of 0°, 30°, 60°, and 90°.

in these simulations, the same as used in this study for the titanium simulations.

It was also advantageous to use a modified set of units for values in Abaqus; those units are listed in Table 3.3. The length and force units have been changed to microns and micronewtons, respectively. The change of the length units reduces the number of significant figures needed to define nodal positions, while changing both the length and force units provides a common unit system for stress (MPa). This can be beneficial when visualizing results with Abaqus/CAE [87].

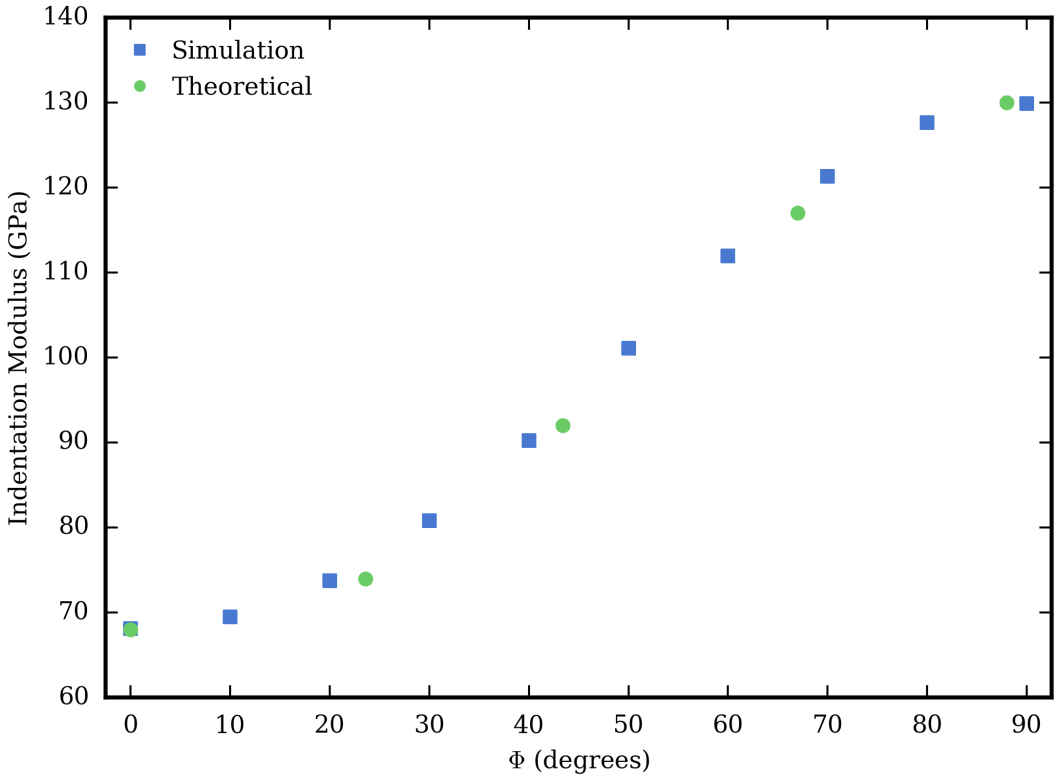

Figure 3.5: The indentation modulus for Zinc is compared with theoretical values [180].

Table 3.3: Consistent units used in Abaqus for this study.

Quantity	Units
Length	μm
Force	μN
Mass	g
Time	sec
Stress	MPa
Energy	fJ
Density	g/μm^3

3.2.1.1 Titanium Dataset

For the finite element method simulations, the elastic constant ranges are shown in Table 3.4. When discretizing the elastic constants, care was taken to allow for a minimum of five data points along each direction so the functional fitting of the data would have a sufficient number of points. A total of 108,000 FEM simulations were performed, which required approximately 14,400 compute hours. Given the computational expense of this dataset, leveraging it for multiple studies is advantageous.

Table 3.4: Titanium elastic constant ranges used in this study

Value	Elastic Constants (GPa)				
	c_{11}	c_{33}	c_{44}	c_{12}	c_{13}
Minimum	135.0	160.0	40.0	75.0	55.0
Maximum	175.0	195.0	50.0	100.0	75.0
Spacing	5.0	5.0	2.5	5.0	5.0

In terms of Bunge Euler angles, the elastic modulus of transversely isotropic materials is only a function of Φ. To confirm this, the entire Euler angle space was sampled, for a specific set of elastic constants, the indentation modulus values plotted as a function of each of the three Euler angles, as shown in Figure 3.6. It is quite evident that Φ is the only angle that demonstrates a non-constant relationship with the indentation modulus.

While it is not convenient to visualize the indentation modulus for the entire six variable input space, it is quite useful to gain some perspective of the impact of each input variable and how it relates to resultant indentation modulus. Figure 3.7 demonstrates the variability of the indentation modulus as a function of the Φ angle for the minimum and maximum values (see Table 3.4) of each of the five elastic constants. In each of these violin plots, the selected elastic constant is held constant and the resultant violin plot represents the distribution of the elastic modulus from varying the other four elastic constants. It can be seen that each elastic constant has a

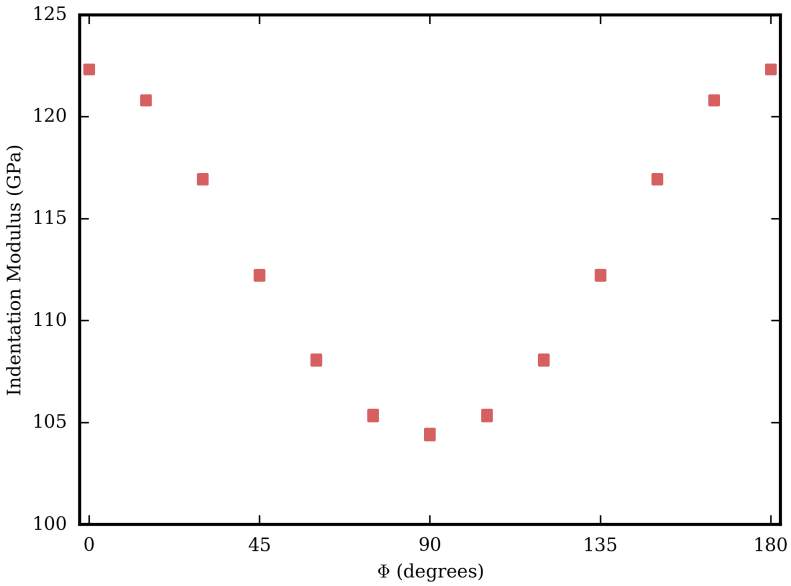

(a)

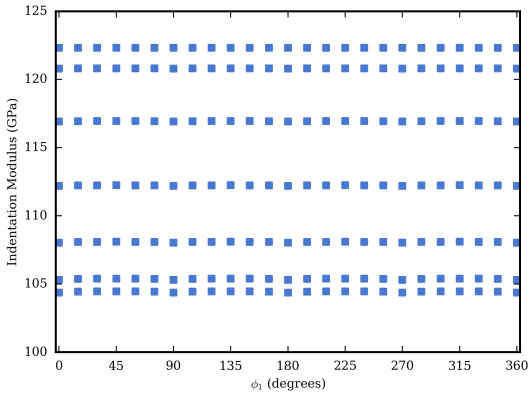

(b)

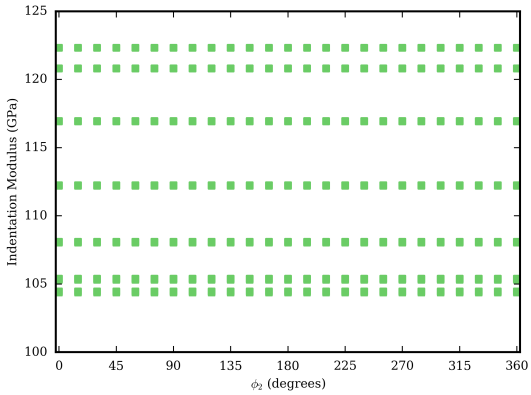

(c)

Figure 3.6: Indentation modulus versus each of the three Bunge Euler angles.

varying degree on the range of possible indentation modulus values as a function of Φ. For example, c_{11} has a rather significant effect on the resultant indentation modulus for higher values of Φ, while varying c_{13} has very little influence on the indentation modulus regardless of Φ angle.

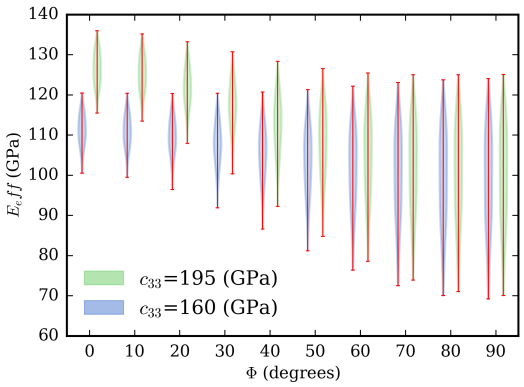

(a)

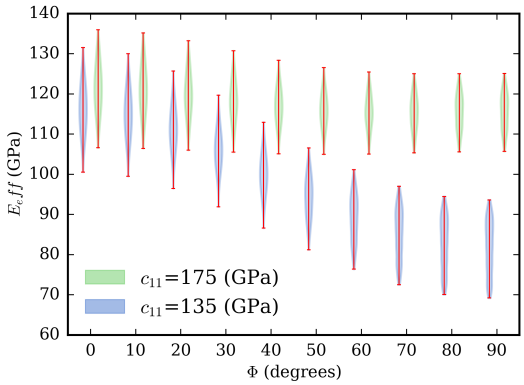

(b)

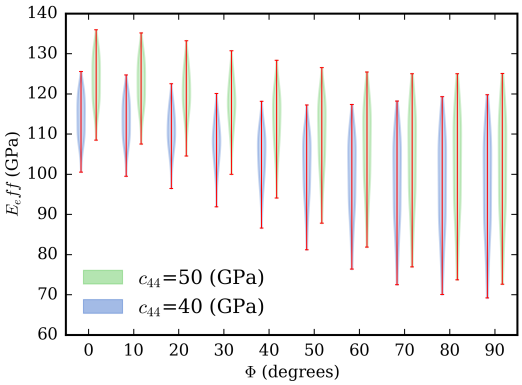

(c)

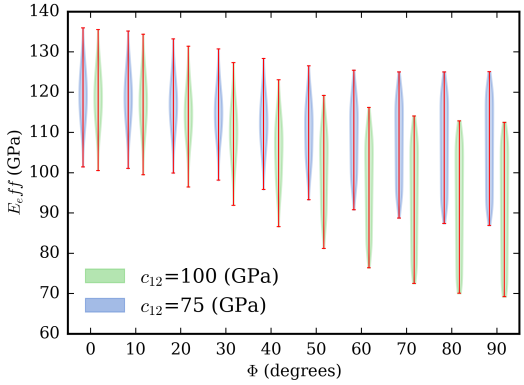

(d)

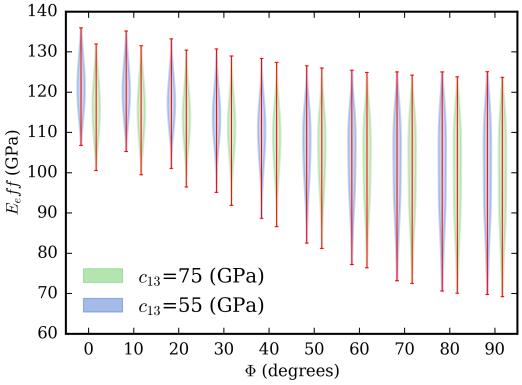

(e)

Figure 3.7: Representation of the simulation data used in this work.

3.2.2 Experiment and Computation Interactions

As previously stated, the purpose of performing the computational simulations is to provide guidance to the experimental data analysis. The interaction between the experiments and computational analyses is shown in Figure 3.8. The analysis of experimental spherical nanoindentation datasets can be aided both in accuracy and by reducing the number of iterations needed to find a satisfactory solution, given the ability to compare the experimental results with accurate indentation modulus values, such as those found with the FEM method presented.

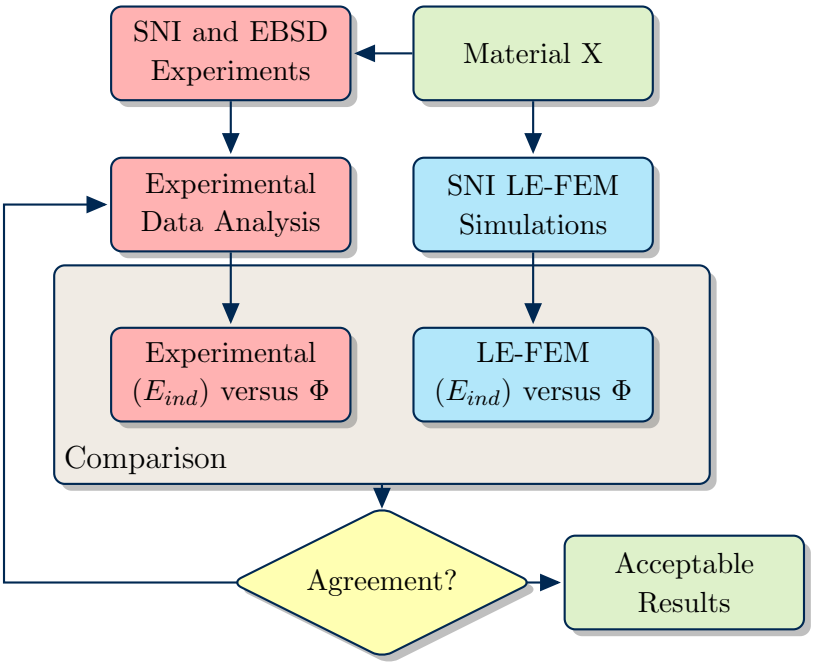

Figure 3.8: Flowchart for the interaction between experimental and computational analysis of indentation modulus for titanium and its alloys.

3.2.3 Numerical Analysis

The numerical analysis in this work was performed with Python [214] and support packages including numpy [215], scipy [216], and scikit-learn [217]. It is planned to make both the numerical analysis procedure and FEM simulation data available to the public, therefore open-source software such as Python was utilized. Within the numerical analysis procedure, three major techniques are leveraged to solve the inverse problem, which is the determination of titanium-specific elastic constants given indentation moduli.

- Linear regression was performed to fit a polynomial function to the FEM effective indentation modulus dataset. This provides a robust function for estimating the effective indentation modulus given particular elastic constants and the Euler angle Φ.

- Least-squares optimization was performed between the experimental effective indentation modulus dataset and the resultant function from linear regression. This returns an optimized set of elastic constants given the experimental dataset.

- Bayesian inference with Markov Chain Monte Carlo was performed to estimate the likelihood of specific elastic constants returning acceptable effective indentation modulus values when compared to the experimental data.

3.2.4 Linear Regression

The elastic constants and Euler angles were treated as independent variables while the dependent variable was the indentation modulus. Due to the symmetry of transversely isotropic materials (e.g. HCP metals), the indentation modulus is only a function of Φ and not ϕ_1 or ϕ_2. Therefore, the independent variables used in the linear regression were the elastic constants $(c_{11}, c_{33}, c_{44}, c_{12}, c_{13})$ and Φ.

Linear regression was used to determine a function fit for the FEM simulation data. A fourth-order polynomial (210 coefficients) was found to be of satisfactory fit; the mean error between the fitting function and the input data is 0.11% and the maximum error is 0.82%. A compact representation of the polynomial function given the maximum degree ($d = 4$) and number of independent variables ($n = 6$) is given,

$$f\left(c_{11}, c_{33}, c_{44}, c_{12}, c_{13}, \Phi\right) = \sum_{i_1+\ldots+i_n \leqslant d} a_{i_1 i_2 \ldots i_n} \prod_{j=1}^{n} x_j^{i_j} \tag{3.7}$$

where i is the degree of each component, x_j is each independent variable, and $a_{i_1 i_2 \ldots i_d}$ are the coefficients.

3.2.5 Least Squares Optimization

The inverse problem, estimating the elastic constants from the experimental indentation modulus, can now be addressed with a least squares optimization scheme. A set of N equations are constructed according to

$$S_r = \sum_{i=1}^{N} \left(E_i^{ind} - f_i\left(c_{11}, c_{33}, c_{44}, c_{12}, c_{13}, \Phi_i\right)\right)^2, \tag{3.8}$$

where N is the number of experimental data points used to estimate the elastic constants and S_r is the sum of the squares of the residuals. The sum of the squares of the residuals is then minimized to determine the elastic constants that minimize the set of equations. Additionally, weighted least squares can be used to include the standard deviation (σ) for each experimental data point.

$$S_r = \sum_{i=1}^{N} \frac{\left(E_i^{ind} - f_i\left(c_{11}, c_{33}, c_{44}, c_{12}, c_{13}, \Phi_i\right)\right)^2}{\sigma_i^2}, \tag{3.9}$$

Both of these optimization schemes can be performed with either the full set of experimental data or some reduced set. For example, the experimental data used in this study has many more experimental data points with $\Phi > 75^\circ$ than $\Phi < 15^\circ$ which can skew the results of the optimization without proper weighting. To combat

this, the experimental indentation modulus values have also been averaged within a certain range of Φ angles (binned in 10° increments) and the optimization performed on the reduced set as well.

Previous work relating indentation experiments to models [218] have attempted to bound the experimental data by varying the elastic constants to provide a minimum and maximum set that are acceptable when visually inspecting the comparison of the experimental and simulation data. While this might prove satisfactory for some applications, it lacks a statistical rigor that can aid the researcher in determining if the fit is satisfactory or if more experimental data points are needed.

3.3 Results and discussion

3.3.1 Least Squares Optimization

An optimized fit to the commercially-pure titanium indentation modulus experimental data illustrates the effectiveness of this procedure. The CP-Ti was generated with both 16 and 100 µm indenters; both experimental datasets show general agreement. The resultant elastic constant values are shown in Table 3.5. The fits were performed for both the entire dataset as well as the averaged data set. In addition, the least squares optimization (Equation (3.8)) and weighted least squares optimization (Equation (3.9)) were performed. From Table 3.5, the only elastic constant that significantly varied for each of these fits was c_{12}. The varying of c_{12}, as shown in Figure 3.7d, leads to variation of the indentation modulus for larger values of Φ. However, the fits do not appear to be exceptional given the range of R^2 score values of 0.62-0.68.

Table 3.5: Elastic constants found for commercially-pure titanium in this work.

Experimental Data	Optimization Type	Elastic Constants (GPa)					R^2 Score
		c_{11}	c_{33}	c_{44}	c_{12}	c_{13}	
All	LSR	175.0	195.0	50.0	90.3	55.0	0.68
	wLSR	175.0	195.0	50.0	92.1	55.0	0.67
Averaged	LSR	175.0	195.0	50.0	83.6	55.0	0.62
	wLSR	175.0	195.0	50.0	83.8	55.0	0.62

Although there are a few outliers for the CP-Ti experimental dataset, they do not seem to have an extremely large effect on each of the fit, as shown in Figure 3.9. However, as stated in the previous section, there are quite a few more data points for the higher values of Φ as compared to the lower values. In belief that this could possible skew results, the experimental data points were further averaged (both mean and standard deviation) to minimize the number of points fit and to provide equal weighting to the entire range of Φ, as shown in Figure 3.10.

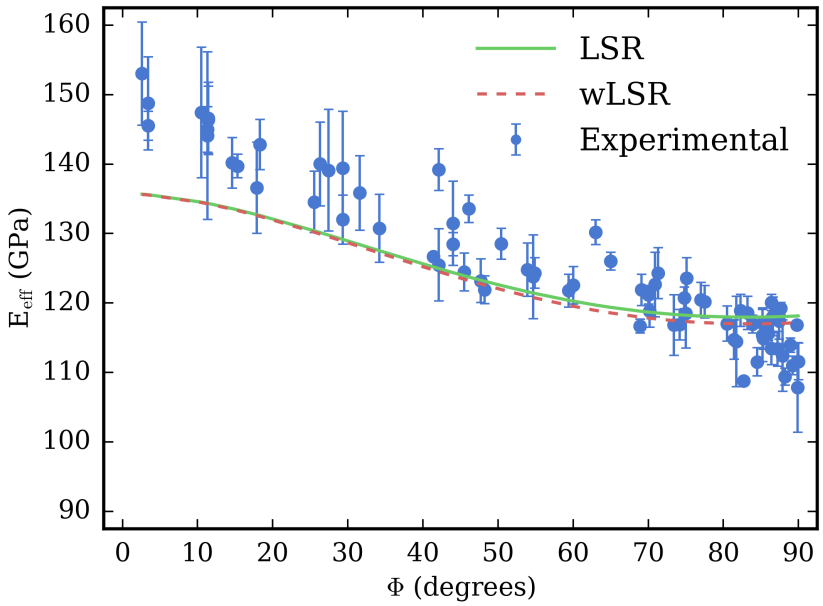

Figure 3.9: The fit for the optimized elastic constants is shown for the CP-Ti indentation modulus experimental data. Least square optimization was performed with only the mean values (LSR) as well as the mean and standard deviation (wLSR).

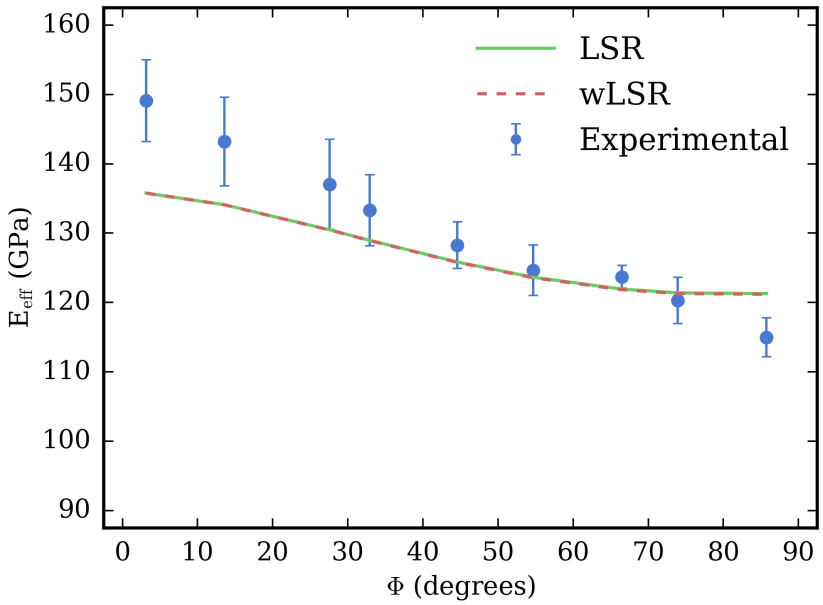

Figure 3.10: The fit for the optimized elastic constants is shown for the averaged CP-Ti indentation modulus experimental data. Least square optimization was performed with only the mean values (LSR) as well as the mean and standard deviation (wLSR).

An optimized fit was also performed for the α-titanium indentation modulus experimental data. The α-Ti was generated for only the 16 µm indenter. The resultant elastic constant values are shown in Table 3.6. Again, the fits were performed for both the entire dataset as well as the averaged data set as well as the least squares and weighted least squares optimization. From Table 3.6, the only elastic constant that significantly varied for each of these fits was c_{44} with small variation in c_{11}. The varying of c_{44} leads to variation of the indentation modulus for smaller values of Φ, while the opposite is true for c_{11}. The fits for the α-titanium seem satisfactory, as the range of R^2 score values of 0.83-0.97, which the higher values of R^2 being associated with the fits to the averaged dataset.

Table 3.6: Elastic constants found for α-titanium in this work.

Experimental Data	Optimization Type	Elastic Constants (GPa)					R^2 Score
		c_{11}	c_{33}	c_{44}	c_{12}	c_{13}	
All	LSR	164.0	195.0	50.0	100.0	55.0	0.84
	wLSR	164.9	195.0	48.1	100.0	55.0	0.83
Averaged	LSR	164.3	195.0	49.5	100.0	55.0	0.97
	wLSR	166.0	195.0	47.6	100.0	55.0	0.96

The α-Ti dataset has a larger number of experimental data points for larger values of Φ, as shown in Figure 3.11. Additionally, there are no data points between approximately 15° and 30°. However, the maximum indentation modulus values for α-Ti are much lower than CP-Ti, which led to a more accurate fit to the experimental dataset. Figure 3.12 shows extremely good agreement for the averaged dataset with equal weighting of the entire range of Φ.

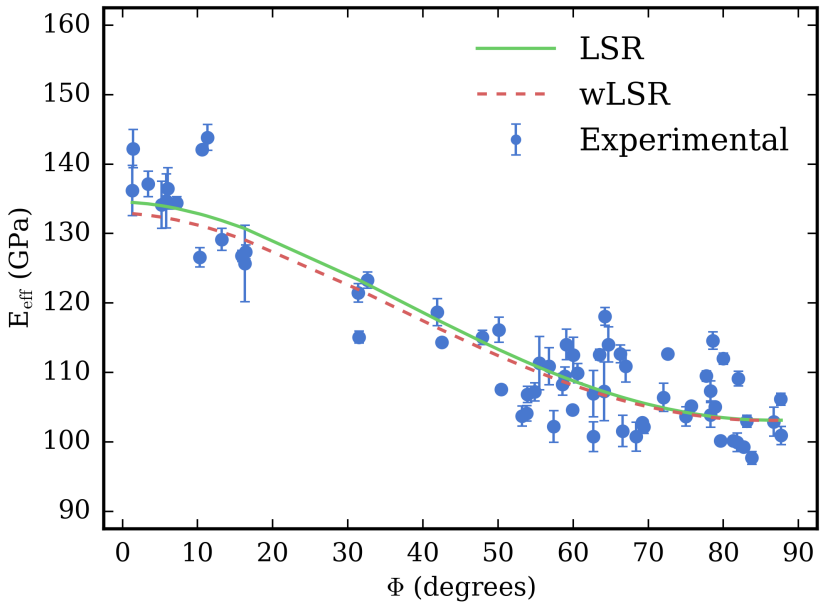

Figure 3.11: The fit for the optimized elastic constants is shown for the α-Ti indentation modulus experimental data. Least square optimization was performed with only the mean values (LSR) as well as the mean and standard deviation (wLSR).

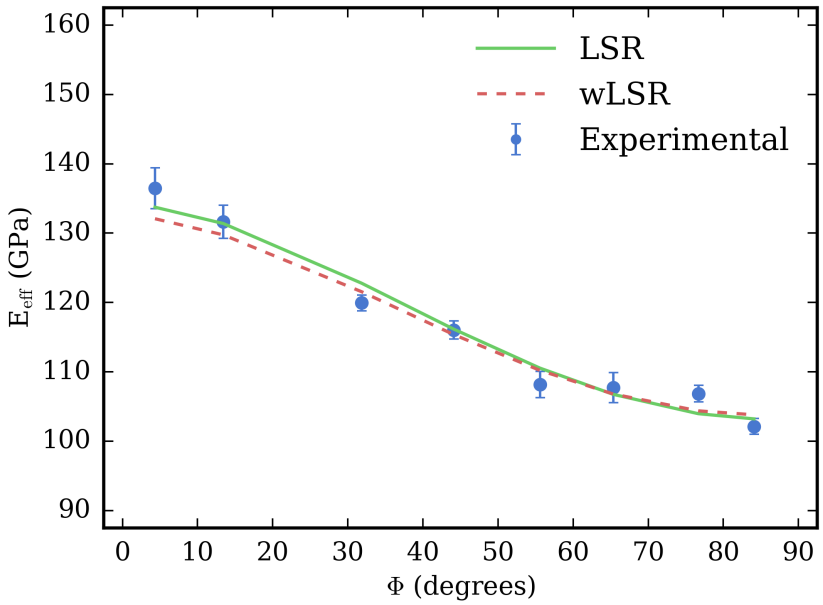

Figure 3.12: The fit for the optimized elastic constants is shown for the averaged α-Ti indentation modulus experimental data. Least square optimization was performed with only the mean values (LSR) as well as the mean and standard deviation (wLSR).

Finally, an optimized fit was performed for the $\alpha + \beta$ colony grains indentation modulus experimental data. The colony-Ti dataset was generated for only the 100 µm indenter. The resultant elastic constant values are shown in Table 3.7. Again, the fits were performed for both the entire dataset as well as the averaged data set as well as the least squares and weighted least squares optimization. From Table 3.7, all elastic constants were varied among optimization type and data. This is quite an interesting result considering the small range of returned values for CP-Ti and α-Ti. The fits for the colony-Ti also seem satisfactory, as the range of R^2 score values of 0.83-0.87.

Table 3.7: Elastic constants found for $\alpha + \beta$ titanium in this work.

Experimental Data	Optimization Type	Elastic Constants (GPa)					R^2 Score
		c_{11}	c_{33}	c_{44}	c_{12}	c_{13}	
All	LSR	173.0	195.0	43.7	100.0	55.0	0.87
	wLSR	162.5	187.0	48.3	91.0	55.0	0.85
Averaged	LSR	175.0	175.0	43.1	100.0	56.5	0.85
	wLSR	154.1	154.1	50.0	75.0	75.0	0.83

The colony-Ti dataset contains few data points as compared to CP-Ti and α-Ti. The complete dataset and associated fits are shown in Figure 3.13. As with the α-Ti, the maximum indentation modulus values for colony-Ti are much lower than CP-Ti, which led to a more accurate fit to the experimental dataset. However, as shown in Figure 3.14, there are so few data points that the resultant fit to the averaged data seems to approximate a linear relationship between indentation modulus and Φ for smaller values of Φ, which is contrary to the CP-Ti and α-Ti datasets.

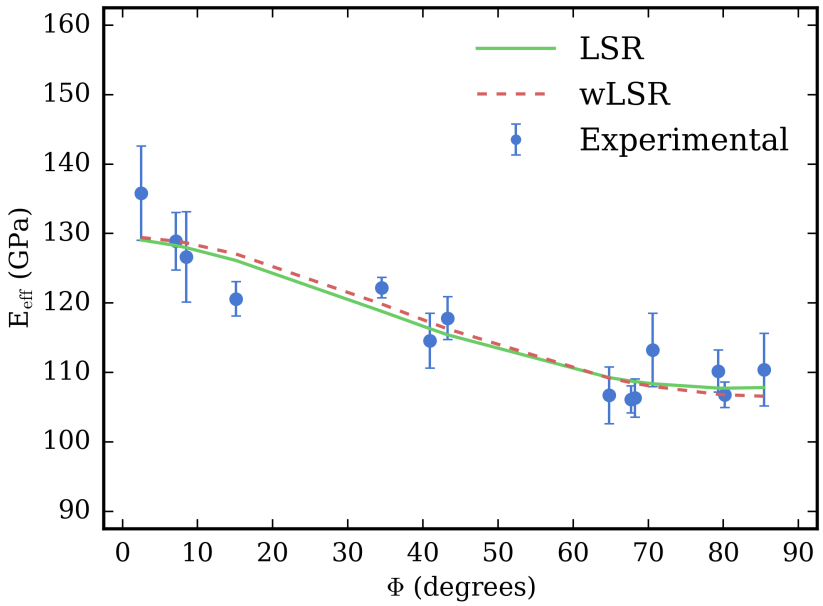

Figure 3.13: The fit for the optimized elastic constants is shown for the *alpha* + β-Ti indentation modulus experimental data. Least square optimization was performed with only the mean values (LSR) as well as the mean and standard deviation (wLSR).

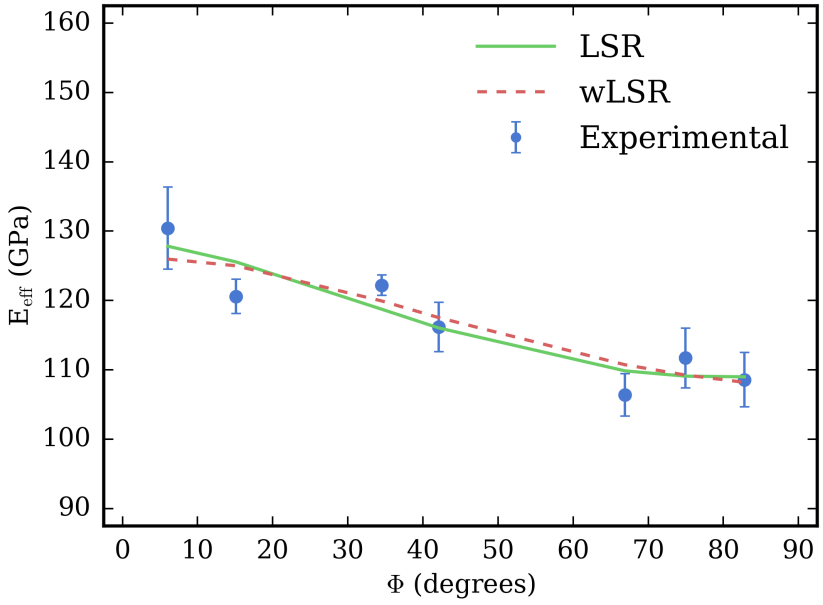

Figure 3.14: The fit for the optimized elastic constants is shown for the averaged $\alpha + \beta$-Ti indentation modulus experimental data. Least square optimization was performed with only the mean values (LSR) as well as the mean and standard deviation (wLSR).

3.3.2 Bayesian Inference

A Bayesian framework [219–224] has become popular in mechanics to help better calibrate model parameters and quantify the uncertainty associated with each of them [225–229]. For this study, Bayesian inference is used to assess each elastic constant to ascertain a valid range of values that provide a sufficient fit to the experimental indentation modulus datasets. The updated probability distribution (posterior distribution), $P\left(C|E_{mod}\right)$), comes from Bayes theorem:

$$P\left(C|E_{mod}\right) = \frac{P\left(E_{mod}|C\right)P\left(C\right)}{P\left(E_{mod}\right)}, \tag{3.10}$$

$$P\left(E_{mod}|C\right) = \frac{1}{\left(2\pi\sigma^2\right)^{\frac{n}{2}}} \exp^{\sum_{i=1}^{n}\left(\frac{-\left(E_i^{ind}-f(C)\right)^2}{2\sigma^2}\right)}, \tag{3.11}$$

where E_{mod} is the experimental data and C is the set of five elastic constants. The steps for producing the algorithm used in this work, which performs uncertainty quantification using Bayesian inference, Markov Chain Monte Carlo, and Metropolis-Hastings sampling include:

- Define the likelihood $P\left(E_{mod}|C\right)$ of observing the data (E_{mod}) given parameter realizations (C). This function follows a normal distribution in this work.
- Define the prior distributions $\pi^{(0)}\left(x\right)$ for all parameters ($c_{11}, c_{33}, c_{44}, c_{12}, c_{13}$). A uniform distribution applied over the input range for each elastic constant is used in this work.
- Define the proposal distributions $q\left(x\right)$ for all parameters. A normal distribution with a standard deviation of 0.1% was used.
- Select initial value for each parameter, which are chosen as the values returned from the least-squares optimization.

- Perform component-wise Metropolis-Hastings sampling until N acceptable parameter sets are found.

The Markov Chain Monte Carlo method samples the weighted least squares regression (Equation 3.9), starting with the values determined in the previous results section. Then the component-wise Metropolis-Hastings sampling varies each of the elastic constants by a small increment and a new probability distribution is calculated. If the new probability distribution meets a set criteria (typically a comparison with the old probability distribution), then the values of each variable are acceptable and appended to a list of feasible input variables. This is performed for 50,000 successful iterations, which provides a significant number of values for each elastic constant.

The distributions of the acceptable values for each elastic constant for CP-TI are shown in Figure 3.15. From is plot, it is quite evident that a range of elastic constants would provide a satisfactory fit to the CP-Ti experimental data. By comparing these histograms to Table 3.5, it can be determined if the least squares optimization values were returned at the highest frequency from the Bayesian analysis. The elastic constants c_{11}, c_{33}, and c_{13} from the least squares optimization correspond with the highest peaks in the corresponding histograms, while c_{44} and c_{12} are different. Nonetheless, a uniform distribution was applied to each elastic constant in this analysis, but distributions of varying shapes were returned.

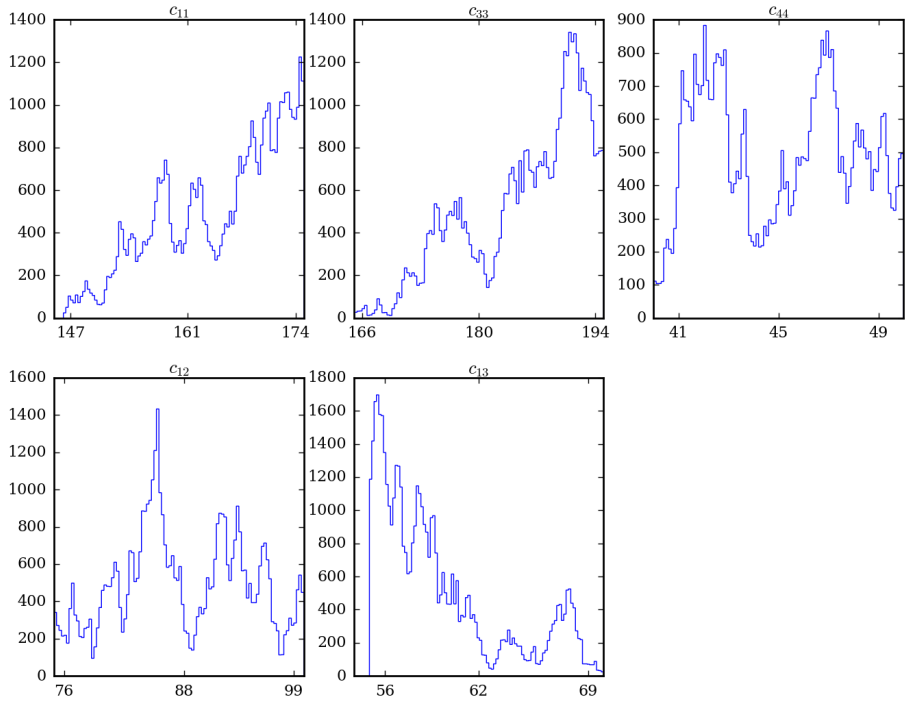

Figure 3.15: 50,000 MCMC iterations were performed for CP-Ti and the result is a distribution for each elastic constant given its likelihood as an acceptable solution to the experimental data.

The distributions of the acceptable values for each elastic constant for α-TI are shown in Figure 3.16. As with CP-Ti, a range of elastic constants would provide a satisfactory fit to the α-Ti experimental data. The elastic constants c_{11} and c_{44} from the least squares optimization correspond with the highest peaks in the corresponding histograms, while the Bayesian analysis found most frequent values that differed for the other three elastic constants. The distributions for each elastic constant are quite distinct for α-Ti, with a bimodal distribution for c_{11} and non-symmetric distributions for the remaining elastic constants.

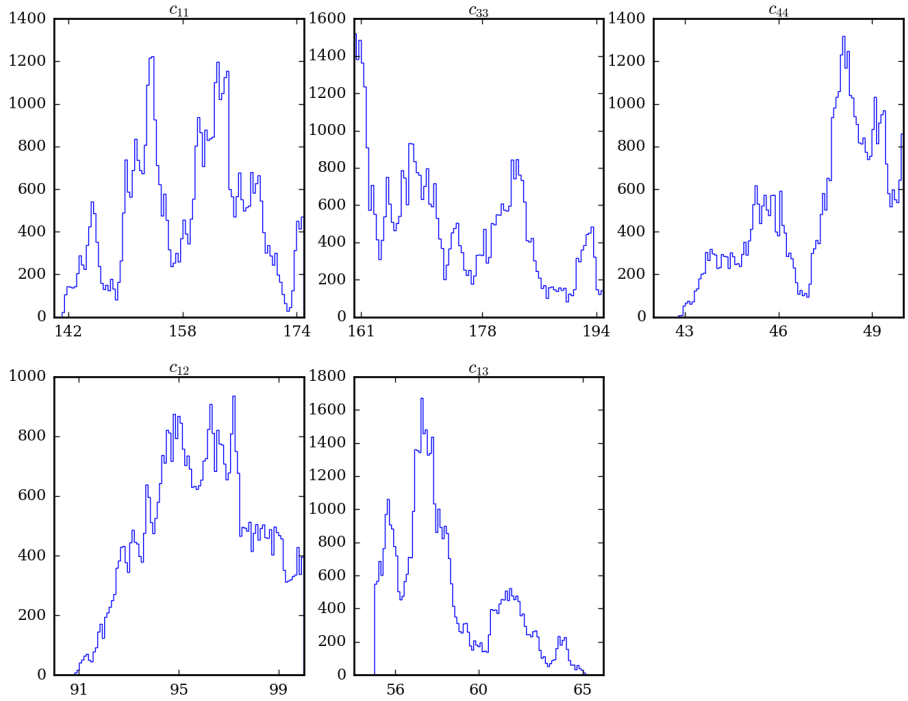

Figure 3.16: 50,000 MCMC iterations were performed for α-Ti and the result is a distribution for each elastic constant given its likelihood as an acceptable solution to the experimental data.

Additionally, the distributions of the acceptable values for each elastic constant for colony-TI are shown in Figure 3.17. Again, a range of elastic constants would provide a satisfactory fit to the colony-Ti experimental data, as found CP-Ti and α-Ti.

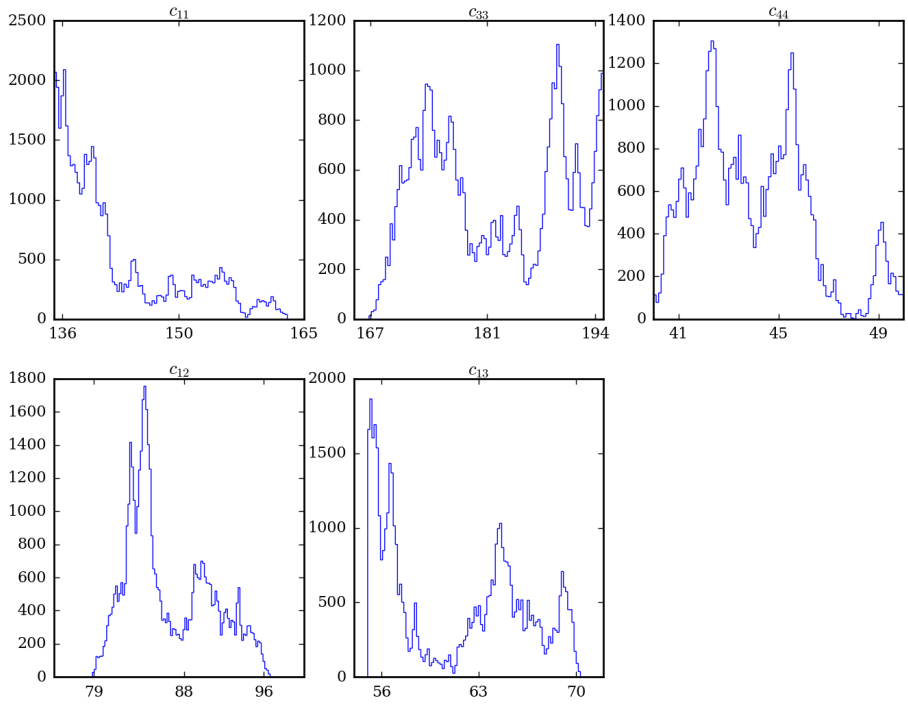

Figure 3.17: 50,000 MCMC iterations were performed for $\alpha + \beta$-Ti and the result is a distribution for each elastic constant given its likelihood as an acceptable solution to the experimental data.

3.4 Conclusions

The purpose of this work was to develop forward and inverse protocols to assess titanium-specific elastic constants as the relate to the estimation of experimental indentation modulus datasets. This work performed a rigorous least square regression of a LE-FEM simulation dataset, performed a least-squares optimization between the experimental and function fit to the simulation data, and expressed the range of

acceptable elastic constants through Bayesian inference. This type of procedure is vital in linking experimental results and simulation tools in an effort to increase decision-making on a materials-specific basis.

CHAPTER 4

EXTRACTION OF CPFEM MODEL PARAMETERS FROM SPHERICAL INDENTATION DATASETS

4.1 Introduction

Physics-based models such as the crystal plasticity finite element method (CPFEM) are reliant on experimental data for model calibration and validation. Historically, the experimental datasets have come in the form of single crystal or polycrystalline uniaxial tests, as well as combined loading and complex stress-states. Single crystal experimental datasets are advantageous because the crystal orientation is known precisely, whereas the polycrystalline experimental results are a function of many crystal orientations. Conversely, polycrystalline specimens are economical to produce, while single crystal specimens can be laborious to generate. Recent work in the field of spherical nanoindentation has been able to capture local structure-property relations in polycrystalline cubic metals by relating the indentation load and displacement to the indentation stiffness and yield strength [45–47]. These values are a function of the local microstructure in the indentation zone. Nanoindentation requires relatively simple equipment and sample preparation; sample preparation is similar to procedures used in metallography (sectioning, grinding, and polishing) and large surfaces can be prepared quickly.

The purpose of the present study is to assess the validity and form of the current CPFEM model for α-Ti and $\alpha+\beta$ colonies by comparing results with that of spherical nanoindentation experiments.

4.1.1 Indentation

Indentation experiments are performed on a materials surface and were initially used to determine the hardness of materials [116]. These tests are appealing because of their versatility for exploring a range of material classes, but the indenter size was initially too large to isolate properties from thin films or single crystals. Therefore, nanoindentation was introduced [121] to perform indents with a minimum depth of a few nanometers to measure elastic modulus in addition to hardness [120].

However, experiments were not able to ascertain the specifics of the material deformation directly beneath the indenter, so FEM simulations were first performed to model the elastic-plastic deformation during the indentation of FCC materials [122]. Early FEM analysis showed that indentation testing could be used to determine the material hardness and stiffness [123]. Additionally, early FEM analysis also showed there was a general correlation between load and indentation depth with mechanical properties such as elastic modulus, yield strength, and strain hardening [122, 123].

Many previous studies have employed sharp indenters and performed the analysis on the unloading segment of the load-displacement curve. This is done because the unloading segment is assumed to be elastic [120]. In recent years, spherical indenters have been used due to their smoother stress fields and the generation of indentation stress-strain curves from spherical indentation data; a thorough review of indentation and the indentation stress-strain curve has been performed by Pathak and Kalidindi [117]. A limitation of many of these studies is the calibration to experimental load-displacement data. The key features of indentation load-displacement curves are the slope of the loading and unloading portions in addition to the peak load. However, properties such as the elastic-plastic transition are indistinguishable (in most cases), making it difficult to determine the dominant mode of deformation.

More recently, CPFEM studies have been able to estimate CRSS and hardening values for HCP materials from load-displacement curves [124] and analyze the

size/shape of the plastic region attributed to indentation in bulk single crystals and thin films [125]. CPFEM results have also produced good agreement when comparing plastic zone sizes with plastic slip traces from nanoindentation experiments [126]. However, these studies still utilize certain specimen symmetry in order to employ reduced portions of the crystal sample while applying pertinent boundary conditions on symmetry planes. This limits the range of orientations and responses that can be studied with these schemes.

Computational nanoindentation studies have also been explored with molecular dynamics (MD) simulations. They utilize smaller indenter radii (on the order of 100 nm) to elucidate phenomena such as grain growth as a function of indentation rate in nanocrystalline nickel [128] or observe active slip plane families during indentation [129]. Specific to titanium, nanoindentation MD simulations have found a difference in hardness and elastic modulus based on the shape of the indenter [130].

The exploration of Ti-6Al-4V (combination of α and β within the same grain) with a Berkovich indenter has found a high level of $\langle a \rangle$-type slip activity (basal, prismatic, and pyramidal) regardless of crystal orientation, while second-order $\langle c + a \rangle$ pyramidal slip was active, particularly in the grains where the c-axis was closely aligned with the loading direction [230]. Additionally, load-displacement curves of Berkovich nanoindenter experiments and CPFEM simulations (model parameters taken from [41]) of Ti-6Al-4V showed decent agreement when compared for a variety of crystal orientations [203]. Surface polishing has been shown to have a large impact on the nanohardness and effective Youngs modulus of commercially-pure titanium [231].

4.1.2 Spherical Indentation

One of the common themes among indentation studies is their use of the load-displacement curve for model calibration/validation. The indenter creates a highly

heterogeneous stress field, which typically leads to oversimplified analyses of the force-displacement data and the extraction of underwhelming material properties like hardness. The theory of Hertz [132,133,135] is the basis for the mathematical formulation used for spherical nanoindentation. Hertz theory assumes the contact between two axisymmetric surfaces is frictionless and isotropic. From this theory, the relationship between the force and indenter displacement can be represented as

$$P = \frac{4}{3} E_{eff} \left(R_{eff}\right)^{\frac{1}{2}} \left(h_e\right)^{\frac{3}{2}} \tag{4.1}$$

where P is the indentation force, E_{eff} is the effective indentation modulus, R_{eff} is the effective radius, and h_e is the elastic penetration depth. Additionally, the contact radius a_i of the spherical indenter can be determined from

$$a_i = \left(R_{eff}\right)^{\frac{1}{2}} \left(h_e\right)^{\frac{1}{2}} . \tag{4.2}$$

The effective indentation modulus is a function indenter and the specimen, i.e.

$$\frac{1}{E_{eff}} = \frac{1}{E_{ind}} + \frac{1 - \nu_i^2}{E_i} \tag{4.3}$$

where E_{ind} is the indentation modulus and E_i & ν_i are the elastic modulus and Poissons ratio of the indentation specimen [179, 180]. For anisotropic materials, the contact area is also elliptical in shape and not round [178, 181]. However, this difference has had a minimal effect on the calculation of the indentation modulus in previous studies [181–183]. The indentation force and displacement can be extended to equations for true indentation stress (σ_{ind}) and true indentation strain (ϵ_{ind}) through

$$\epsilon_{ind} = \frac{3}{4\pi} \frac{h}{a_i} \quad \& \quad \sigma_{ind} = \frac{P}{\pi a_i^2} \tag{4.4}$$

where h is the indenter displacement. These definitions of indentation stress and strain have a physical reference; the primary zone can be thought of as a cylinder with

a radius of and a height of [136]. Various definitions for indentation stress and strain were evaluated for a isotropic, elastic-plastic material model and the strain hardening behavior of the above equations were deemed most realistic [137]. Additionally, some of the deficiencies of nanoindentation analyses protocols have been addressed [136], but the protocol has mainly only been applied to cubic symmetries [117, 177].

4.2 Methodology

4.2.1 Materials

A commercially pure (grade 2) bar of titanium from McMaster-Carr was heat treated at 800°C for 2 hours in air and allowed to furnace cool to room temperature. This was done to anneal the material and grow the grain size to make indentation measurements with 16 and 100 µm radii indenter tips inside individual grains possible. In order to overcome the texture in the original material and survey a variety of grain orientations, two different samples were sectioned: (i) indentation plane parallel to the ND and (ii) indentation plane parallel to the RD.

A bar of Ti-6Al-4V from McMaster-Carr (Grade 5) was used in this study. The starting material had a duplex microstructure (equiaxed primary α-grains and lamellar $\alpha + \beta$ grains). The raw material was heat treated to produce larger primary α-grains to make the process of nanoindentation with a 16 µm radius indenter less difficult. The raw material was annealed at approximately 1025°C for two hours, slowly cooled (0.1°C/min) to 950°C and held for one hour, then allowed to furnace cool. This produced larger primary α-grains, some having elongated shapes, as well as larger lamellar regions. For more specifics about the materials and experimental testing procedure, please refer to [47, 186].

4.2.2 Simulation Configuration

The simulation of indentation of titanium and its alloys is challenging by virtue of significant elastic and plastic anisotropy, along with the low symmetry HCP crystal

structure. Multiple meshing procedures were considered for the indentation simulations to ascertain a sufficient mesh for extracting indentation stress-strain curves but to also limit the total number of elements. Meshes with multi-point constraints, graded hexahedral regions, and a combination of tetrahedral and hexahedral regions were tested, but none could reach the required coarseness away from the indenter to achieve a satisfactory simulation volume.

The indentation specimen is three-dimensional and is composed of an inner and outer region. The inner region consists of hexahedral elements (type C3D8) with eight integration points and is designed for direct contact with the indenter. The outer region is comprised of infinite elements (type CIN3D8) that require the sharing of at least one face with a hexahedral elements. The indenter is defined as a rigid sphere with a radius of 10 µm. The contact surface between the indenter and indentation specimen is modeled as frictionless, an estimate that has been proven valid in previous studies for relatively flat indentation surfaces [116,122,194–196] but that contact with sharp indenters might need to account for friction [197,198]. More details regarding the mesh used can be found in Section 3.2.1.

The spherical nanoindentation CPFEM simulations were performed with Abaqus 6.10-1 [87]. The simulation is a series of load-unload displacement combinations, where each load-unload combination provides a single data point on the indentation stress-strain curves. The simulations are displacement-controlled at with a strain rate of $2.5\text{x}10^{-4}$ to $7\text{x}10^{-4}$, which differs from the experiments where the indenter is force-controlled at a rate of $dP/dh = 0.05$, where P is the indenter force and h is the indenter depth. Indentation was performed to maximum depth of 40 nm, with a total of 20 load-unload cycles to achieve the maximum depth. A load-unload schematic is shown in Figure 4.1. The first load-unload cycle, which consists of indenter displacements of 1.0 nm and 0.1 nm, respectively, was used to determine the indentation elastic modulus. The same mesh configuration was used for all simulations

in this study.

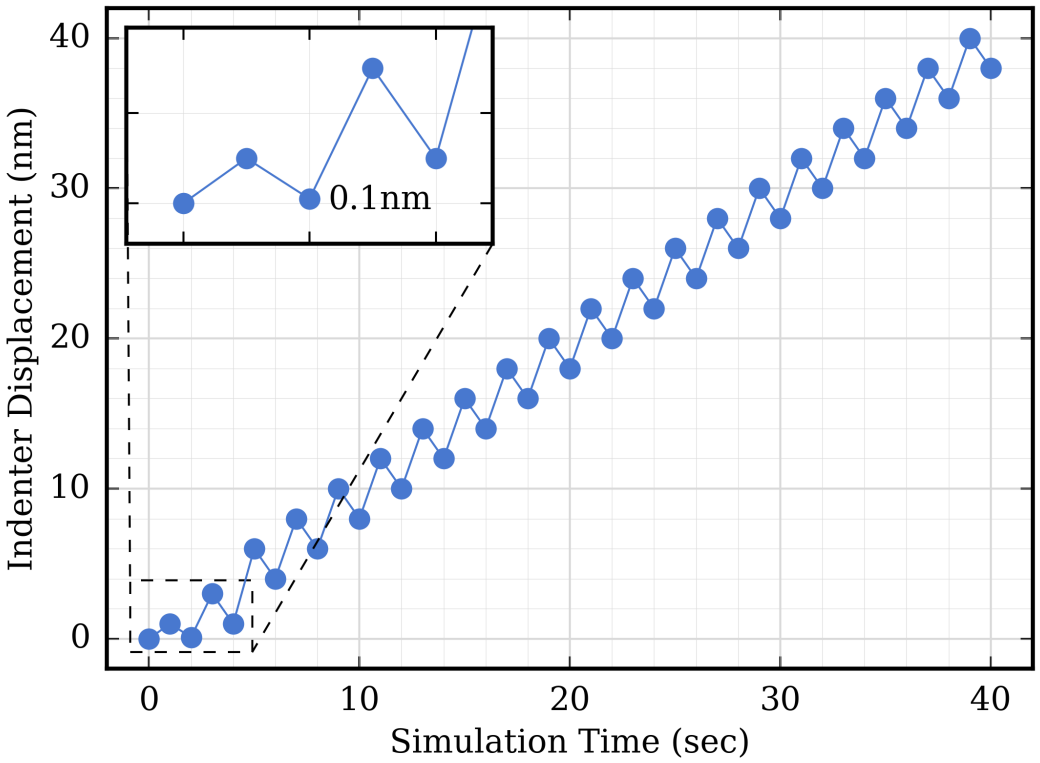

Figure 4.1: The indenter displacement versus simulation time.

The FE mesh used in this study has 13,500 C3D8 and 3,400 CIN3D8 elements, making the simulation quite computationally expensive due to the lack of parallel element operations introduced by the infinite elements (see Section 3.2.1 for additional information). The run time for the 20 load-unload cycles is approximately 72-96 hours of wall time on 12 AMD Opteron 6378 (2.4Ghz) processors with a total of 24GB memory. The CPFEM model parameters that have been calibrated previously [50] and are used in this work are shown in Table 4.1. The rest of the model parameters are presented in the results section with their specific material system results.

4.2.3 Calculation of ISS Curves

The estimation of the indentation stress and indentation strain from the spherical nanoindentation simulations requires the determination of the contact radius 4.2,

Table 4.1: Model parameters used for CPFEM simulations of α-Ti and colony grains.

Parameter	Value	Parameter	Value
c_{11}	172.8 GPa	h	50 MPa
c_{12}	97.91 GPa	h_D	50 MPa
c_{13}	73.43 GPa	d	146 μm
c_{33}	192.3 GPa	μ	2
c_{44}	49.70 GPa	κ_s	50 MPa

which is a function of the elastic indenter depth and the effective indenter radius. The total indenter displacement is defined as

$$h = h_e - h_r, \tag{4.5}$$

where h_r is the residual surface displacement if the indenter is fully unloaded. Equations (4.1) and (4.5) are combined as

$$h = \left(\frac{4}{3} E_{ind} \left(R_{eff}\right)^{\frac{1}{2}}\right)^{-\frac{2}{3}} (P)^{\frac{2}{3}} - h_r. \tag{4.6}$$

The algorithm for determining the indentation stress-strain points is shown in Figure 4.2. First, a load-unload (LU_j) sequence is defined by determining the maximum loading that is also followed by an unloading step. The maximum load and minimum unload points are determined, then linear regression is performed on load-displacement data for the defined load-unload segment. If the deformation is elastic, then the y-intercept is known ($h_r = 0$) and thus the effective radius is equal to the radius of the indenter (i.e., $R_{eff} = R_{ind}$). In this situation, the slope from the linear regression can be used to determine E_{ind}; this value is assumed constant for a specific simulation. If the y-intercept is non-zero, then there is plastic deformation and the slope of the linear regression can be used to determine R_{eff}. This procedure is followed for the entire force-displacement curve; each load-unload sequence provides a single data point on the indentation stress-strain curve.

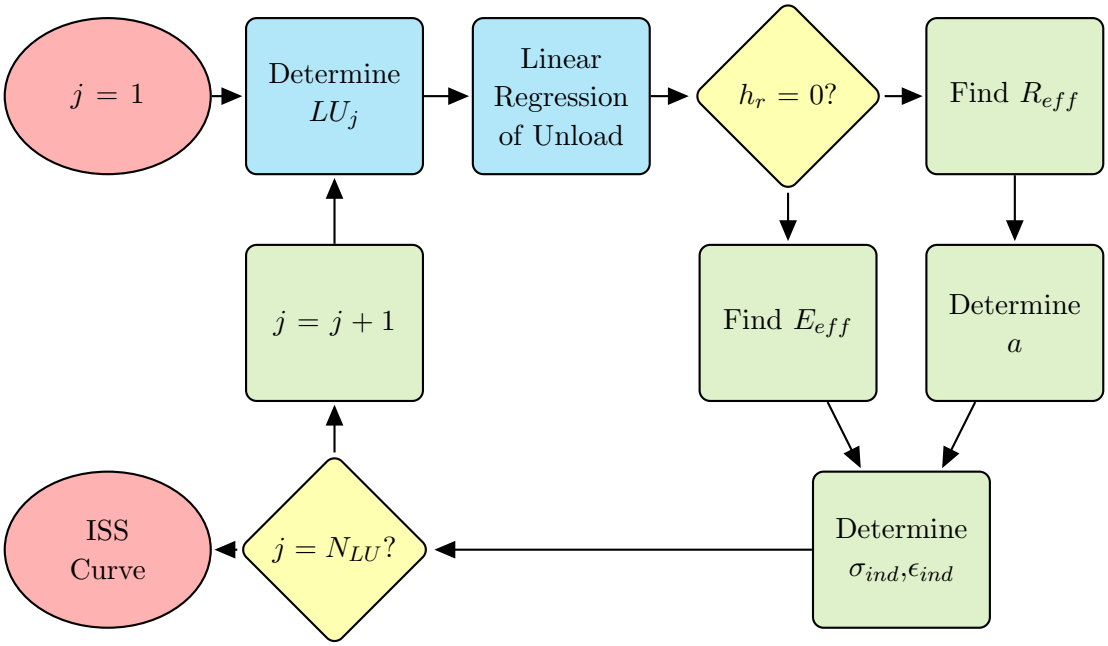

Figure 4.2: Flowchart for the generation of the ISS curves.

4.2.4 Kinetics of the Crystal Plasticity Model

The heterogeneity of the microstructure and the anisotropic deformation response of Ti-64 dictate that crystal plasticity be used [9, 13, 232]. Specifically, the CPFEM model considered in this work was initially developed for duplex Ti-6Al-4V for 2D analysis [52], extended to 3D [39], then further modified by various authors [40, 43, 44, 54, 55, 57]. Most recently, Smith et al. [43] calibrated the model to three distinct titanium alloy microstructures via uniaxial tension and fully-reversed cyclic tension-compression experimental data.

This model is based on the two-term multiplicative decomposition of the deformation gradient into elastic and plastic parts (i.e., $\mathbf{F} = \mathbf{F}^{\mathrm{e}} \cdot \mathbf{F}^{\mathrm{p}}$). The plastic velocity gradient is determined in the intermediate configuration [9] which is both isoclinic and lattice invariant. The model considers duplex microstructures that can consist of either primary α grains and/or colony grains that are a lamellar structure and contain secondary α phase and β regions. The $\alpha + \beta$ colony grains are homogenized in this model due to the size range of microstructure features such as β laths. The BOR

is utilized in order to transform the BCC slip systems into a hexagonal coordinate system [233]. The isothermal slip system shearing rate, $\dot{\gamma}^{(\xi)}$, where the superscript (ξ) denotes an individual slip system, is defined according to a power-law flow rule of the form

$$\dot{\gamma}^{(\xi)} = \dot{\gamma}_0 \left\langle \frac{\left|\tau^{(\xi)} - \chi^{(\xi)}\right| - \kappa^{(\xi)}}{D^{(\xi)}} \right\rangle^{M} \operatorname{sgn}\left(\tau^{(\xi)} - \chi^{(\xi)}\right), \tag{4.7}$$

where $\dot{\gamma}_0$ is the reference shearing rate, $\tau^{(\xi)}$ is the resolved shear stress, $\chi^{(\xi)}$ is the back stress, $\kappa^{(\xi)}$ is the threshold stress, $D^{(\xi)}$ is the drag stress, and M is the inverse strain-rate sensitivity exponent. The threshold stress is defined as the sum of a Hall-Petch strength term and a softening term due to breakdown of short-range order, i.e.,

$$\kappa^{(\xi)} = \frac{\kappa_y}{\sqrt{d}} + \kappa_s^{(\xi)}. \tag{4.8}$$

In Equation (4.8), κ_y is the Hall-Petch slope, d is the mean slip distance in the α-phase (primary or secondary), and $\kappa_s^{(\xi)}$ is a softening parameter. The evolution of the threshold stress is governed solely by the softening term (μ is the softening rate coefficient), which follows a dynamic recovery law and takes the form

$$\dot{\kappa}^{(\xi)} = \dot{\kappa_s}^{(\xi)} = -\mu\kappa_s \left|\dot{\gamma}^{(\xi)}\right|. \tag{4.9}$$

The drag stress is the difference in the between the CRSS (τ_{CRSS}) and the initial threshold stress [41], i.e.

$$D^{(\xi)} = \tau_{CRSS}^{(\xi)} - \kappa^{(\xi)}\big|_{t=0}. \tag{4.10}$$

The drag stress does not evolve (i.e., $\dot{D}^{(\xi)} = 0$), while the back stress is initially set to zero and evolves according to a direct hardening/dynamic recovery relation of the form

$$\dot{\chi}^{(\xi)} = h\dot{\gamma}^{(\xi)} - h_D \chi^{(\xi)} \left|\dot{\gamma}^{(\xi)}\right|, \tag{4.11}$$

where h is the direct hardening coefficient and h_D is the dynamic recovery coefficient.

It is a common assumption in the literature that $\alpha + \beta$ titanium is stronger than α titanium and the α/β interface is one of the main contributors to the increase in strength [85]. The constitutive relations [41,50] assume an increase in basal and prismatic slip system CRSS values for colony grains, $\tau^{(\xi)}_{CRSS}(\alpha+\beta) = 1.25\tau^{(\xi)}_{CRSS}(\alpha)$ [41]. Additionally, the diameter used in the threshold stress (Equation (4.8)) is assumed to be the α-lath spacing for the hard orientations in the colony grains. Finally, the CPFEM model does not differentiate between the primary-α and $\alpha+\beta$ colony grains in terms of elastic stiffness. This coarse assumption is based on comparing with experimental information on cyclic stress-strain response at the macroscale rather than at the scale of individual phases. However, the elastic constants for $\alpha + \beta$ Ti-6242 have been found to be extremely close to the elastic constants for the α-phase of the same material [86].

Single crystal elastic constants for α-titanium are assigned to all grains in the polycrystal [43]; the $\alpha+\beta$ colonies are predominantly composed of α laths. The crystal plasticity formulation is coded into an Abaqus/Standard [87] via a User MATerial subroutine (UMAT) [88]; the numerical integration scheme is similar to that of fully implicit method [89].

4.3 Results

Due to the computational expense of these simulations, it was advantageous to only modify a few of the model parameters to assess the potential modifications required for calibrating to the indentation experimental dataset. Therefore, model calibration was performed by refining the critical resolved shear stress (CRSS) values for the prismatic, basal, and pyramidal slip systems in the CPFEM model, while all other

model parameters were held constant. Some of the other model parameters (e.g., back stress) are specific to cyclic loading conditions, and while the load-unload nature of indentation could be considered as such, this first effort is to ascertain the quality of the relationship between the indentation stress-strain curve and commonly reported values such as the critical resolved shear stress.

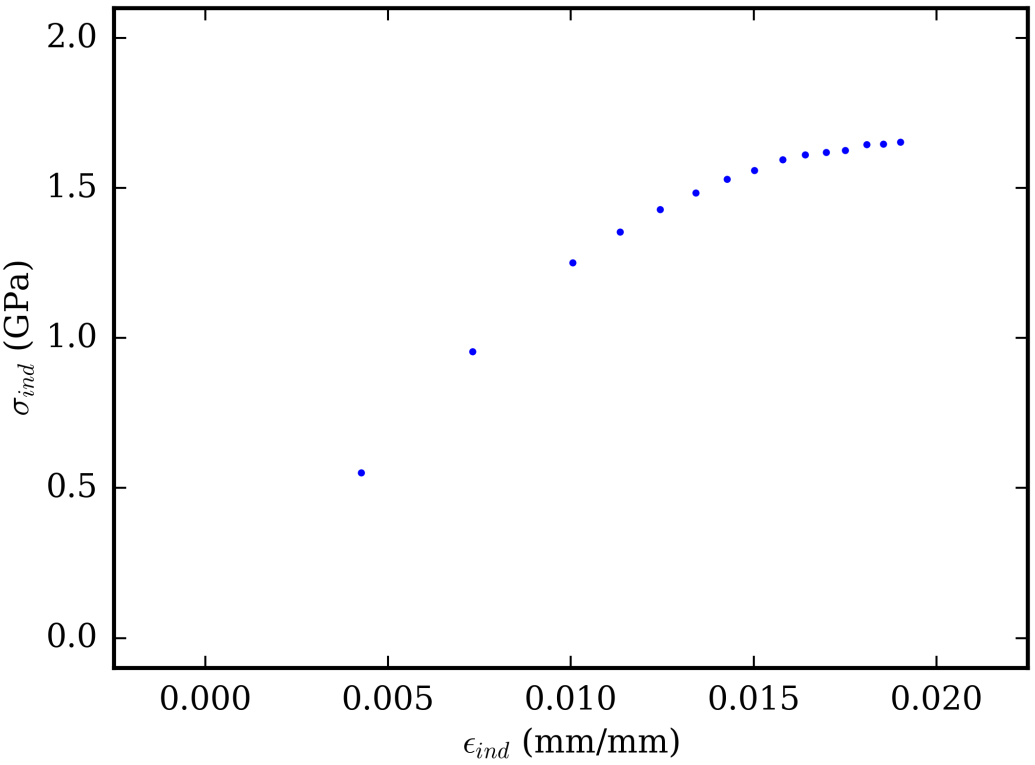

Figure 4.3: The CPFEM indentation stress-strain curve for $\Phi = 60°$ for commercially pure titanium.

Figure 4.3 is an indentation stress-strain curve for commercially pure titanium with $\Phi = 60°$. As previously stated, each load-unload combination provides a single indentation stress-strain point for plotting, therefore a series of load-unloads are performed with increasing displacement to generate the indentation stress-strain plot. The elastic and elastic-plastic transition are clearly defined in this representation. The indentation yield strength is determined with a 0.2% offset, precisely the same method that is commonly used for macroscopic tension testing. The hardening rate

is estimated as the slope of the indentation stress-strain curve ($d\sigma/d\epsilon$) immediately after the yield strength. The two indentation stress-strain plots immediately following the yield strength to calculate that slope. Note that the hardening rate calculated in this work differs from hardening rates commonly presented in the literature ($d\sigma/d\epsilon^p$).

Table 4.2: CRSS CPFEM model parameters

Material System	τ_{CRSS}^{basal}	τ_{CRSS}^{prism}	$\tau_{CRSS}^{pyr\langle a\rangle}$	$\tau_{CRSS}^{pyr\langle a+c\rangle}$
Previous Values	350 MPa	275 MPa	470 MPa	570 MPa
CP-Ti	225 MPa	195 MPa	470 MPa	570 MPa
α-Ti	350 MPa	275 MPa	700 MPa	800 MPa

4.3.1 Comparison of Indentation Yield Strength

The experimental dataset for commercially pure titanium was generated with two indenter sizes – 16 and 100 µm – and those results are in good agreement, despite the change in indenter size. Although the CPFEM model was not intended for and has never been calibrated with commercially-pure titanium experiment data, it was thought useful to compare the trend of the indentation stress-strain response. The basal and prismatic CRSS values were reduced relative to those of the previously-calibrated model to fit the experimental data. The experimental and CPFEM indentation yield strength values both decrease with increasing Φ angle, see Figure 4.4.

The α-titanium comparison demonstrates good agreement between the experimental and CPFEM indentation yield strength values. These yield strength values are much larger than the commercially pure titanium values. Table 4.2 illustrates a significant increase in the CRSS values for both pyramidal slip systems.

The same CRSS values as were used for α-titanium also apply to the colony grains in the CPFEM model. The CRSS of the BCC slip systems is a function of the prismatic slip system CRSS. Although the experimental data is not as plentiful as the

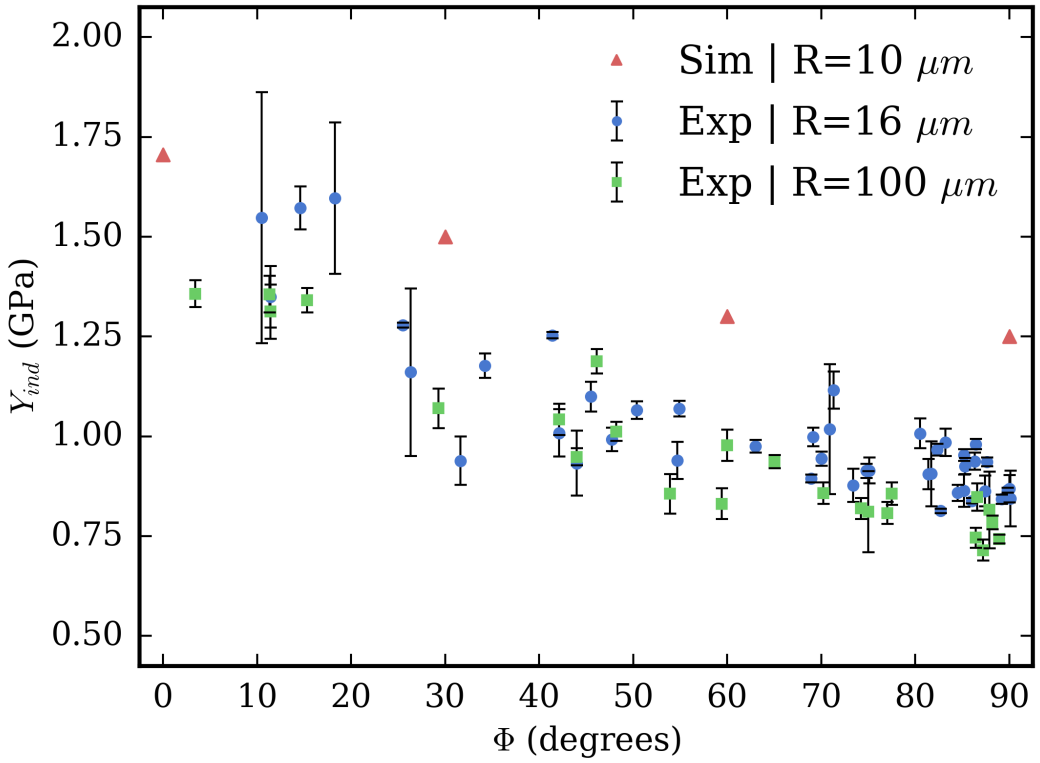

Figure 4.4: The comparison of the experimental and CPFEM indentation yield strength as a function of Φ for commercially-pure titanium.

commercially pure or α-titanium, the general trend seen for the other two systems follows here as well. Interestingly, the indentation yield strength values are extremely similar between the α-titanium and $\alpha + \beta$ titanium single crystals. This finding will have important implications in a later chapter when slip transfer phenomena are discussed specifically for $\alpha + \beta$ titanium alloys.

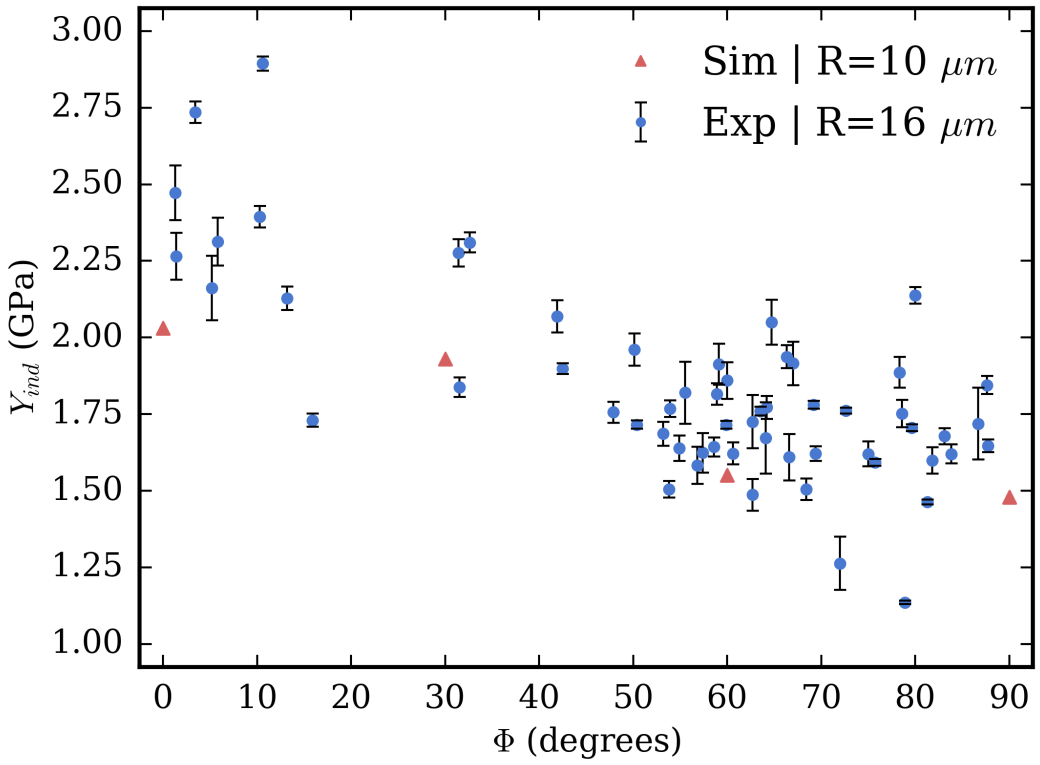

Figure 4.5: The comparison of the experimental and CPFEM indentation yield strength as a function of Φ for α-titanium.

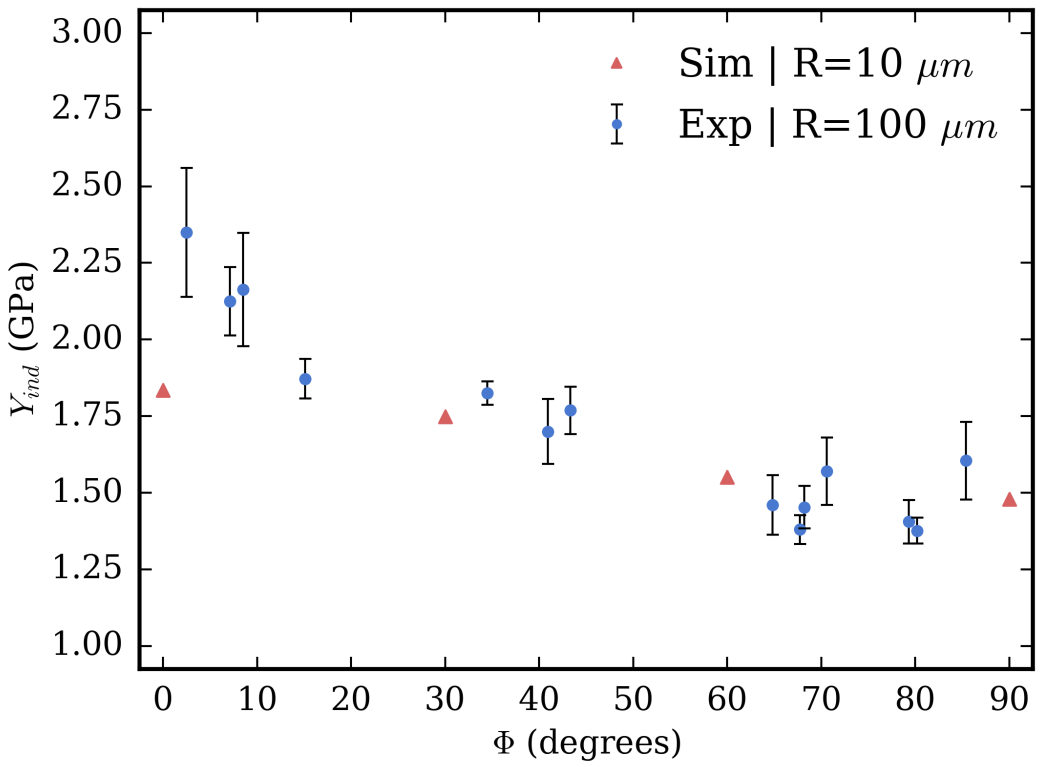

Figure 4.6: The comparison of the experimental and CPFEM indentation yield strength as a function of Φ for $\alpha + \beta$ titanium.

4.3.2 Comparison of Initial Indentation Hardening Rate

The indentation hardening rate can provide information about the hardening of single crystals, which is vital information for assessing the plastic deformation of specific slip systems. For the experimental datasets, the initial indentation hardening slopes (H_{ind}) were determined from the slope of the indentations stress-strain curves after yield (0.2% offset) and inside a 2% offset. The CPFEM simulations were not performed to significant amounts of plastic deformation due to computational restrictions, therefore the 3 indentation stress-strain points immediately following the indentation yield strength were used to determine the initial indentation hardening slopes. The values for commercially pure and α-titanium both follow a trend with decreasing indentation hardness rate with increasing Φ angle. And the CRSS model provides values that are in general agreement for both material systems as well.

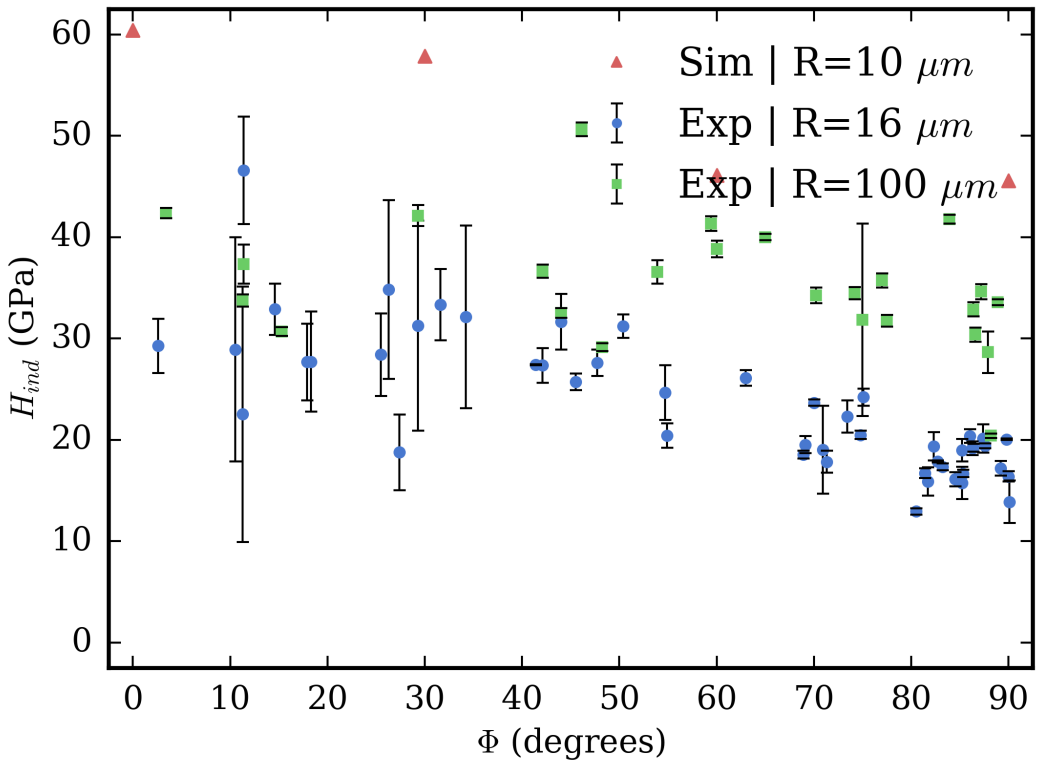

Figure 4.7: The comparison of the experimental and CPFEM indentation hardening rate as a function of Φ for commercially-pure titanium.

The implication of matching the trends of the indentation hardening rate is that the current model implementation is capturing the correct hardening phenomena in the single crystal response and that the other model parameters were well calibrated in previous studies [50].

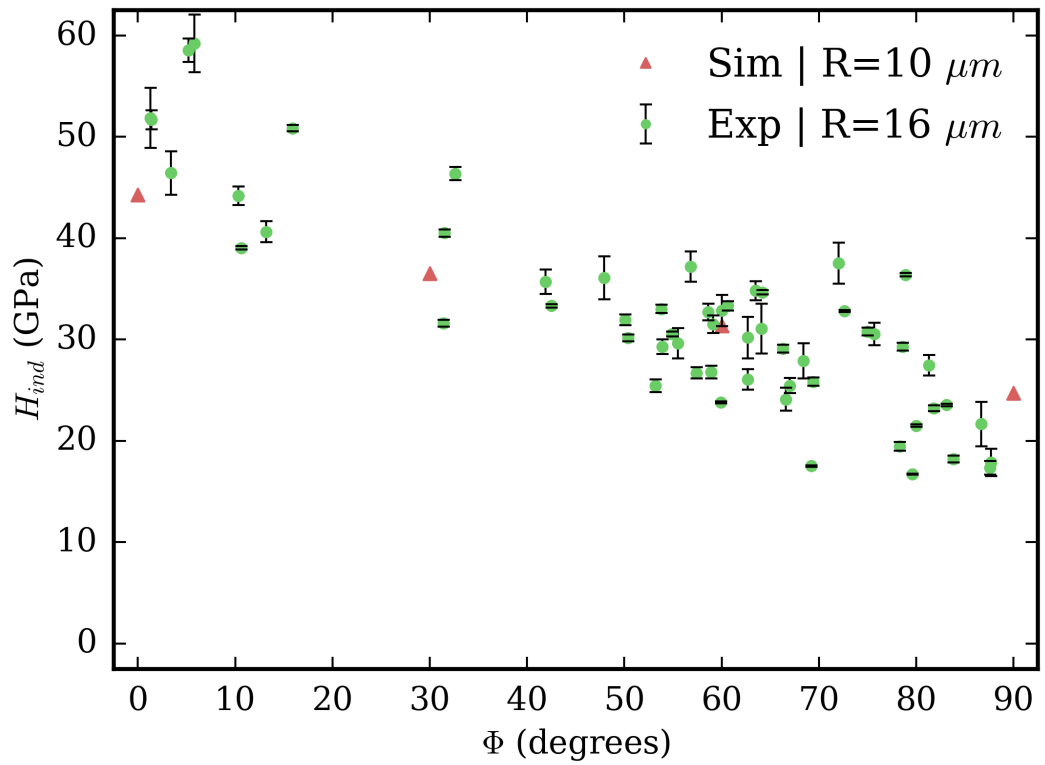

Figure 4.8: The comparison of the experimental and CPFEM indentation hardening rate as a function of Φ for α-titanium.

However, the trend does not hold true for the indentation hardening rate for the $\alpha+\beta$ colony grains. It is difficult to discern the underlying phenomena that led to the oscillatory nature of the experimental data in Figure 4.9. One explanation could be that various amounts of α and β were directly beneath the indenter, and each phase has a different initial hardening rate. The CPFEM trend is linear, but the values are within the same order of magnitude, so the colony grain response is reasonably represented by the CPFEM simulations.

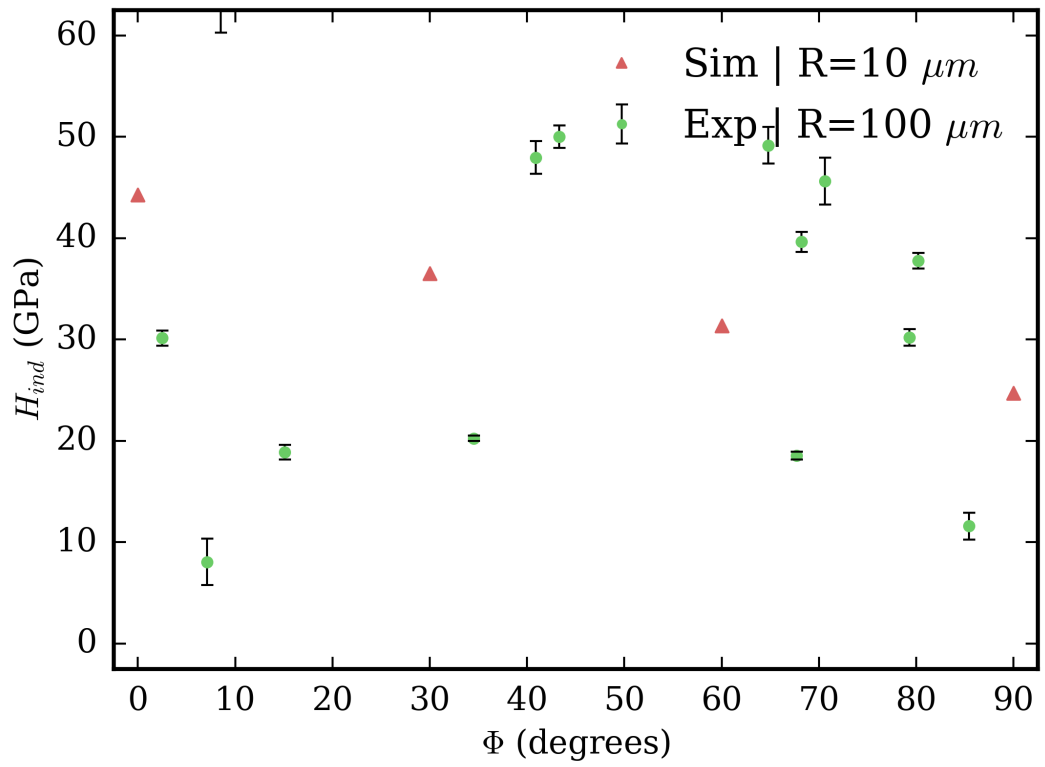

Figure 4.9: The comparison of the experimental and CPFEM indentation hardening rate as a function of Φ for $\alpha + \beta$ titanium.

4.3.3 Von Mises Stress Below the Indenter

One of the assumptions made with the modeling scheme presented is that the indentation stress-strain response is solely due to the deformation of the crystal directly beneath the indenter. In the experimental procedure, it is extremely difficult to determine the depth of a particular grain; laborious methods would be required to determine the change in the cross-section of the material with depth. Therefore, experimental indentation is performed in the center of large grains and multiple tests are performed in the same grain to provide an average response.

To assess the spatial response of the deformation into the depth of the specimen, the von Mises stress beneath the indenter is plotted in Figure 4.10. These values were selected from the three-dimensional model at a point in the indentation process which coincided with the indentation yield strength for each material. As expected, the von Mises stress increases immediately beneath the surface and then decreases with increasing depth. The uniaxial yield strength of titanium is approximately 900 MPa, meaning that plasticity is most likely occurring within 0.50-1.00 µm from the surface, depending on the orientation of the single crystal. Therefore, if the grains are on the order of 1 µm (or larger) in diameter, the single crystal deformation response is most likely very reasonable. However, at this level of deformation, the anisotropy of the elastic response could also play a role. Therefore, simulations and/or experiments to larger indenter displacements might also need to consider the presence of neighboring grains beneath the grain being indented to accurately capture the indentation elastic modulus, indentation yield strength, and initial indentation hardening rate.

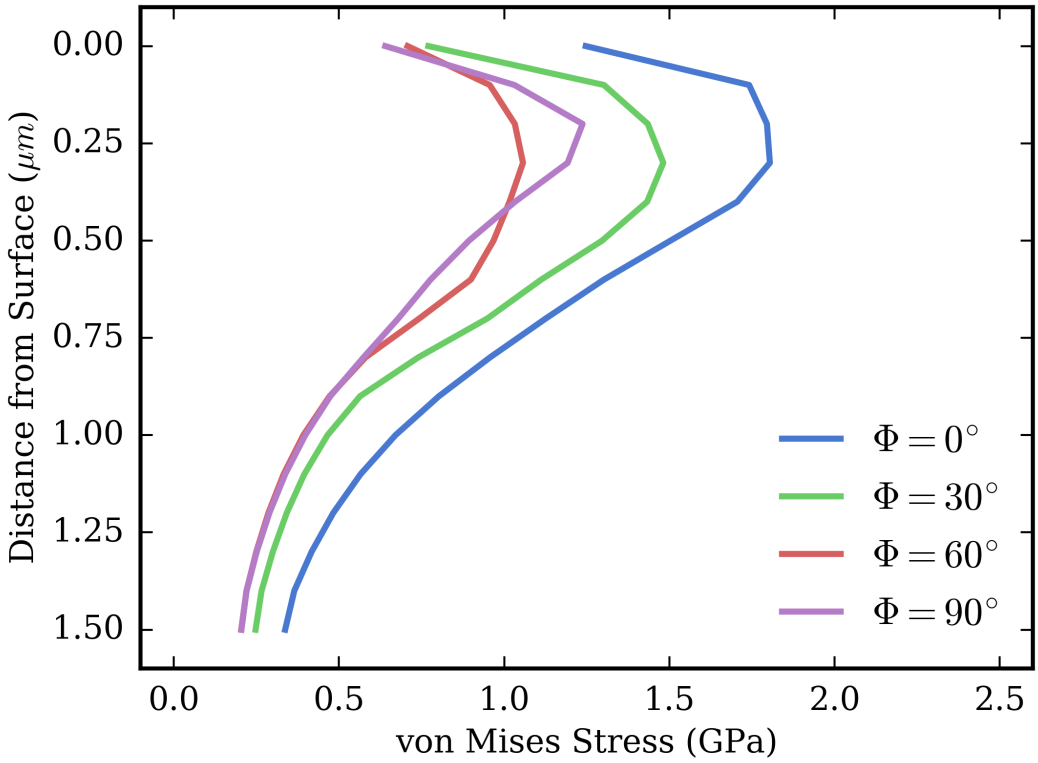

Figure 4.10: The von Mises stress directly beneath the indenter for α-titanium single crystal CPFEM simulations results for $\Phi = 0°$, $\Phi = 30°$, $\Phi = 60°$, and $\Phi = 90°$. The values were taken when the indentation stress was equal to indentation yield for each simulation.

4.4 Conclusion

Spherical nanoindentation are imperative for the advancement of physics-based materials models such as CPFEM. As shown in this work, previous calibration schemes utilizing polycrystalline experimental datasets have provided approximate model parameters, but more detail is needed to enhance specific values. Particularly, the CRSS values for the pyramidal slip systems had to be significantly increased to more closely match the experimental datasets.

CHAPTER 5

HIGH-CYCLE FATIGUE ANALYSIS OF α-TITANIUM

5.1 Introduction

Titanium and its alloys have an attractive strength-to-weight ratio and corrosion resistance, both of which are vital for the aerospace, automotive, and biomedical industries. The α-phase of titanium has a hexagonal close packed (HCP) crystal structure while the β-phase has a body centered cubic (BCC) crystal structure. In general, titanium alloys can be categorized as α or near α, $\alpha + \beta$, or β alloys [61]. Ti-6Al-4V (Ti-64) is one of the most commonly used $\alpha + \beta$ titanium alloys in the aerospace industry because of its balance of strength, ductility, and favorable elevated temperature properties; it is frequently used in airframes and aeroengines [60]. The $\alpha + \beta$ titanium alloys contain a combination of α and β phases, resulting in a wide range of microstructures and mechanical properties depending on the heat treatment and thermomechanical processing route. Specifically, the microstructure can range from a bimodal combination of α-grains and β-grains with embedded α-laths to fully lamellar $\alpha + \beta$ [64]. This variation in microstructure and resultant mechanical properties can lead to competing objectives in the material selection or optimization process.

Fatigue resistance is also an important characteristic for $\alpha + \beta$ titanium alloys because of their applications of use. Experimental evaluation of the fatigue resistance of materials is costly and labor intensive. In addition, the information extracted is often limited to simple metrics such as the number of cycles to failure. Unfortunately, it can be difficult to relate this data to microstructural variables (e.g., grain size distribution and crystallographic texture) because this requires parametric arrays of experiments and material characterization. Computational frameworks such as

crystal plasticity finite element method (CPFEM) have been used recently for relating microstructural features to macroscopic material properties [13, 234, 235]. CPFEM allows for the computation of local plastic deformation; thus it predicts stress and plastic shear heterogeneity within polycrystalline materials. However, the scope of CPFEM for HCF simulations are limited due to the high computational expense required, particularly for large domains involving many grains.

To compensate for the shortcomings of experimental testing and CPFEM simulations for high-cycle fatigue (HCF), an alternate approach is proposed in this work where local material response values are obtained by combining the advanced constitutive relations of CPFEM with the computationally-efficient materials knowledge system (MKS) [14–20]. This local information is used to assess the relative fatigue resistance of various hexagonal close-packed (HCP) textures.

5.1.1 Deformation Modes of Titanium Alloys

HCP crystal structures comprise the following slip families: (i) basal slip $\{0001\}\langle 11\bar{2}0\rangle$, (ii) prismatic slip $\{10\bar{1}0\}\langle 11\bar{2}0\rangle$, (iii) $\langle \mathrm{a}\rangle$ pyramidal slip $\{10\bar{1}1\}\langle 11\bar{2}0\rangle$, (iv) first-order $\langle \mathrm{a}+\mathrm{c}\rangle$ pyramidal slip $\{10\bar{1}1\}\langle 11\bar{2}3\rangle$, and (v) second-order $\langle \mathrm{a}+\mathrm{c}\rangle$ pyramidal slip $\{11\bar{2}2\}\langle 11\bar{2}3\rangle$. These slip planes and their associated slip directions are shown in Figure 5.1.

In Ti-64, prismatic slip has the smallest critical resolved shear stress (CRSS), followed by basal slip, while the pyramidal families having much higher slip resistance values. Deformation twinning can also be present in Ti alloys, but is severely diminished with an Al content above 6% [63] in Ti-64. The β phase has a BCC crystal structure and up to 48 slip systems, but it is common to only consider the 12 $\{110\}\langle 111\rangle$ and 12 $\{112\}\langle 111\rangle$ slip systems because of the difficulty to activate the 24 $\{123\}\langle 111\rangle$ slip systems due to alternating slip on primary systems.

Ti-64 is made up of an α-matrix that is combined with β rich grains. The lamellar

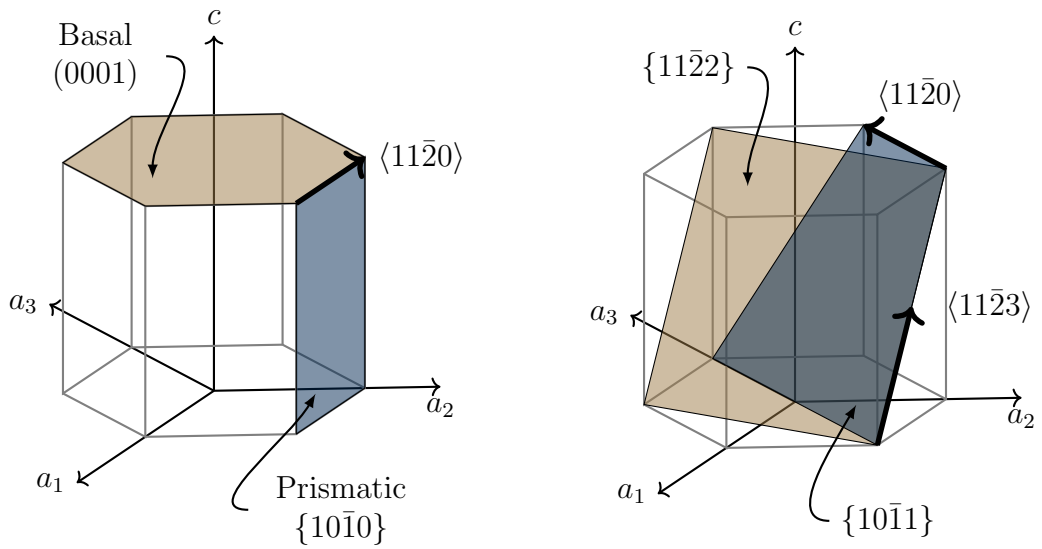

(a) Basal and Prismatic Slip

(b) Pyramidal Slip

Figure 5.1: Schematic of the crystallographic slip direction and associated planes for α-titanium, including (a) basal and prismatic slip plane and associated slip directions along with (b) $\langle \mathrm{a} \rangle$ pyramidal and $\langle \mathrm{a} + \mathrm{c} \rangle$ pyramidal slip plane and associated slip directions.

colonies are formed during cooling and there exists a Burgers orientation relation (BOR) that relates the HCP and BCC crystal orientation, given by $(110)_\beta \parallel (0001)_\alpha$ and $[1\bar{1}1]_\beta \parallel [11\bar{2}0]_\alpha$. This BOR was originally determined for zirconium [65] and then later confirmed for titanium [66]. In general, there are 12 possible HCP variants for a single BCC crystal [60], but typically only one of them is present in the duplex microstructure.

5.1.2 Microstructure-Sensitive CPFEM Model

The heterogeneity of the microstructure and the anisotropic deformation response of Ti-64 dictate that crystal plasticity be used [9, 13, 232]. Specifically, the CPFEM model considered in this work was initially developed for duplex Ti-6Al-4V for 2D analysis [52], extended to 3D [39], then further modified by various authors [40, 43, 44, 54, 55, 57]. Most recently, Smith et al. [43] calibrated the model to three

distinct titanium alloy microstructures via uniaxial tension and fully-reversed tension-compression experimental data. The specifics for the CPFEM used in this study are presented in depth in Chapter 4.

5.1.3 Fatigue Indicator Parameters

The driving force for growth of long cracks in metals is adequately described by the stress intensity factor in the context of LEFM [236]. In particular, a variety of stress-, strain-, and energy-based relations have been employed to predict fatigue crack growth at the macroscopic length scale [237]. However, the driving force for small fatigue crack nucleation and early growth is highly dependent on the local driving force, which in turn is directly linked to the microstructure of the material [106]. Fatigue Indicator Parameters (FIPs) have been used in macro- and microscale data analysis to serve as surrogate measures of the driving force for fatigue crack nucleation and early growth [29, 31].

The high-cycle fatigue (HCF) regime typically requires more than 100,000 cycles to failure and is characterized by heterogeneous plastic deformation among grains with majority elastic deformation throughout the specimen. The majority of cycles to failure for HCF involve processes of crack nucleation and early growth through the first few grains. Additionally, the fatigue crack formation process is strongly affected by spatial variation of microstructure features (e.g., grain size, orientation, disorientation) that give rise to heterogeneous stress and plastic strain states. These local elevated states of cyclic plastic shear strain can then lead to localized damage and, ultimately, the formation of a single dominant flaw that ultimately propagates to failure [238]. For Ti-64 tested at room temperature with R=0.1, more than 85% of the high-cycle fatigue life (unknown strain amplitude) was spent initiating and propagating small cracks (up to 0.5 mm in length) [97].

FIPs were introduced [29] to explicitly account for cumulative directional slip and

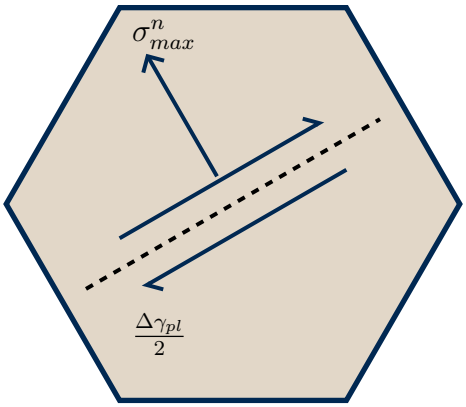

Figure 5.2: Illustration of the Fatemi-Socie Fatigue Indicator Parameter (FS_{FIP}).

have since been used in conjunction with macroscopic experimental [239–244] and computational [245] data of titanium alloys. FIPs have also been combined with finite element simulations to make life estimates [110, 111] or compare the relative fatigue resistance of multiple microstructures or materials [42]. In these cases, the selection of a specific FIP is important to reflect the deformation mechanism that leads to fatigue crack formation and early growth. For example, the Fatemi-Socie [107, 108] shear-based parameter has been shown to correlate well in the LCF and HCF regimes for multiaxial fatigue crack initiation [30] and is defined by

$$FIP_{FS} = \frac{\Delta\bar{\gamma}^p_{max}}{2}\left[1 + k\frac{\bar{\sigma}^n_{max}}{\sigma_y}\right], \tag{5.1}$$

where $\Delta\gamma^p_{max}$ is the maximum cyclic plastic shear strain range, σ^n_{max} is the maximum normal stress acting on the plane of maximum cyclic plastic shear strain, σ_y is the macroscopic yield strength of the material, and k is a constant with typical values between 0.5 and 1. The overbar ($\Delta\bar{\gamma}^p_{max}$, $\bar{\sigma}^n_{max}$) indicates that volumetric averaging should is performed [42]. In CPFEM simulations, this requires averaging FIP values of neighboring elements. The Fatemi-Socie FIP correlates well with the early fatigue behavior of metals that exhibit planar slip [41]; a graphical representation is shown in Figure 5.2. Additionally, FIP values can also be extended to assist in the calculation of life estimates [109–111].

5.1.4 Extreme Value Statistics

The largest FIP value found with Equation (5.1) is associated with the location in the microstructure that has the lowest resistance to fatigue crack formation. Multiple instantiations can be simulated and the maximum FIP found for each instantiation can be used to conduct an extreme value distribution analysis. In previous work [42, 44], the FIP distribution has been fit to a Gumbel distribution [246], i.e.

$$F_{Y_n}(y_n) = \exp\left[-e^{\alpha_n(y_n - u_n)}\right], \tag{5.2}$$

where $F_{Y_n}(y_n)$ is the probability that Y_n will be equal to or less than y_n, u_n is the characteristic largest value of the sampled population, and α_n is an inverse measure of dispersion of largest value of the population. The Gumbel distribution is unbounded and the shape of the probability density function curve is the same regardless of the fitting parameters. The maximum FIP values are arranged in increasing magnitude and their probability estimated by

$$F_{Y_j}(y_j) = \frac{j - 0.3}{n + 0.4}, \tag{5.3}$$

where n is the total number of simulations and j is the rank order of each maximum FIP value. For plotting and regression purposes, the Gumbel distribution can be rewritten as a linear function of y with expressions for slope (α_n) and y-intercept ($\alpha_n u_n$), i.e.,

$$\ln\left[\frac{1}{\ln\left[F_{Y_n}(y_n)\right]}\right] = \alpha_n y_n - \alpha_n u_n. \tag{5.4}$$

These resultant distributions are the basis for comparing fatigue resistance among different microstructures.

5.1.5 Materials Knowledge System

In recent years, a computationally efficient localization framework for hierarchical material microstructure called the Materials Knowledge System (MKS) has been developed [14–20]. The MKS is an algebraic series capable of predicting response fields on the micro-scale given some macro-scale averaged loading or boundary conditions.

The response of hierarchical materials systems has been addressed using generalized composite theories [33–38], wherein a localization tensor relates the material response at the microscale to the macroscale averaged values. In the case of linear elastic response, the fourth order localization tensor $\mathbf{A}$ relates the elastic strain at a location in the microstructure $\mathbf{x}$ to the average macroscopic strain on the statistical volume element (SVE):

$$\boldsymbol{\epsilon}\left(\mathbf{x}\right) = \mathbf{A}\left(\mathbf{x}\right)\left\langle \boldsymbol{\epsilon}\left(\mathbf{x}\right)\right\rangle, \tag{5.5}$$

$$\mathbf{A}\left(\mathbf{x}\right) = \left(\mathbf{I} - \left\langle \boldsymbol{\Gamma}\left(\mathbf{x},\mathbf{x}'\right)\boldsymbol{C}'\left(\mathbf{x}'\right)\right\rangle + \left\langle \boldsymbol{\Gamma}\left(\mathbf{x},\mathbf{x}'\right)\boldsymbol{C}'\left(\mathbf{x}'\right)\boldsymbol{\Gamma}\left(\mathbf{x}',\mathbf{x}''\right)\boldsymbol{C}'\left(\mathbf{x}''\right)\right\rangle - \ldots\right), \tag{5.6}$$

In Equation (5.6), $\mathbf{I}$ is the fourth-rank identity tensor, $\boldsymbol{C}'\left(\mathbf{x}\right)$ is the deviation in elastic stiffness from some arbitrary reference medium at a location $\mathbf{x}$, $\boldsymbol{\Gamma}$ is a symmetrized derivative of the Greens function defined with the elastic properties of the reference medium and $\left\langle f\right\rangle$ signifies the ensemble average of a function, f, over all spatial locations in the SVE.

Equation (5.6) can be transformed to a more convenient format through the introduction of the microstructure function, $\mathbf{m}\left(\mathbf{x},\mathbf{n}\right)$ [247], which captures the probability density of finding local state $\mathbf{n}$ at the spatial location $\mathbf{x}$. The local state descriptors are selected in such a manner that allows one to define the local microscale properties at the spatial location $\mathbf{x}$ (these may include phase identifiers, crystal orientation, etc.). Through the introduction of $\mathbf{m}\left(\mathbf{x},\mathbf{n}\right)$, substitution of $\mathbf{r} = \mathbf{x} - \mathbf{x}'$ and invocation

of the ergodic hypothesis, Equations (5.5) and (5.6) can be rewritten as

$$\begin{aligned}\boldsymbol{\epsilon}(\mathbf{x}) = \Big(&\mathbf{I} \\ &- \int_R \int_H \mathbf{a}(\mathbf{r},\mathbf{n})\,\mathbf{m}(\mathbf{x}+\mathbf{r},\mathbf{n})\,d\mathbf{n}d\mathbf{r} \\ &+ \int_R \int_R \int_H \int_H \tilde{\mathbf{a}}(\mathbf{r},\mathbf{r}',\mathbf{n},\mathbf{n}')\,\mathbf{m}(\mathbf{x}+\mathbf{r},\mathbf{n})\,\mathbf{m}(\mathbf{x}+\mathbf{r}+\mathbf{r}',\mathbf{n}')\,d\mathbf{n}d\mathbf{n}'d\mathbf{r}d\mathbf{r}' \\ &- \dots\Big)\langle\boldsymbol{\epsilon}(\mathbf{x})\rangle\end{aligned} \tag{5.7}$$

where $\mathbf{a}(\mathbf{r},\mathbf{n})$ and $\tilde{\mathbf{a}}(\mathbf{r},\mathbf{r}',\mathbf{n},\mathbf{n}')$ are the first and second order influence functions respectively, H is the set of all possible distinct local states ($\mathbf{n} \in H$) and R is the set of all vectors ($\mathbf{r} \in R$). The first order influence function $\mathbf{a}(\mathbf{r},\mathbf{n})$ quantifies the contribution to the local response in the current spatial location from the presence of local state $\mathbf{n}$ at a vector $\mathbf{r}$ away. The influence functions are computationally advantageous as they are completely independent of microstructure and can be efficiently computed using through Fourier transforms. Equation (5.7) is an infinite series where each successive term captures the influence of the local topology for higher levels of interactions between the local states [20]. It is worth noting that when the variation of local properties (or contrast) throughout the range of H is low, the series can be truncated to the first order terms with minimal loss of accuracy [15–18, 20].

Unfortunately $\boldsymbol{\Gamma}(\mathbf{r})$ has a singularity as $\mathbf{r}$ approaches zero, and the convergence of the series is highly sensitive to the selection of the reference medium. The MKS avoids these computational issues through a calibration of the influence functions using results from numerical simulations (e.g., based on finite element methods) that include a variety of microstructures and their local response fields. Once the influence functions are calibrated, the resulting linkages can be used to predict the response field of any new microstructure in the materials system at a far lower computational cost than with existing numerical frameworks.

Next, a generalized MKS framework is presented which converts Equation (5.7)

into a more computationally tractable form. First, $\mathbf{m}(\mathbf{x},\mathbf{n})$ and $\mathbf{a}(\mathbf{x},\mathbf{n})$ are expressed as linear combinations of an orthonormal basis $Q_L(\mathbf{n})$ and the indicator basis $\chi_s(\mathbf{x})$ [247], i.e.,

$$\mathbf{m}(\mathbf{x},\mathbf{n}) = \sum_L \sum_s M_s^L Q_L(\mathbf{n}) \chi_s(\mathbf{x}), \tag{5.8}$$

$$\mathbf{a}(\mathbf{x},\mathbf{n}) = \sum_L \sum_t A_t^L Q_L(\mathbf{n}) \chi_t(\mathbf{r}), \tag{5.9}$$

where L and s index the coefficients associated with $Q_L(\mathbf{n})$ and $\chi_s(\mathbf{x})$. The indicator basis returns one for all values of $\mathbf{x}$ within the spatial bin indexed by s and zero elsewhere. This uniform discretization of the spatial domain allows for the application of the FFT algorithm in the evaluation of Equations (5.8) and (5.9). If the same indicator basis is chosen for $Q_L(\mathbf{n})$ the local state space will be binned discretely (e.g., a two phase composite material). If the desired local state space is crystal lattice orientation, this binning strategy proves computationally inefficient as the number of bins required to accurately represent the orientation space is very large (1,944,000 bins for 1° spacing in each of the three Bunge-Euler [73] angles ϕ_1, Φ, and ϕ_2 used to describe the lattice orientation in a hexagonal crystal). It is far more efficient in this case to use the generalized spherical harmonics (GSH) [73]; a continuous, periodic, and orthonormal basis for functions on the orientation space defined using the Bunge-Euler angles.

Through the utilization of the orthogonality of the bases, expressions for M_s^L and A_t^L can be derived from Equations (5.8) and (5.9). Introducing these definitions, MKS can be expressed as:

$$\mathbf{p}_s = \left(\sum_L \sum_t \frac{\Delta}{N_L} A_t^L M_{s+t}^L + \sum_L \sum_{L'} \sum_t \sum_{t'} \frac{\Delta^2}{N_L N_{L'}} A_t^{LL'} M_{s+t+t'}^L + \ldots \right) \langle \mathbf{p} \rangle, \tag{5.10}$$

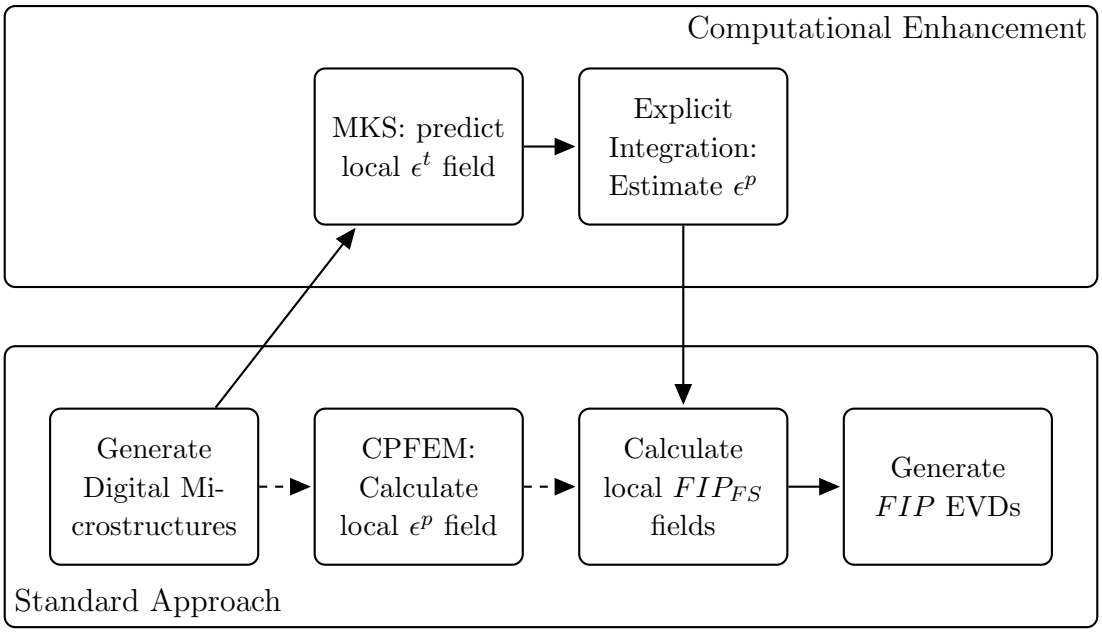

Figure 5.3: Flowchart for the insertion of MKS into the traditional workflow for producing extreme value distribution (EVD) plots.

5.2 Methodology

The purpose of this work is to explore a novel computationally-efficient method for determining local plastic strain tensors in polycrystalline SVEs. This standard approach is shown in the bottom row in Figure 5.3 and follows the general steps: (i) generate digital microstructures, (ii) use CPFEM to determine local plastic strain tensors, (iii) calculate FIP fields for each microstructure, and (iv) construct extreme value distributions of FIP values to determine rank order of microstructures. The new approach explored in this study (also described in Figure 5.3) utilizes the MKS method to determine the local total strain fields and calculates the local plastic strain tensors with an explicit integration scheme that employs the relevant constitutive relations described earlier.

5.2.1 Boundary and Loading Conditions

The MKS requires calibration data that, in this case, is generated via anisotropic linear-elastic simulation in Abaqus/Standard [87]. In the HCF regime, the material

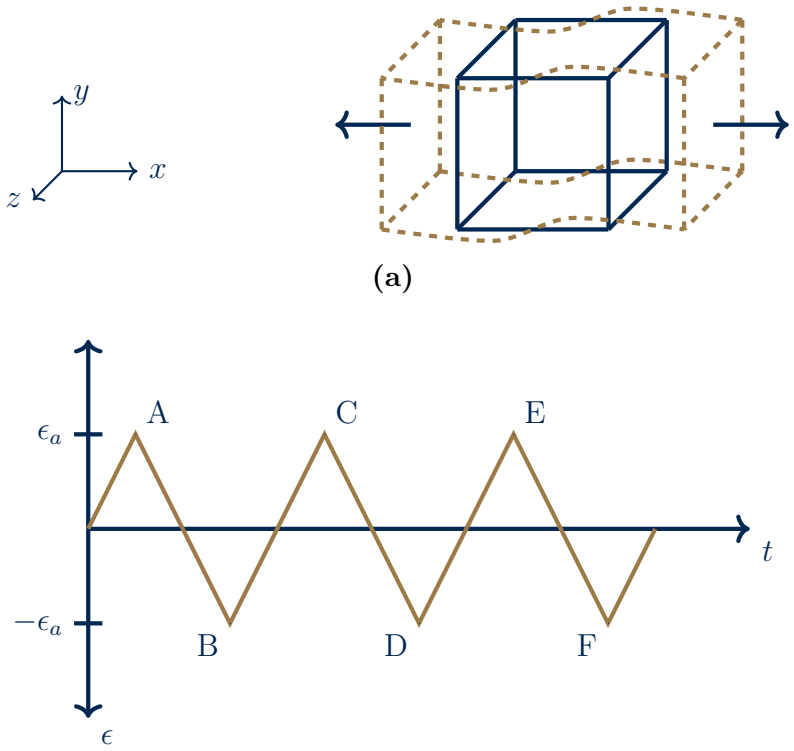

Figure 5.4: Schematic of (a) the loading conditions and periodic boundary conditions in the nonloading directions, as well as (b) the strain versus time curve used in the work.

response is dominated by elastic deformation; therefore the response is approximated as fully elastic in this work. The accuracy of this assumption is discussed subsequently in Section 5.3.1. For the MKS method, periodic boundary conditions are required to take advantage of the computational benefits of the FFT algorithm. An applied displacement is defined for one loading direction (on opposing faces) normal to the face and the other two displacements are set equal to zero. This is an important distinction from previous work [42, 43] where uniaxial stress boundary conditions were employed with periodic boundary conditions.

An example of loading in the x-direction is shown in Figure 5.4a. Additionally, loading in the y- and z-directions are also performed in an effort to sample the digital microstructures in three orthogonal loading directions.

The tension-compression cyclic loading is fully-reversed (R=-1) with a strain amplitude of 0.5% and is performed for the initial tensile and compressive loading, indicated by points A and B in Figure 5.4b. The specimens are loaded for three cycles and evaluated using with the explicit integration scheme to ensure saturation of cyclic plastic strain values. To perform these additional cycles, the subsequent tensile (C,E) and compressive (D,F) points are assumed to have the same local strain tensors as A and B, respectively.

5.2.2 Explicit Integration Procedure

The explicit integration scheme is a post-processing routine written in Python [214] that determines the local plastic strain tensor from the total strain tensor found for each voxel with the MKS. The MKS is calibrated to local strain tensors generated via Abaqus. The stress tensor is calculated from the strain tensor given the fourth-order elastic stiffness tensor, i.e. $\boldsymbol{\sigma} = \mathbf{C} : \boldsymbol{\epsilon}$. The stress tensor for each element is then discretized into 50 increments for each loading segment (e.g., A-B, B-C, etc.) assuming a linear relationship between the beginning and ending tensor values. The stress tensor is then used to determine the resolved shear stress for each slip system ($\tau^{(\xi)}$) for each time increment, according to

$$\tau^{(\xi)} = \boldsymbol{\sigma} : \left(\mathbf{s}^{(\xi)} \otimes \mathbf{n}^{(\xi)}\right), \tag{5.11}$$

where $\mathbf{s}^{(\xi)}$ and $\mathbf{n}^{(\xi)}$ are the slip direction and slip plane normal, respectively. The resolved shear stress is then used to solve for the slip system shearing rate (Equation (4.7)) and evolution equations (Equations (4.9) and (4.11)). The plastic strain tensor may be approximated as

$$\boldsymbol{\epsilon}^{p} = \sum_{\xi} \gamma^{(\xi)} \left(\mathbf{s}^{(\xi)} \otimes \mathbf{n}^{(\xi)}\right)_{sym}. \tag{5.12}$$

A graphical representation of this process is shown in Figure 5.5. The integrated

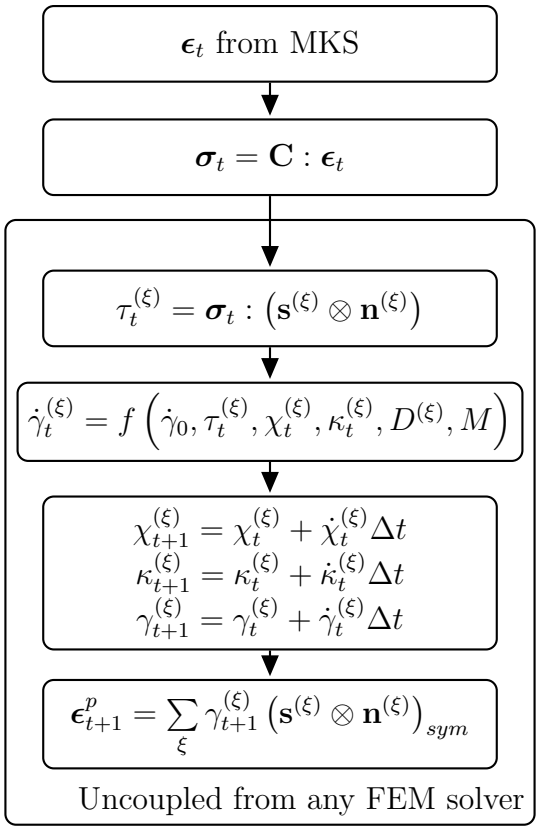

Figure 5.5: Flowchart for the forward Euler explicit integration scheme used to determine the local plastic strain tensor ($\boldsymbol{\epsilon}^p$) from the local total strain tensor ($\boldsymbol{\epsilon}$) provided by MKS.

scheme is a forward Euler routine that is commonly used in explicit CPFEM simulations [248]. The plastic strain quantities are orders of magnitude smaller than the total strain quantities in the HCF regime, therefore their impact on the stress and total strain tensors are minimal. Additionally, phenomena such as stress redistribution and relaxation are neglected in this work.

The model parameters used for all simulations (linear-elastic FEM, CPFEM, and explicit integration) are shown in Table 5.1.

5.2.3 Digital Microstructures

CPFEM has been used to model grain-scale plasticity and capture the heterogeneous deformation response in previous studies [42, 44]. This is typically done with an ensemble of statistical volume elements (SVEs), which are constructed such that

Table 5.1: Model parameters used for all simulations (linear-elastic FEM, CPFEM, and explicit integration).

Parameter	Value	Parameter	Value	Parameter	Value
c_{11}	172.8 GPa	τ_{CRSS}^{basal}	350 MPa	h	50 MPa
c_{12}	97.91 GPa	τ_{CRSS}^{prism}	275 MPa	h_D	50 MPa
c_{13}	73.43 GPa	$\tau_{CRSS}^{pyr\langle a\rangle}$	470 MPa	d	146 μm
c_{33}	192.3 GPa	$\tau_{CRSS}^{pyr\langle a+c\rangle}$	570 MPa	μ	2
c_{44}	49.70 GPa	κ_s	50 MPa		

their size is sufficient to sample microstructure-specific features (e.g., grains), but their overall response might differ from that of a representative volume element. RVEs are intended to approximate the response of the overall material microstructure by encompassing a volume that is large enough to contain a sufficient number of microstructure-specific features for statistical homogeneity [32]. Additionally, RVEs must also have measurable properties (e.g., elastic modulus, thermal conductivity) that are in agreement with the properties of an infinite volume of the actual material microstructure.

The microscale, denoted by d, is the size of microstructure features such as the average grain size or size and/or spacing of precipitates/inclusions, while the mesoscale, denoted by L, is the size of the representative volume element [32]. Previous studies [249] have stated that the $\delta = L/d$ ratio for SVEs is between 5 and 10, while the ratio is between 10 and 100 for proper RVEs. SVEs must be large enough to encompass important features at second nearest neighbor correlations, for example. From this definition, it is obvious that these ranges are dependent on the specific microstructures features and the application of the volume elements. Although representative volume elements (RVEs) are larger than SVEs, thus containing more microstructure-sensitive features, their size also increases the computational resources required to complete a particular study. Therefore, the digital microstructures employed in this work are statistical volume elements (SVEs). It is therefore necessary to sample many SVEs, in general.

Four crystallographic textures representative of titanium alloys were analyzed in this work: (a) random texture, (b) β-annealed, (c) transverse, and (d) basal/transverse. The β-annealed texture was taken from previous work [43] while the other textures were extracted from the literature [60, 64, 250, 251]. All three-dimensional digital microstructures were instantiated using the open source DREAM.3D software [252] with inputs of desired grain size, orientation, and misorientation distributions. The grain size distribution for all textures is modeled as a log-normal distribution with a mean and standard deviation of 30 μm and 15 μm, respectively. The instantiated microstructures contain 9,261 hexahedron elements, each with 8 integration points (i.e., C3D8-type in Abaqus 6.10-1 [87]) and an individual side length of 10 μm. In previous work [42, 43], reduced integration elements (i.e. C3D8R) have been successfully used for this type of study, but MKS prefers the centroidal averaging of the eight integration point values to minimize error due to discretization effects. The digital microstructure has a total sidelength length of 210 μm in the x-, y-, and z-directions. A total of 500 microstructures were instantiated for each of the four textures and their microstructure statistics were compared to the desired statistics. Representative statistics plots of typical outputs are shown in Figure 5.6. All resultant digital microstructures were periodic.

To determine an adequate number of SVEs for property estimation to mimic RVE results, the mean and standard deviation of a particular value of interest (elastic stiffness in this instance) are compared with tolerance values [253]. As shown in Figure 5.7, the mean of the elastic stiffness converges extremely quickly (less than 50 simulations) for loading in each direction while the standard deviation requires approximately 250 simulations for each loading direction. Therefore, 250 simulations for each loading direction are required for SVE characterization of this specific texture, which is less than the 500 simulations performed for each texture. Similar results were found for the other textures [50, 67].

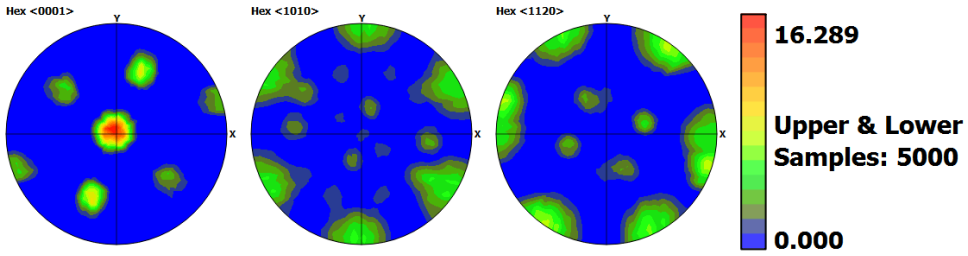

(a)

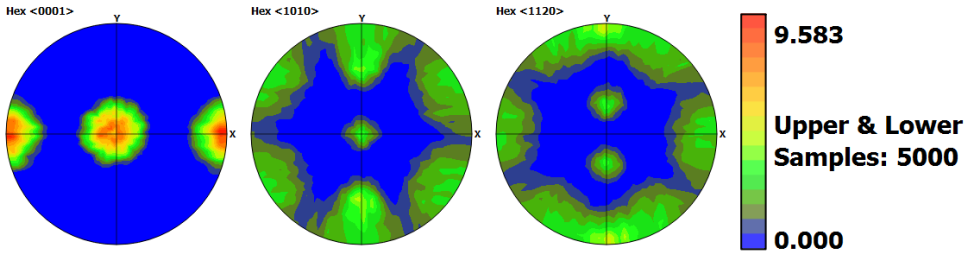

(b)

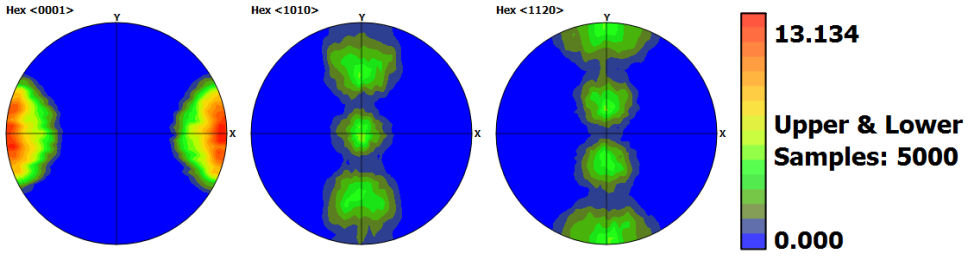

(c)

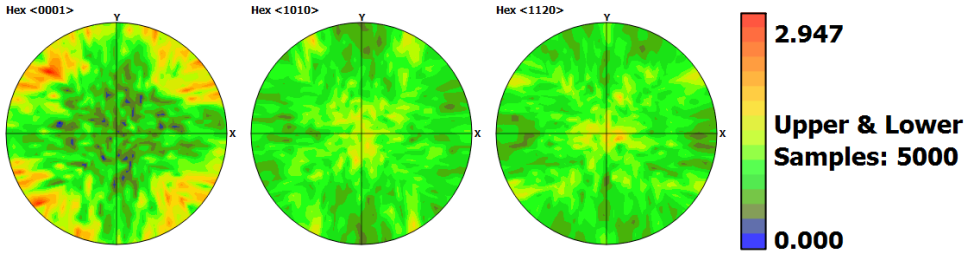

(d)

Figure 5.6: Representative pole figures by row for (a) β-annealed, (b) basal/transverse, (c) transverse, and (d) random texture inputs for DREAM.3D.

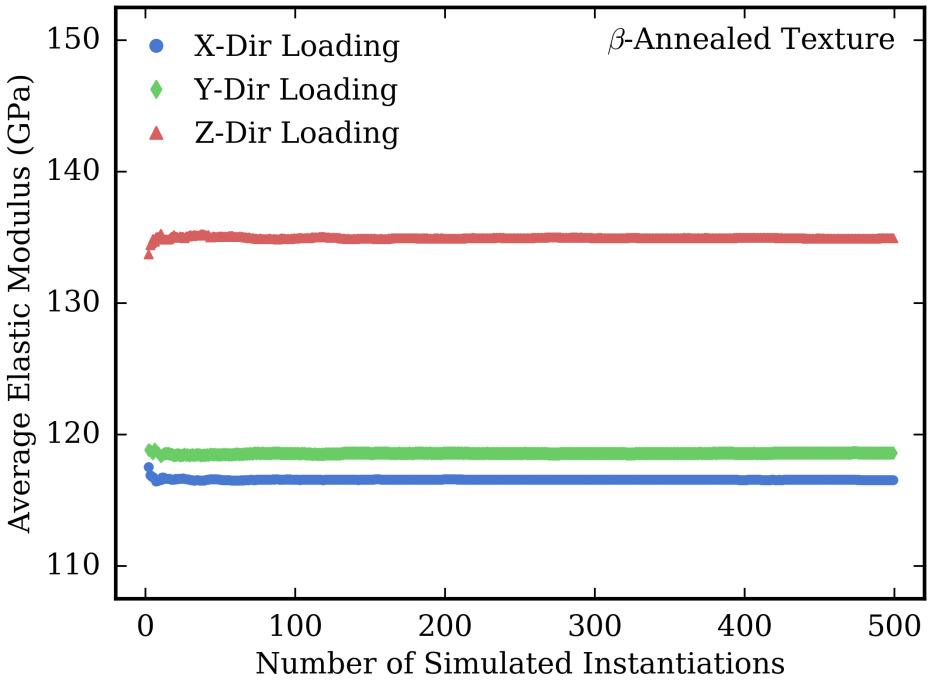

(a)

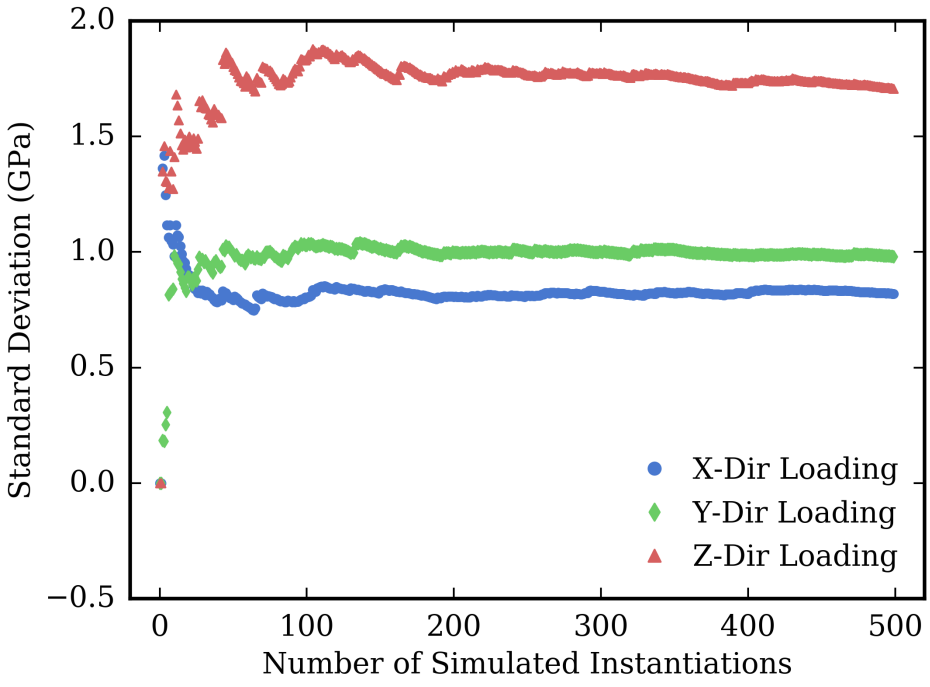

(b)

Figure 5.7: The (a) mean and (b) standard deviation for N number of MKS simulations of the β-annealed microstructure.

5.3 Results

5.3.1 MKS Model Calibration

In this work, the MKS is utilized to provide a computationally efficient framework for the prediction of local tensorial strain fields for a wide range of realistic α-Ti microstructures. For each set of boundary conditions, the MKS is calibrated for the local strain tensor. In practice, a calibration is performed for each independent component of the tensor $(\epsilon_{11}, \epsilon_{22}, \epsilon_{33}, \epsilon_{12}, \epsilon_{13}, \epsilon_{23})$, where periodic boundary conditions were formulated such that the average value of the applied component (over all spatial cells) matches the imposed strain. More specifically, the imposed strain is selected such that only one component is non-zero.

In this study only the first term in the MKS infinite series is utilized. In prior work, it was shown that the truncation to the first term provides excellent results for composite systems with low to moderate contrasts [15–18, 20]. In the present case, truncation to the first term is justified as α-Ti single crystals exhibit low contrast (e.g., the ratio of the highest modulus to the lowest modulus is approximately 1.40). Furthermore, following the earlier work [18] Only fifteen GSH basis functions are needed in the representation of the influence kernels in the MKS representation for the present work.

The MKS localization relationships are calibrated using the responses of SVEs generated via DREAM.3D. These microstructures have realistic grain size distributions but exhibit random textures. This ensures that the interactions between grains of different orientations are captured such that the localization relationship can be used to predict the responses of microstructures with a variety of textures. The number of SVEs used in calibration of the MKS is determined through examining the mean and maximum error metrics in the stress and strain field predictions for different sets of validation SVEs. Specifically, it was found in this work (data not shown) that the error metrics changed little when 400 SVEs are used for MKS calibration

instead of 200. In order to achieve the best possible MKS calibration, the full set of 400 SVEs were used in the final calibration procedure.

The value of the MKS approach is particularly apparent when the computational benefits are examined. While the determination of the local stress and total strain fields in an SVE with FEM takes 10 minutes on four processors, the MKS requires only 0.70 seconds (on a single processor) to produce the same information. Regarding local states, the MKS prediction of the total strain fields is also highly accurate; the mean voxel-to-voxel difference between the MKS and linear elastic FEM response is 0.28% and the maximum error per microstructure averages to only 1.50% for the ϵ_{11} component. Additionally, the mean voxel-to-voxel difference between the MKS and CPFEM response for 100 instantiations of the β-annealed microstructure for ϵ_{11} component is 0.28%, while the maximum error per microstructure averages only 1.65%. Therefore, the MKS prediction is extremely accurate as compared with the linear-elastic FEM and CPFEM simulations, providing justification for the approximation that the local strain tensor can be approximated as the the local elastic strain tensor.

5.3.2 Comparison of Integration Scheme and CPFEM Simulations

After verifying that the MKS has produced accurate results when compared with linear-elastic FEM and CPFEM simulations for the local total strain tensor, the procedure was extended to determine the local (grain scale) plastic strain tensor. The explicit integration scheme was utilized for a total of three cycles; a comparison of the plastic strain fields with that of CPFEM is shown in Figure 5.8. The CPFEM simulation requires approximately 45 minutes to complete on four processors (and a total of eight Abaqus licenses), while the explicit integration scheme requires 70 seconds on a single processor.

The plastic strain comparison is in acceptable agreement; the mean and average of the maximum error for the ϵ^p_{11} component are 105% and 353%, respectively,

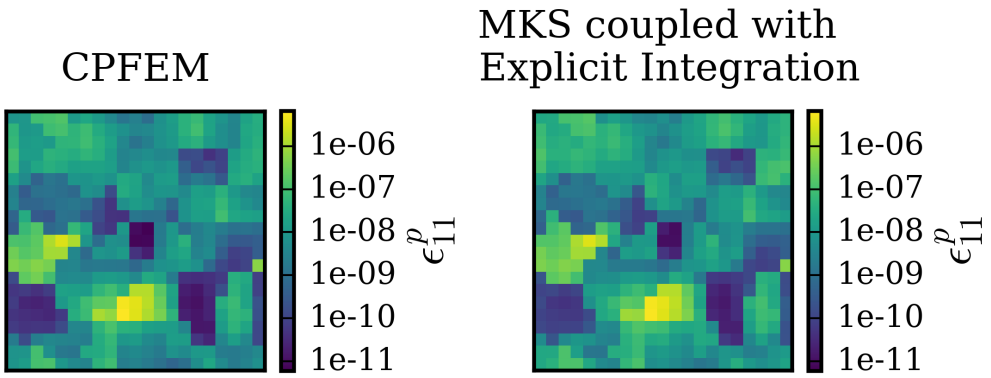

Figure 5.8: A two-dimensional cross-section comparison of the ϵ_{11}^p values from CPFEM (left) and MKS plus explicit integration (right).

from 100 instantiations of the β-annealed texture simulated with CPFEM and MKS coupled with explicit integration. However, the determination of plastic strain is an approximation that is a function of the local plastic shear strain rate and the time increment in the integration scheme. Therefore, the precision of the CPFEM local plastic strain tensor is dependent on the number of time increments in the CPFEM simulation. Later results will demonstrate that this level of agreement is sufficient for the purpose of this work.

The local stress fields also have a high accuracy with mean and average maximum error per microstructure for the σ_{11} component of 1.00% and 2.37%, respectively, from 100 instantiations of the β-annealed texture simulated with CPFEM and MKS coupled with explicit integration. These results indicate that stress relaxation or redistribution are minimal in the CPFEM simulations, which is an expected result for the HCF regime.

5.3.3 Macroscopic Elastic Stiffness

HCP crystal structures have a transversely isotropic elastic response, meaning the elastic properties are the same in one plane and different normal to that plane. For

α-Ti, the elastic modulus can vary between 104 and 146 GPa, the shear modulus between 40 and 47 GPa, and Poissons ratio between 0.265 and 0.337. This degree of anisotropy for the elastic modulus (40%) and the shear modulus (18%) is much higher than that of other HCP metals [254] and can have a pronounced effect on the material deformation response.

Mechanical properties, such as elastic stiffness, can be determined from the types of datasets generated in this study. However, since the boundary conditions used in this work result in non-zero normal stress components in all normal directions, additional steps are taken to determine directional elastic stiffness values. The MKS only determines local quantities, therefore the normal stress and strain components were volume-averaged (e.g., $\langle \sigma_{ij} \rangle = \sum_{k=1}^{N} \sigma_{ij}^{k}/N$ where N is the total number of elements) for each loading direction (x-, y-, and z-) to determine an effective stiffness tensor. The effective stiffness tensor can then be inverted to recover the effective compliance tensor. Subsequently, the elastic stiffness values for each loading direction are then equal to the diagonal components of the compliance tensor. Note that shear loading conditions are not required for this procedure because they do not contribute to the volume-averaged normal stress or strain quantities. The mean and standard deviation of the elastic stiffness values for each loading direction for each texture are shown in Table 5.2.

Table 5.2: Mean directional elastic stiffness ($\pm$ std. dev.) for each texture analyzed in this study.

Texture	$\mathbf{E}_{11}$ (GPa)	$\mathbf{E}_{22}$ (GPa)	$\mathbf{E}_{33}$ (GPa)
Random	123.4 $\pm$ 1.2	123.4 $\pm$ 1.2	120.0 $\pm$ 1.0
β-Annealed	116.5 $\pm$ 0.8	118.6 $\pm$ 1.0	135.0 $\pm$ 1.7
Basal/Transverse	122.8 $\pm$ 2.0	114.1 $\pm$ 0.2	135.6 $\pm$ 1.8
Transverse	144.8 $\pm$ 0.6	112.7 $\pm$ 0.2	112.8 $\pm$ 0.2

5.3.4 High-Cycle Fatigue Analysis

The FIP distributions computed from the plastic strain tensor for each voxel predicted by MKS coupled with the explicit integration scheme were found to show good agreement with those computed using the CPFEM plastic strains and stress. Fatigue resistance for the four textures and loading in each of the three orthogonal direction (x-, y-, and z-) were compared by their extreme value distributions, where each distribution is defined by the maximum FIP value from each SVE in the dataset. These results qualitatively agree with the Fatemi-Socie FIP calculated with plastic strains from CPFEM results, as shown in Figure 5.9. 100 CPFEM simulations were performed for each loading direction and compared with 100 MKS plus explicit integration simulations (same microstructure instantiations). The comparison indicates that at a high probability of failure, the two methods are in agreement in terms of the rank ordering of the loading directions. However, at a low probability of failure, the rank ordering is different between the two methods. This discrepancy can be traced back to the difference in the local plastic strain tensors and that both methods are approximating the local plastic strain tensors via Equation (5.12).

The z-direction loading corresponds to the $\langle 0001 \rangle$ pole figure, the x-direction loading corresponds to the $\langle 10\bar{1}0 \rangle$, and the y-direction loading corresponds to the $\langle 11\bar{2}0 \rangle$. An interesting finding from these results is that the z-direction loading has a lower fatigue resistance as compared with the x- and y-direction loading. The z-direction loading has a higher elastic stiffness due to the increased alignment of individual grain c-axes with the loading direction, which would typically imply less plasticity for similar deformation. However, the boundary conditions result in significant normal stresses perpendicular to loading, resulting in something more complex than a uniaxial stress-state.

Similar plots are constructed for the other four textures with the full 500 microstructure instantiations. Figure 5.10 is the FIP distribution for the basal/transverse

and transverse textured generated with MKS coupled with explicit integration and Figure 5.11 is the same for the β-annealed and random textures. As expected, the random texture results in very similar FIP distributions for loading in all directions. The basal/transverse texture has similar distributions as that of the β-annealed texture with the z-direction loading producing the lowest fatigue resistance out of the three loading directions. Finally, the transverse texture seems relatively uniform, but fatigue resistance is improved for all loading directions as compared with the other three textures.

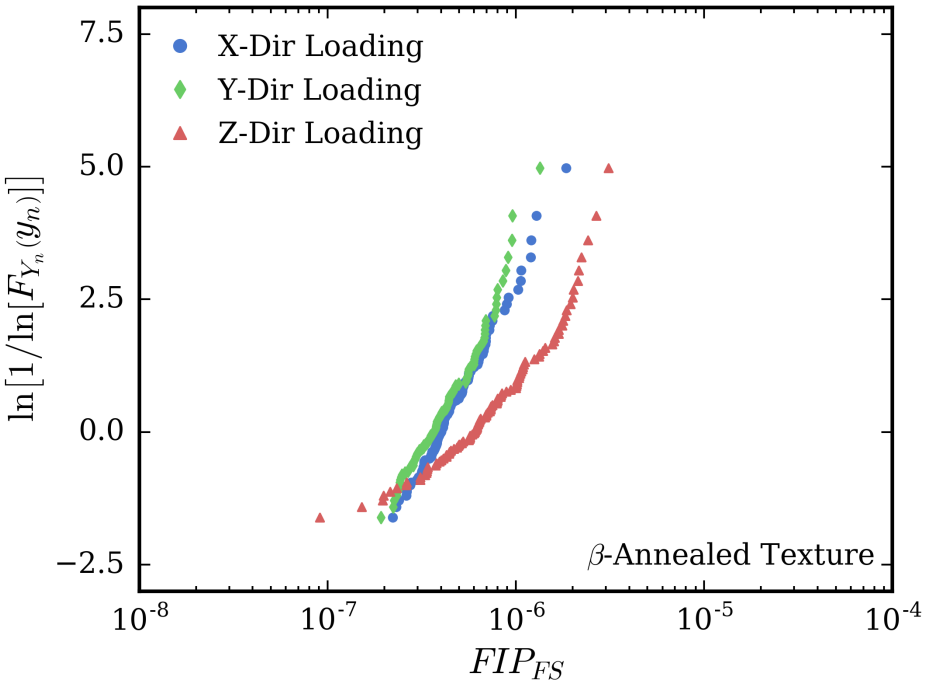

(a)

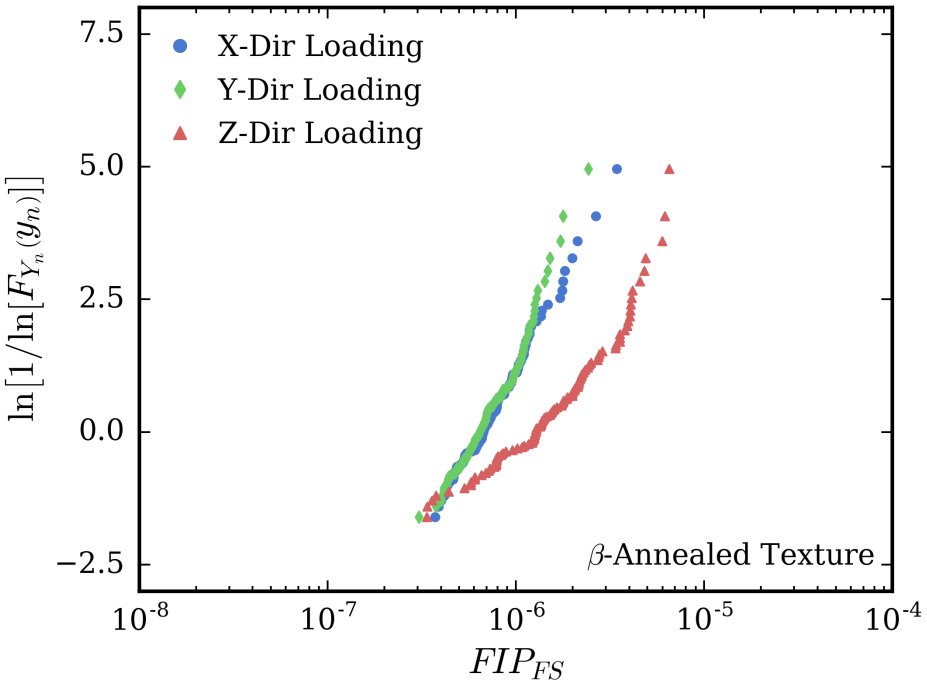

(b)

Figure 5.9: Comparison of the β-annealed microstructure extreme value distribution Fatemi-Socie FIP plot with 100 SVEs for (a) MKS plus explicit integration and (b) CPFEM.

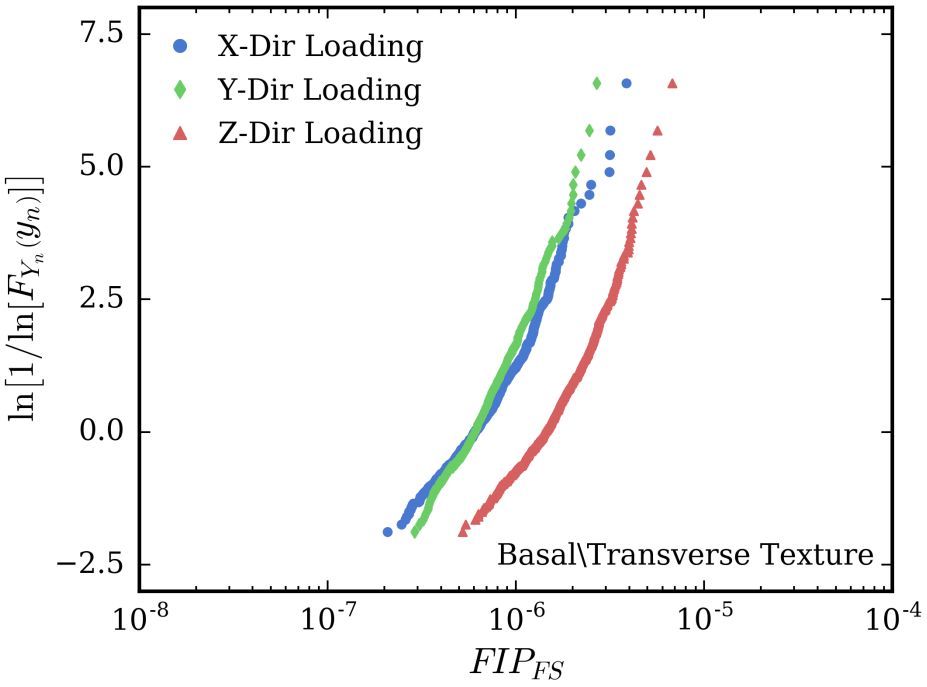

(a)

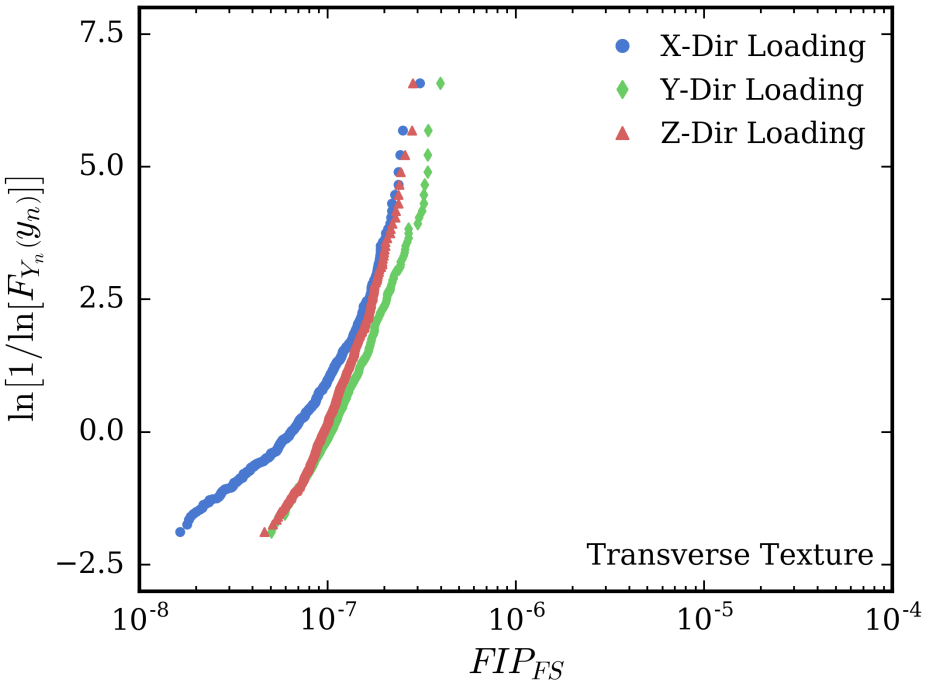

(b)

Figure 5.10: The extreme value distribution Fatemi-Socie FIP plot generated from the MKS and the explicit integration scheme with 500 SVEs for the (a) basal/transverse and (b) transverse textures.

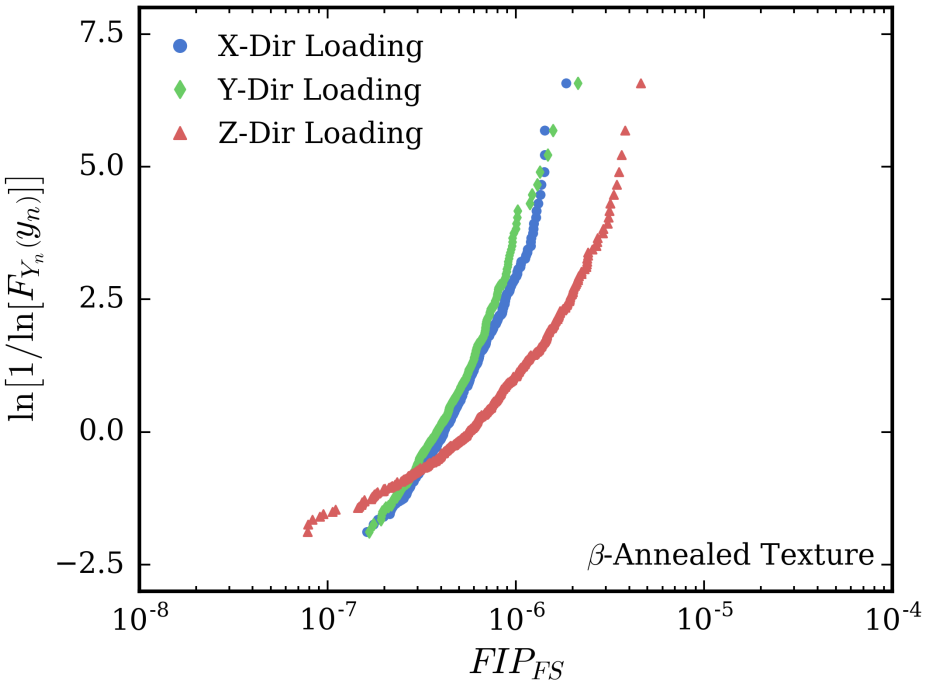

(a)

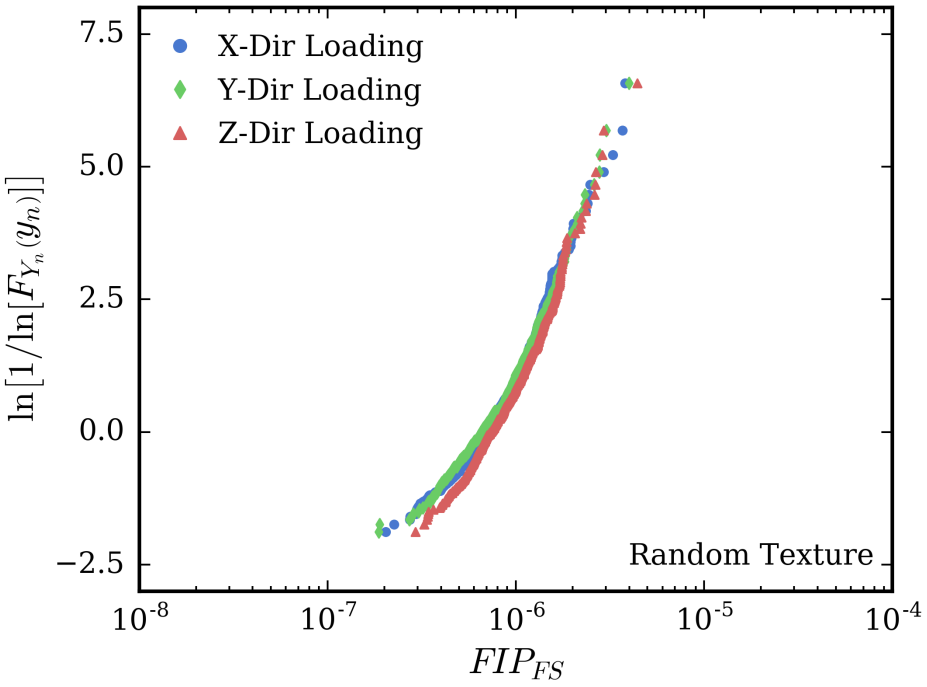

(b)

Figure 5.11: The extreme value distribution Fatemi-Socie FIP plot generated from the MKS and the explicit integration scheme with 500 SVEs for the (a) β-annealed and (b) random textures.

5.4 Conclusion

A new methodology coupling MKS with an explicit integration scheme has been presented for accurately predicting the local plastic strain tensor in hexagonal polycrystalline aggregates, which can then be used to reliably compute FIP distributions needed for rank ordering of HCF properties. This type of analysis is tailored for rapid microstructure selection and optimization, assuming the proper material and application have been identified. To perform the analyses contained within this work using a traditional approach, over 6,000 CPFEM simulations would be necessary; this would not only be computationally intensive, but would require a substantial number of Abaqus licenses for these particular analyses. In contrast, the new approach is computationally inexpensive, providing an approximate speed-up of 40x versus traditional CPFEM, and does not require Abaqus simulations once the MKS is calibrated. Even greater computational improvements could be achieved through the formulation and calibration of a suitable functional representation relating the FIP at each spatial location in an SVE to the local strain tensor and crystalline lattice orientation. In future studies, the computational framework presented here will be extended to include more other microstructures such as a combination of primary-α and $\alpha + \beta$ colony grains.

CHAPTER 6

APPLICATION OF IDEM TO TI-64

6.1 Introduction

To this point, microstructure-sensitive modeling has been performed for the purposes of comparing the CPFEM models to spherical indentation experimental data to assess the validity and form of the model, as well as to demonstrate the generation of extreme value distributions with a more computationally-efficient method than CPFEM. Studies that assess the calibration/validation of microstructure-sensitive models or present updated methods for property generation are not unique to this dissertation; it is a common theme in the literature when presenting and working with microstructure-sensitive models. However, the goal of this work is to aid the materials design exploration process of Ti-64, which requires connecting the model to higher-level design objectives or criteria. This chapter will discuss these connections and the data necessary for improving the material exploration process.

Response surfaces produced by microstructure-sensitive modeling efforts can be highly nonlinear, as demonstrated in the previous Chapters with indentation modulus (Chapter 3), indentation yield strength (Chapter 4), and extreme value distributions of FIPs (Chapter 5). For this reason, microstructure-sensitive modeling is a very good candidates for robust design methods such as IDEM. Previous work in the high-cycle fatigue (HCF) regime has found a correlation between fatigue indicator parameters (FIPs) and the number of cycles to failure [110, 111]. The majority of HCF deformation is elastic with localized regions of plasticity in grains or features that are favorably oriented for deformation slip. Therefore, a combination of fatigue crack formation and microstructurally small crack growth within the first few grains

or phases consumes the majority of the HCF cycle life and the determination of local driving forces can aid in identifying the location and magnitude of said driving forces. To capture local driving forces, the employed modeling scheme must account for the heterogeneity of the material, including grain morphology and texture.

Fatigue resistance is of importance to Ti-6Al-4V, commonly referred to as Ti-64. This $\alpha + \beta$ titanium alloy has high strength and relatively low density, ideal for aerospace applications. Previous microstructure-sensitive computational studies on Ti-64 [40–42, 44, 54] have demonstrated an ability to accurately capture elastic and plastic anisotropy for the α and $\alpha + \beta$ regions using crystal plasticity finite element method (CPFEM). Cyclic loading CPFEM simulations have been used to capture local driving forces with FIP quantities. In particular, the Fatemi-Socie FIP [107,108] has been extensively used due to its correlation with early stage fatigue crack formation behavior of metals that exhibit planar slip. The FIP calculations are performed on local cyclic responses, such as being averaged over each element in a finite element model.

The motivation behind the Inductive Design Exploration Method (IDEM) was presented in Section 2.7. This chapter will utilize the IDEM to evaluate two different datasets specific to α-titanium: (i) data generated from a combination of CPFEM simulations and MKS coupled with the explicit integration scheme that extends the dataset presented in Chapter 5, as well as (ii) data generated from Taylor-type model that explores all loading orientations within the Bunge-Euler angle space.

6.2 Deductive and Inductive Design

One of the major goals of the MGI [1] is to integrate experimental testing, computational tools, and data science approaches to decrease the time and cost associated with material design from discovery to deployment. As previously mentioned in this dissertation, a potential application for this kind of integration is the selection and/or

optimization of particular material systems, in addition to the design and development of novel material systems. Olson proposed the simultaneous use of inductive and deductive decision paths commonly employed in materials development [156]. The deductive path is referred to as a cause-and-effect path (bottom-up experiments and/or models) and the inductive path is the goals-means (top-down) path. One method for developing the deductive path for materials development is the defining of process-structure-property-performance (PSPP) mappings [26]. PSPP mappings represent cause-and-effect relationships between process-structure, structure-property, and property-performance. In general, PSPP mappings are unique for individual material systems [255], but many common features exist between PSPP mappings of different material classes. However, the deductive path is unpredictable and laborious to employ while simultaneously offering utility for accelerating materials development. Therefore, much effort is devoted to inverse methods in inductive design.

A multi-level model chain, such as a PSPP mapping, is even more sensitive to uncertainty due to its propagation through the levels. One multi-level robust design method that allows for the user to account for uncertainty is the Inductive Design Exploration Method (IDEM) [24]. Given design variables (input space) and performance requirements, IDEM discretizes the input variables, projects each set of discretized input values to a range in the output space, and then determines which set of discrete input values satisfy the output space [24, 29, 157, 158]. The IDEM is an inherently recursive process that links multiple levels of performance requirements.

Figure 6.1 presents the deductive and inductive paths related to IDEM. Step 1 involves bottom-up simulations (e.g., CPFEM) or experiments. Model 1 and Model 2 represent a connecting function/dataset that relates one level with the next. With the PSPP mapping as an example, Model 1 could represent a process–structure relationship and Model 2 a structure–property relationship. The yellow region encompasses the feasible region of points that are a result of the initial input parameters. Step

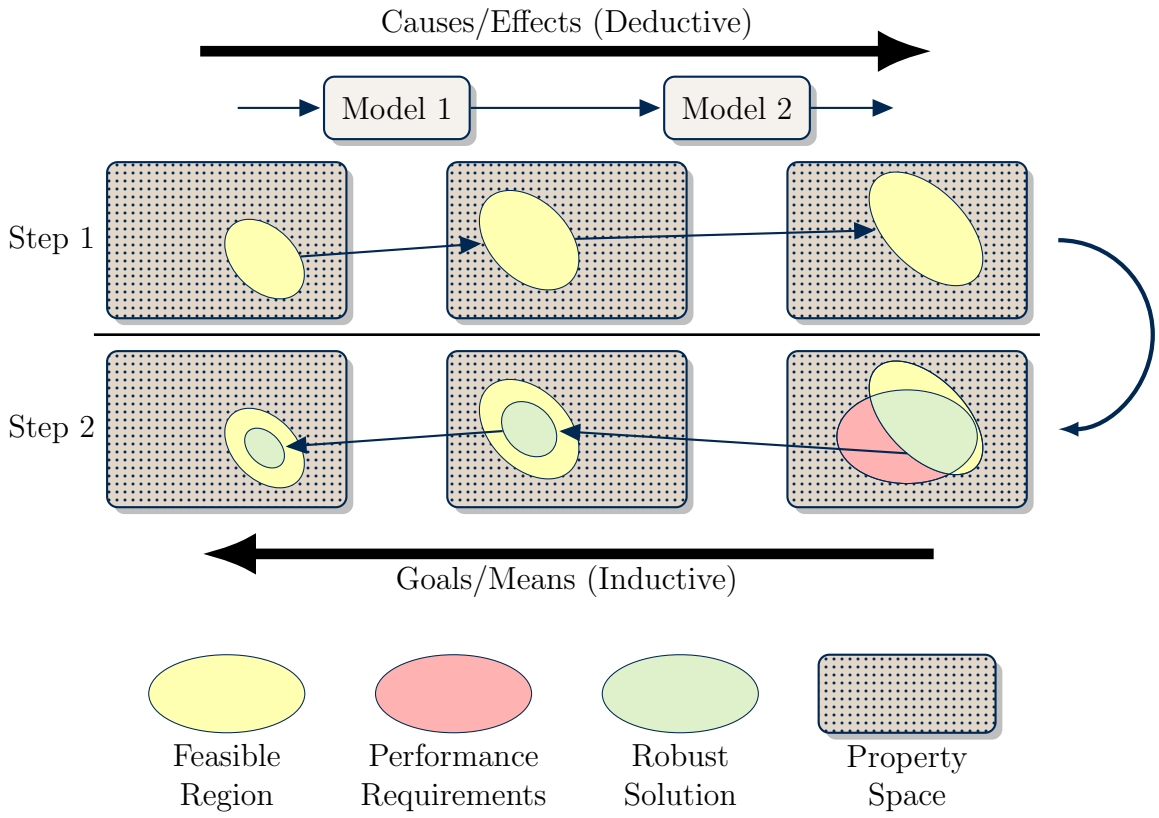

Figure 6.1: Schematic of Steps 1 and 2 in the Inductive Design Exploration Method (IDEM). Step 1 involves bottom–up simulations or experiments for Model 1 and 2 relations, with regions in yellow encompassing the feasible ranged sets of points from these mappings. Step 2 involves top–down (inductive, goals/means) evaluation of points from the ranged set of specified performance requirements that overlap feasible regions established by bottom-up (deductive, cause and effect) simulations in Step 1.

2 involves top-down evaluation of the feasible points found in Step 1 by comparing with the specified performance requirements or design criteria. The red region is the performance requirements and the green region is the overlap of the performance requirements and the feasible region. The robust solution is traced back to the original input parameters in Step 2.

6.3 Overview of IDEM Implementation

The specific mathematics and computations related to IDEM implementation are detailed in subsequent sections, but it can be helpful to first understand the overall flowchart of the IDEM. When connecting two levels, structure–property for example,

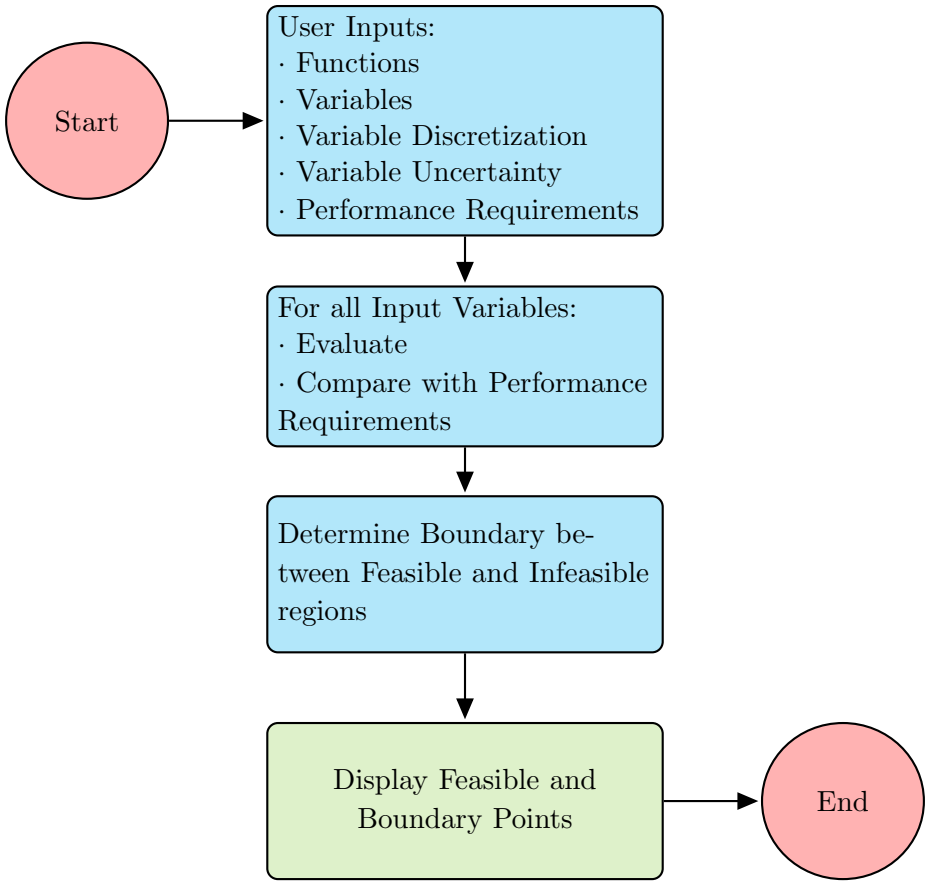

Figure 6.2: Simplified flowchart for the implementation of IDEM.

functions and/or discrete datasets are needed to relate the input (structure) to the response (property) variables.

The input variables are defined to have extents (min/max values) and performance requirements must also be selected for comparison to the values returned for the response variables. To ensure complete sampling of the input variables, each variable is discretized with a researcher-defined spacing between the min and max values. Therefore, a list of points is generated for evaluation. The IDEM algorithm iterates over the list of points, evaluating the function and determining the response value for each point. Each response value is compared with the performance requirements. If the response value is deemed satisfactory (i.e., meets the performance requirements), then the input value associated with the response value is considered a feasible point.

Likewise, if the response value is deemed unsatisfactory, the associated input value is considered an infeasible point. The list of feasible points is the solution to the performance requirements.

If multiple levels were to be evaluated, it would also be important to determine the boundary surrounding the satisfactory response values. To perform this task, linear interpolation between neighboring feasible and infeasible points can be used to find the feasible point that lies on the boundary of the performance requirement. Once the boundary is determined, it along with the response values can be used as input for another linkage. This is an idealized example of boundary determination; in IDEM, this is performed in a more sophisticated manner to account for uncertainty with the input and response values. This, along with other aspects of IDEM, are explained in more detail in the next Section.

6.4 Generalized Inductive Design Exploration Method

The implementation of IDEM demonstrated in this dissertation was constructed to support the objectives of this work, however a by-product has been the generation of an open-source, generalized platform for IDEM that can be utilized for a variety of datasets [256]. The previous IDEM source-code was written in Matlab [257] and constructed for a multi-level design scenario of ultra-high performance concrete (UHPC) [26]. While the previous version was extreme powerful in connecting multiple design levels that included three distinct length scale phenomena, the code was also not taking full advantage of time-saving measures such as vectorization. Additionally, the multi-level approach was hard-coded, making it quite difficult for a user to adapt the code for a different application. Therefore, much effort was taken to generalize the IDEM procedure for its use with various datasets and design scenarios. In its current form, the Python Design Exploration Method (pyDEM) provides a robust platform for design exploration.

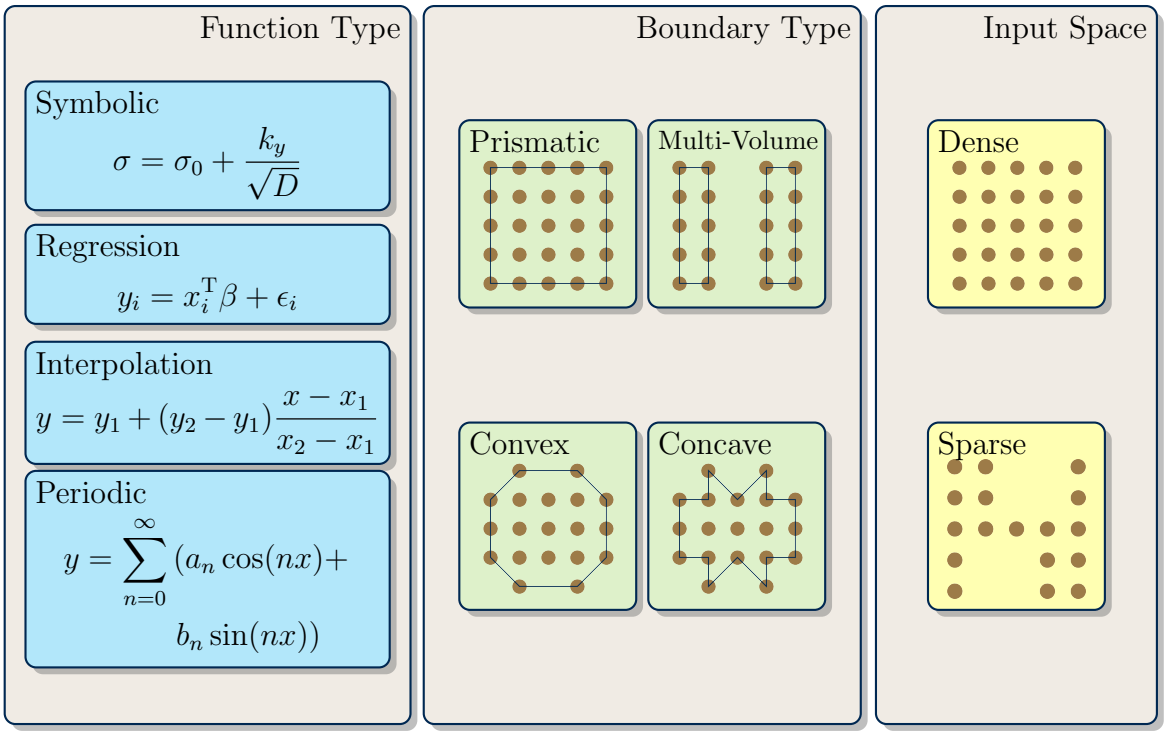

Figure 6.3: The various function types, boundary types, and input spaces available in pyDEM.

Figure 6.3 illustrates the various input function types, boundary types, and input spaces available in pyDEM. The function type used to map input variables to response values is extremely versatile. Available function types include a symbolic representation either taken from literature or generated by the researcher, the use of regression techniques to fit a response surface to a specific dataset or performing interpolation with the dataset if function fitting is not possible, and the use of periodic functions for datasets with input values that are periodic, such as Bunge-Euler angles.

The generalized framework can also work with multiple boundary types, where the boundaries are useful for defining regions being used as input spaces for subsequent levels. These boundary types include prismatic boundaries, multi-volume boundaries where a region is void of feasible points, as well as convex and concave boundaries. The use of specific boundary types is application- and dataset-specific. Additionally,

the input space can either be dense or sparse, allowing the designer to omit sampling regions where the input parameters are either known to be unsatisfactory or unrealistic.

IDEM has been implemented in a generalized sense to allow for the linkage of l levels, m functions, and n input variables, where l, m, and n are positive integers. For this work, two levels will be connected with multiple functions. The two levels are denoted the input and output space. The input space is comprised of the loading directions and/or textures of interest, while the output space is comprised of elastic stiffness, yield strength, and FIPs.

6.4.1 Defining the Output Range

At every level of design to be addressed using IDEM, a mapping (Figure 6.1) or projection step must occur to relate every nominal input in the $k-1$ level to a region in k output level. The projection to the output space from a nominal input $\bar{x}$ to nominal output $\bar{y}$ is represented by $\bar{y} = \langle f_1(\bar{x}), f_2(\bar{x}), ..., f_m(\bar{x}) \rangle$, where m is the number of output functions and thus the dimension of the output space. Due to various uncertainties, the potential solution is more accurately described by a range incorporating the uncertainty of the input space and projection process. Each mapping function (f_i) can be bounded by a set of functions $f_{i,lower}(x) \leq f_i(x) \leq f_{i,upper}(x)$ which incorporate any uncertainties from the regression process. Thus, in general, an mx3 matrix, denoted by z, can be constructed to describe the nominal and bounding functions with components z_{ij} being the j^{th} bounding function of the i^{th} output dimension. A hyperrectangle (generalization of a rectangle to the m-dimensional space) approximation of the boundary of the mapped output region can thus be constructed using Eq. (6.1). Type II robustness is incorporated into the variation of the input parameters Δx and Type III robustness (and indirectly Type I robustness) is incorporated via the inclusion of z_{ij} bounding functions. Together

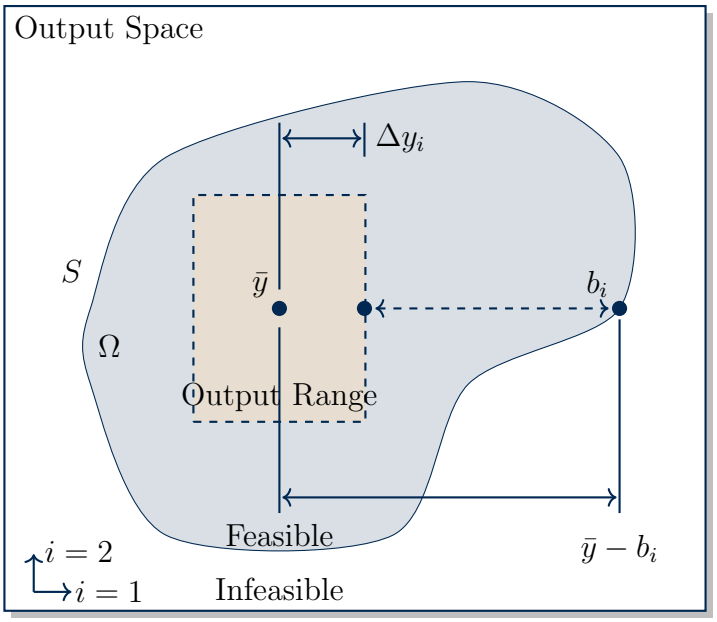

Figure 6.4: Schematic of the Hyper-Dimensional Error Margin Index (HD_{EMI}) showing the range of outputs for a nominal input value (adapted from [24]).

these values describe the total assumed variability in the i^{th} dimension Δy_i i.e.,

$$\Delta y_i = \begin{cases} \left| \max_j \left(z_{ij}\left(\bar{x}\right) + \left| \frac{\partial z_{ij}}{\partial x_k} \Delta x_k \right| \right) - \bar{y} \right|, & b_i > \bar{y}_i \\ \left| \min_j \left(z_{ij}\left(\bar{x}\right) - \left| \frac{\partial z_{ij}}{\partial x_k} \Delta x_k \right| \right) - \bar{y} \right|, & b_i \leq \bar{y}_i \end{cases} \tag{6.1}$$

The boundary point $b_i \in S$ where S is the $(m-1)$-dimensional boundary containing the feasible space Ω, is selected to minimize the distance required to reach the boundary along the i^{th} dimension (Figure 6.4). The pyDEM selects b_i using a binary search along the path $\langle \bar{y}, max\left(S_i\right) \rangle$. This binary search is implemented as an improvement to the initial proposal of the IDEM by Choi [23], which utilized a gridded space with no explicit representation of the associated hypervolume.

Computation of the distance to the boundary was performed along the nearest neighbor points within this discretized space. While this is sufficient for problems of academic interest, engineering applications requiring robust design are likely to include objective functions which are computationally expensive; thus, the initial discretization of the feasible spaces for linked design levels may not be sufficiently dense

relative to the output uncertainties, Δy_i. Assuming the existence of a representation of the feasibility hypervolume for which the location of a given point in space may be determined as interior or exterior, a binary search allows for a significant improvement in the ability to define the distance $|\bar{y} - b_i|$ when compared to a coarsely gridded space.

6.4.2 Hyper-Dimensional Error Margin Index

An error margin is employed to determine if the output range satisfies the performance requirements, and thus may be considered a robust solution. The error margin must have a consistent threshold for accepting or rejecting a potential solution and be defined for all positive integer dimensions in the input and output spaces. Multiple error margins are implemented in pyDEM; the one used in this work is the Hyper-Dimensional Error Margin Index (HD_{EMI}), which satisfies the previously mentioned requirements and is defined by

$$HD_{EMI} = \begin{cases} min_i \left[\frac{\|\bar{y} - b_i\|}{\Delta y_i} \right], & \text{for } \bar{y} \in \Omega \\ -1, & \text{for } \bar{y} \notin \Omega \end{cases} \tag{6.2}$$

where $HD_{EMI} < 1$ indicates that the uncertainty associated with the potential solution exceeds the feasible boundary and is thus not a robust solution. This can be verified by examining the formulation and seeing this condition only arises if the distance to the boundary is less than the output range in any dimension, that is a portion of the output range lies outside the feasible region. Since the current implementation of pyDEM considers only the boundary along $\mathbf{e}_i$ directions, there is potential for output ranges to include some of the infeasible space while not having $HD_{EMI} < 1$. Eliminating this scenario requires parameterization of the search for the closest b_i over the range of outputs $y_{j \neq i}$. In the case of an arbitrary S and point $\bar{y}$, the detection of such a minimum must be repeated for all $i \leq m$ dimensions.

6.4.3 IDEM combined with MKS and the Explicit Integration of CPFEM Constitutive Relations

In Chapter 5, the MKS method is coupled with an explicit integration scheme to determine plastic strain, and ultimately FIP, response fields for SVEs. This method was shown to be much more computationally-efficient than CPFEM while providing a reasonable level of accuracy. This approach is the basis for the robust design scenarios presented here. Eight titanium-specific textures are simulated with loading in three orthogonal directions to estimate directional elastic stiffness, directional yield strength, and extreme value distributions used to assess the fatigue resistance to fully-reversed, cyclic loading. CPFEM simulations were performed to estimate the directional elastic stiffness and yield strength, while the MKS coupled with the explicit integration scheme was utilized to generate the extreme value distributions of FIPs.

6.4.3.1 Simulation Datasets

For microstructure generation, Dream.3D [252] was used to construct 500 SVEs for each of the eight textures. Four of these microstructures are the same as was presented in Chapter 5, while four additional textures were also generated that were not originally used in that study. The eight textures simulated (and their abbreviations) for this study are β-annealed (β-Ann), basal/transverse (B/T), dice (Dice), double donut (DD), inner donut (ID), outer donut (OD), random (Rndm), and transverse (Trans). Representative pole figures for each of the textures can be found in the Appendix.

Uniaxial tension CPFEM simulations loaded to 1.5% nominal strain were used to estimate the directional elastic stiffness and yield strength of each SVE. A total of 100 of the instantiations for each texture were loaded in the three orthogonal directions, corresponding to the x-, y-, and z-directions specified by the FEM software for the generated samples. To relate this convention with the pole figures and the more common convention of normal direction (ND), rolling direction (RD), and transverse

direction (TD): z=ND and aligns with the (0001) pole figure, x=RD and aligns with the $(10\bar{1}0)$, and y=TD and aligns with the $(\bar{1}2\bar{1}0)$

Periodic boundary conditions were employed in these simulations [67]. The resultant directional elastic stiffness and yield strength values were averaged for each texture for each loading direction. The averages and standard deviations are shown in Tables 6.1 and 6.2. These results indicate there is quite an anisotropy, for both of these measures, depending on the texture and loading direction. The complete dataset, including elastic stiffness and yield strength for each individual simulation, is located in Appendix C.

Table 6.1: Mean and Standard Deviation of directional elastic stiffness for each texture and loading direction

Texture	Elastic Stiffness (GPa)		
	X-Direction	Y-Direction	Z-Direction
β-Ann	116.9 ± 0.8	118.9 ± 1.0	135.2 ± 1.8
B/T	123.1 ± 2.0	114.4 ± 0.2	135.6 ± 1.9
Dice	121.8 ± 1.1	121.5 ± 1.1	123.0 ± 0.7
DD	122.3 ± 1.0	121.3 ± 1.0	125.4 ± 1.2
ID	115.2 ± 0.2	115.3 ± 0.3	136.5 ± 0.5
OD	128.8 ± 1.3	126.4 ± 1.3	114.2 ± 0.1
Rndm	123.8 ± 1.2	123.6 ± 1.1	120.5 ± 1.1
Trans	145.1 ± 0.6	113.0 ± 0.1	113.1 ± 0.2

Table 6.2: Mean and Standard Deviation of directional yield strength for each texture and loading direction

Texture	Yield Strength (MPa)		
	X-Direction	Y-Direction	Z-Direction
β-Ann	764.3 ± 15.9	772.2 ± 17.9	1060.2 ± 22.9
B/T	826.2 ± 33.0	759.0 ± 11.2	1018.2 ± 36.7
Dice	878.4 ± 14.2	886.6 ± 14.1	845.0 ± 7.9
DD	855.8 ± 12.8	848.4 ± 12.5	878.8 ± 17.4
ID	782.2 ± 7.9	783.3 ± 9.1	1032.4 ± 11.0
OD	932.0 ± 15.5	902.5 ± 18.1	753.6 ± 6.7
Rndm	870.9 ± 13.9	871.3 ± 13.8	835.0 ± 15.1
Trans	1177.4 ± 9.8	696.2 ± 7.2	696.9 ± 9.0

Fully reversed, cyclic loading (for three cycles) was performed through the MKS coupled with an explicit integration scheme, as detailed in Chapter 5. This procedure was performed for all 500 SVEs for each of the eight textures and the three loading directions. The Fatemi-Socie FIP value was calculated for each voxel for each instantiation and volume-averaged to the same specifics as used in Chapter 5. The extreme value distribution of the Fatemi-Socie FIP was then constructed for each texture and each loading direction. The complete set of results, including the complete extreme value distribution for all textures and loading directions, are located in Appendix C. Specific probability levels or ranges of probability levels can be extracted from the extreme value distributions and compared across textures and loading direction. The extreme value distribution FIP plot for the β-annealed texture is shown in Figure 6.5. The horizontal lines on the plot correspond to the 0.01, 0.10, 0.25, 0.50, 0.75, 0.90, and 0.99 probability levels.

The lower probability regime of the extreme value distributions of the Fatemi-Socie FIP, where the FIPs are of lower magnitude, is associated with greater numbers of cycles for fatigue crack formation (N_{FOR}). Similarly, the higher probability regime corresponds to higher magnitude FIP values and is associated with shorter fatigue life (i.e., fatigue crack formation). Therefore, the purpose for defining the probability levels is to provide a single value for comparing the extreme value distributions across texture and/or loading direction. For example, Figure 6.6 displays FIP values for a range of probabilities from 1% to 99% for all textures and loading directions.

Another useful measure taken from the extreme value distribution is the change in the FIP value between two probability levels. For example, although the z-direction loading (Figure 6.5) has lower magnitude FIP values at the 0.1 probability level, the slope of the extreme value distribution is also lower, meaning there is a larger change in FIP values between 0.01 and 0.10 probability levels, as compared with the x- and y-direction loading. This larger range in FIP values would indicate there is also a

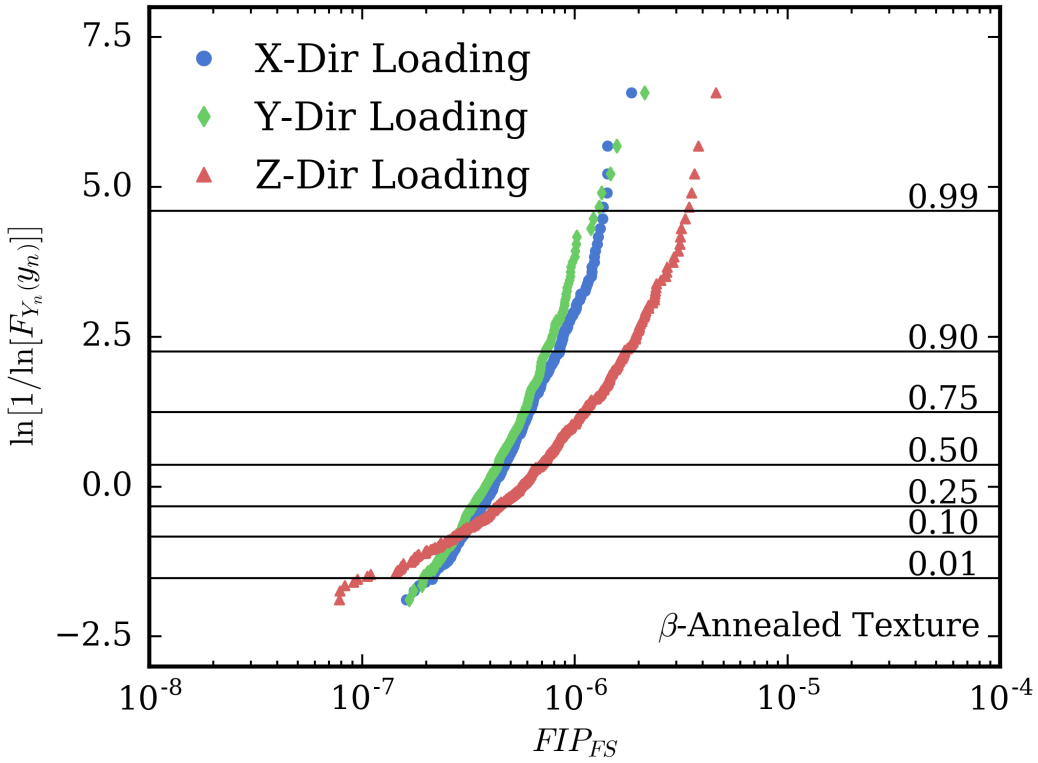

Figure 6.5: The extreme value distribution Fatemi-Socie FIP plot generated from the MKS and the explicit integration scheme with 500 SVEs for the β-annealed texture. The 0.01, 0.10, 0.25, 0.50, 0.75, 0.90, and 0.99 probability levels are indicated with horizontal lines.

larger scatter in fatigue lives. Figure 6.7 depicts the range of the FIP values between two specific probability levels. The purpose of this plot is to demonstrate that FIP values are not a constant measure and, depending on the specific design objective, FIPs can be used in a variety of ways to provide the end user with representative datasets.

Figure 6.8 depicts the directional mean directional elastic stiffness, mean directional yield strength, and the FIP value for the 0.10 probability level from the extreme value distribution of the Fatemi-Socie FIP for each of the textures and loading directions.

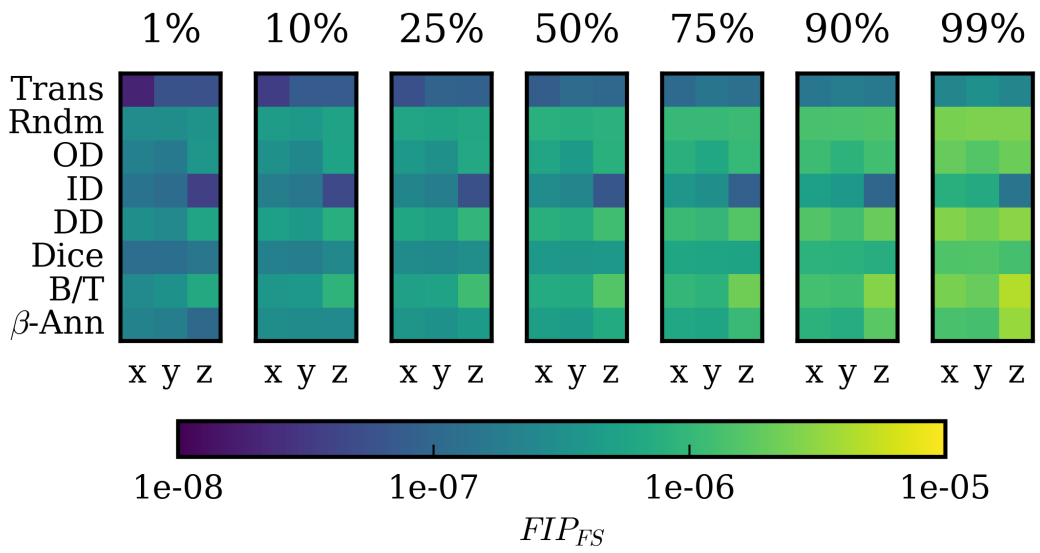

Figure 6.6: The FIP values corresponding to the 0.01, 0.10, 0.25, 0.50, 0.75, 0.90, and 0.99 probability levels values for the eight textures and three loading (x-, y-, and z-) directions simulated using MKS coupled with the explicit integration scheme.

6.4.3.2 Design Scenarios

For the purposes of pyDEM, the input space can be thought of as two-dimensional, a function of texture and loading direction. The output space is comprised of three measures which include the directional elastic stiffness, directional yield strength, and a Fatemi-Socie FIP value. The dataset in this study is quite discrete, meaning it is not appropriate to interpolate between loading directions or textures to calculate intermediate values. Therefore, the output response values (i.e., (E), (σ_y), and FIP_{FS}) were fit to a piece-wise constant function, specifically a two-dimensional, zero-order spline. This allows the data to be input into pyDEM similarly to datasets that are generated with continuous functions, without the need to alter methods for estimating derivatives or calculating intermediate values.

However, there is also some uncertainty associated with each of the output values. Therefore, the minimum and maximum of the directional elastic stiffness and yield

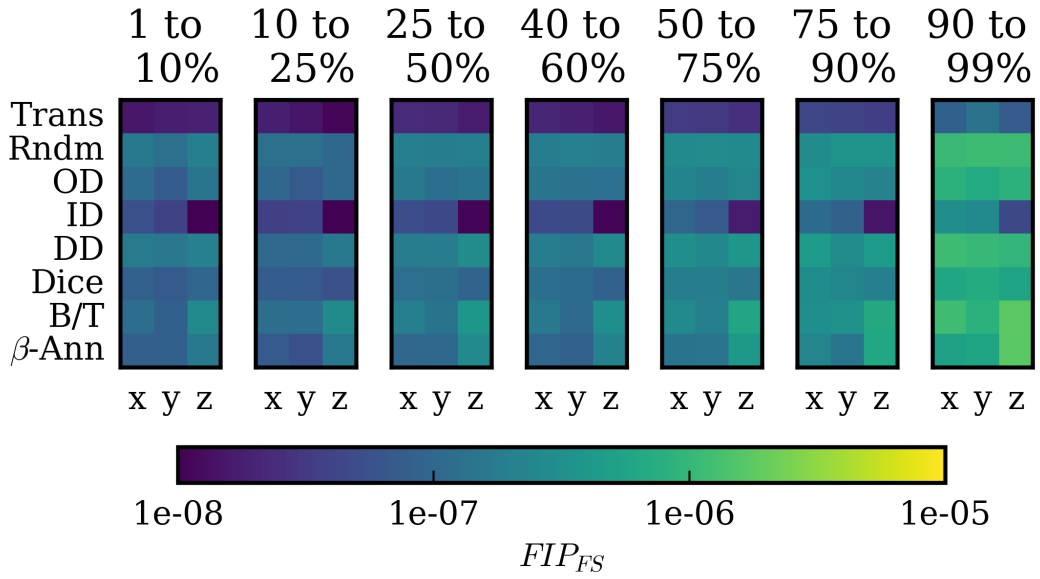

Figure 6.7: The FIP value range corresponding to the 0.01–0.10, 0.10–0.25, 0.25–0.50, 0.40–0.60, 0.50–0.75, 0.75–0.90, and 0.90–0.99 probability level ranges for the eight textures and three loading (x-, y-, and z-) directions simulated using MKS coupled with the explicit integration scheme.

strength are modeled as the mean value plus/minus one standard deviation; these values were given in Tables 6.1 and 6.2. The uncertainty of the FIP response for a given texture and loading direction is modeled as a 10% uncertainty, meaning the FIP measure can have a possible value that is plus/minus 10% of the response taken from the extreme value distributions. Including the variability of each of these response values is an important feature in generating robust solutions with IDEM. However, in this case, there is no way to capture the uncertainty associated with the input variables. Additional simulations would be required to capture a small change in the texture or the loading direction.

Three design scenarios are executed on this dataset; each is shown below in Table 6.3. The first design scenario seeks to maximize the mean directional elastic

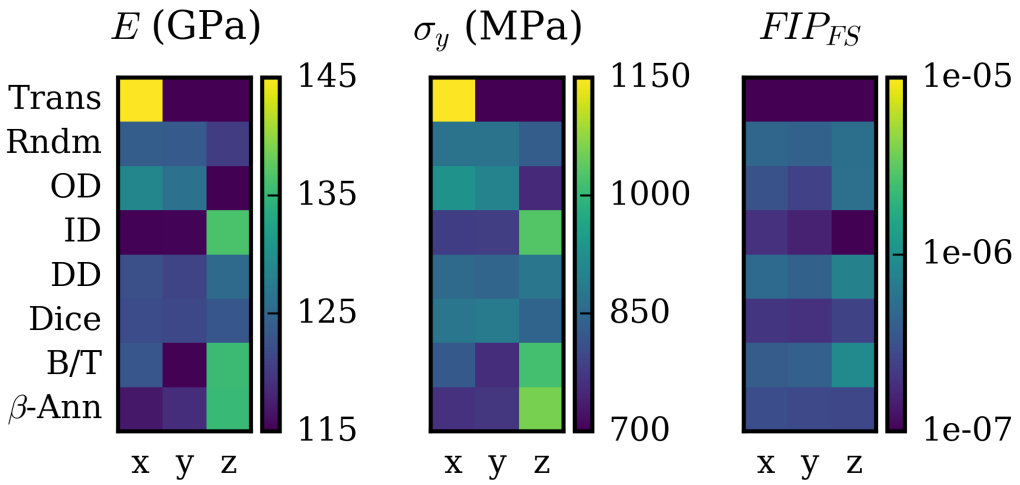

Figure 6.8: The mean directional elastic stiffness (E), mean directional yield strength (σ_y), and FIP value (FIP_{FS}) corresponding to the 0.10 probability level for each of the eight textures and three loading (x-, y-, and z-) directions.

stiffness while minimizing the Fatemi-Socie FIP value associated with the 0.10 probability level. The second design scenario seeks to maximize the directional mean yield strength while minimizing the Fatemi-Socie FIP value associated with the 0.10 probability level. The third and final design scenario combines the first and second to maximize the mean directional elastic stiffness and mean directional yield strength while also minimizing the Fatemi-Socie FIP value associated with the 0.10 probability level.

Each of these design scenarios are founded from component design, where there is most likely a need to maximize either the elastic stiffness (to minimize shape change) or the yield strength (to maximize load capacity). Additionally, minimizing the Fatemi-Socie FIP value for the 0.10 probability level would correspond to an increase in the fatigue life of the component. While the FIP values can be determined for a variety of complex loading conditions, fully-reversed tension-compression cyclic loading was performed for this study.

Table 6.3: Texture IDEM Design Requirements

Scenario	E	σ_y	FIP_{FS}
#1	$>$ 130 GPa	–	$< 5 \times 10^{-6}$
#2	–	$>$ 900 MPa	$< 5 \times 10^{-6}$
#3	$>$ 130 GPa	$>$ 900 MPa	$< 5 \times 10^{-6}$

6.4.3.3 Results

The input variables, response variables, uncertainty associated with the response variables, and performance requirements for each design scenario were used as the input data for the generalized IDEM framework. The texture and loading direction were assessed via the HD_{EMI} calculation to determine whether each point was satisfactory. Due to the discrete nature of the data and that this study only contains two levels (i.e., structure and property), the boundary of the feasible region was not assessed.

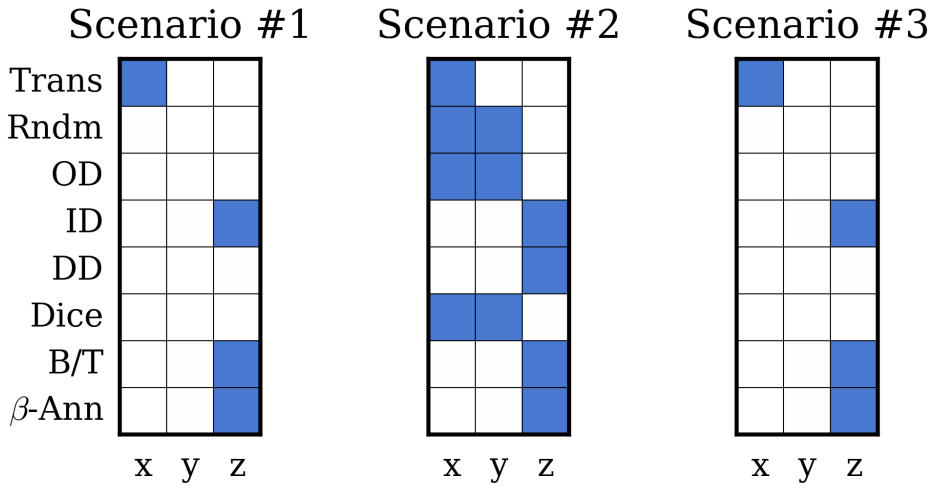

Figure 6.9: Two-dimensional representation of the feasible space for each of the design scenarios applied to each of the eight textures and three loading directions. Filled squares (blue) indicate the satisfaction of the performance requirements.

The results for each of these design scenarios are given in Figure 6.9. A colored square (blue) indicates the specific texture and loading direction satisfied the design requirements, while a blank square indicates that an HD_{EMI} value of -1.0 was returned for the specific texture/direction combination and that the design requirements

were not met.

The first design scenario only found four texture/loading direction combinations that provided a robust solution for maximizing the elastic stiffness and minimizing the FIP response for the 0.10 probability level. From comparing the acceptable to solutions to their respective pole figures, it is evident that each of the feasible points has many grains with their respective c-axes aligned with the loading direction, thus increasing the directional elastic stiffness.

The second design scenario found many texture/loading direction combinations with a satisfactory yield strength and FIP response for the 0.10 probability level. This is a direction result of the high yield strength of titanium. From a design perspective, this solution would most likely lead to the designer enlisting additional performance requirements to limit the number of satisfactory solutions.

The third design scenario is a combination of the first and second design scenario, seeking satisfactory response for elastic stiffness, yield strength, and FIP response for the 0.10 probability level. The results of this design scenario are identical to the first design scenario, which indicates that the four texture/loading direction combinations with an elastic stiffness greater than 130 GPa also have yield strength values greater than 900 MPa.

Given more particular design scenarios or an expanded dataset, this procedure could be quite useful for aiding a designer in selecting particular materials or, at a minimum, narrowing the list of possible materials for selection.

6.4.4 Taylor-Type Model of Ti-64

In the previous section, CPFEM simulations as well as MKS coupled with an explicit integration scheme were used to generate a dataset that had two input variables and three response values of interest. However, the generalized IDEM framework was constructed for use with an arbitrary number of input variables and response values. Therefore, the purpose of this test case is to illustrate the use of IDEM with an increased number of input variables and response values.

For this study, a Taylor-type model is applied to Ti-6Al-4V with a β-annealed texture to determine the loading orientations (relative to the texture) that produce a robust solution when designing for various mechanical properties. The Taylor-type model prescribes the same deformation to all grains and the macroscopic response is the average response of those grains [258]. The constitutive relations and model parameters were taken from previous work on Ti-6Al-4V [43,44] that has been presented in previous Chapters. The Taylor-type model citeTaylor1938 used in this work is most similar to the constraint-type Taylor model because the forces are not set to zero on nonloading faces [259,260]. A Taylor-type model was utilized instead of crystal plasticity finite element method (CPFEM) for computational efficiency. However, some accuracy is lost due to the treatment of the deformation as homogeneous [261,262], the main purpose in this work is to demonstrate the capabilities of the pyDEM and not the accuracy of a specific microstructure-sensitive modeling scheme.

The loading orientation of the specimen is iterated over the entire Bunge Euler angle space ($0 \leq \phi_1 \leq 360°, 0 \leq \Phi \leq 180°, 0 \leq \phi_2 \leq 360°$) with response variables of elastic stiffness (E), yield strength (σ_y), and high-cycle fatigue resistance via fatigue indicator parameters (FIPs) measured for each loading orientation. The polycrystalline specimens are rotated by three Bunge-Euler angles before deformation. And since Taylor-type modeling does not account for neighboring grains or the shape of grains, this rotation is a dot product between the grain's crystal orientation and the

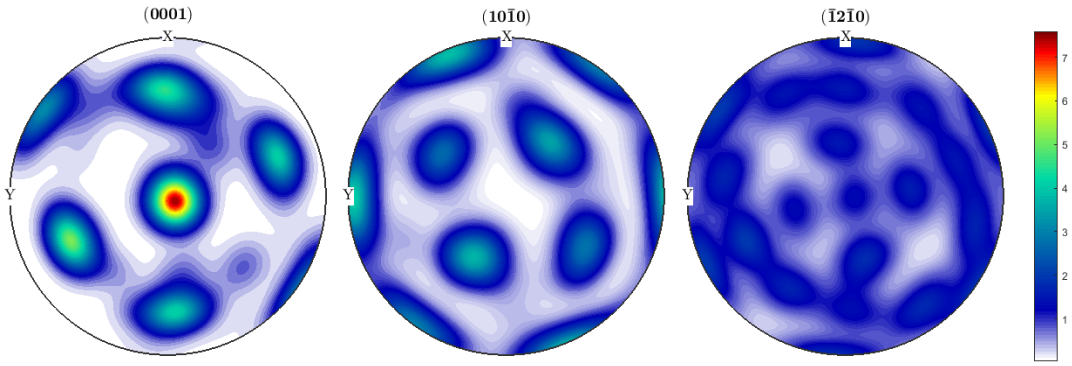

Figure 6.10: A pole figure generated from the 1,000 Euler angle sets used in the Taylor-type model analysis of β-annealed Ti-64.

resultant rotation matrix from the specified Bunge-Euler angle set. Uniaxial tension simulations are used to determine the elastic stiffness and yield strength for a given loading orientation, while cyclic loading of three cycles were performed to determine FIPs. Fatemi-Socie FIPs were calculated from three types of loading conditions:

- fully-reversed ($R = -1$) uniaxial cyclic loading (FIP_u) in the RD with a strain amplitude (ϵ_a) of 0.5%,
- combined uniaxial in the RD ($R = -1, \epsilon_a = 0.5\%$) and simple shear ($\epsilon_a = 0.05\%$) on the ND in the TD loading (FIP_s), and
- biaxial ($R = -1, \epsilon_a = 0.5\%, \epsilon_a = 0.25\%$) loading in the ND and TD (FIP_b), respectively.

These loading conditions were used to represent the complex loading of turbine blade stresses from the work of Rajasekaran and Nowell [263]. These simulations were performed at room temperature, the temperature for which all model calibration has been performed in this dissertation.

6.4.4.1 Simulation Datasets

The results from the uniaxial tension simulations are shown in Figures 6.11 and 6.12. To assist in reading the plots, it can be useful to thing about each discrete point as

a specific loading direction relative to the specimen orientation, with the color of the point relaying the magnitude of the measured property. The calculated range for the elastic stiffness (115-140 GPa), is strongly varied depending on the specific loading direction. However, these values are in reasonable agreement with values presented in the other IDEM study in the previous Section.

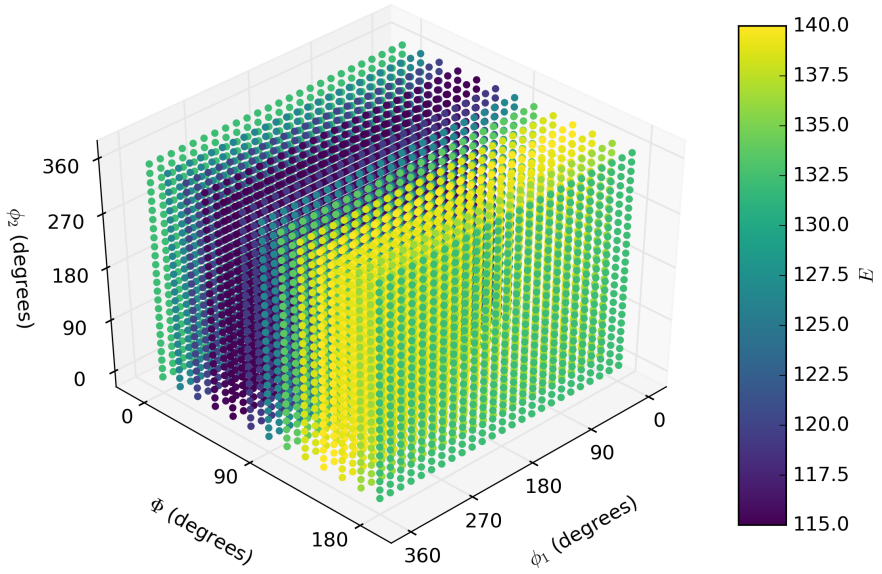

Figure 6.11: The elastic stiffness (E) of the simulated polycrystal as a function of the Bunge-Euler angles (ϕ_1, Φ, ϕ_2) used to rotate the specimen.

Similarly, the calculated range for yield strength (900-1240 MPa) is also strongly varied depending on the specified loading direction. Additionally, these values seem to be increased from the values determined in the previous IDEM study for the β-annealed microstructure. Also, due to the asymmetry of the texture, the maximum and minimum values do not correspond with any principal loading orientation, such as a RD or ND. Therefore, this type of information could be quite beneficial when machining a specific component from bulk material.

Additionally, the FIP responses are strongly varied with loading direction, as

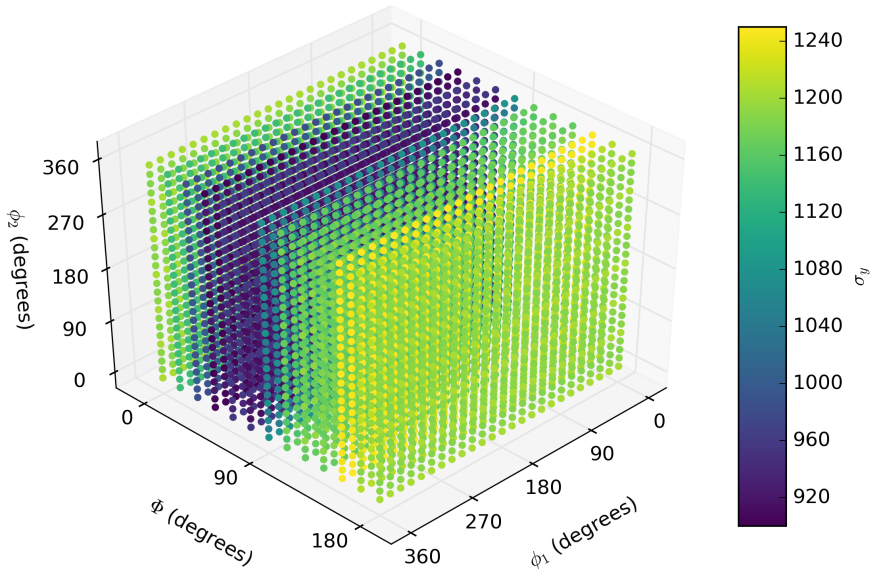

Figure 6.12: The yield strength (σ_y) of the simulated polycrystal as a function of the Bunge-Euler angles (ϕ_1, Φ, ϕ_2) used to rotate the specimen.

shown in Figures 6.13, 6.14, and 6.15. It should be noted that the FIP responses presented are maximum values for each loading orientation and each FIP value is implicitly volume-averaged over a single grain, as opposed to the volume-averaging procedure performed for CPFEM simulations in Chapter 5. Also, there are no extreme value distributions to sample for these simulations; there is only one maximum value for each specified loading direction. The Taylor-type model does not define neighbors, as all grains are estimated to undergo the same deformation. The three FIP responses also correspond to different loading directions, depending on the applied loading conditions.

From the data presented for elastic stiffness, yield strength, and maximum Fatemi-Socie FIP, it would be quite difficult to visually determine the Bunge Euler angles that result in a specific loading direction that satisfies more than one performance criteria. That is precisely the purpose of pyDEM: to provide the user with a visual

inspection of a robust solution given multiple design criteria.

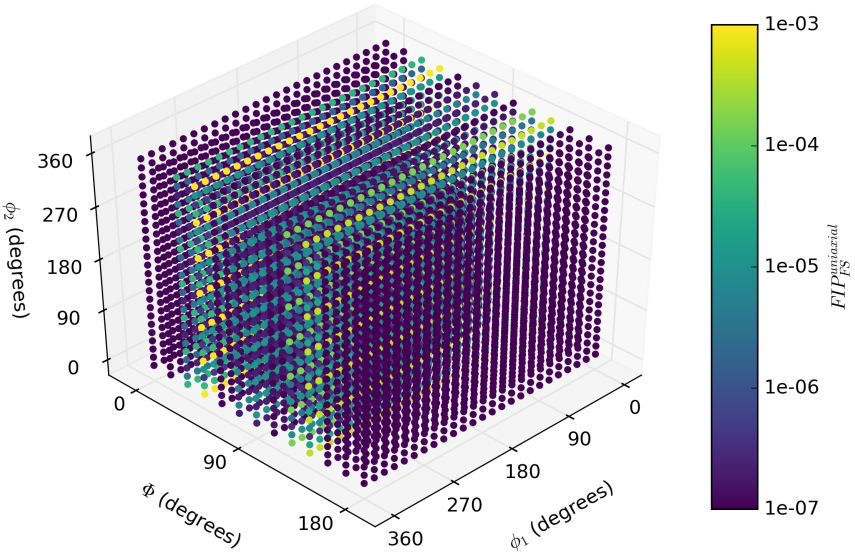

Figure 6.13: The uniaxial tension-compression maximum Fatemi-Socie FIP value $\left(FIP_{FS}^{uniaxial}\right)$ of the simulated polycrystal as a function of the Bunge-Euler angles (ϕ_1, Φ, ϕ_2) used to rotate the specimen.

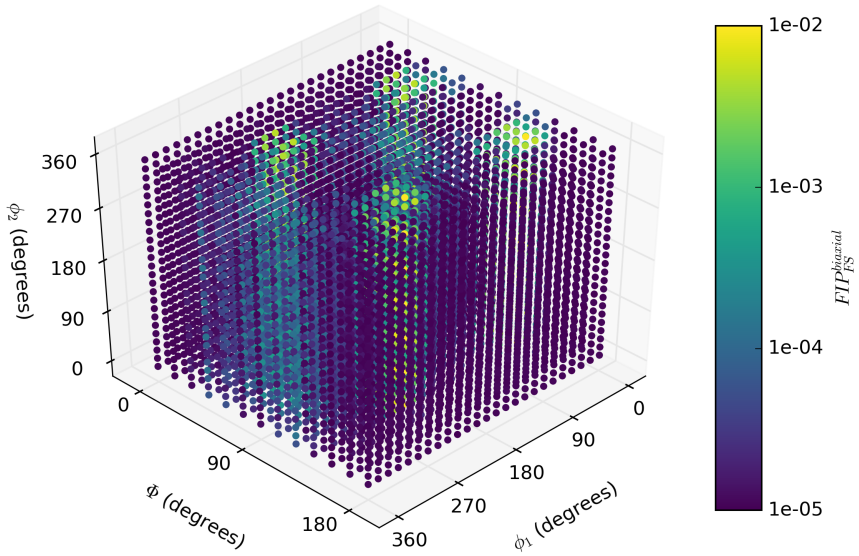

Figure 6.14: The biaxial tension-compression maximum Fatemi-Socie FIP value $\left(FIP_{FS}^{biaxial}\right)$ of the simulated polycrystal as a function of the Bunge-Euler angles (ϕ_1, Φ, ϕ_2) used to rotate the specimen.

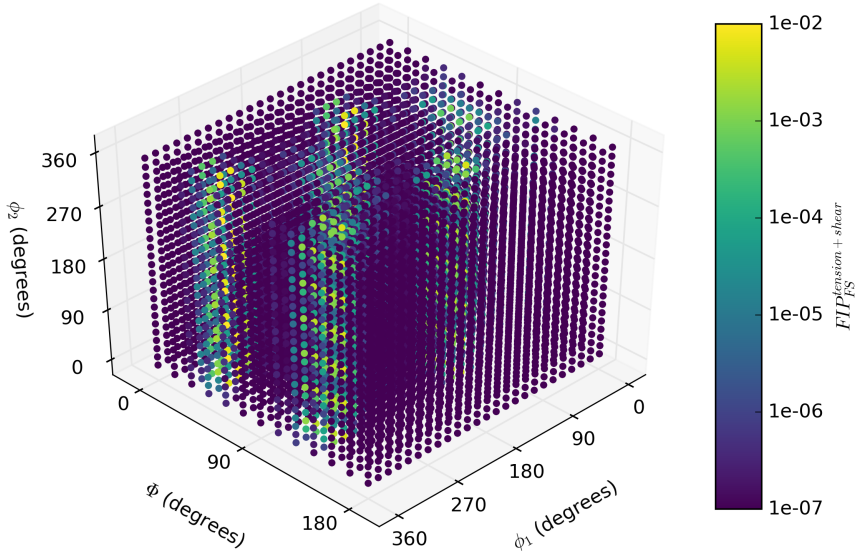

Figure 6.15: The combined uniaxial tension-compression simple-shear maximum Fatemi-Socie FIP value $\left(FIP_{FS}^{tension+shear}\right)$ of the simulated polycrystal as a function of the Bunge-Euler angles (ϕ_1, Φ, ϕ_2) used to rotate the specimen.

6.4.4.2 Performance Requirements

The design requirements employed in this study are shown in Table 6.4. The elastic stiffness and yield strength are given minimum requirements, while the Fatemi-Socie FIP values are supplied a maximum value that must not be exceeded. The input dataset was generated for a 15° binning of each Bunge-Euler angle, which resulted in the assessment of 8,125 specific loading orientations. For preparation for pyDEM, a three-dimensional interpolation function was defined for each output variable. The interpolation function was also constructed such that it was periodic, which is quite beneficial when evaluating derivatives or regions around a specific loading direction that correspond to the min/max value of the Bunge-Euler angle.

Table 6.4: Taylor-type Model IDEM Design Requirements.

Parameter		Performance Requirement
E	$>$	130 GPa
σ_y	$>$	850 MPa
FIP_u	$<$	5×10^{-6}
FIP_s	$<$	5×10^{-6}
FIP_b	$<$	1×10^{-4}

The periodic functions were evaluated over the entire Bunge-Euler angle space, where each angle was discretized into 10 values, resulting in the assessment of 1,000 points. This was mainly to keep the computational time down for the pyDEM module, which took approximately 400 seconds to complete. Additionally, a more refined input space did not alter the solution in any meaningful way.

6.4.4.3 Results

The resultant feasible space indicates the possible sample orientations that would meet the above design requirements for elastic stiffness, yield strength, and a sample fatigue resistance. The combination of the various inputs to determine the total feasible space with associated uncertainties of 0.1% are depicted in Figure 6.16. The

acceptable loading orientations are planes with $\Phi = 0$ and $\Phi = 180$; this would provide uniaxial loading that is parallel to ND, depicted in Figure 6.10.

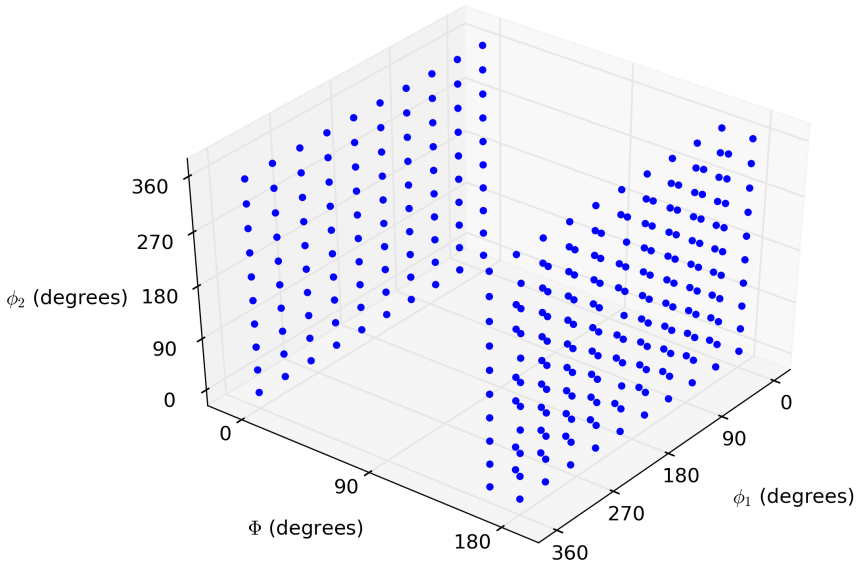

Figure 6.16: The feasible points found for the multi-objective performance requirements applied to the elastic stiffness, yield strength, and multiple Fatemi-Socie FIP value datasets generated with a Taylor-Type Model of a β-annealed texture.

The purpose of this test case was to present an additional design scenario to illustrate the utility of the generalized IDEM framework. While the use of a Taylor-type model with an HCP metal has shown to produce less accurate results than with systems of higher crystal symmetry (e.g., FCC and BCC), the response values generated with the Taylor-type model were of decent agreement when compared with the datasets generated for the previous test case with CPFEM or MKS coupled with an explicit integration scheme. Nonetheless, the functionality demonstrated here is similarly applicable to more detailed designs of strongly textured alloys undergoing fatigue loading. The microstructure level design shown here can be integrated with component design levels through the pyDEM as well as multi-scale material models to more fully incorporate inductive design principles in actual applications.

6.5 Conclusion

The eight texture study performed with a combination of CPFEM and MKS coupled with the explicit integration scheme simulated 4,000 SVEs, but loading was only performed in three orthogonal directions. The limited exploration of loading orientations is less than ideal, particularly given the need to maximize material usage when machining. On the other hand, the Taylor-type model results represent the types of data that are desperately needed to push material selection/optimization towards a computational-minded decision process. However, generating and simulating an excess of 8,000 SVEs (for a single texture) with CPFEM would be quite laborious and computationally-expensive. Both of these case studies demonstrate the ability of pyDEM to couple the material selection/optimization process with modeling and simulation results.

CHAPTER 7

THE INCORPORATION OF SLIP TRANSFER CRITERIA INTO CPFEM

7.1 Introduction

The last objective of this dissertation is to explore the viability of concepts from existing slip transfer correlations with regard to formulation of constitutive relations to address the behavior of slip transfer across grain and phase boundaries in $\alpha + \beta$ titanium alloys. The purpose for the incorporation of additional relations to capture boundary effects is to increase the prediction capabilities of the CPFEM model. A variety of methods have been proposed in the literature, as detailed in Chapter 2, but little emphasis has been placed on extending them to $\alpha + \beta$ titanium alloy systems.

This Chapter will present some of the more commonly accepted slip transfer relations from the literature and apply them to α/β interfaces, something that has not been done previously in the literature, to help determine the level of sophistication needed in proposed slip transfer relations that could be incorporated into CPFEM models. Additionally, a couple of slip transfer relations already incorporated into other CPFEM models in the literature will be discussed in the context of $\alpha + \beta$ titanium alloys.

7.2 Slip Transfer Relations applied to the $\alpha + \beta$ titanium interfaces

There have been multiple slip transfer relations presented in the literature since Livingston's was first presented in 1957 [146]. The majority of the slip transfer relations utilize crystallographic information from the two neighboring grains/phases, e.g. slip

directions and slip plane normals. Additionally, the grain boundary orientation, residual burgers vector, and Schmid factor have been used in calculation of slip transfer relations. However, these relations have not previously assessed for α/β interfaces. Each parameter presented is calculated for a pair of slip systems, with one slip system residing in grain A and the other residing in grain B (see Figure 2.10 for a schematic).

7.2.1 Criteria that Account for Slip System Orientations

7.2.1.1 Livingston Parameter

Livingston first studied pure aluminum bicrystals and determined that dislocations were being transferred across the boundary on slip systems that had the highest resolved shear stress (RSS) in the neighboring grain [146]. This relationship was later termed the transmission factor [264] and is expressed as

$$\mathrm{M}_{\mathrm{Livingston}} = (\mathbf{s}_{\mathrm{A}} \cdot \mathbf{s}_{\mathrm{B}}) \cdot (\mathbf{n}_{\mathrm{A}} \cdot \mathbf{n}_{\mathrm{B}}) + (\mathbf{s}_{\mathrm{A}} \cdot \mathbf{n}_{\mathrm{B}}) \cdot (\mathbf{n}_{\mathrm{A}} \cdot \mathbf{s}_{\mathrm{B}}) \tag{7.1}$$

where $\mathbf{s}$ and $\mathbf{n}$ are the slip direction and slip plane normal for grains A and B, respectively. This relation ranges from 0.0 to 1.0, with a larger number representing an increased likelihood of slip transfer occurring on those specific systems across the boundary.

7.2.1.2 Luster Parameter

Luster later simplified the Livingston parameter by eliminating the second term, therefore the basis of slip transmission is strictly a function of the alignment of the slip directions and slip plane normal [150]. This parameter showed very good agreement for a two-phase titanium alloy comprised of γ-TiAl and α_2-Ti_3Al when comparing active slip systems across grain boundaries. The Luster parameter is similar to the Livingston parameter in that it has a range from 0.0 to 1.0; it is expressed as

$$\mathrm{M}_{\mathrm{Luster}} = (\mathbf{s}_{\mathrm{A}} \cdot \mathbf{s}_{\mathrm{B}}) \cdot (\mathbf{n}_{\mathrm{A}} \cdot \mathbf{n}_{\mathrm{B}})\,. \tag{7.2}$$

This factor is combined with the Schmid factors [91] and a stress intensity factor resulting from pile-ups (based on [92]) in the transmission evaluation of [31]. It was found that a lower stress intensity factor (leading to a lower RSS) on the emission slip system correlated to larger RBVs. For controlling the slip system activation, good alignment of slip systems has proved to be more important than a high Schmid factor. The importance of misalignment of slip systems for slip transmission processes has also been demonstrated with the preceding geometric factor in micro-hardness measurements of GBs [93].

7.2.2 Criteria that Account for Slip System and GB Orientations

7.2.2.1 Shen Parameter

To this point, only the slip direction and slip plane normal have been considered in the determination of slip transfer relations. Shen studied 304 stainless steel undergoing tension and found that minimizing the slip direction was important in predicting the active slip system [147], as was minimizing the angle between the intersection of the incoming slip plane normal with the grain boundary and the outgoing slip plane normal with the grain boundary. The Shen parameter is expressed as

$$\mathrm{M_{Shen}} = (\mathbf{p}_\mathrm{A} \cdot \mathbf{p}_\mathrm{B}) \cdot (\mathbf{s}_\mathrm{A} \cdot \mathbf{s}_\mathrm{B}) \tag{7.3}$$

where $\mathbf{p}_\mathrm{A}$ and $\mathbf{p}_\mathrm{B}$ is the projection of the slip plane normal on the grain boundary for grains A and B, respectively. Shen combined this with the maximum resolved shear stress on the outgoing slip system to predict the active slip systems.

7.2.2.2 Lee Parameter

The Lee parameter is commonly referred to as the LRB criteria [149]. The Lee parameter is similar to the Shen parameter in that it accounts for the projection of the slip plane normals onto the grain boundary plane, i.e.

$$\mathrm{M_{Lee}} = (\mathbf{p}_\mathrm{A} \cdot \mathbf{p}_\mathrm{B}) \tag{7.4}$$

Additionally, the LRB also combined this with a maximum resolved shear stress (on the outgoing slip system) and a minimum residual Burgers vector., i.e.

$$|\mathbf{b}_\mathrm{res}| = \mathbf{b}_\mathrm{B} - \mathbf{b}_\mathrm{A} \tag{7.5}$$

7.2.3 Criteria that Consider Threshold Values

7.2.3.1 Werner parameter

All of the previously presented slip transfer relations were calculated for individual slip systems, but additional relations have been proposed that sum over the individual components to provide a scalar measure for adjacent grains. One such parameter is the Werner parameter [265], which takes the form

$$M_{Werner} = \sum_{i=1}^{N_\mathrm{A}^{slip}} \sum_{j=1}^{N_\mathrm{B}^{slip}} \cos\left(\frac{90^\circ}{\omega_c} \arccos\left(\mathbf{n}_\mathrm{A}^{(i)} \cdot \mathbf{n}_\mathrm{B}^{(j)}\right)\right) \cos\left(\frac{90^\circ}{\kappa_c} \arccos\left(\mathbf{s}_\mathrm{A}^{(i)} \cdot \mathbf{s}_\mathrm{B}^{(j)}\right)\right) \tag{7.6}$$

Critical angles, ω_c and κ_c, are defined as angles above which no slip transfer is expected to occur on the particular pair of slip systems. In other words, a particular slip system pair is not considered (and eliminated from the summation) if the angle between them is larger than the respective critical angle. The critical angle values are material system dependent.

7.3 Calculation of Slip Transfer Relations for α/β interfaces

7.3.1 Methods

The introduction of the slip transfer relations in the previous Section presented the relations for a pair of slip system, one slip system in grain A and another slip system in

grain B. However, each grain on either side of the interface has multiple slip systems. Therefore, the slip transfer relations have $N_{\mathrm{A}}^{slip} \times N_{\mathrm{B}}^{slip}$ components, where N_{A}^{slip} and N_{B}^{slip} are the number of slip systems in grain A and B, respectively. If neighboring grains are of the same phase, $N_{\mathrm{A}}^{slip} = N_{\mathrm{B}}^{slip}$, but that may not necessarily be the case if the neighboring grains have different crystal structures. In this study, each slip transfer relation will be calculated for each pair of slip systems present in $\alpha + \beta$ titanium alloys.

To calculate the Livingston and Luster parameter for each pair of slip systems, the slip direction and slip plane normals must be known. This information is already known for the implementation of CPFEM. In addition to the slip direction and slip plane normals, the grain boundary normal needs to be known to calculate the Shen, Lee, and Werner parameters. The BOR relation is known for $\alpha + \beta$ titanium alloys, therefore an assumption can be made about the orientation of the grain boundary between the two phases.

For this study, it was chosen to model Grain A and Grain B as both having 24 available slip systems – 12 HCP and 12 BCC slip systems – as the homogenized colony grains were modeled in Chapter 4. Although the primary focus of this study is the α/β interface, calculating each slip transfer parameter for pairs of all 24 slip systems will also allow for the analysis of α/α and β/β interfaces. These results will help aid in the understanding of the slip transfer relation values because α/α and β/β contain the symmetry of having identical slip systems on either side of the boundary.

The resultant slip transfer relation values are calculated with a Python [214] script and presented in two-dimensional plots. Each plot contains 576 (24×24) values. The x-axis of the plot represents the i^{th} slip system and the y-axis represents the j^{th} slip system, where i and j represent the selected system for grains A and B, respectively. These plots are symmetric about the diagonal, meaning that the slip transfer relation value for ij is equal to the slip transfer relation value for ji.

Figure 7.1 labels each region of the two-dimensional plot by the phase/phase boundary: bottom-left is α/α, top-right is β/β, and α/β is in the top-left and bottom-right. Specifically, slip systems 1-3 are basal, 4-6 are prismatic, 7-12 are pyramidal, and 13-24 are the BCC slip systems. The specific slip directions and slip plane normal directions for each of the 24 slip systems is presented in the Appendix.

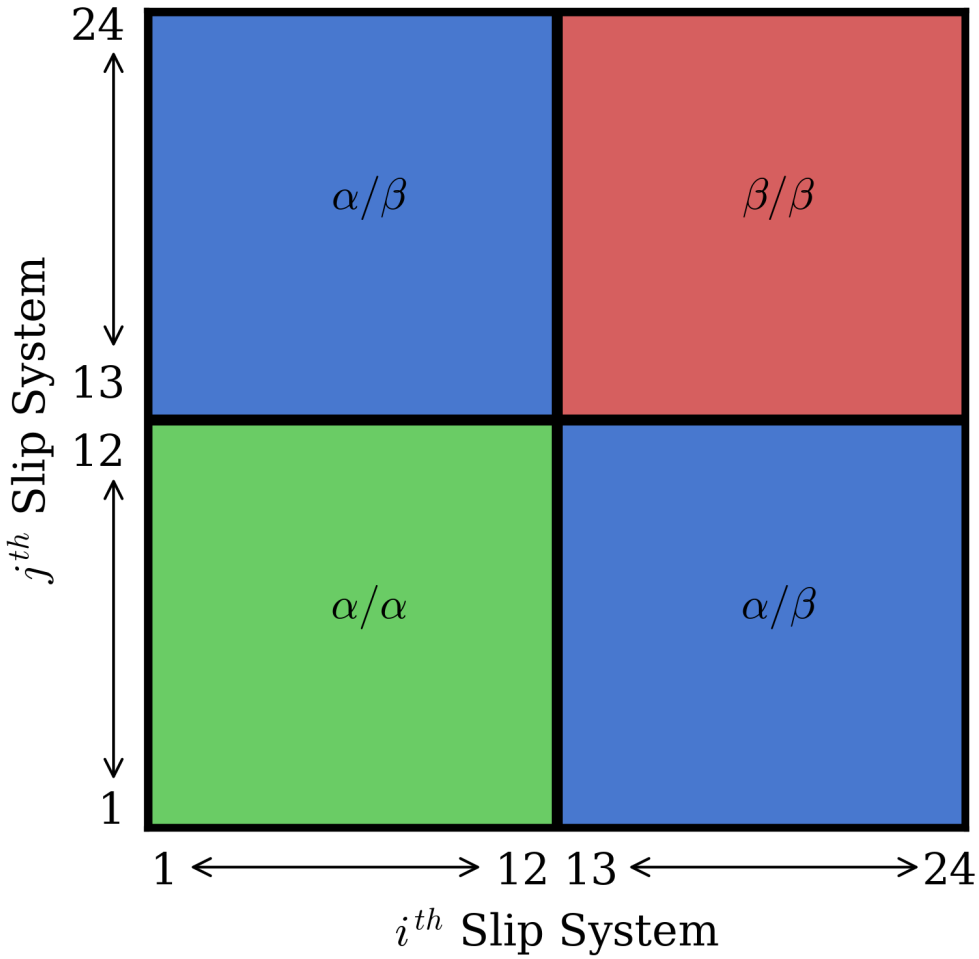

Figure 7.1: A representative two-dimensional schematic of the slip transfer relation value plots that labels the α/α, α/β, and β/β regions.

It is important to remember that the α and β phases within $\alpha+\beta$ titanium have a predetermined orientation relationship with one another, which allows for this type

of analysis. However, for the α/α and β/β paired slip transfer relation values, one of the implicit assumptions in the data presented is that the neighboring grains have the same crystal orientation (e.g., the grains have the same Bunge Euler angles). This is obviously an invalid assumption for a realistic pair of neighboring grains with an interface, but the analysis can nonetheless help in providing context when discussing the results for the α/β interface.

7.3.2 Accounting for Slip System Orientations

The Livingston slip transfer relation (Equation 7.1) was calculated for each combination of slip systems for grains A and B. The resultant plot of those values is shown in Figure 7.2. There are quite a few features of interest as a result of these calculations. For instance, the Livingston parameter returns a value of 1.0 on the diagonal, meaning the incoming and outgoing slip system are perfectly aligned. This was to be assumed since there is no rotation between grains A and B. Also, the Livingston parameter between the basal and prismatic slip systems is 0.0. Although this slip directions are the same for both of these systems (i.e., the $\langle 11\bar{2}0 \rangle$ direction), the slip plane normals are perpendicular to one another.

The primary region of interest for this analysis is the α/β region, which is located in the top-left or the bottom-right of the plot. Slip systems 1-12 are HCP slip systems and 13-24 are BCC slip systems. For the α/β region, two of the three basal slip systems are highly aligned with at least one of the BCC slip systems, illustrated by the high Livingston parameter values of 1.0 and 0.98 in locations ($i = 13$, $j = 3$) and ($i = 14$, $j = 1$), respectively. Additionally, two of the prismatic slip systems (j= 4 and $j = 6$) have values of 0.81 and 0.87 with the BCC slip systems (($i = 17$, $j = 4$) and ($i = 19$, $j = 6$)), respectively. Finally, four of the pyramidal slip systems have one Livingston parameter value greater than 0.925. In fact, only 10 of 144 Livingston parameter values in the α/β are greater than 0.80, while only 36 of the 144 are greater

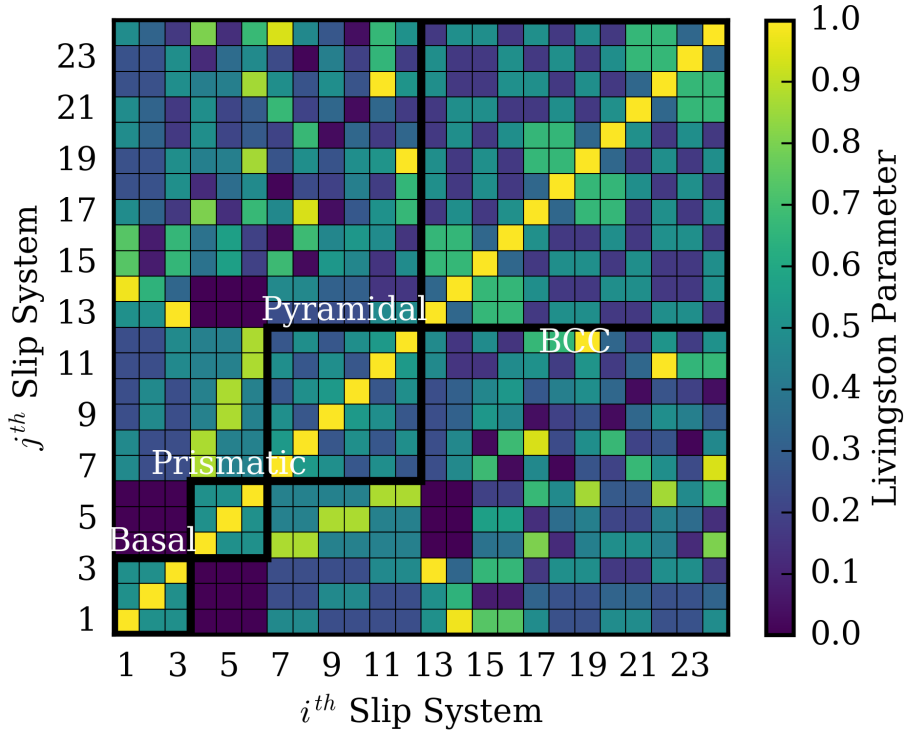

Figure 7.2: The Livingston slip transfer relation values calculated for each combination of the 24 slip systems in the $\alpha + \beta$ colony grain.

than 0.50. However, each of the α slip systems has at least one Livingston parameter value greater than 0.5 when calculated with a neighboring β slip system.

The Luster slip transfer relation (Equation 7.2) was also calculated for each combination of slip systems for grains A and B. The resultant plot of the parameter values is shown in Figure 7.3. There are some similarities when compared with the Livingston parameter, for example all diagonal values are 1.0 and the basal/prismatic interaction is 0.0. This is to be expected, because the Luster parameter is equal to the first term of the Livingston parameter. When slip directions align or are orthogonal to each other, the second term of the Livingston parameter will be equal to zero.

However, the elimination of the second term also leads to some differences in the Luster and Livingston parameter values. For example, the mean of the Luster parameter values, averaged overall all 576 interactions (24×24), is 0.30 while the mean

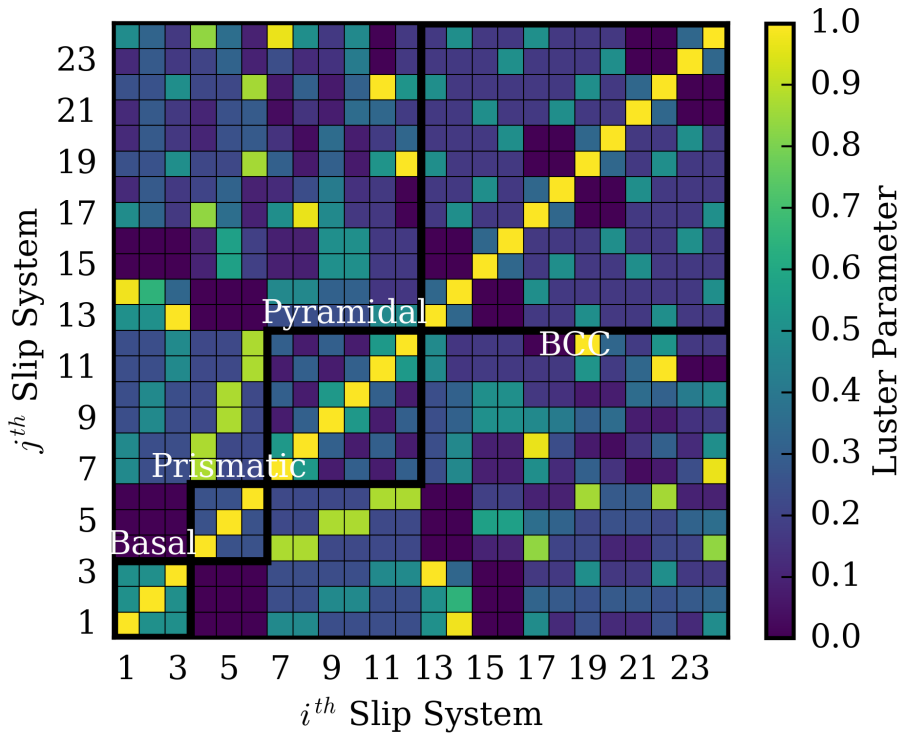

Figure 7.3: The Luster slip transfer relation calculated for each of the 24 slip systems in the $\alpha + \beta$ colony grain.

of the Livingston parameter values is 0.41. Averaged over the α/β region, the mean of the Luster parameter values is 0.28 while the mean of the Livingston parameter values is 0.38. The high alignment for basal (1 and 3) and prismatic (4 and 6) slip systems with BCC slip systems is more easily seen with the Luster parameter as well.

The result of the analysis of the Livingston and Luster parameter values indicates that many of the slip systems in the $\alpha + \beta$ colony grain do not align well across the α/β boundary. However, there is one pair of high alignment for all of the α slip systems looking to transfer dislocations to β slip systems.

7.3.3 Accounting for Slip System and GB Orientations

To account for the grain boundary orientation, it was assumed the interface between Grain A and Grain B has a grain boundary normal vector parallel to the **1010**

direction, as implied in Figure 2.2. In other words, it is assumed that the α/β schematic in Figure 2.2 has a constant cross-section. To test the accuracy of this assumption, more information would have to be known about a specific sample. For example, serial sectioning could be performed to determine the how this boundary is oriented through the thickness of a particular colony grain.

Then Shen parameter values (Equation 7.3) are shown in Figure 7.4 for each slip system pair. It is quite obvious the orientation of the grain boundary has quite an effect on particular values. For example, many of the diagonal values are less than 1.0. Additionally, the grain boundary is parallel to one of the prismatic planes, meaning the Shen parameter is 0.0 for slip system $i = j = 6$. This result is quite intriguing because [138] the result correlates to work done previously in crystal plasticity modeling regarding the slip resistance of prismatic slip systems.

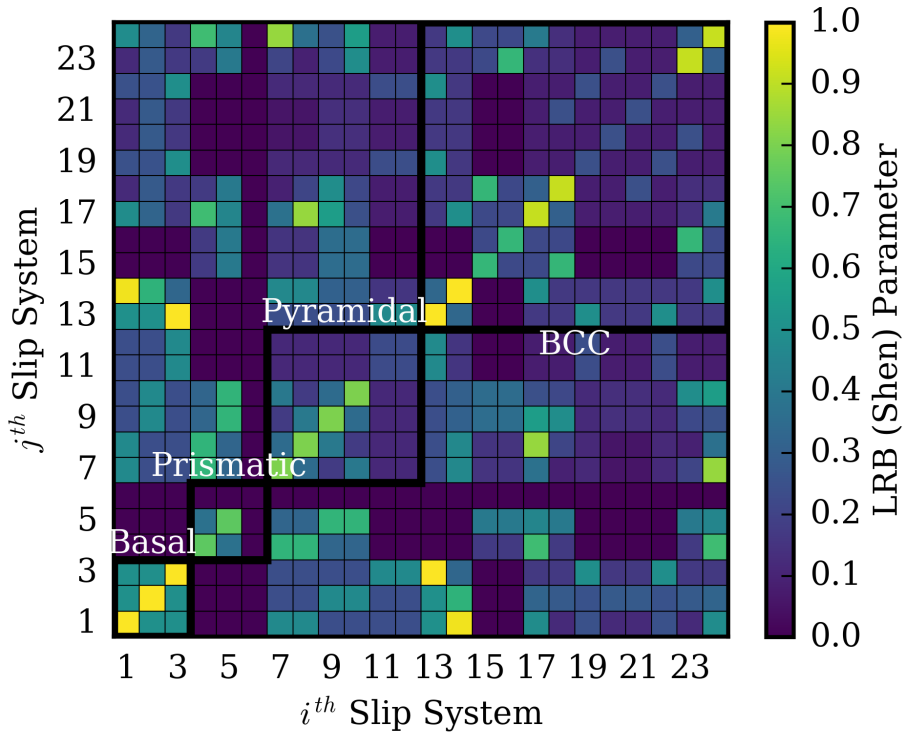

Figure 7.4: The Shen slip transfer relation calculated for each of the 24 slip systems in the $\alpha + \beta$ colony grain.

While the Livingston and Luster parameters indicated that each α slip system in the α/β region had at least one corresponding β slip system that was in general alignment (0.5 or greater), the values for the Shen parameter results in 10 of the 12 α slip systems having at least one corresponding β slip system that results in a Shen parameter value greater than 0.5. However, there are also clusters of 0.0 values in the α/β region.

The plot of the Lee parameter values, shown in Figure 7.5, looks very similar to the Shen parameter, but more values are constant since it is only accounting for slip plane and not also slip directions (see Equation 7.4). And again, one prismatic slip system has all values of 0.0 because of the slip plane being parallel to the grain boundary.

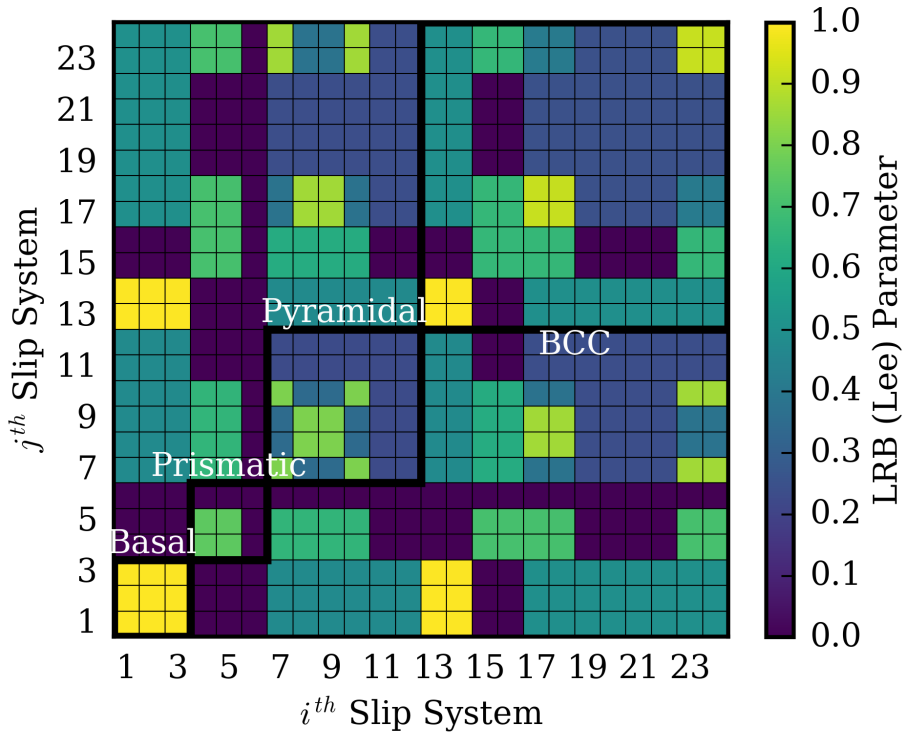

Figure 7.5: The LRB (Lee) slip transfer relation calculated for each of the 24 slip systems in the $\alpha + \beta$ colony grain.

Given that prismatic slip is typically the most common active slip system in α-titanium, this analysis would imply that the possibility of slip transfer between the α and β phase is quite high. In the literature, the Lee parameter is also coupled with the residual Burgers vector for each pair of slip systems. The residual Burgers vector (Equation (7.5)) can be found given the unit cell measurements for α titanium (a=0.295 nm, c=0.468 nm) and β titanium (a=0.295/1.04 nm) and the slip direction unit vectors used in other calculations in this Chapter. The residual Burgers vector values are plotted in Figure 7.6.

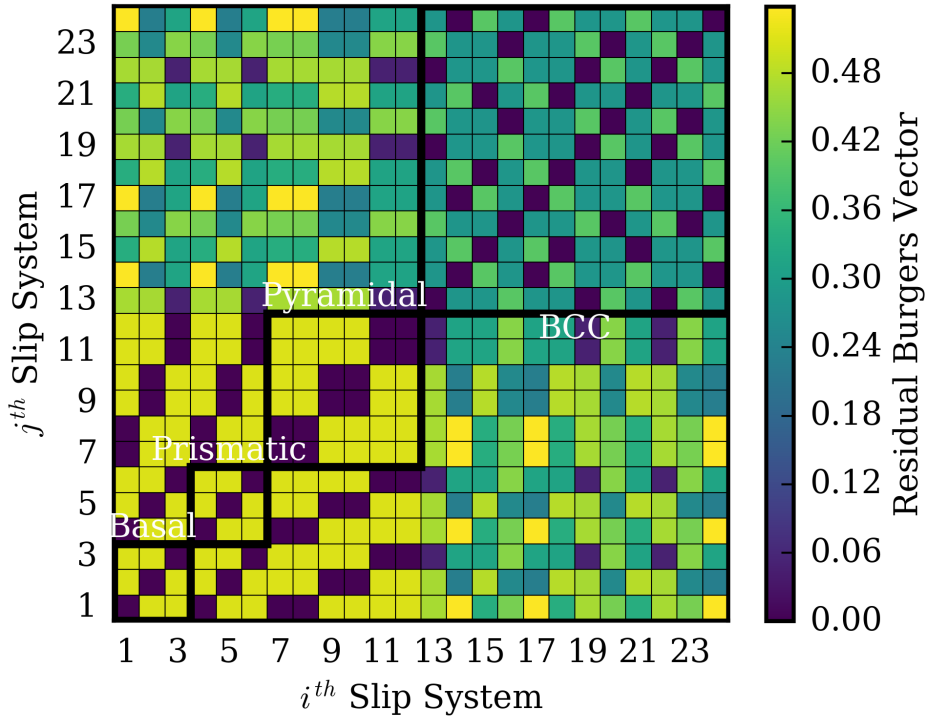

Figure 7.6: The residual Burgers vector calculated for each of the 24 slip systems in the $\alpha + \beta$ colony grain.

Coupling these findings with the indentation yield strength values presented in Chapter 4 would also indicate that although the α/β interface is extremely difficult to characterize, it might not be the most important boundary in these titanium alloys. In fact, the $\alpha/\alpha+\beta$ boundary is potentially the root source of the increase in strength

in these titanium alloys [53]. If that is the case, then the objective is still very similar, but the methods to achieve the objective are different than first thought.

7.3.4 Considering Threshold Values

The previous analyses looked at individual values for pairs of slip systems that reside across a boundary. The Werner parameter sums all of the interactions to return a scalar value. Applying this parameter to α-titanium and $\alpha + \beta$ colony grains can provide some measure of ease of slip transmission between grains. With the Werner parameter, grain boundary information is not accounted for in the calculation. Two boundaries are analyzed with the Werner parameter, the α/α boundary and the $(\alpha + \beta)/(\alpha + \beta)$ boundary. The critical angle values (see Equation 7.6) applied to this analysis are 45° for both angles.

For a baseline comparison, neighboring α grains are analyzed in Figure 7.7. The 12 HCP slip systems (basal, prismatic, and pyramidal) modeled in the colony grains are specifically what is used for the calculations in Figure 7.7. Two of the Bunge Euler angles (ϕ_1 and Φ) are varied and used to rotate one of the grains in the analysis, while the other grain remains stationary for all calculations. The resultant plot depicts a contour surface of the Werner parameter. In an effort to compare this parameter with other configurations that have a different number of slip systems, the Werner parameter was scaled by the number of slip systems modeled in each scenario. For the $\alpha/alpha$ interface, the total number of components is 144 (12×12). The α/α interface depicts a symmetry while varying both the ϕ_1 and Φ angles, which is to expected given the symmetry of the HCP unit cell.

In comparison, the $(\alpha + \beta)/(\alpha + \beta)$ interface (shown in Figure 7.8) does not have that symmetry due to the combination of HCP and BCC slip systems. Comparing these plots would indicate that slip transfer between the α/α interface should more easily occur than with the $(\alpha + \beta)/(\alpha + \beta)$ interface. However, this is also not taking

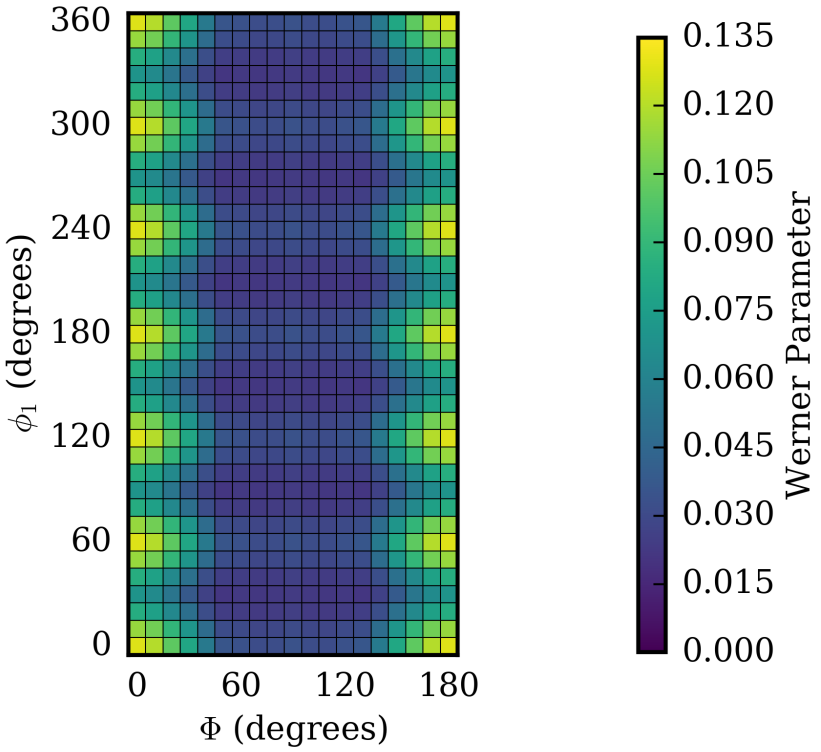

Figure 7.7: The Werner slip transfer relation calculated for each of the 12 HCP slip systems in the $\alpha + \beta$ colony grain.

into account the preferred misorientation present in $\alpha + \beta$ titanium alloys.

The Werner parameter for the α/β boundary is 0.05. There is only one value for the α/β boundary because the relationship between the two phases is known, therefore there is no need to further rotate one phase in relation to assess various orientations. In comparison with the α/α and $(\alpha+\beta)/(\alpha+\beta)$ boundaries, a Werner parameter of 0.05 is higher than the mean value $(\alpha + \beta)/(\alpha + \beta)$ boundary (0.43), but lower than the mean value for the for the α/α boundary (0.52).

Like some of the previous slip transfer parameters, combining this with the resolved shear stress or Schmid factor would most likely provide a better indicator of the likelihood of slip transfer. However, these types of analysis can aid in the understanding of interfaces for specific material systems.

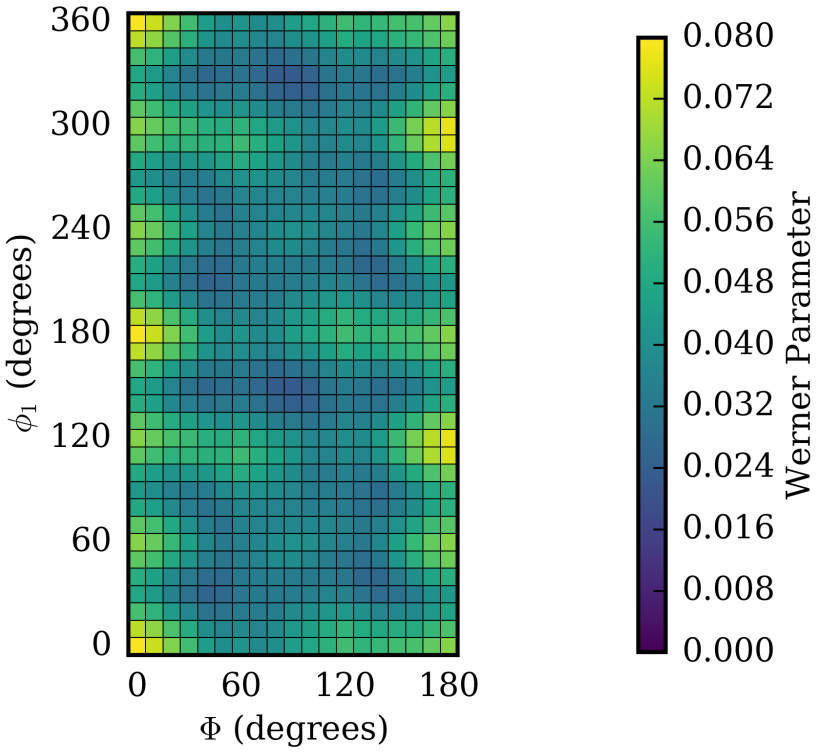

Figure 7.8: The Werner slip transfer relation calculated for each of the 24 slip systems (12 HCP and 12 BCC) in the $\alpha + \beta$ colony grain.

7.4 Extension to CPFEM Modeling

Given the experimental and CPFEM results shown in Chapter 4 and the analysis shown here, it is likely that the increase in strength in $\alpha + \beta$ is due to a combination of the intragranular interfaces (α/β) within a single colony grain, as well as the intergranular interfaces ($\alpha/(\alpha+\beta)$ and $(\alpha+\beta)/(\alpha+\beta)$) of the polycrystalline material. Therefore, extension for the CPFEM model for both scenarios are proposed in the subsequent sections of this chapter.

7.4.1 α/β interface

The CPFEM model treats the α/β colony grains as a homogenized structure, meaning the boundaries are not explicitly modeled in the three-dimensional microstructure.

Therefore, these boundaries can be more easily treated because there is no requirement to account for microstructural information in neighboring elements or grains. Additionally, since the grain boundary information is known for the α/β interface, sophisticated transfer criteria can be analyzed without much additional computational expense.

The slip transmission parameter proposed for the α/β interface is the Shen parameter (Equation 7.4), which accounts for both the slip direction and the misorientation of the slip plane normals in the grain boundary plane. This method would require an interaction coefficient matrix, i.e.

$$\mathrm{M}_{\mathrm{Shen}}^{(\mathrm{ij})} = \left(\mathbf{p}_{\mathrm{A}}^{(i)} \cdot \mathbf{p}_{\mathrm{B}}^{(j)}\right) \cdot \left(\mathbf{s}_{\mathrm{A}}^{(i)} \cdot \mathbf{s}_{\mathrm{B}}^{(j)}\right). \tag{7.7}$$

This matrix would have 144 components (12 HCP slip system $\times$ 12 BCC slip systems), and as can be seen in Figure 7.4, the matrix would not be symmetric. To reduce the number of components in the above relation, the Lee parameter could be used instead. It shows great similarity to the Shen parameter, with fewer unique values. However, the use of either the Lee or Shen parameter should be dictated by experimental data and not necessarily the ease of implementation. This type of procedure has been implemented in both two- and three-dimensional simulations in the literature.

This parameter could be utilized to increase the CRSS values for individual interactions, therefore the updated CRSS would have the form

$$\tau_{CRSS}^{updated} = \tau_{CRSS} + c_0 \left(1 - M_{Shen}^{(ij)}\right) \tau_{CRSS}, \tag{7.8}$$

where c_0 is a multiplication factor, most likely between 0 and 1. One of the advantages of this type of method is that it can be combined with the local stress-state of each element to determine active slip systems. The introduction of this parameter is a straight-forward placement in the UMAT; the difficult portion of implementation is calibration. Microstructure-sensitive experiments, such as indentation experiments,

would be required to generate a dataset that could provide local values that are sufficient for calibrating c_0. Obviously, the Shen matrix could be set to zero except for a few specific interactions. In fact, that would be a good starting point for the introduction of this method into the CPFEM.

Similarly, one of the parameters already present in the current α_β CPFEM model could also be altered. For example, the threshold stress (Equation 4.8) contains a parameter, the mean slip distance (d), that varies whether the material point represents α-titanium or an $\alpha + \beta$ colony grain. In the current implementation, value for d is smaller for the colony grain than for α-titanium. However, this measurement was simply averaged for colony grains. Instead, the value for d could vary by slip family or for individual slip systems, providing a strength increase or decrease that is a function of the actual slip distance within the α phase. This could be calculated by determining the fraction of the slip direction normal to the α/β interface and dividing the current mean slip distance by that fraction.

Both of these strategies have great potential for more accurately representing the complexity introduced by the α/β interface. However, it is also important to keep in mind that the findings of Chapter 4 indicate that the current treatment of the α/β interface is sufficient for predicting the indentation datasets presented. Additionally, the findings in this Chapter imply that slip across the α/β interface has the same, not more, difficulty as slip across other boundaries in $\alpha + \beta$ titanium.

7.4.2 $(\alpha + \beta)/(\alpha + \beta)$ interface

The treatment of intergranular boundaries is a much more difficult proposition than what was presented for the α/β interface. There are multiple complications introduced that need to be analyzed. For example, determining grain boundary normals between neighboring elements is non-trivial depending on shape of each voxellated

mesh. Also, stress-state or microstructural information might need to be shared during the simulation, which is a possibility in Abaqus, but is extremely computational expensive and requires additional runtime for the simulation.

To minimize adding computational complexity to the CPFEM simulation, the utilization and sharing of microstructural information before deformation is the recommended approach. Previous work [266] has found that the increase in strength to an individual grain can be isolated to a region immediately adjacent to the boundary. The edge of the grain is termed the mantle, while the center of the grain is the core. The method proposed here is to increase the strength of the mantle by some average value that accounts for all neighbors of a specific grain.

A simplistic approach would be to determine the misorientation angle between a grain and all of its neighbors and developing a simplistic function that increases the critical resolved shear stress values for a given grain by either the average or maximum misorientation angle. All of this would be done in the pre-processing portion of the simulation, essentially increasing the number of grains in the simulation by a factor of two. Again, the important (and missing) step in this process is to develop a sophisticated dataset for calibration/validation purposes. It would not be efficient to pursue such a method without a specific application for the updated CPFEM model.

7.5 Conclusion

The analysis of various slip transfer relations reveals that although slip transfer across α/β interfaces is quite complex, it could be no more difficult than slip transfer across other boundaries present in $\alpha+\beta$ titanium alloys. This preliminary analysis revealed that including the Shen or Lee parameter as a basis for improving the predictive capability of α/β interface in the current model shows potential. However, although the introduction of slip transfer criteria in CPFEM models are important for advancing the nature of local continuum models such as CPFEM, but need to be treated with

great care and caution. These types of modifications to CPFEM implementations can increase the computational demand of such algorithms, and their benefit is tied to the availability and accuracy of experimental datasets. The introduction of extraneous complexity makes it difficult to calibrate these models, which is a vital step in their predictive capability.

CHAPTER 8

CONCLUSIONS AND RECOMMENDATIONS

8.1 Overview

The research presented in this dissertation encompasses a variety of topics related to microstructure-sensitive modeling, including the utilization of high throughput methods for calibration/validation, the development of computational efficient methods for assessing relative fatigue resistance, and the extension of microstructure-sensitive model datasets to robust solution methods. There exists a considerable amount of interest in extending microstructure-sensitive modeling to multi-objective design scenarios, which was one of the primary motivators of this work. A number of individual studies were undertaken in this dissertation, they include:

- ◇ The development of a computationally-efficient FEM model of the SNI process for investigation of anisotropic elastic deformation and its connection to the indentation elastic modulus.

- ◇ The assessment of the CPFEM model form and parameter estimation for α and $\alpha + \beta$ phases of Ti-64 with direct comparison to experimental indentation yield strength and hardening rate datasets.

- ◇ The extension of CPFEM modeling and local deformation fatigue simulations for coupling with the MKS for the purposes of assessing multiple textures deformed in the HCF regime.

- ◇ The exploration of robust, multi-objective design solutions with IDEM with datasets developed from CPFEM simulations as well as the MKS coupled with

the explicit integration scheme for elastic stiffness, yield strength, and Fatemi-Socie FIP distributions.

- ◇ The investigation of extending Ti-64 CPFEM models to address the behavior of slip transfer across the α/β boundary with existing slip transfer relations.

Each of these individual studies is addressed within the previous chapters of the dissertation. Additionally, each chapter presents the appropriate introduction, computational methodology, results, and discussion of the work. The significant contributions and innovative findings of this research are summarized in the following sections and presented for each individual study listed above.

8.1.1 The Extraction of Elastic Constants from Ti-64 SNI Experimental Datasets

The FEM method was employed to study the effect of anisotropic elasticity on the indentation elastic modulus of commercially pure and α-titanium. A combination of finite and infinite elements were employed for the construction of a three-dimensional geometry capable of replicating single crystal indentation elastic moduli. A mesh convergence study was performed to select the total number of elements and proper height-to-width ratio of the finite elements beneath the indenter. Because of the computational efficiency of the new FEM model, the possible ranges of the five elastic constants were sampled to construct a thorough dataset of indentation elastic modulus as a function of elastic constants and the loading orientation (i.e., Φ). A fourth-order polynomial was fit to the computational dataset with linear regression to provide a forward protocol for estimating indentation elastic modulus given elastic constants and loading orientation. Additionally, a least squares and weighted least squares optimization technique was constructed to provide the inverse protocol – the estimation of elastic constants given an experimental dataset which includes indentation moduli and loading orientation. Finally, Bayesian inference was combined with

the Markov Chain Monte Carlo method to assess the uncertainty associated with each of the elastic constants found with the inverse protocol.

The significant conclusions of this research include:

(i) A high level of precision is needed when relating FEM indentation elastic moduli to experimental values. Even a small error (5-10%) that is commonly accepted for other finite element applications is too large for determining elastic constants for individual phases and/or specific crystallographic orientations from FEM simulation results.

(ii) A combination of finite and infinite elements in a three-dimensional configuration provides converged indentation elastic modulus values for anisotropic elasticity.

(iii) Some of the elastic constants (c_{11},c_{33}) of HCP materials have a strong impact on the resultant indentation elastic modulus as a function of Φ, while others (c_{12},c_{13}) have very little impact.

(iv) There is a range of acceptable elastic constants when fitting an experimental dataset, meaning proper treatments of the solution uncertainty are required to extract the most accuracy from the model.

8.1.2 The Extraction of CPFEM Model Parameters from Ti-64 SNI Experimental Datasets

The FEM model crafted for the examination of elastic deformation during SNI was extended to capture deformation at larger indenter displacements to generate indentation stress-strain curves. The CPFEM model was calibrated to experimental SNI datasets for CP-titanium, α-titanium, and $\alpha + \beta$ titanium. The critical resolved shear stress values for each material system were determined from the comparison of the experimental and simulation indentation yield strengths trends. Additionally,

the hardening rate immediately following yield was also compared. Finally, the von Mises stress beneath the indenter was analyzed to determine the spatial change of the stress as a function of distance from the surface.

The significant conclusions of this research include:

(i) The ability to capture the indentation elastic modulus, indentation yield strength, and indentation hardening rate with the same FEM model is a challenging task that requires a significantly number of elements and adequate coarsening with increased distance from the indenter.

(ii) The indentation yield strength is primarily a function of the critical resolved shear stress of the single crystal, thus providing a fertile foundation for the determination of CPFEM model parameters for individual phases and/or grains.

(iii) The indentation hardening rate is controlled by many modeling parameters, making it quite difficult to connect with any individual parameter.

(iv) The assumption that plastic deformation is primarily occurring only within the grain being indented is valid for initial plasticity encountered in the indentation stress-strain plot.

8.1.3 The HCF Analysis of α-Titanium

The microstructure-sensitive modeling procedure of CPFEM was coupled with MKS to provide a more computationally-efficient manner for generating extreme value distributions related to fatigue resistance. The MKS was calibrated with anisotropic elastic FEM simulations of α-titanium polycrystalline digital microstructure created with Dream.3D. This allowed the MKS to predict, with high accuracy, the total strain tensor for each element (voxel) for any subsequent α-titanium microstructure. The total strain tensor was used to calculate the stress tensor for each element for the same microstructure. An explicit integration scheme was employed to calculate the

resolved shear stress, evolution equations, and the plastic shear strain rate for each slip system within a polycrystalline microstructure. Fully-reversed cyclic loading in the HCF regime was performed for three cycles and the Fatemi-Socie volume-averaged FIP values were calculated in a manner identical to the method used with traditional CPFEM results. This procedure was used to analyze four textures and three loading directions.

The significant conclusions of this research include:

(i) The total strain generated from MKS was highly accurate when compared with anisotropic elastic FEM and CPFEM simulation results. Additionally, the elemental stress tensor calculated from the MKS total strain tensor closely matched the tensor values from anisotropic elastic FEM and CPFEM simulations.

(ii) The explicit integration scheme was found to calculate local plastic strain tensors that were on the same order of magnitude as similar quantities from CPFEM simulations. Given the approximations associated with both method, this was deemed a highly successful comparison.

(iii) The extreme value Fatemi-Socie volume-averaged FIP plots were also in good agreement when compared with results from CPFEM simulations. And the new procedure allows for the sampling of a larger number of SVEs, providing additional confidence in the rank ordering of microstructure with FIP responses.

(iv) Given the 40x increase in computational efficiency and removing the FE licensing restriction, the MKS method coupled with the explicit integration scheme presents a tool that shows great promise for future research in loading regimes dominated by fatigue crack formation.

8.1.4 The Development of Multi-Objective Robust Design Solutions from Microstructure-Sensitive Modeling Results

In an effort to connect microstructure-sensitive modeling with the multi-objective decision making regarding material selection/optimization, two case studies were examined with IDEM to make robust design solutions. For the first case study, a titanium-specific dataset was generated via a combination of CPFEM and MKS coupled with the explicit integration scheme simulations. The dataset included directional elastic stiffness, yield strength, and extreme value distribution plots related to fatigue resistance. These values were calculated for eight textures and three loading directions. The second case study utilized a single texture (β-annealed) and a Taylor-type model to deform a 1,000 polycrystalline construct. This specimen's orientation relative to loading was rotated in an effort to generate directional elastic stiffness, yield strength, and maximum FIP response for all possible loading directions. In the first case study, the texture and loading direction was selected to satisfy the specific design scenarios, while the loading orientation of the specimen was selected based on a multi-objective design scenario in the second case study.

The significant conclusions of this research include:

(i) The IDEM was performed on two separate case studies, both of which highlight the future direction for calibrated microstructure-sensitive modeling schemes. Both datasets have their limitations in terms of complete representation, but provide a significant improvement for extension to IDEM-like environments which require large datasets for analysis.

(ii) Both case studies also demonstrated the importance of c-axis alignment with the loading direction of individual grains within the polycrystalline specimen to increase the elastic stiffness and yield strength, while simultaneously minimizing Fatemi-Socie FIP values.

(iii) An open-source algorithm and Python module were created to perform generalized IDEM analyses of a variety of datasets. This tool has the capability of accelerating both the understanding and use of robust solution procedures because of its highly portable and computationally-efficient nature.

(iv) The IDEM algorithm is extremely fast even when performed on a desktop computer, completing in seconds or a few minutes depending on the number of sampling points.

8.1.5 The Extension of CPFEM Model to Explicitly Account for Grain Boundaries

In an effort to assist the future extension of the $\alpha + \beta$ titanium CPFEM model used in this work, slip transfer parameters were applied to $\alpha + \beta$ grains and analyzed for possible inclusion into the CPFEM procedure. A number of slip transfer parameters were calculated for the relevant HCP and BCC slip systems in colony grains. Additionally, both the intragranular and intergranular treatment of boundaries was explored in accordance with their incorporation into the CPFEM model.

The significant conclusions of this research include:

(i) The examination of the various slip transfer parameters highlighted the selective compatibility among the HCP and BCC slip systems present in colony grains.

(ii) The use of the Shen and/or Lee parameters show promise as a basis for modification of the current CPFEM model to more accurately capture the complexity of slip transfer at the α/β interface.

(iii) Given the indentation yield strength results showing comparable values forα-titanium and $\alpha+\beta$ colony grains, the intergranular boundaries (e.g., $(\alpha+\beta)/(\alpha+\beta)$) were also noted as a boundary that should be considered when modifying the CPFEM model.

8.1.6 Novel Contributions and Findings of this Research

Research conducted in this dissertation utilized various computational tools (e.g., CPFEM, IDEM, MKS, etc.) and post-processing algorithms (e.g. explicit integration scheme, indentation stress-strain curve, etc.) to craft a computational workflow that enhances the nature of computational materials selection and optimization. Collectively, this dissertation has addressed the four main objectives outlined in Chapter 1; however, the major accomplishments of this work include:

- ◇ The development of a computationally-efficient FEM model of the SNI process for investigation of anisotropic elastic deformation and plastic deformation. Previous work in this field has yet to produce a FE mesh that exhibits both mesh convergence and a limited number of elements required for CPFEM simulations. This model was shown to be highly accurate for indentation elastic modulus, which provides increased utility for experimentalists in need of approximate values before or after testing.

- ◇ The coupling of the MKS method with the explicit integration scheme presents a very fruitful computational tool that has the prospect of supplanting traditional CPFEM modeling in the HCF regime. This study examined 2,000 SVEs in the matter of a couple of minutes per SVE; a comparable CPFEM study would have required close to 45 minutes per SVE. Additionally, the new couple procedure removes the FE license restriction, which allows for simultaneous simulation of more SVEs because most end-users are now limited by number of software licenses and not processing power.

- ◇ The development of the generalized IDEM procedure in association with this work shows great promise in thrusting robust design to the forefront of computational materials selection and optimization. The algorithm is quite flexible,

making it quite useful for a variety of datasets, material systems, and applications.

8.2 Recommendations for Future Work

The results found in the various studies in this dissertation provide a wealth of information concerning the application of microstructure-sensitive modeling to titanium and its alloys as well as the extension of these procedures to material selection and optimization. The results of this dissertation answer some of the questions presented in Chapter 1 while additional questions still remain. Below are possible extensions of work conducted in this dissertation and future directions for that work:

- ◇ The computationally-efficient FEM model of the SNI process is more than adequate for the investigation of anisotropic elastic deformation. However, the titanium-specific dataset generated with it contained more data than was absolutely necessary for successful representation with a polynomial function. Additional work should be performed to optimize the amount of FEM data required to accurately predict the indentation elastic modulus for specific elastic constants and loading orientation. This would require advanced sampling methods or cross-validation, but could provide immense benefit to the generation of future datasets. Additionally, the Bayesian analysis performed in this study should be made standard in the post-processing approach and data analysis of microstructure-sensitive modeling studies. Much can be learned from such uncertainty quantification, even for a seemingly simplistic dataset such as elastic moduli as a function of elastic constants.

- ◇ While the FEM model of the SNI process is adequate for capturing elastic deformation, it can be quite computationally-expensive for the repeated load-unload cycles required to generate indentation stress-strain curves with CPFEM modeling. The current limiting process of the FEM model is the infinite elements.

While they provide great utility, they also restrict the FE solver's functionality to partition the implicit integration procedure to all compute nodes reserved for analysis. Without this functionality, the FE solver is unable to parallelize the per-element calculations, which leads to a considerable increase in runtime. A possible extension of this work would be to eliminate this deficiency by including a different type of infinite element through the a User ELement (UEL) subroutine. This has the possibility of providing the parallelization required for decreasing the runtime. Provided the success of this future extension, it would also be quite beneficial to apply the Bayesian analysis to the indentation yield strength, in a similar manner as was used for the indentation elastic modulus. This would allow for an in-depth study of the direct effect of the CRSS values on the resultant indentation yield strength.

- The MKS coupled with the explicit integration scheme shows great promise for rapid generation of distributions of material-specific properties typical of the HCF regime, specifically extreme value distributions of Tips. However, increased speed-up could most likely be gained from the explicit integration scheme with additional vectorization of calculations within the algorithm. But this increased speed-up is still limited from this approach. And the method is still limited to the HCF regime where the assumption is valid that total strain equates to elastic strain. Instead, structure-property linkages should be explored to predict properties such as the directional elastic stiffness, yield strength, and maximum FIP value for a specific microstructure. This would completely eliminate the need to perform microstructure-sensitive simulations once calibration/validation has been performed. These functions could assess the properties of new microstructures in seconds, providing a true connection from the research-specific CPFEM results to an end-user designer/analyst in a commercial setting.

- ◇ The generalized and open-source algorithm for IDEM has much potential, but a more thorough microstructure-sensitive modeling dataset is needed. In an ideal study, the advantages of both of the presented case studies would be combined, producing a dataset that samples over multiple textures similar the CPFEM study, performs loading in all possible sample orientations like the Taylor-type model, and has the geometrical representation of digital microstructures in FEM. The construction of such a dataset would require either a modification to digital microstructures generated with Dream.3D to allow for arbitrary rotation of the grains (and Euler angles) in relation to the FE mesh, or a modification of the boundary conditions to simulate uniaxial loading in a general direction.

- ◇ The addition of slip transfer criteria to CPFEM models could be very beneficial for specific applications and/or material systems, but the immediate focus of future work should seek to generate experimental datasets that necessitate these additions. Additions to CPFEM models should be rooted in a needs-based foundation, and the proper datasets for assessing these additions are few in number. Recent advances in small-scale experimental testing are making it more likely to generate datasets specific to grain interactions at boundaries. These types of studies will be very important moving forward for increasing the accuracy of microstructure-sensitive modeling techniques such as CPFEM.

APPENDIX A

EXPLANATION OF FATIGUE INDICATOR PARAMETER CALCULATION

The purpose of this section is to provide the reader with a more detailed description of how the fatigue indicator parameters (FIPs) are calculated in the post-processing scripts used in this work. We will use the Fatemi-Socie FIP as our example, but the process is very similar if performed for other FIP measures.

For the HCF study in this work (see Chapter 5), three fully-reversed cycles were performed with our CPFEM model in Abaqus/Standard with a UMAT. The full stress, total strain, and plastic strain tensors are output to the ODB file for each peak and valley on the strain amplitude versus time plot. This data is then extracted with Abaqus Python, for all elements, from the ODB and saved in some accessible file format (e.g., TXT, VTK, CSV, etc.). A standalone version of Python is used for the FIP calculation in this work. The below description is calculated on a per-element basis initially and then volume-averaged over some finite domain of elements.

The change in the plastic strain tensor ($\Delta\boldsymbol{\epsilon}^p$) is calculated for the cycle of interest and since the loading in this case is fully-reversed, according to

$$\Delta\boldsymbol{\epsilon}^p = \boldsymbol{\epsilon}^p_{max} - \boldsymbol{\epsilon}^p_{min}. \tag{A.1}$$

The loading is fully-reversed in this work, therefore it is assumed that the maximum plastic strain tensor, $\Delta\boldsymbol{\epsilon}^p_{max}$, occurs at the peak of the cycle and the minimum plastic strain tensor, $\Delta\boldsymbol{\epsilon}^p_{min}$, occurs at the valley of the cycle. The eigenvalues and eigenvectors are determined for the change in the plastic strain tensor to determine the maximum plastic shear strain and the plane on which it operates. The maximum

plastic shear strain is then half the difference of the largest (λ_1) and smallest (λ_3) eigenvalues, i.e.

$$\gamma^p_{max} = \frac{1}{2}\left(\lambda_1 - \lambda_3\right). \tag{A.2}$$

The maximum plastic shear strain operates on two orthogonal planes; those planes are a function of the eigenvectors associated with the largest and smallest eigenvalues, i.e.

$$\mathbf{v}_{max1} = \mathbf{v}_1 - \mathbf{v}_3 \tag{A.3}$$

$$\mathbf{v}_{max2} = \mathbf{v}_1 + \mathbf{v}_3 \tag{A.4}$$

The eigenvectors are normalized into unit vectors. The maximum normal stress, σ^n_{max}, is determined for both of the planes found above and the maximum of those two values is selected, i.e.

$$\sigma^n_{max} = \max\left(\mathbf{v}^T_{max1} \cdot \boldsymbol{\sigma} \cdot \mathbf{v}_{max1}, \mathbf{v}^T_{max2} \cdot \boldsymbol{\sigma} \cdot \mathbf{v}_{max2}\right) \tag{A.5}$$

It should be noted that the above step is extremely important in determining the maximum FIP value. Previous works have excluded the determination of finding the maximum normal stress on both of the maximum plastic shear strain planes. Finally the Fatemi-Socie FIP value is determined via

$$FIP_{FS} = \frac{\bar{\gamma}^p_{max}}{2}\left(1.0 + k\frac{\bar{\sigma}^n_{max}}{\sigma_y}\right) \tag{A.6}$$

where k is constant that typically ranges between 0.5 and 1.0 and σ_y is the macroscopic yield strength of the material. Finally, the per-element FIP values are averaged over a region of elements (e.g., 2x2x2, 3x3x3, etc.) with periodicity included in the averaging scheme. These values have been compared with volume-averaging of the stress and

plastic strain tensors to then calculate a volume-averaged FIP value and both methods have been found to be equivalent. It is advantageous to calculate the FIPs on a per-element basis for the simplication of the post-processing algorithm.

APPENDIX B

THE USE OF DREAM.3D FOR MICROSTRUCTURE GENERATION

Dream.3D version 6.2.63-Win64 (released Dec 2015) was used to generate all microstructures simulated and used in this dissertation [252]. A total of 4,000 statistical volume elements (SVEs) were generated, 500 SVEs for each of the eight textures.

The first step in using Dream.3D is to generate the microstructure statistics that are used when creating the synthetic microstructure. In this dissertation, grain size distribution and texture information were provided to StatsGenerator [252]. The same grain size distribution was used for all textures. Due to a lack of a EBSD data, the input textures were generated manually using the ODF feature within StatsGenerator. Each of those textures are shown below, along with the input Euler angles, weights, and sigma values.

With the relevant microstructure statistics now saved in the proper file format by Dream.3D, the following *pipeline* is used in Dream.3D to generate the synthetic microstructures. The pipeline is shown in Figure B.2. The resultant microstructures have 21^3 elements with a cube sidelength of 210 μm.

Note that Dream.3D will output Abaqus nodes, elements, and element sets, but it is up to the user to extract the grain IDs and associated Euler angles from the "Features Data" and then use that information to either rotate the elastic stiffness tensor or be used as input for a material model.

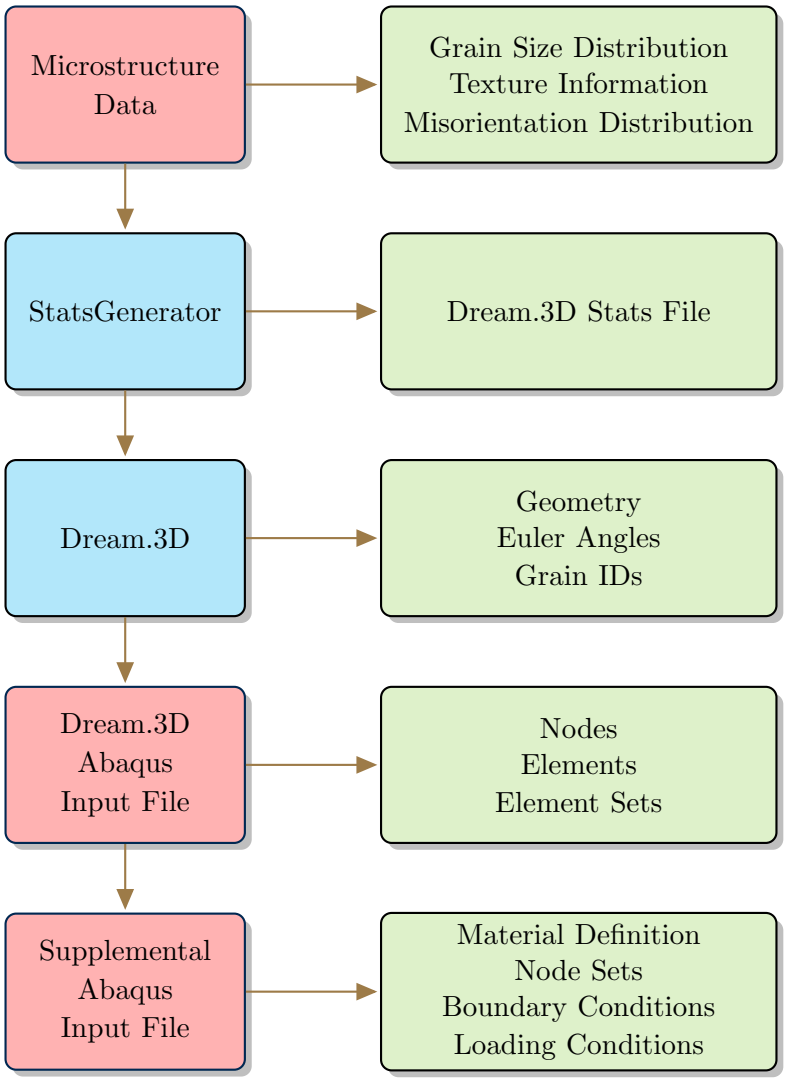

Figure B.1: Flowchart for the generation Dream.3D microstructures used in Abaqus.

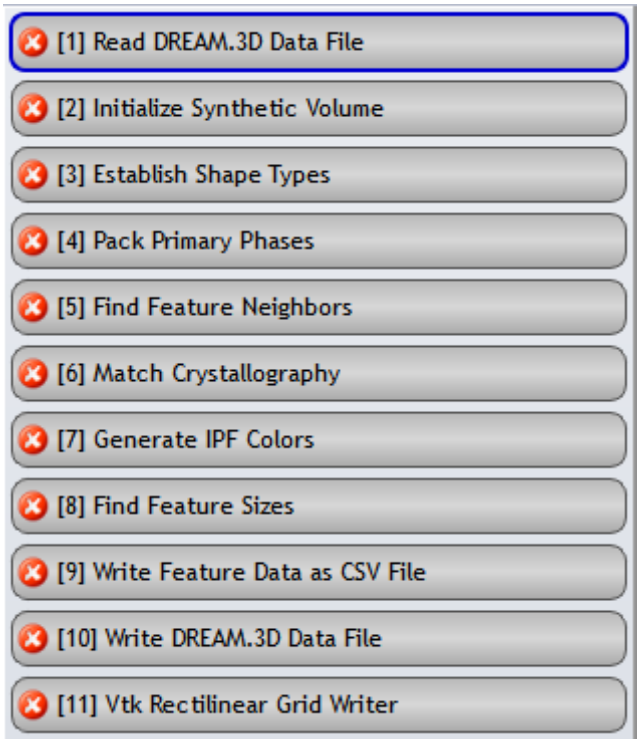

Figure B.2: The Dream.3D pipeline used through this dissertation.

B.1 StatGenerator Inputs and Resultant Pole Figures

Table B.1: Input values for StatsGenerator and Dream.3D for the β-annealed texture

Euler 1 (ϕ_1)	Euler 2 (Φ)	Euler 3 (ϕ_2)	Weight	Sigma
0	0	0	1500	5
-20	60	0	1500	3
160	60	0	1500	3
50	60	0	750	3
230	60	0	750	3
110	90	0	750	3

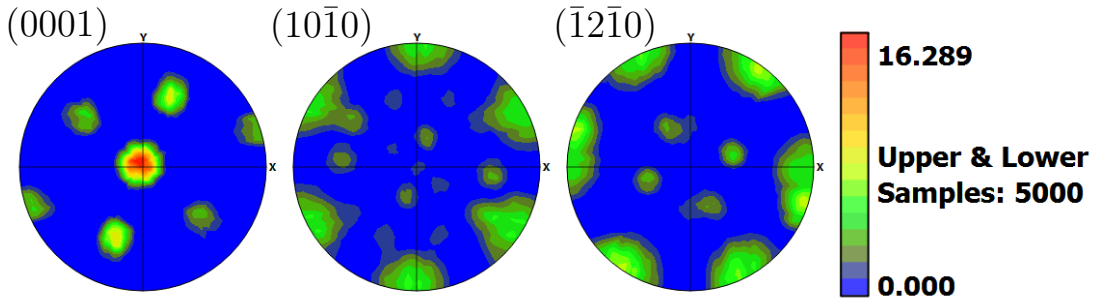

Figure B.3: Pole figure generated by StatsGenerator that depicts the β-annealed texture used as an input for Dream.3D.

Table B.2: Input values for StatsGenerator and Dream.3D for the basal/transverse texture

Euler 1 (ϕ_1)	Euler 2 (Φ)	Euler 3 (ϕ_2)	Weight	Sigma
0	0	0	30	8
91	91	0	25	5
91	89	0	25	5
89	91	0	25	5
89	89	0	25	5

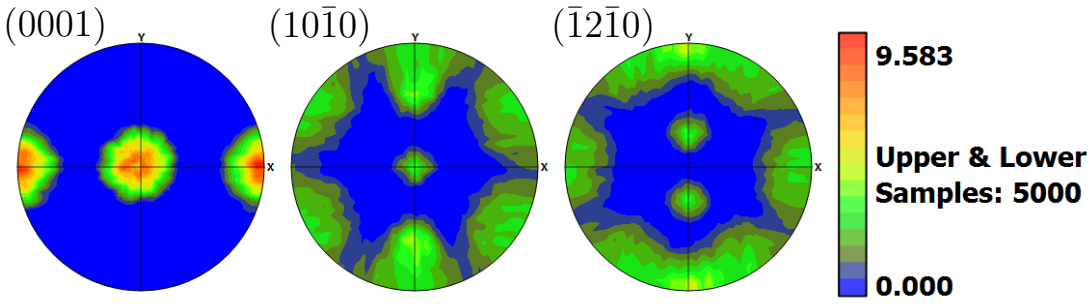

Figure B.4: Pole figure generated by StatsGenerator that depicts the basal/transverse texture used as an input for Dream.3D.

Table B.3: Input values for StatsGenerator and Dream.3D for the dice texture

Euler 1 (ϕ_1)	Euler 2 (Φ)	Euler 3 (ϕ_2)	Weight	Sigma
91	91	0	75	3
91	89	0	75	3
89	91	0	75	3
89	89	0	75	3
179	91	0	75	3
179	89	0	75	3
181	91	0	75	3
181	89	0	75	3
45	45	0	125	4
45	135	0	125	4
135	45	0	125	4
135	135	0	125	4

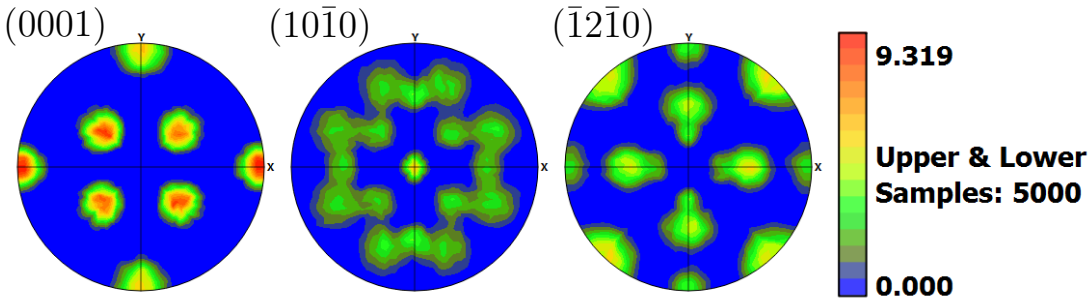

Figure B.5: Pole figure generated by StatsGenerator that depicts the dice texture used as an input for Dream.3D.

Table B.4: Input values for StatsGenerator and Dream.3D for the double donut texture

Euler 1 (ϕ_1)	Euler 2 (Φ)	Euler 3 (ϕ_2)	Weight	Sigma
0	90	0	100	4
15	90	0	100	4
30	90	0	100	4
...	...	...	...	...
330	90	0	100	4
345	90	0	100	4
360	91	0	100	4
0	30	0	100	4
15	30	0	100	4
30	30	0	100	4
...	...	...	...	...
330	30	0	100	4
345	30	0	100	4

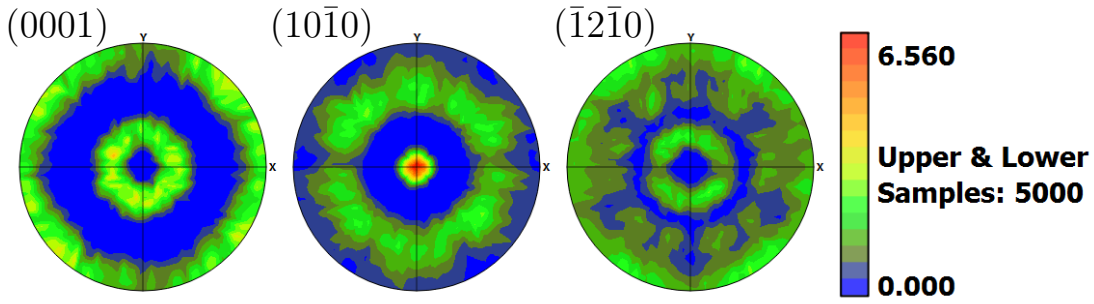

Figure B.6: Pole figure generated by StatsGenerator that depicts the double donut texture used as an input for Dream.3D.

Table B.5: Input values for StatsGenerator and Dream.3D for the inner donut texture

Euler 1 (ϕ_1)	Euler 2 (Φ)	Euler 3 (ϕ_2)	Weight	Sigma
0	30	0	100	3
15	30	0	100	3
30	30	0	100	3
...	...	...	...	...
330	30	0	100	3
345	30	0	100	3

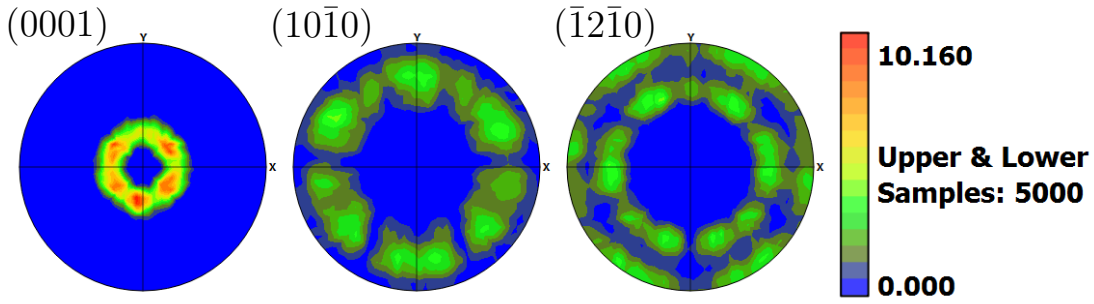

Figure B.7: Pole figure generated by StatsGenerator that depicts the inner donut texture used as an input for Dream.3D.

Table B.6: Input values for StatsGenerator and Dream.3D for the outer donut texture

Euler 1 (ϕ_1)	Euler 2 (Φ)	Euler 3 (ϕ_2)	Weight	Sigma
0	90	0	100	5
15	90	0	100	5
30	90	0	100	5
...	...	...	...	...
330	90	0	100	5
345	90	0	100	5
360	91	0	100	5

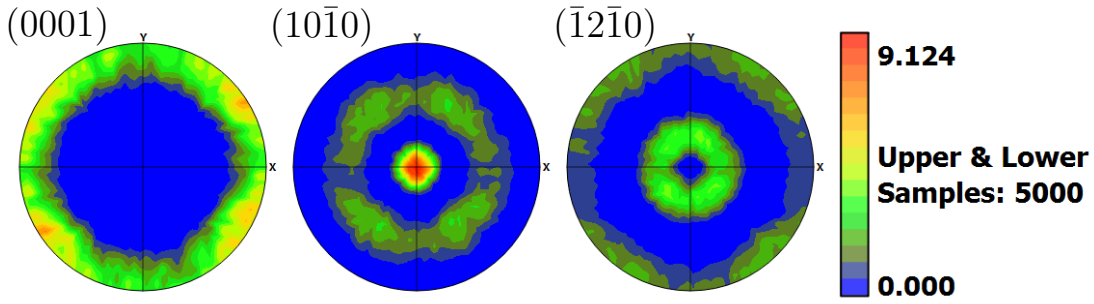

Figure B.8: Pole figure generated by StatsGenerator that depicts the outer donut texture used as an input for Dream.3D.

Table B.7: Input values for StatsGenerator and Dream.3D for the random texture

Euler 1 (ϕ_1)	Euler 2 (Φ)	Euler 3 (ϕ_2)	Weight	Sigma
0	0	0	0	1

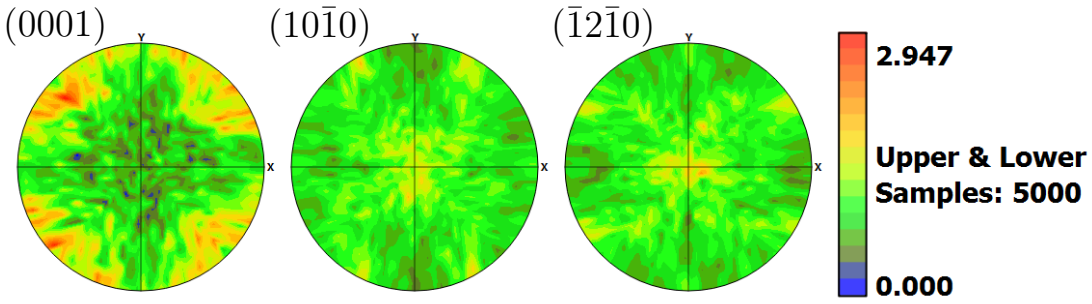

Figure B.9: Pole figure generated by StatsGenerator that depicts the random texture used as an input for Dream.3D.

Table B.8: Input values for StatsGenerator and Dream.3D for the transverse texture

Euler 1 (ϕ_1)	Euler 2 (Φ)	Euler 3 (ϕ_2)	Weight	Sigma
91	91	0	15	8
91	89	0	15	8
89	91	0	15	8
89	89	0	15	8

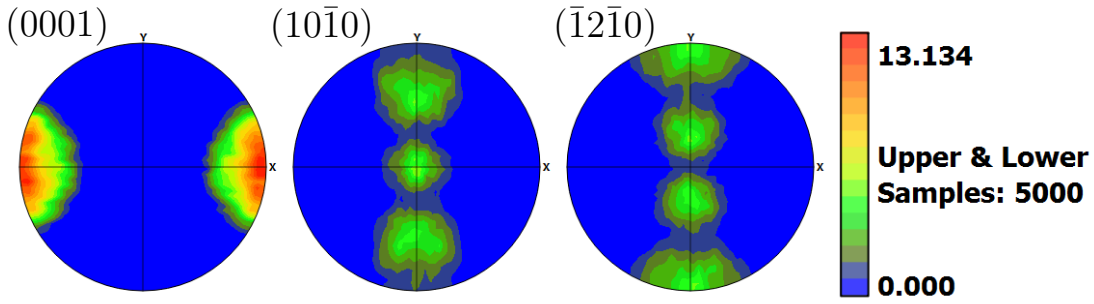

Figure B.10: Pole figure generated by StatsGenerator that depicts the transverse texture used as an input for Dream.3D.

APPENDIX C

MICROSTRUCTURE-SPECIFIC PLOTS

This appendix is a collection of plots that present various data for each of the eight textures simulated with MKS coupled with the explicit integration scheme or with CPFEM. The datasets are organized as follows:

- Elastic modulus values for 100 SVEs for each of the eight textures and three loading directions. CPFEM was used to generate this data.
- Yield strength values for 100 SVEs for each of the eight textures and three loading directions. CPFEM was used to generate this data.
- Fatemi-Socie FIP extreme value distribution for 500 SVEs for each of the eight textures and three loading directions. MKS coupled with the explicit integration routine was used to generated this data.

C.0.1 Elastic Modulus For Each Simulation

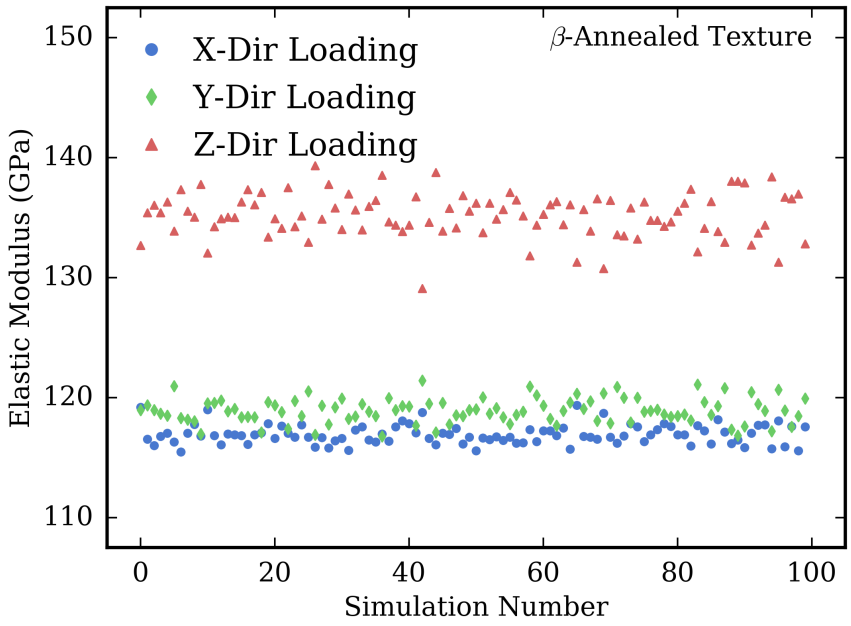

Figure C.1: The directional elastic modulus (E) of each of the 100 SVEs simulated with CPFEM for the β-annealed texture.

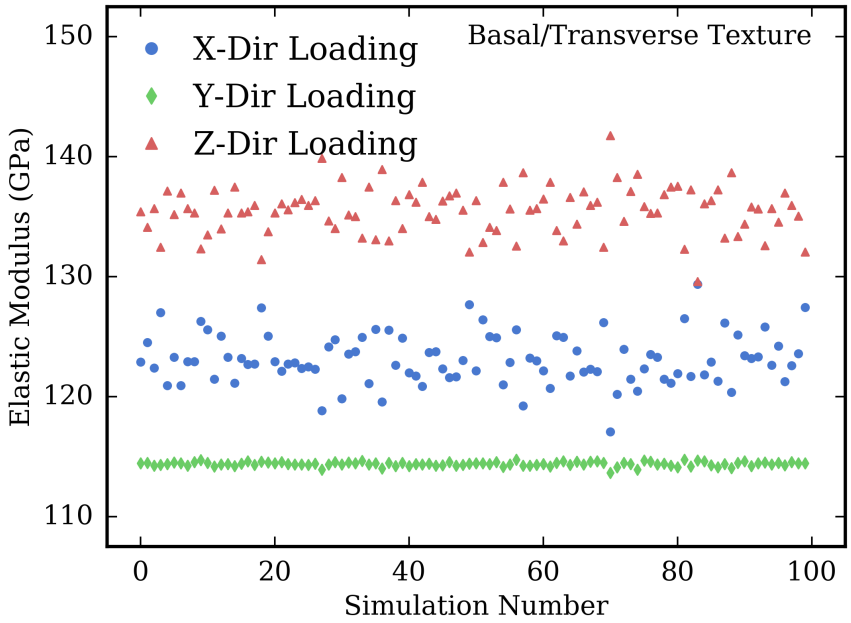

Figure C.2: The directional elastic modulus (E) of each of the 100 SVEs simulated with CPFEM for the basal/transverse texture.

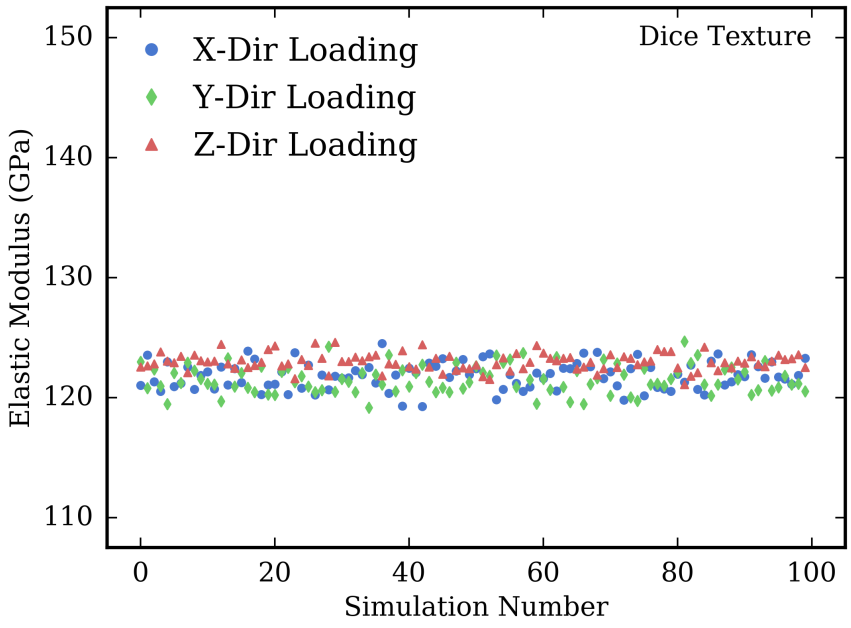

Figure C.3: The uniaxial tension yield strength (σ_y) of each of the 100 SVEs simulated with CPFEM for the dice texture.

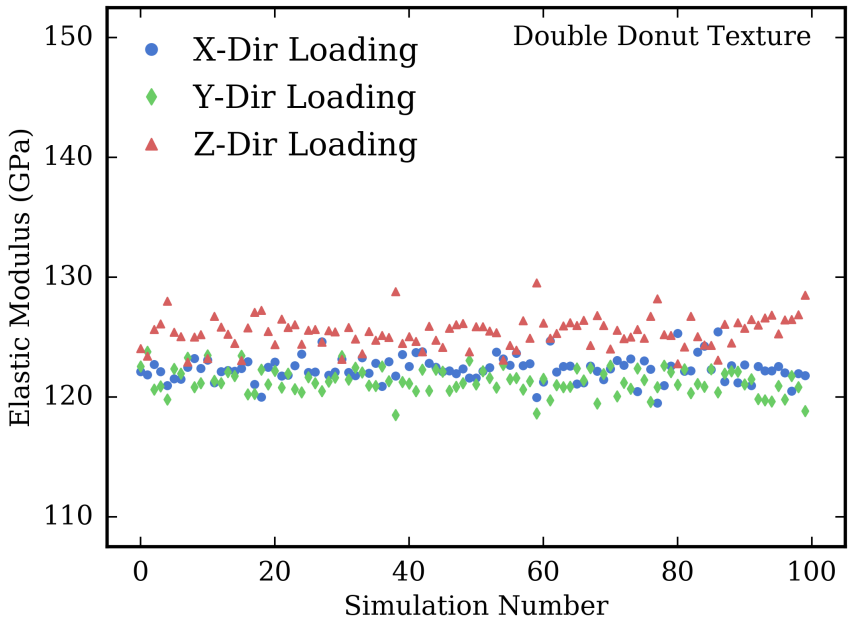

Figure C.4: The directional elastic modulus (E) of each of the 100 SVEs simulated with CPFEM for the double donut texture.

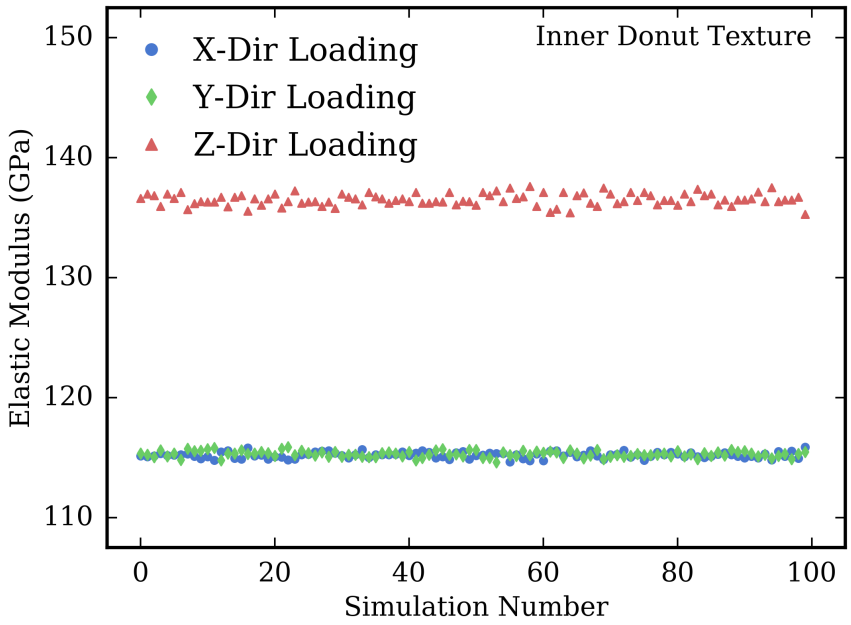

Figure C.5: The directional elastic modulus (E) of each of the 100 SVEs simulated with CPFEM for the inner donut texture.

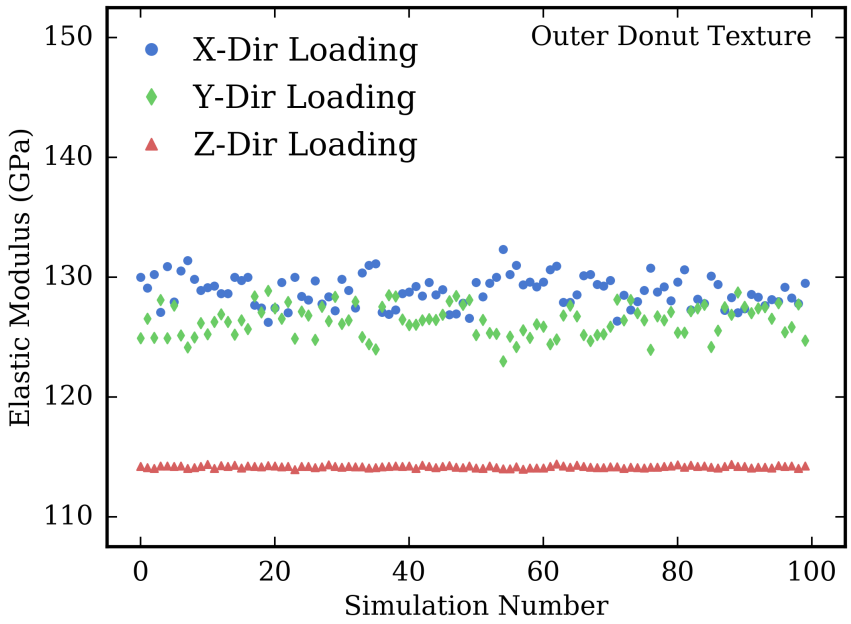

Figure C.6: The directional elastic modulus (E) of each of the 100 SVEs simulated with CPFEM for the outer donut texture.

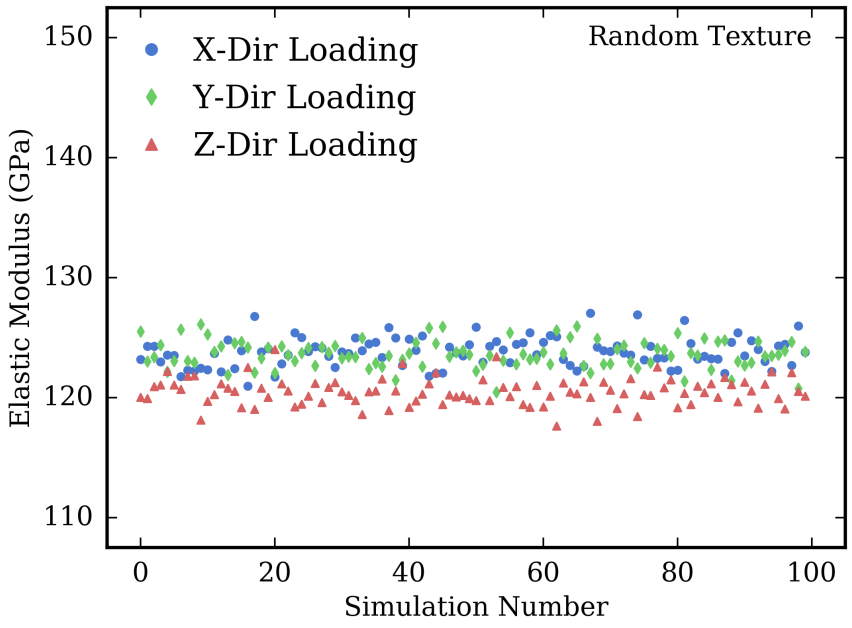

Figure C.7: The directional elastic modulus (E) of each of the 100 SVEs simulated with CPFEM for the random texture.

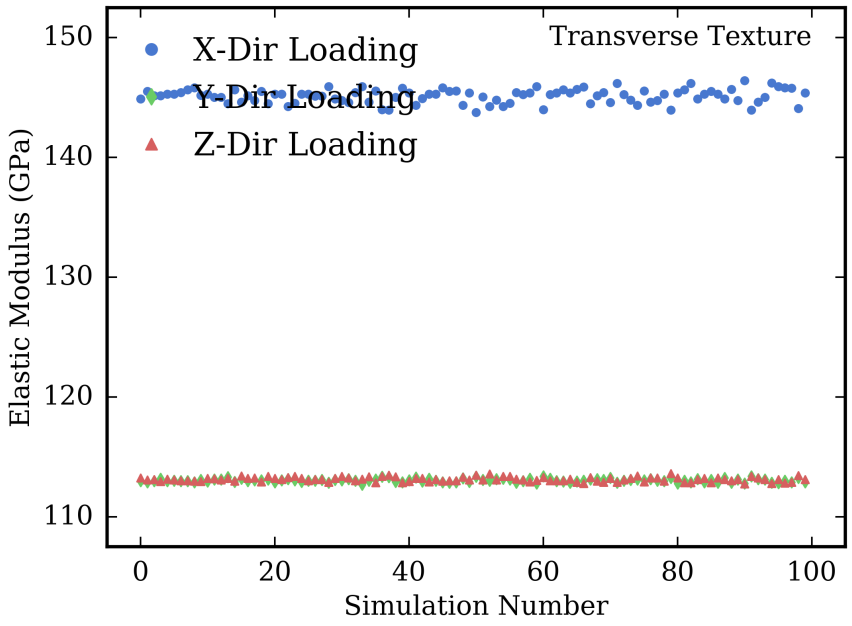

Figure C.8: The directional elastic modulus (E) of each of the 100 SVEs simulated with CPFEM for the transverse texture.

C.0.2 Yield Strength For Each Simulation

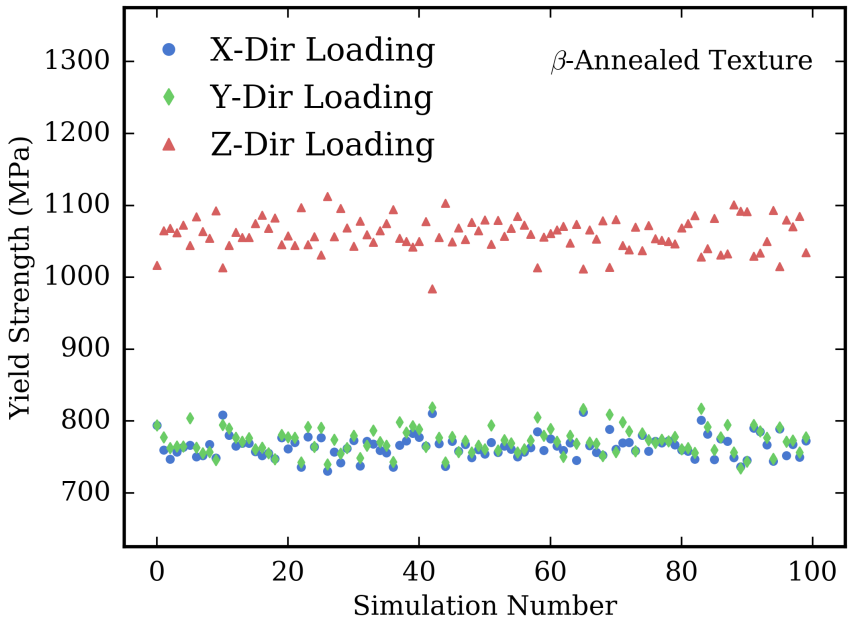

Figure C.9: The uniaxial tension yield strength (σ_y) of each of the 100 SVEs simulated with CPFEM for the β-annealed texture.

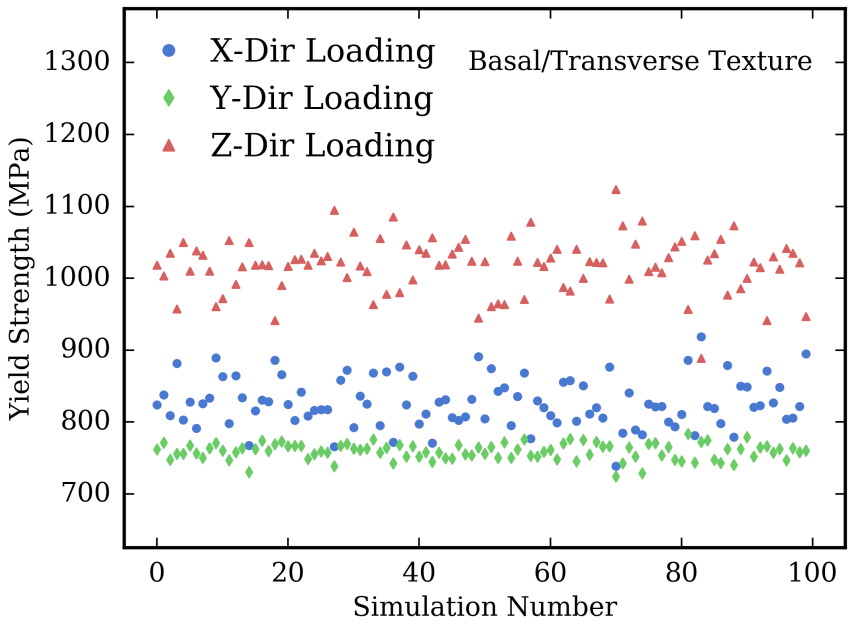

Figure C.10: The uniaxial tension yield strength (σ_y) of each of the 100 SVEs simulated with CPFEM for the basal/transverse texture.

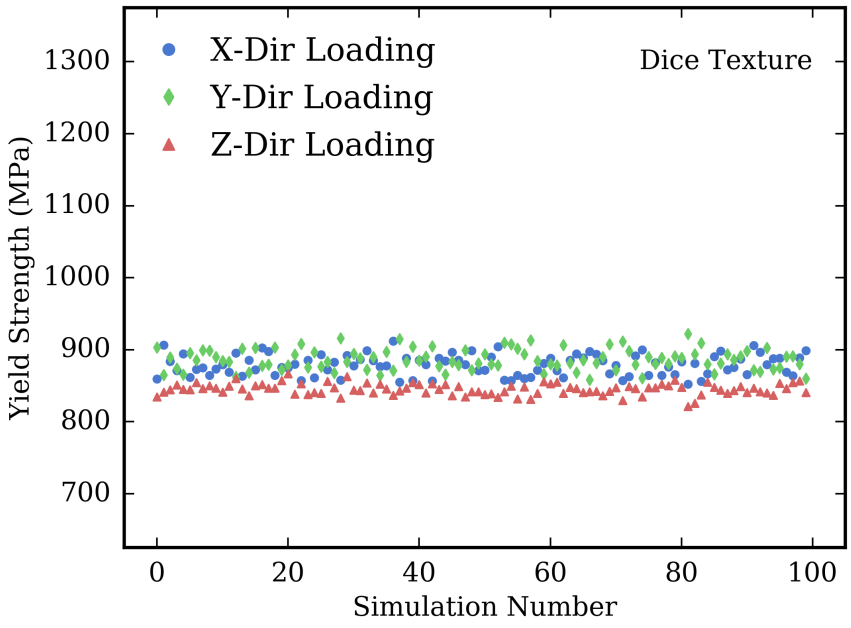

Figure C.11: The uniaxial tension yield strength (σ_y) of each of the 100 SVEs simulated with CPFEM for the dice texture.

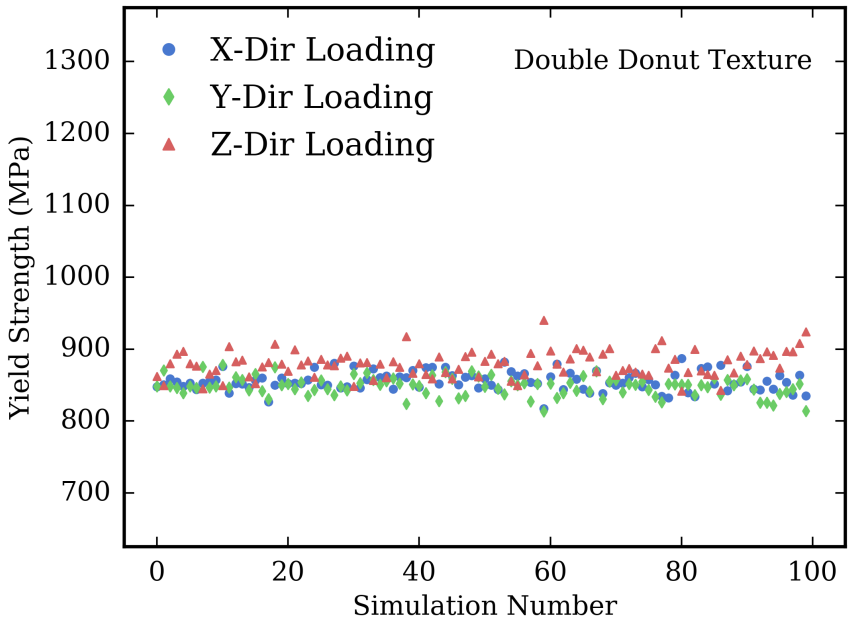

Figure C.12: The uniaxial tension yield strength (σ_y) of each of the 100 SVEs simulated with CPFEM for the double donut texture.

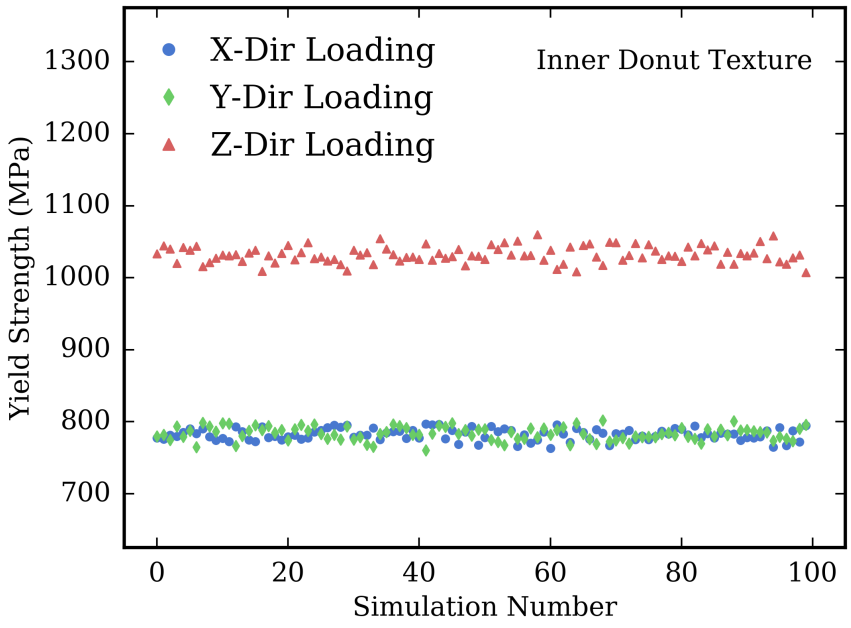

Figure C.13: The uniaxial tension yield strength (σ_y) of each of the 100 SVEs simulated with CPFEM for the inner donut texture.

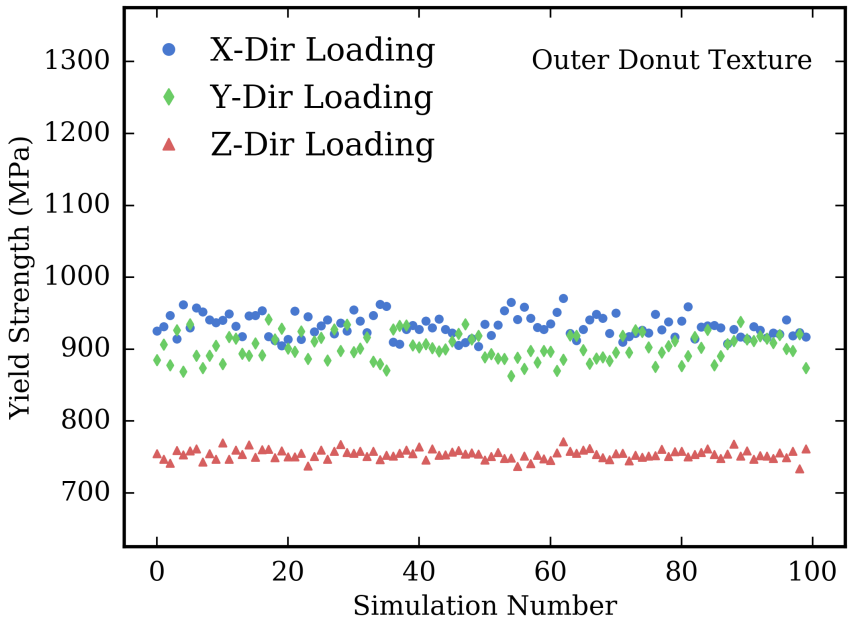

Figure C.14: The uniaxial tension yield strength (σ_y) of each of the 100 SVEs simulated with CPFEM for the outer donut texture.

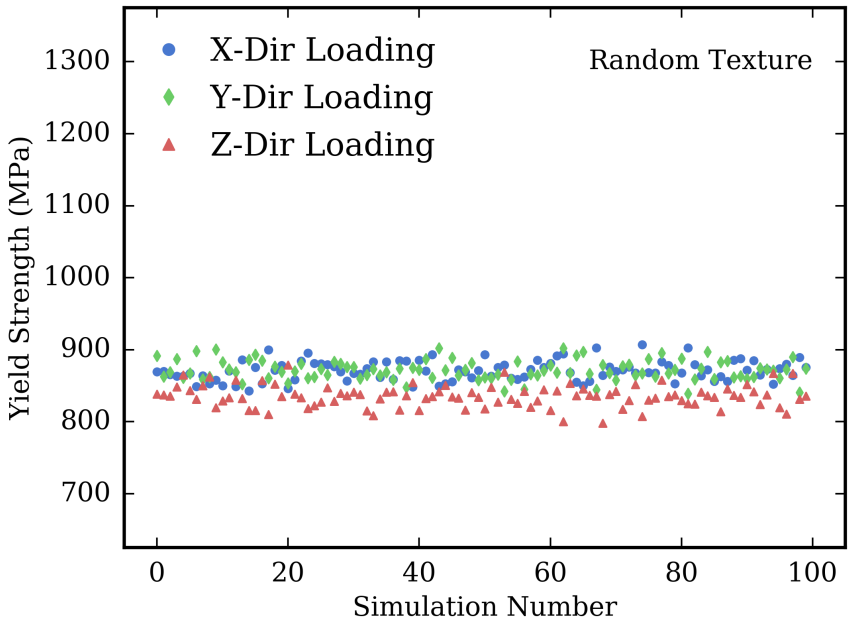

Figure C.15: The uniaxial tension yield strength (σ_y) of each of the 100 SVEs simulated with CPFEM for the random texture.

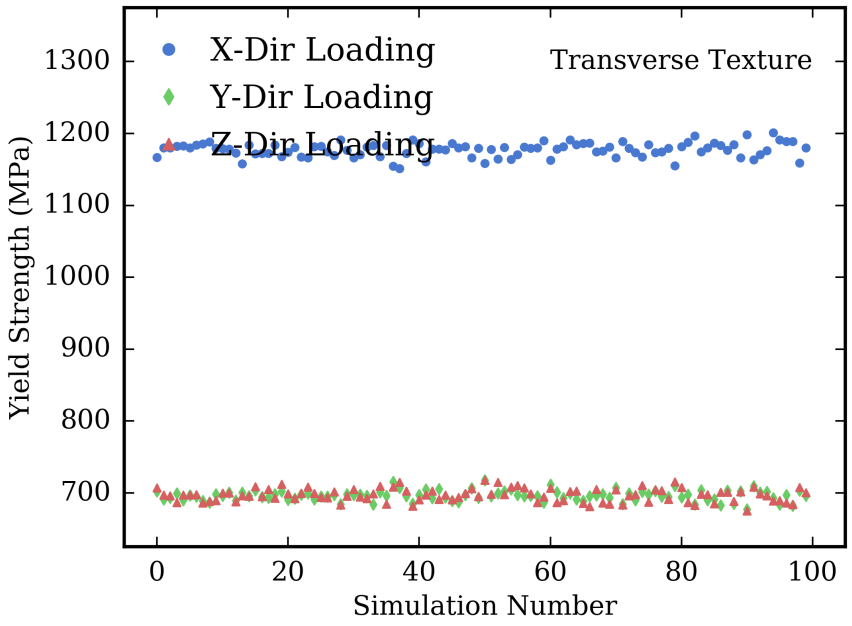

Figure C.16: The uniaxial tension yield strength (σ_y) of each of the 100 SVEs simulated with CPFEM for the transverse texture.

C.0.3 Fatemi-Socie FIP Distribution for Each Texture

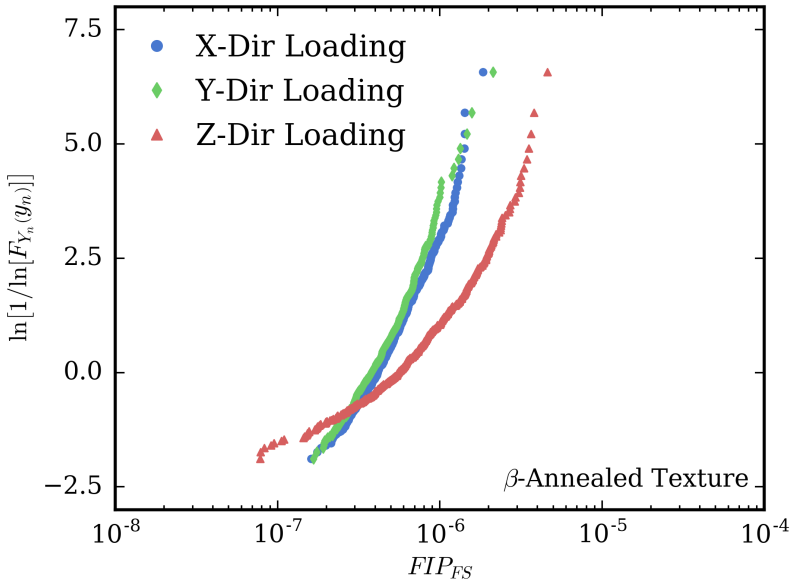

Figure C.17: The Fatemi-Socie FIP extreme value distribution (FIP_{FS}) of each of the 500 SVEs simulated with MKS coupled with the explicit integration scheme for the β-annealed texture.

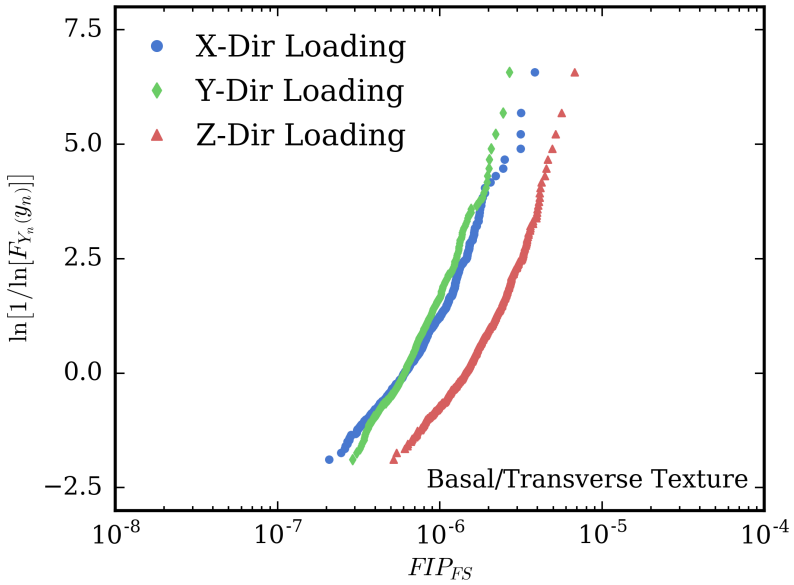

Figure C.18: The Fatemi-Socie FIP extreme value distribution (FIP_{FS}) of each of the 500 SVEs simulated with MKS coupled with the explicit integration scheme for the basal/transverse texture.

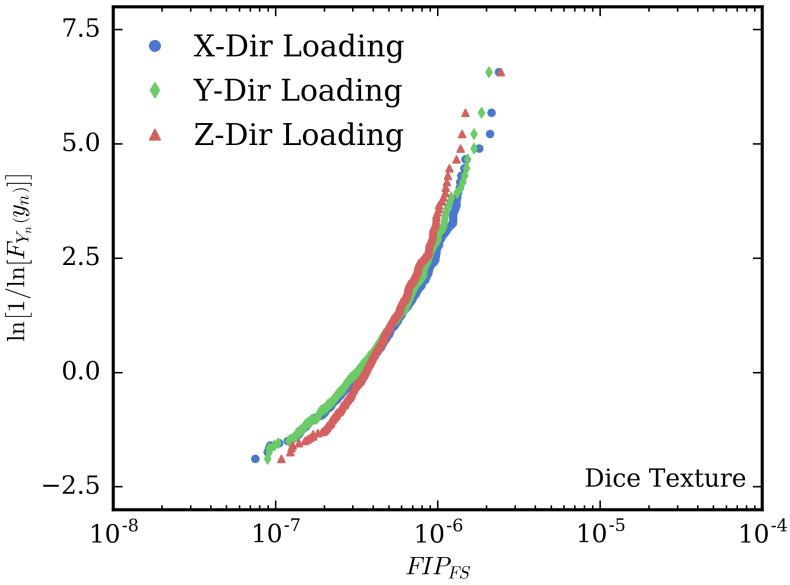

Figure C.19: The Fatemi-Socie FIP extreme value distribution (FIP_{FS}) of each of the 500 SVEs simulated with MKS coupled with the explicit integration scheme for the dice texture.

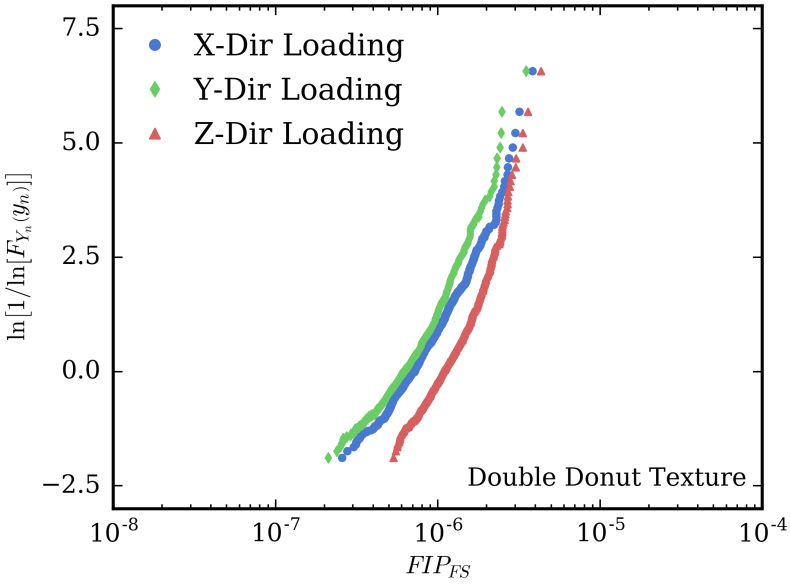

Figure C.20: The Fatemi-Socie FIP extreme value distribution (FIP_{FS}) of each of the 500 SVEs simulated with MKS coupled with the explicit integration scheme for the double donut texture.

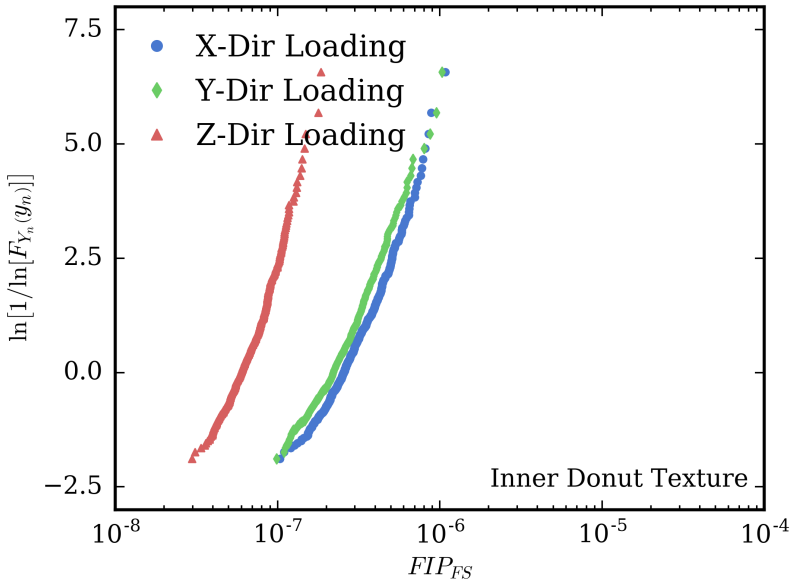

Figure C.21: The Fatemi-Socie FIP extreme value distribution (FIP_{FS}) of each of the 500 SVEs simulated with MKS coupled with the explicit integration scheme for the inner donut texture.

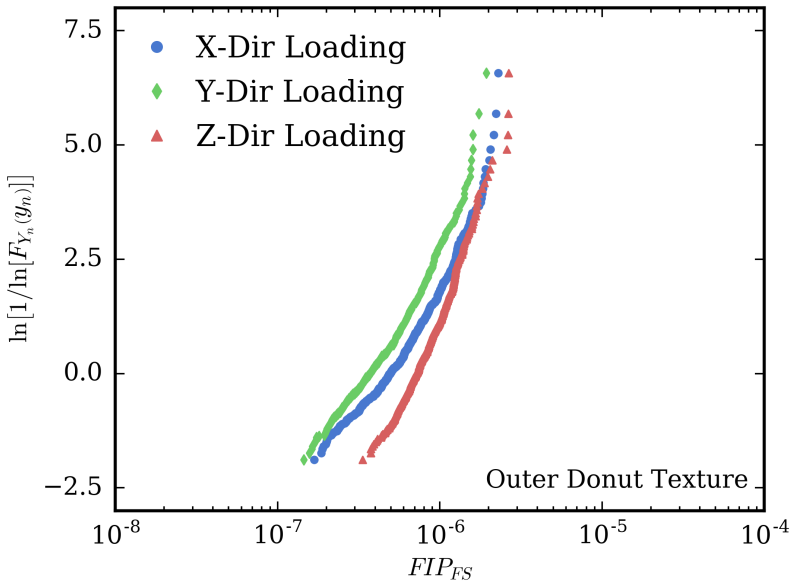

Figure C.22: The Fatemi-Socie FIP extreme value distribution (FIP_{FS}) of each of the 500 SVEs simulated with MKS coupled with the explicit integration scheme for the outer donut texture.

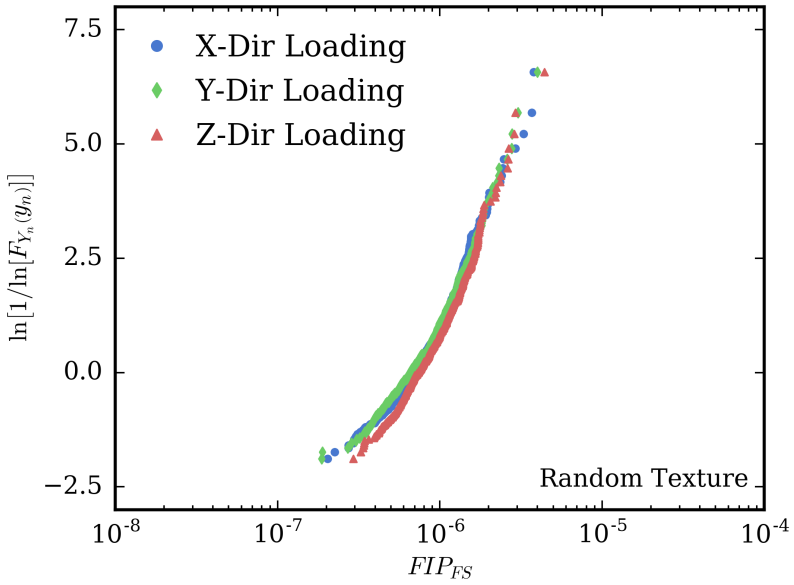

Figure C.23: The Fatemi-Socie FIP extreme value distribution (FIP_{FS}) of each of the 500 SVEs simulated with MKS coupled with the explicit integration scheme for the random texture.

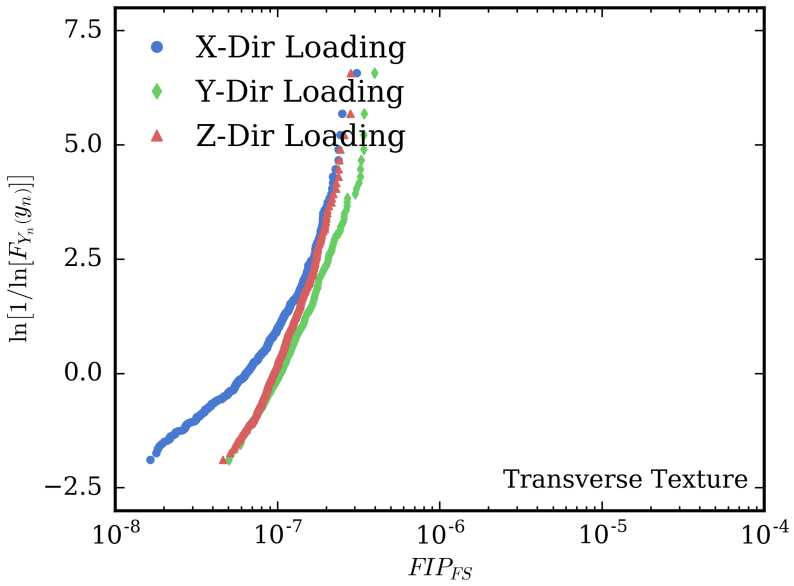

Figure C.24: The Fatemi-Socie FIP extreme value distribution (FIP_{FS}) of each of the 500 SVEs simulated with MKS coupled with the explicit integration scheme for the transverse texture.

REFERENCES

[1] Kalil, T. and Wadia, C., "Materials Genome Initiative for Global Competitiveness," *Committee on Technology National Science and Technology Council*, 2011.

[2] Hill, R., "Generalized constitutive relations for incremental deformation of metal crystals by multislip," *Journal of the Mechanics and Physics of Solids*, vol. 14, pp. 95–102, Mar. 1966.

[3] Lee, E. H., "Elastic-Plastic Deformation at Finite Strains," *Journal of Applied Mechanics*, vol. 36, pp. 1–6, Mar. 1969.

[4] Rice, J., "Inelastic constitutive relations for solids: An internal-variable theory and its application to metal plasticity," *Journal of the Mechanics and Physics of Solids*, vol. 19, pp. 433–455, Nov. 1971.

[5] Hill, R. and Rice, J., "Constitutive analysis of elastic-plastic crystals at arbitrary strain," *Journal of the Mechanics and Physics of Solids*, vol. 20, pp. 401–413, Dec. 1972.

[6] Asaro, R. J. and Rice, J., "Strain localization in ductile single crystals," *Journal of the Mechanics and Physics of Solids*, vol. 25, pp. 309–338, Oct. 1977.

[7] Hill, R. and Havner, K., "Perspectives in the mechanics of elastoplastic crystals," *Journal of the Mechanics and Physics of Solids*, vol. 30, pp. 5–22, Apr. 1982.

[8] Peirce, D., Asaro, R. J., and Needleman, A., "Material rate dependence and localized deformation in crystalline solids," *Acta Metallurgica*, vol. 31, no. 12, pp. 1951–1976, 1983.

[9] Asaro, R. J., "Crystal plasticity," *Journal of applied mechanics*, vol. 50, no. December 1983, pp. 921–934, 1983.

[10] Asaro, R. J., "Micromechanics of Crystals and Polycrystals," in *Advances in Applied Mechanics* (John, W. H. and Theodore, Y. W., eds.), vol. Volume 23, pp. 1–115, Elsevier, 1983.

[11] Needleman, A., Asaro, R. J., Lemonds, J., and Peirce, D., "Finite element analysis of crystalline solids," *Computer Methods in Applied Mechanics and Engineering*, vol. 52, pp. 689–708, Sept. 1985.

[12] Kalidindi, S. R., Bronkhorst, C., and Anand, L., "Crystallographic texture evolution in bulk deformation processing of FCC metals," *Journal of the Mechanics and Physics of Solids*, vol. 40, pp. 537–569, Jan. 1992.

[13] Roters, F., Eisenlohr, P., Hantcherli, L., Tjahjanto, D. D., Bieler, T. R., and Raabe, D., "Overview of constitutive laws, kinematics, homogenization and multiscale methods in crystal plasticity finite-element modeling: Theory, experiments, applications," *Acta Materialia*, vol. 58, no. 4, pp. 1152–1211, 2010.

[14] Fast, T., Niezgoda, S. R., and Kalidindi, S. R., "A new framework for computationally efficient structurestructure evolution linkages to facilitate high-fidelity scale bridging in multi-scale materials models," *Acta Materialia*, vol. 59, no. 2, pp. 699–707, 2011.

[15] Kalidindi, S. R., Niezgoda, S. R., Landi, G., Vachhani, S. J., and Fast, T., "A novel framework for building materials knowledge systems," *Computers, Materials & Continua*, vol. 17, no. 2, pp. 103–126, 2010.

[16] Landi, G. and Kalidindi, S. R., "Thermo-elastic localization relationships for multi-phase composites," *Computers, Materials, & Continua*, vol. 16, no. 3, pp. 273—-293, 2010.

[17] Landi, G., Niezgoda, S. R., and Kalidindi, S. R., "Multi-scale modeling of elastic response of three-dimensional voxel-based microstructure datasets using novel DFT-based knowledge systems," *Acta Materialia*, vol. 58, no. 7, pp. 2716–2725, 2010.

[18] Yabansu, Y. C., Patel, D. K., and Kalidindi, S. R., "Calibrated localization relationships for elastic response of polycrystalline aggregates," *Acta Materialia*, vol. 81, pp. 151–160, Dec. 2014.

[19] Adams, B. L., Kalidindi, S. R., and Fullwood, D. T., *Microstructure-sensitive design for performance*. Amsterdam: Butterworth-Heinemann, 2013.

[20] Yabansu, Y. C. and Kalidindi, S. R., "Representation and calibration of elastic localization kernels for a broad class of cubic polycrystals," *Acta Materialia*, vol. 94, pp. 26–35, Aug. 2015.

[21] Taguchi, G., *Taguchi on robust technology development : bringing quality engineering upstream*. New York: ASME Press, 1993.

[22] Chen, W., Allen, J. K., Tsui, K.-L., and Mistree, F., "A procedure for robust design: minimizing variations casued by noise factors and control factors," *Design*, vol. 118, pp. 478–485, 1996.

[23] Choi, H.-J., Austin, R., Allen, J. K., McDowell, D. L., Mistree, F., and Benson, D. J., "An approach for robust design of reactive power metal

mixtures based on non-deterministic micro-scale shock simulation," *Journal of Computer-Aided Materials Design*, vol. 12, no. 1, pp. 57–85, 2005.

[24] Choi, H.-J., McDowell, D. L., Allen, J. K., Rosen, D., and Mistree, F., "An Inductive Design Exploration Method for Robust Multiscale Materials Design," *Journal of Mechanical Design*, vol. 130, no. 3, p. 031402, 2008.

[25] McDowell, D. L., Panchal, J. H., and Choi, H.-J., *Integrated design of multiscale, multifunctional materials and products*. Burlington, MA; Oxford; Amsterdam; Boston; Paris: Butterworth-Heinemann ; Elsevier, 2009.

[26] Ellis, B. D., *Multiscale Modeling and Design of Ultra-High-Performance Concrete Multiscale Modeling and Design of Ultra-High-Performance Concrete*. PhD thesis, Georgia Institute of Technology, Atlanta, 2013.

[27] Bennett, V. and McDowell, D. L., "Cyclic crystal plasticity analyses of stationary, microstructurally small surface cracks in ductile single phase polycrystals," *Fatigue & Fracture of Engineering Materials & Structures*, vol. 25, pp. 677–693, July 2002.

[28] Bennett, V. and McDowell, D. L., "Polycrystal orientation distribution effects on microslip in high cycle fatigue," *International Journal of Fatigue*, vol. 25, no. 1, pp. 27–39, 2003.

[29] McDowell, D. L., "Simulation-based strategies for microstructure-sensitive fatigue modeling," *Materials Science and Engineering: A*, vol. 468-470, pp. 4–14, Nov. 2007.

[30] McDowell, D. L. and Dunne, F. P. E., "Microstructure-sensitive computational modeling of fatigue crack formation," *International Journal of Fatigue*, vol. 32, pp. 1521–1542, Sept. 2010.

[31] Castelluccio, G. M., Musinski, W. D., and McDowell, D. L., "Computational Micromechanics of Fatigue of Microstructures in the HCF-VHCF Regimes," *International Journal of Fatigue*, 2016.

[32] Ostoja-Starzewski, M., "Material spatial randomness: From statistical to representative volume element," *Probabilistic Engineering Mechanics*, vol. 21, pp. 112–132, Apr. 2006.

[33] Kröner, E., "Bounds for effective elastic moduli of disordered materials," *Journal of the Mechanics and Physics of Solids*, vol. 25, pp. 137–155, Apr. 1977.

[34] Kröner, E., "Modelling Small Deformations of Polycrystals," ch. Statistica, pp. 229–291, Dordrecht: Springer Netherlands, 1986.

[35] Binci, M., Fullwood, D. T., and Kalidindi, S. R., "A new spectral framework for establishing localization relationships for elastic behavior of composites and their calibration to finite-element models," *Acta Materialia*, vol. 56, pp. 2272–2282, June 2008.

[36] Fullwood, D. T., Niezgoda, S. R., and Kalidindi, S. R., "Microstructure reconstructions from 2-point statistics using phase-recovery algorithms," *Acta Materialia*, vol. 56, pp. 942–948, Mar. 2008.

[37] Michel, J., Moulinec, H., and Suquet, P., "Effective properties of composite materials with periodic microstructure: a computational approach," *Computer Methods in Applied Mechanics and Engineering*, vol. 172, pp. 109–143, Apr. 1999.

[38] Torquato, S., *Random heterogeneous materials: microstructure and macroscopic properties*. Springer Science & Business Media, 16 ed., 2013.

[39] Mayeur, J. R. and McDowell, D. L., "A three-dimensional crystal plasticity model for duplex Ti6Al4V," *International Journal of Plasticity*, vol. 23, no. 9, pp. 1457–1485, 2007.

[40] Zhang, M., Zhang, J., and McDowell, D. L., "Microstructure-based crystal plasticity modeling of cyclic deformation of Ti6Al4V," *International Journal of Plasticity*, vol. 23, no. 8, pp. 1328–1348, 2007.

[41] Bridier, F., McDowell, D. L., Villechaise, P., and Mendez, J., "Crystal plasticity modeling of slip activity in Ti6Al4V under high cycle fatigue loading," *International Journal of Plasticity*, vol. 25, no. 6, pp. 1066–1082, 2009.

[42] Przybyla, C. P. and McDowell, D. L., "Simulated microstructure-sensitive extreme value probabilities for high cycle fatigue of duplex Ti-6Al-4V," *International Journal of Plasticity*, vol. 27, no. 12, pp. 1871–1895, 2011.

[43] Smith, B. D., Shih, D. S., and McDowell, D. L., "Fatigue Hot Spot Simulation for Two Widmanstätten Titanium Microstructures," *International Journal of Fatigue*, 2013.

[44] Smith, B. D., Shih, D. S., and McDowell, D. L., "Cyclic Plasticity Experiments and Polycrystal Plasticity Modeling of Three Distinct Ti Alloy Microstructures," *International Journal of Plasticity*, 2013.

[45] Pathak, S., *Development and validation of a novel data analysis procedure for spherical nanoindentation*. PhD thesis, Drexel University, 2009.

[46] Vachhani, S. J., *Stored energy maps in deformed metals using spherical nanoindentation*. PhD thesis, Georgia Institute of Technology, 2014.

[47] Weaver, J. S., *Hierarchical and high throughput mechanical characterization of titanium alloys using spherical indentation stress-strain curves*. Thesis, Georgia Institute of Technology, 2015.

[48] Bieler, T. R., Eisenlohr, P., Zhang, C., Phukan, H. J., and Crimp, M. A., "Grain boundaries and interfaces in slip transfer," *Current Opinion in Solid State and Materials Science*, vol. 18, no. 4, pp. 212–226, 2014.

[49] Bieler, T. R., Eisenlohr, P., Roters, F., Kumar, D., Mason, D. E., Crimp, M. A., and Raabe, D., "The role of heterogeneous deformation on damage nucleation at grain boundaries in single phase metals," *International Journal of Plasticity*, vol. 25, no. 9, pp. 1655–1683, 2009.

[50] Smith, B. D., *Microstructure-sensitive plasticity and fatigue of three titanium alloy microstructures*. PhD thesis, Georgia Institute of Technology, Atlanta, 2013.

[51] Morrissey, R. J., McDowell, D. L., and Nicholas, T., "Microplasticity in HCF of Ti6Al4V," *International Journal of Fatigue*, vol. 23, pp. 55–64, 2001.

[52] Goh, C.-h., Wallace, J., Neu, R. W., and McDowell, D. L., "Polycrystal plasticity simulations of fretting fatigue," *International Journal of Fatigue*, vol. 23, pp. 423–435, 2001.

[53] Mayeur, J. R., *Three dimensional modeling of Ti-Al alloys with applications to attachment fatigue*. PhD thesis, Georgia Institute of Technology, Atlanta, 2004.

[54] Mayeur, J. R., McDowell, D. L., and Neu, R. W., "Crystal plasticity simulations of fretting of Ti-6Al-4V in partial slip regime considering effects of texture," *Computational Materials Science*, vol. 41, no. 3, pp. 356–365, 2008.

[55] Bridier, F., Villechaise, P., and Mendez, J., "Slip and fatigue crack formation processes in an α/β titanium alloy in relation to crystallographic texture on different scales," *Acta Materialia*, vol. 56, no. 15, pp. 3951–3962, 2008.

[56] Zhang, M., *Crystal plasticity modeling of Ti-6Al-4V and its application in cyclic and fretting fatigue analysis*. PhD thesis, Georgia Institute of Technology, Atlanta, 2008.

[57] Przybyla, C. P. and McDowell, D. L., "Microstructure-sensitive extreme value probabilities for high cycle fatigue of Ni-base superalloy IN100," *International Journal of Plasticity*, vol. 26, pp. 372–394, Mar. 2010.

[58] Kacher, J., Eftink, B., Cui, B., and Robertson, I. M., "Dislocation interactions with grain boundaries," *Current Opinion in Solid State and Materials Science*, June 2014.

[59] Bayerschen, E., McBride, A. T., Reddy, B. D., and Böhlke, T., "Review on slip transmission criteria in experiments and crystal plasticity models," *Journal of Materials Science*, vol. 51, no. 5, pp. 2243–2258, 2016.

[60] Lütjering, G. and Williams, J. C., *Titanium*. Engineering Materials and Processes, Springer, 2007.

[61] Boyer, R. R., "An overview on the use of titanium in the aerospace industry," *Materials Science and Engineering A*, vol. 213, no. 1-2, pp. 103–114, 1996.

[62] Boyer, R. R., Welsch, G., and Collings, E., "Materials properties handbook titanium alloys," 1994.

[63] Williams, J. C., Baggerly, R. G., and Paton, N. E., "Deformation behavior of HCP Ti-Al alloy single crystals," *Metallurgical and Materials Transactions a-Physical Metallurgy and Materials Science*, vol. 33, no. 3, pp. 837–850, 2002.

[64] Philippe, M., Bouzy, E., and Fundenberger, J.-J., "Textures and Anisotropy of Titanium Alloys," *Materials Science Forum*, vol. 273-275, pp. 511–522, 1998.

[65] Burgers, W., "On the process of transition of the cubic-body-centered modification into the hexagonal-close-packed modification of zirconium," *Physica*, pp. 561–586, 1934.

[66] Newkirk, J. and Geisler, A., "Crystallographic aspects of the beta to alpha transformation in titanium," *Acta Metallurgica*, vol. 1, pp. 370–374, 1953.

[67] Przybyla, C. P., *Microstructure-sensitive extreme value probabilities of fatigue in advanced engineering alloys*. PhD thesis, Georgia Institute of Technology, Atlanta, 2010.

[68] Peirce, D., Asaro, R. J., and Needleman, A., "An analysis of nonuniform and localized deformation in ductile single crystals," *Acta Metallurgica*, vol. 30, pp. 1087–1119, June 1982.

[69] Becker, R., Butler, J. F., Hu, H., and Lalli, L. A., "Analysis of an aluminum single crystal with unstable initial orientation (001) [110] in channel die compression," *Metallurgical Transactions A*, vol. 22, no. 1, pp. 45–58, 1991.

[70] Becker, R., "Analysis of texture evolution in channel die compressionI. Effects of grain interaction," *Acta Metallurgica et Materialia*, vol. 39, pp. 1211–1230, June 1991.

[71] Bilby, B. A., Gardner, L. R. T., and Stroh, A. N., "Continuous distributions of dislocations and the theory of plasticity," in *Proceedings of the Ninth International Congress on Applied Mechanics, Bruxelles*, vol. 8, pp. 35–44, 1957.

[72] Bunge, H.-J., "Zur darstellung allgemeiner texturen," *Zeitschrift fur metallkunde*, vol. 56, no. 12, p. 872, 1965.

[73] Bunge, H.-J., *Texture Analysis in Materials Science: Mathematical Methods*. Butterworth, 1982.

[74] Randle, V. and Engler, O., *Introduction to texture analysis: macrotexture, microtexture and orientation mapping*. CRC press, 2000.

[75] Conrad, H., "Thermally activated deformation of metals," *Journal of metals*, vol. 16, no. 7, pp. 582–588, 1964.

[76] Kocks, U. F., Argon, A. S., and Ashby, M. F., *Thermodynamics and Kinetics of Slip*, vol. 19. Oxford: Pergamon Press, 1975.

[77] Frost, H. J. and Ashby, M. F., *Deformation-mechanism maps: the plasticity and creep of metals and ceramics*. Pergamon Press, 1982.

[78] Argon, A. S., *Strengthening mechanisms in crystal plasticity*. Oxford University Press Oxford, 2008.

[79] Orowan, E., "Problems of plastic gliding," *Proceedings of the Physical Society*, vol. 52, no. 1, p. 8, 1940.

[80] Dorn, J. E. and Mitchell, J. B., "Slip mechanisms in single crystals of hexagonal close-packed phases," in *High-Strength Materials, Proceedings of the Second High-Strength Materials Berkeley International Materials Conference*, pp. 510–577, California. Univ., Berkeley. Lawrence Radiation Lab., 1964.

[81] Kothari, M. and Anand, L., "Elasto-viscoplastic constitutive equations for polycrystalline metals: Application to tantalum," *Journal of the Mechanics and Physics of Solids*, vol. 46, no. 1, pp. 51–67, 1998.

[82] Prager, W., "The Theory of Plasticity: A Survey of Recent Achievements," *Proceedings of the Institution of Mechanical Engineers*, vol. 169, no. 1, pp. 41–57, 1955.

[83] McDowell, D. L., "Multiaxial effects in metallic materials," *Durability and damage tolerance*, pp. 213–267, 1994.

[84] Meyers, M. A., *Dynamic behavior of materials*. John Wiley & Sons, 1994.

[85] Sen, I., Gopinath, K., Datta, R., and Ramamurty, U., "Fatigue in Ti6Al4VB alloys," *Acta Materialia*, vol. 58, pp. 6799–6809, Dec. 2010.

[86] Kim, J.-Y. and Rokhlin, S. I., "Determination of elastic constants of generally anisotropic inclined lamellar structure using line-focus acoustic microscopy.," *The Journal of the Acoustical Society of America*, vol. 126, pp. 2998–3007, Dec. 2009.

[87] Hibbett, Karlsson, and Sorensen, *ABAQUS/standard: User's Manual*. Hibbitt, Karlsson & Sorensen, 1 ed., 1998.

[88] McGinty, R. D. and McDowell, D. L., "Multiscale Polycrystal Plasticity," *Journal of Engineering Materials and Technology*, vol. 121, pp. 203–209, Apr. 1999.

[89] Cuitino, M. A. and Ortiz, M., "Computational modelling of single crystals," *Modelling and Simulation in Materials Science and Engineering*, vol. 1, no. 3, pp. 225–263, 1993.

[90] McGinty, R. D., *Multiscale representation of polycrystalline inelasticity*. PhD thesis, Georgia Institute of Technology, Atlanta, 2001.

[91] Ling, X., Horstemeyer, M. F., and Potirniche, G. P., "On the numerical implementation of 3D rate-dependent single crystal plasticity formulations," *International Journal for Numerical Methods in Engineering*, vol. 63, no. 4, pp. 548–568, 2005.

[92] Forsyth, P. J. E., "A two stage process of fatigue crack growth," in *Proceedings of the Crack Propagation Symposium*, vol. 1, pp. 76–94, 1961.

[93] Suresh, S., *Fatigue of materials*. Cambridge University Press, 1998.

[94] Miller, K. J., "Metal FatiguePast, Current and Future," *Proceedings of the Institution of Mechanical Engineers, Part C: Journal of Mechanical Engineering Science*, vol. 205, pp. 291–304, Sept. 1991.

[95] Miller, K. J., "Materials science perspective of metal fatigue resistance," *Materials Science and Technology*, vol. 9, pp. 453–462, July 2013.

[96] Wells, C. H. and Sullivan, C. P., "Low-cycle fatigue crack initiation in Ti-6Al-4V," tech. rep., Pratt and Whitney Aircraft, 1969.

[97] Eylon, D. and Pierce, C., "Effect of microstructure on notch fatigue properties of Ti-6Al-4V," *Metallurgical Transactions A*, vol. 7, no. January, pp. 111–121, 1976.

[98] Bridier, F., Villechaise, P., and Mendez, J., "Analyis of slip and crack initiation processes activated by fatigue in a α/β titanium alloy in relation with local crystallographic orientation," in *9th International Fatigue Congress, Atlanta, GA*, 2006.

[99] Bache, M., Evans, W., Suddell, B., and Herrouin, F., "The effects of texture in titanium alloys for engineering components under fatigue," *International Journal of Fatigue*, vol. 23, pp. 153–159, 2001.

[100] Bache, M. and Evans, W., "Impact of texture on mechanical properties in an advanced titanium alloy," *Materials Science and Engineering: A*, vol. 319, pp. 409–414, 2001.

[101] Mahajan, Y. and Margolin, H., "Low Cycle Fatigue Behavior of Ti-6AI-2Sn-4Zr-6Mo: Part I. The Role of Microstructure in Low Cycle Crack Nucleation and Early Crack Growth," *Metallurgical Transactions A*, vol. 13, no. 2, pp. 257–268, 1982.

[102] Jha, S. K. and Larsen, J. M., "Random heterogeneity scales and probabilistic description of the long-lifetime regime of fatigue," in *Fourth International Conference on Very High Cycle Fatigue (VHCF-4)*, pp. 385–396, Ann Arbor, Michigan, USA: The Minerals, Metals and Materials Society (TMS), 2007.

[103] Szczepanski, C. J., Jha, S. K., Larsen, J. M., and Jones, J. W., "Microstructural Influences on Very-High-Cycle Fatigue-Crack Initiation in Ti-6246," *Metallurgical and Materials Transactions A*, vol. 39, no. 12, pp. 2841–2851, 2008.

[104] Jha, S. K. and Caton, M., "A new paradigm of fatigue variability behavior and implications for life prediction," *Materials Science and Engineering: A*, vol. 468, pp. 23–32, 2007.

[105] Hall, J., "Fatigue crack initiation in alpha-beta titanium alloys," *International Journal of Fatigue*, vol. 19, no. 93, pp. 23–37, 1997.

[106] McDowell, D. L., "A perspective on trends in multiscale plasticity," *International Journal of Plasticity*, vol. 26, no. 9, pp. 1280–1309, 2010.

[107] Fatemi, A. and Socie, D. F., "Critical Plane Approach To Multiaxial Fatigue Damage Including Out-of-Phase Loading.," *Fatigue and Fracture of Engineering Materials and Structures*, vol. 11, no. 3, pp. 149–165, 1988.

[108] Fatemi, A. and Kurath, P., "Multiaxial Fatigue Life Predictions Under the Influence of Mean-Stresses," *Journal of Engineering Materials and Technology*, vol. 110, no. 4, p. 380, 1988.

[109] Shenoy, M. M., Zhang, J., and McDowell, D. L., "Estimating fatigue sensitivity to polycrystalline Ni-base superalloy microstructures using a computational approach," *Fatigue & Fracture of Engineering Materials and Structures*, vol. 30, pp. 889–904, Oct. 2007.

[110] Castelluccio, G. M. and McDowell, D. L., "Fatigue Life Prediction of Microstructures," in *Volume 8: Mechanics of Solids, Structures and Fluids*, vol. 8, pp. 45–53, ASME, Nov. 2012.

[111] Musinski, W. D. and McDowell, D. L., "Microstructure-sensitive probabilistic modeling of HCF crack initiation and early crack growth in Ni-base superalloy IN100 notched components," *International Journal of Fatigue*, vol. 37, pp. 41–53, Apr. 2012.

[112] Castillo, E., *Extreme value theory in engineering*. Elsevier, 2012.

[113] Haldar, A. and Mahadevan, S., *Probability, reliability, and statistical methods in engineering design*. John Wiley, 2000.

[114] Brinell, J. A., "Way of determining the hardness of bodies and some applications of the same," *Teknisk Tidskrift*, vol. 5, p. 69, 1900.

[115] Brinell, J. A., "2ième congres," *Internationale Métheodes dEssai, Paris*, 1900.

[116] Tabor, D., *The hardness of metals*, vol. 10. Oxford: Clarendon Press, 1951.

[117] Pathak, S. and Kalidindi, S. R., "Spherical nanoindentation stressstrain curves," *Materials Science and Engineering: R: Reports*, vol. 91, pp. 1–36, 2015.

[118] ASTM, "ASTM E10-12: Standard Test Method for Brinell Hardness of Metallic Materials," *Annual Book of ASTM Standards*, pp. 1–32, 2014.

[119] ASTM, "ASTM E384: Standard Test Method for Microindentation Hardness of Materials," *Annual Book of ASTM Standards*, pp. 1–42, 2016.

[120] Oliver, W. and Pharr, G. M., "An improved technique for determining hardness and elastic modulus using load and displacement sensing indentation experiments," *Journal of materials research*, vol. 7, no. 6, pp. 1564–1583, 1992.

[121] Fischer-Cripps, A. C., *Nanoindentation*. Springer Science & Business Media, 2011.

[122] Bhattacharya, A. and Nix, W. D., "Finite element simulation of indentation experiments," *International Journal of Solids and Structures*, vol. 24, no. 9, pp. 881–891, 1988.

[123] Giannakopoulos, A., Larsson, P.-L., and Vestergaard, R., "Analysis of Vickers indentation," *International Journal of Solids and Structures*, vol. 31, no. 19, pp. 2679–2708, 1994.

[124] Sánchez-Martín, R., Pérez-Prado, M. T., Segurado, J., Bohlen, J., Gutiérrez-Urrutia, I., Llorca, J., and Molina-Aldareguia, J. M., "Measuring the critical resolved shear stresses in Mg alloys by instrumented nanoindentation," *Acta Materialia*, vol. 71, pp. 283–292, June 2014.

[125] Casals, O. and Forest, S., "Finite element crystal plasticity analysis of spherical indentation in bulk single crystals and coatings," *Computational Materials Science*, vol. 45, pp. 774–782, May 2009.

[126] Sabnis, P. A., Forest, S., Arakere, N. K., and Yastrebov, V. A., "Crystal plasticity analysis of cylindrical indentation on a Ni-base single crystal superalloy," *International Journal of Plasticity*, vol. 51, pp. 200–217, Dec. 2013.

[127] Salehinia, I., Lawrence, S., and Bahr, D., "The effect of crystal orientation on the stochastic behavior of dislocation nucleation and multiplication during nanoindentation," *Acta Materialia*, vol. 61, pp. 1421–1431, Mar. 2013.

[128] Tucker, G. J. and Foiles, S. M., "Molecular dynamics simulations of rate-dependent grain growth during the surface indentation of nanocrystalline nickel," *Materials Science and Engineering: A*, vol. 571, pp. 207–214, June 2013.

[129] Kumar, N. N., Tewari, R., Durgaprasad, P., Dutta, B., and Dey, G., "Active slip systems in bcc iron during nanoindentation: A molecular dynamics study," *Computational Materials Science*, vol. 77, pp. 260–263, Sept. 2013.

[130] Verkhovtsev, A. V., Yakubovich, A. V., Sushko, G. B., Hanauske, M., and Solov'Yov, A. V., "Molecular dynamics simulations of the nanoindentation process of titanium crystal," *Computational Materials Science*, vol. 76, pp. 20–26, Aug. 2013.

[131] Xu, S., Che, R., Xiong, L., Chen, Y., and McDowell, D. L., "A quasistatic implementation of the concurrent atomistic-continuum method for FCC crystals," *International Journal of Plasticity*, vol. 72, pp. 91–126, 2015.

[132] Hertz, H., "Ueber die Berührung fester elastischer Körper," *Journal für die reine und angewandte Mathematik*, vol. 92, pp. 156–171, 1882.

[133] Hertz, H., *Miscellaneous papers*. London: Macmillan, 1896.

[134] Sneddon, I. N., "The relation between load and penetration in the axisymmetric boussinesq problem for a punch of arbitrary profile," *International Journal of Engineering Science*, vol. 3, no. 1, pp. 47–57, 1965.

[135] Johnson, K. L., *Contact mechanics*. Cambridge ; New York: Cambridge University Press, 1987.

[136] Kalidindi, S. R. and Pathak, S., "Determination of the effective zero-point and the extraction of spherical nanoindentation stressstrain curves," *Acta Materialia*, vol. 56, no. 14, pp. 3523–3532, 2008.

[137] Donohue, B. R., Ambrus, A., and Kalidindi, S. R., "Critical evaluation of the indentation data analyses methods for the extraction of isotropic uniaxial mechanical properties using finite element models," *Acta Materialia*, vol. 60, no. 9, pp. 3943–3952, 2012.

[138] Ambrus, A., Guétaz, L., Louchet, F., and Guichard, D., "Role of interphases in the deformation mechanisms of an α/β titanium alloy at 20 K," *Materials Science and Engineering: A*, vol. 319, pp. 404–408, 2001.

[139] Suri, S., Viswanathan, G. B., Neeraj, T., Hou, D.-H., and Mills, M. J., "Room temperature deformation and mechanisms of slip transmission in oriented single-colony crystals of an $\alpha/\ \beta$ titanium alloy," *Acta Materialia*, vol. 47, no. 3, pp. 1019–1034, 1999.

[140] Zherebtsov, S., Salishchev, G., and Lee Semiatin, S., "Loss of coherency of the alpha/beta interface boundary in titanium alloys during deformation," *Philosophical Magazine Letters*, vol. 90, pp. 903–914, Dec. 2010.

[141] Cabibbo, M., Zherebtsov, S., Mironov, S., and Salishchev, G., "Loss of coherency and interphase α/β angular deviation from the Burgers orientation relationship in a Ti6Al4V alloy compressed at 800C," *Journal of Materials Science*, vol. 48, pp. 1100–1110, Sept. 2012.

[142] Seal, J. R., Crimp, M. a., Bieler, T. R., and Boehlert, C. J., "Analysis of slip transfer and deformation behavior across the α/β interface in Ti5Al2.5Sn (wt.%) with an equiaxed microstructure," *Materials Science and Engineering: A*, vol. 552, pp. 61–68, Aug. 2012.

[143] Castany, P., Pettinari-sturmel, F., Crestou, J., Douin, J., and Coujou, A., "Experimental study of dislocation mobility in a Ti6Al4V alloy," *Acta Materialia*, vol. 55, pp. 6284–6291, Oct. 2007.

[144] Castany, P., Pettinari-sturmel, F., Douin, J., and Coujou, A., "Stress Gradient at the Interface in a Ti-6Al-4V Alloy," in *Ti-2007 Science and Technology: Proceedings of the 11th World Conference on Titanium*, pp. 1655–1658, 2007.

[145] He, D., Zhu, J., Zaefferer, S., and Raabe, D., "Effect of retained beta layer on slip transmission in Ti6Al2Zr1Mo1V near alpha titanium alloy during tensile deformation at room temperature," *Materials & Design*, vol. 56, pp. 937–942, Apr. 2014.

[146] Livingston, J. D. and Chalmers, B., "Multiple slip in bicrystal deformation," *Acta Metallurgica*, vol. 5, pp. 322–327, 1957.

[147] Shen, Z., Wagoner, R. H., and Clark, W. A. T., "Dislocation pile-up and grain boundary interactions in 304 stainless steel," *Scripta Metallurgica*, vol. 20, no. 6, pp. 921–926, 1986.

[148] Shen, Z., Wagoner, R. H., and Clark, W. A. T., "Dislocation and grain boundary interactions in metals," *Acta Metallurgica*, vol. 36, no. 12, pp. 3231–3242, 1988.

[149] Lee, T. C., Robertson, I. M., and Birnbaum, H. K., "Prediction of slip transfer mechanisms across grain boundaries," *Scripta Metallurgica*, vol. 23, no. c, pp. 799–803, 1989.

[150] Luster, J. and Morris, M., "Compatibility of deformation in two-phase Ti-Al alloys: Dependence on microstructure and orientation relationships," *Metallurgical and Materials Transactions A*, vol. 26, no. July, pp. 1745–1756, 1995.

[151] Ashmawi, W. M. and Zikry, M. A., "Prediction of Grain-Boundary Interfacial Mechanisms in Polycrystalline Materials," *Journal of Engineering Materials and Technology*, vol. 124, no. 1, p. 88, 2002.

[152] Lim, H., Lee, M., Kim, J., Adams, B. L., and Wagoner, R. H., "Simulation of polycrystal deformation with grain and grain boundary effects," *International Journal of Plasticity*, vol. 27, pp. 1328–1354, Sept. 2011.

[153] Gonzalez, D., Simonovski, I., Withers, P. J., and Quinta da Fonseca, J., "Modelling the effect of elastic and plastic anisotropies on stresses at grain boundaries," *International Journal of Plasticity*, vol. 61, pp. 49–63, Mar. 2014.

[154] Choi, Y., Groeber, M. A., Turner, T., Dimiduk, D. M., Woodward, C., Uchic, M. D., and Parthasarathy, T. A., "A crystal-plasticity FEM study on effects of simplified grain representation and mesh types on mesoscopic plasticity heterogeneities," *Materials Science and Engineering: A*, vol. 553, pp. 37–44, Sept. 2012.

[155] Selvarajou, B., Shin, J.-h., Ha, T. K., Choi, I.-s., and Joshi, S. P., "Orientation-dependent indentation response of magnesium single crystals: Modeling and experiments," *Acta Materialia*, vol. 81, pp. 358–376, 2014.

[156] Olson, G. B., "Computational Design of Hierarchically Structured Materials," *Science*, vol. 277, pp. 1237–1242, Aug. 1997.

[157] Sinha, A., Bera, N., Allen, J. K., Panchal, J. H., and Mistree, F., "Uncertainty Management in the Design of Multiscale Systems," *Journal of Mechanical Design*, vol. 135, no. 1, p. 011008, 2012.

[158] Jang, S., Park, Y., and Choi, H.-J., "Integrated design of aluminum foam processing parameters and sandwich panels under uncertainty," *Proceedings of the Institution of Mechanical Engineers, Part C: Journal of Mechanical Engineering Science*, vol. 0, no. 0, pp. 1–15, 2014.

[159] Slutsky, L. J. and Garland, C. W., "Elastic Constants of Magnesium from 4.2{\degree}K to 300{\degree}K," *Physical Review*, vol. 107, no. 4, pp. 972–976, 1957.

[160] Alers, G. and Neighbours, J. R., "The elastic constants of zinc between 4.2{\degree} and 670{\degree}K," *Journal of Physics and Chemistry of Solids*, vol. 7, pp. 58–64, Oct. 1958.

[161] Featherston, F. H. and Neighbours, J. R., "Elastic Constants of Tantalum, Tungsten, and Molybdenum," *Physical Review*, vol. 130, pp. 1324–1333, May 1963.

[162] Flowers, J., O'Brien, K., and McEleney, P., "Elastic constants of alpha-titanium single crystals at 25{\degree}C," *Journal of the Less Common Metals*, vol. 7, pp. 393–395, Nov. 1964.

[163] Epstein, S. and DeBretteville, A. P., "Elastic Constants of and Wave Propagation in Antimony and Bismuth," *Physical Review*, vol. 138, pp. A771–A779, May 1965.

[164] Markham, M., "Measurement of the elastic constants of fibre composites by ultrasonics," *Composites*, vol. 1, pp. 145–149, Dec. 1969.

[165] Van Buskirk, W. C., Cowin, S. C., and Ward, R. N., "Ultrasonic Measurement of Orthotropic Elastic Constants of Bovine Femoral Bone," *Journal of Biomechanical Engineering*, vol. 103, pp. 67–72, May 1981.

[166] Kushibiki, J.-i., Ohkubo, A., and Chubachi, N., *Acoustical Imaging*, ch. Material C, pp. 101–111. Boston, MA: Springer US, 1982.

[167] Turner, C. H., Rho, J., Takano, Y., Tsui, T. Y., and Pharr, G. M., "The elastic properties of trabecular and cortical bone tissues are similar: results from two microscopic measurement techniques," *Journal of Biomechanics*, vol. 32, pp. 437–441, Apr. 1999.

[168] Ghassemi-Armaki, H., Maass, R., Bhat, S., Sriram, S., Greer, J., and Kumar, K., "Deformation response of ferrite and martensite in a dual-phase steel," *Acta Materialia*, vol. 62, pp. 197–211, Jan. 2014.

[169] Oliver, W. and Pharr, G. M., "Measurement of hardness and elastic modulus by instrumented indentation: Advances in understanding and refinements to methodology," *Journal of Materials Research*, vol. 19, pp. 3–20, Mar. 2004.

[170] Nix, W. D. and Gao, H., "Indentation size effects in crystalline materials: A law for strain gradient plasticity," *Journal of the Mechanics and Physics of Solids*, vol. 46, pp. 411–425, Mar. 1998.

[171] Huang, Y., Zhang, F., Hwang, K., Nix, W. D., Pharr, G. M., and Feng, G., "A model of size effects in nano-indentation," *Journal of the Mechanics and Physics of Solids*, vol. 54, pp. 1668–1686, Aug. 2006.

[172] Swadener, J., George, E. P., and Pharr, G. M., "The correlation of the indentation size effect measured with indenters of various shapes," *Journal of the Mechanics and Physics of Solids*, vol. 50, pp. 681–694, Apr. 2002.

[173] Shim, S., Bei, H., George, E. P., and Pharr, G. M., "A different type of indentation size effect," *Scripta Materialia*, vol. 59, pp. 1095–1098, Nov. 2008.

[174] Pathak, S., Kalidindi, S. R., Courtland, H. W., Jepsen, K. J., and Goldman, H. M., "Improved analysis of bone nano-mechanical properties

using a novel nanoindentation technique," in *Journal of Bone and Mineral Research*, vol. 22, pp. S480–S480, AMER SOC BONE & MINERAL RES 2025 M ST, NW, STE 800, WASHINGTON, DC 20036-3309 USA, 2007.

[175] Pathak, S., Michler, J., Wasmer, K., and Kalidindi, S. R., "Studying grain boundary regions in polycrystalline materials using spherical nanoindentation and orientation imaging microscopy," *Journal of Materials Science*, vol. 47, no. 2, pp. 815–823, 2012.

[176] Kalidindi, S. R. and Vachhani, S. J., "Mechanical characterization of grain boundaries using nanoindentation," *Current Opinion in Solid State and Materials Science*, June 2014.

[177] Vachhani, S. J. and Kalidindi, S. R., "Grain-scale measurement of slip resistances in aluminum polycrystals using spherical nanoindentation," *Acta Materialia*, vol. 90, pp. 27–36, 2015.

[178] Willis, J., "Hertzian contact of anisotropic bodies," *Journal of the Mechanics and Physics of Solids*, vol. 14, pp. 163–176, 1966.

[179] Vlassak, J. J. and Nix, W. D., "Indentation modulus of elastically anisotropic half spaces," *Philosophical Magazine A*, vol. 67, no. 5, pp. 1045–1056, 1993.

[180] Vlassak, J. J. and Nix, W. D., "Measuring the elastic properties of anisotropic materials by means of indentation experiments," *Journal of the Mechanics and Physics of Solids*, vol. 42, no. 8, pp. 1223–1245, 1994.

[181] Swadener, J. and Pharr, G. M., "Indentation of elastically anisotropic half-spaces by cones and parabolae of revolution," *Philosophical Magazine A*, vol. 81, no. 1966, pp. 447–467, 2001.

[182] Vlassak, J. J., Ciavarella, M., Barber, J. R., and Wang, X., "The indentation modulus of elastically anisotropic materials for indenters of arbitrary shape," *Journal of the Mechanics and Physics of Solids*, vol. 51, no. 9, pp. 1701–1721, 2003.

[183] Gao, Y. F. and Pharr, G. M., "Multidimensional contact moduli of elastically anisotropic solids," *Scripta Materialia*, vol. 57, pp. 13–16, July 2007.

[184] Pathak, S., Shaffer, J., and Kalidindi, S. R., "Determination of an effective zero-point and extraction of indentation stressstrain curves without the continuous stiffness measurement signal," *Scripta Materialia*, vol. 60, pp. 439–442, Mar. 2009.

[185] Patel, D. K., Al-harbi, H. F., and Kalidindi, S. R., "Extracting single-crystal elastic constants from polycrystalline samples using spherical nanoindentation and orientation measurements," *Acta Materialia*, vol. 79, pp. 108–116, 2014.

[186] Weaver, J. S., Priddy, M. W., McDowell, D. L., and Kalidindi, S. R., "On capturing the grain-scale elastic and plastic anisotropy of alpha-Ti with spherical nanoindentation and elactron back-scattered diffraction," *Acta Materialia*.

[187] Herbert, E. G., Pharr, G. M., Oliver, W., Lucas, B., and Hay, J., "On the measurement of stressstrain curves by spherical indentation," *Thin Solid Films*, vol. 398-399, pp. 331–335, Nov. 2001.

[188] Basu, S., Moseson, A., and Barsoum, M. W., "On the determination of spherical nanoindentation stressstrain curves," *Journal of Materials Research*, vol. 21, pp. 2628–2637, Mar. 2006.

[189] Field, J. and Swain, M., "A simple predictive model for spherical indentation," *Journal of Materials Research*, vol. 8, pp. 297–306, Jan. 2011.

[190] Field, J. and Swain, M., "Determining the mechanical properties of small volumes of material from submicrometer spherical indentations," *Journal of Materials Research*, vol. 10, pp. 101–112, Mar. 2011.

[191] Fisher, E. S. and Renken, C. J., "Single-Crystal Elastic Moduli and the hcp bcc Transformation in Ti, Zr, and Hf," *Physical Review*, vol. 135, pp. A482–A494, July 1964.

[192] Simmons, G. and Wang, H., *Single crystal elastic constants and calculated aggregate properties: a handbook*. Cambridge, Mass.: M.I.T. Press, 2 ed., 1971.

[193] Zarkades, A. and Larson, F. R., "Elasticity of titanium sheet allots," tech. rep., 1970.

[194] Liu, Y., Wang, B., Yoshino, M., Roy, S., Lu, H., and Komanduri, R., "Combined numerical simulation and nanoindentation for determining mechanical properties of single crystal copper at mesoscale," *Journal of the Mechanics and Physics of Solids*, vol. 53, no. 12, pp. 2718–2741, 2005.

[195] Wang, Y., Raabe, D., Klüber, C., and Roters, F., "Orientation dependence of nanoindentation pile-up patterns and of nanoindentation microtextures in copper single crystals," *Acta Materialia*, vol. 52, no. 8, pp. 2229–2238, 2004.

[196] Gerday, a. F., Ben Bettaieb, M., Duchêne, L., Clément, N., Diarra, H., and Habraken, a. M., "Interests and limitations of nanoindentation for bulk multiphase material identification: Application to the β phase of Ti-5553," *Acta Materialia*, vol. 57, no. 17, pp. 5186–5195, 2009.

[197] Gerday, a. F., Ben Bettaieb, M., Duchêne, L., Clément, N., Diarra, H., and Habraken, a. M., "Material behavior of the hexagonal alpha phase of a titanium alloy identified from nanoindentation tests," *European Journal of Mechanics, A/Solids*, vol. 30, no. 3, pp. 248–255, 2011.

[198] Bucaille, J. L., Stauss, S., Felder, E., and Michler, J., "Determination of plastic properties of metals by instrumented indentation using different sharp indenters," *Acta Materialia*, vol. 51, no. 6, pp. 1663–1678, 2003.

[199] Sahoo, S. K., Sabat, R. K., Panda, S., Mishra, S. C., and Suwas, S., "Mechanical Property of Pure Magnesium: From Orientation Perspective Pertaining to Deviation from Basal Orientation," *Journal of Materials Engineering and Performance*, 2015.

[200] Ye, C., Chen, J., Xu, M., Wei, X., and Lu, H., "Multi-scale simulation of nanoindentation on cast Inconel 718 and NbC precipitate for mechanical properties prediction," *Materials Science and Engineering: A*, vol. 662, pp. 385–394, Apr. 2016.

[201] Fizanne-Michel, C., Cornen, M., Castany, P., Péron, I., and Gloriant, T., "Determination of hardness and elastic modulus inverse pole figures of a polycrystalline commercially pure titanium by coupling nanoindentation and EBSD techniques," *Materials Science and Engineering A*, vol. 613, pp. 159–162, 2014.

[202] Sánchez-Martín, R., Pérez-Prado, M. T., Segurado, J., and Molina-Aldareguia, J. M., "Effect of indentation size on the nucleation and propagation of tensile twinning in pure magnesium," *Acta Materialia*, vol. 93, pp. 114–128, 2015.

[203] Han, F., Tang, B., Kou, H., Li, J., and Feng, Y., "Experiments and crystal plasticity finite element simulations of nanoindentation on Ti6Al4V alloy," *Materials Science and Engineering: A*, vol. 625, pp. 28–35, 2015.

[204] Zambaldi, C., Yang, Y., Bieler, T. R., and Raabe, D., "Orientation informed nanoindentation of α-titanium: Indentation pileup in hexagonal metals deforming by prismatic slip," *Journal of Materials Research*, vol. 27, no. 01, pp. 356–367, 2012.

[205] Britton, T. B., Liang, H., Dunne, F. P. E., and Wilkinson, A. J., "The effect of crystal orientation on the indentation response of commercially pure titanium: experiments and simulations," *Proceedings of the Royal Society of London A: Mathematical, Physical and Engineering Sciences*, vol. 466, pp. 695–719, Jan. 2010.

[206] Panda, S., Sahoo, S. K., Dash, A., Bagwan, M., Kumar, G., Mishra, S. C., and Suwas, S., "Orientation dependent mechanical properties of commercially pure (cp) titanium," *Materials Characterization*, vol. 98, pp. 93–101, Dec. 2014.

[207] Chen, R., Yang, F., Imam, M. A., Feng, C., and Pao, P., "Microindentation of titanium: Dependence of plastic energy on the indentation depth and

time-dependent plastic deformation," *Journal of Materials Research*, vol. 23, no. 04, pp. 1068–1075, 2008.

[208] Jun, T.-S., Armstrong, D. E., and Britton, T. B., "A nanoindentation investigation of local strain rate sensitivity in dual-phase Ti alloys," *Journal of Alloys and Compounds*, vol. 672, pp. 282–291, July 2016.

[209] Bettess, P., "Infinite elements," *International Journal for numerical methods in engineering*, vol. 11, no. 1, pp. 53–64, 1977.

[210] Beer, G. and Meek, J. L., "Infinite domain elements," *International Journal for Numerical Methods in Engineering*, vol. 17, no. 1, pp. 43–52, 1981.

[211] Zienkiewicz, O. C., Emson, C., and Bettess, P., "A novel boundary infinite element," *International Journal for Numerical Methods in Engineering*, vol. 19, no. 3, pp. 393–404, 1983.

[212] Jing, L., "A review of techniques, advances and outstanding issues in numerical modelling for rock mechanics and rock engineering," *International Journal of Rock Mechanics and Mining Sciences*, vol. 40, pp. 283–353, Apr. 2003.

[213] Kouroussis, G., Van Parys, L., Conti, C., and Verlinden, O., "Using three-dimensional finite element analysis in time domain to model railway-induced ground vibrations," *Advances in Engineering Software*, vol. 70, pp. 63–76, Apr. 2014.

[214] Van Rossum, G. and Drake Jr, F. L., *Python reference manual*. Centrum voor Wiskunde en Informatica Amsterdam, 1995.

[215] van der Walt, S., Colbert, S. C., and Varoquaux, G., "The NumPy Array: A Structure for Efficient Numerical Computation," *Computing in Science & Engineering*, vol. 13, no. 2, pp. 22–30, 2011.

[216] Jones, E., Oliphant, T., and Peterson, P., "SciPy: Open source scientific tools for Python."

[217] Pedregosa, F., Varoquaux, G., Gramfort, A., Michel, V., Thirion, B., Grisel, O., Blondel, M., Prettenhofer, P., Weiss, R., Dubourg, V., Vanderplas, J., Passos, A., Cournapeau, D., Brucher, M., Perrot, M., and Duchesnay, E., "Scikit-learn: Machine Learning in Python," *J. Mach. Learn. Res.*, vol. 12, pp. 2825–2830, Nov. 2011.

[218] Jäger, A., Hofstetter, K., Buksnowitz, C., Gindl-Altmutter, W., and Konnerth, J., "Identification of stiffness tensor components of wood cell walls by means of nanoindentation," *Composites Part A: Applied Science and Manufacturing*, vol. 42, pp. 2101–2109, Dec. 2011.

[219] Beck, J. and Au, S., "Bayesian Updating of Structural Models and Reliability using Markov Chain Monte Carlo Simulation," *Journal of Engineering Mechanics*, vol. 128, pp. 380–391, Apr. 2002.

[220] Beck, J. and Yuen, K., "Model Selection Using Response Measurements: Bayesian Probabilistic Approach," *Journal of Engineering Mechanics*, vol. 130, pp. 192–203, Jan. 2004.

[221] Oden, J. T., Hawkins, A., and Prudhomme, S., "General diffuse-interface theories and an approach to predictive tumor growth modeling," *Mathematical Models and Methods in Applied Sciences*, vol. 20, pp. 477–517, Mar. 2010.

[222] Yuen, K.-V., *Bayesian methods for structural dynamics and civil engineering*. John Wiley & Sons, 2010.

[223] Cheung, S. H., Oliver, T. A., Prudencio, E. E., Prudhomme, S., and Moser, R. D., "Bayesian uncertainty analysis with applications to turbulence modeling," *Reliability Engineering & System Safety*, vol. 96, pp. 1137–1149, Sept. 2011.

[224] Ma, X. and Zabaras, N., "A stochastic mixed finite element heterogeneous multiscale method for flow in porous media," *Journal of Computational Physics*, vol. 230, pp. 4696–4722, June 2011.

[225] Hadjidoukas, P., Angelikopoulos, P., Rossinelli, D., Alexeev, D., Papadimitriou, C., and Koumoutsakos, P., "Bayesian uncertainty quantification and propagation for discrete element simulations of granular materials," *Computer Methods in Applied Mechanics and Engineering*, vol. 282, pp. 218–238, Dec. 2014.

[226] Madireddy, S., Sista, B., and Vemaganti, K., "A Bayesian approach to selecting hyperelastic constitutive models of soft tissue," *Computer Methods in Applied Mechanics and Engineering*, vol. 291, pp. 102–122, July 2015.

[227] Madireddy, S., Sista, B., and Vemaganti, K., "Bayesian calibration of hyperelastic constitutive models of soft tissue.," *Journal of the mechanical behavior of biomedical materials*, vol. 59, pp. 108–27, June 2016.

[228] Babuška, I., Sawlan, Z., Scavino, M., Szabó, B., and Tempone, R., "Bayesian inference and model comparison for metallic fatigue data," *Computer Methods in Applied Mechanics and Engineering*, vol. 304, pp. 171–196, June 2016.

[229] Pacheco, C. C., Dulikravich, G. S., Vesenjak, M., Borovinsek, M., Duarte, I. M. A., Jha, R., Reddy, S. R., Orlande, H. R. B., and Colaço, M. J., "Inverse Parameter Identification in Solid Mechanics Using Bayesian Statistics, Response Surfaces and Minimization," *TECHNISCHE MECHANIK*, vol. 36, no. 1-2, pp. 120–131, 2016.

[230] Viswanathan, G. B., Lee, E., Maher, D. M., Banerjee, S., and Fraser, H. L., "Direct observations and analyses of dislocation substructures in the α phase of an α/β Ti-alloy formed by nanoindentation," *Acta Materialia*, vol. 53, no. 19, pp. 5101–5115, 2005.

[231] Hryniewicz, T., Rokosz, K., Valíček, J., and Rokicki, R., "Effect of magnetoelectropolishing on nanohardness and Young's modulus of titanium biomaterial," *Materials Letters*, vol. 83, pp. 69–72, Sept. 2012.

[232] Asaro, R. J. and Needleman, A., "Overview no. 42 Texture development and strain hardening in rate dependent polycrystals," *Acta Metallurgica*, vol. 33, no. 6, pp. 923–953, 1985.

[233] Niewczas, M., "Lattice correspondence during twinning in hexagonal close-packed crystals," *Acta Materialia*, vol. 58, no. 17, pp. 5848–5857, 2010.

[234] Kalidindi, S. R. and Schoenfeld, S., "On the prediction of yield surfaces by the crystal plasticity models for fcc polycrystals," *Materials Science and Engineering: A*, vol. 293, pp. 120–129, Nov. 2000.

[235] Graff, S., Brocks, W., and Steglich, D., "Yielding of magnesium: From single crystal to polycrystalline aggregates," *International Journal of Plasticity*, vol. 23, no. 12, pp. 1957–1978, 2007.

[236] Anderson, T. L., *Fracture mechanics : fundamentals and applications*. Boca Raton, FL: CRC Press, 2005.

[237] Socie, D. F. and Maraquis, G. B., *Multiaxial Fatigue*. Warrendale (PA): SAE - Society of Automotive Engineers, 2000.

[238] McDowell, D. L., "Basic issues in the mechanics of high cycle metal fatigue," *International Journal of Fracture*, vol. 80, pp. 103–145, 1996.

[239] Shamsaei, N., Gladskyi, M., Panasovskyi, K., Shukaev, S., and Fatemi, A., "Multiaxial fatigue of titanium including step loading and load path alteration and sequence effects," *International Journal of Fatigue*, vol. 32, no. 11, pp. 1862–1874, 2010.

[240] Wu, Z. R., Hu, X. T., and Song, Y. D., "Multiaxial fatigue life prediction for titanium alloy TC4 under proportional and nonproportional loading," *International Journal of Fatigue*, vol. 59, pp. 170–175, 2014.

[241] Nakamura, H., Takanashi, M., Itoh, T., Wu, M., and Shimizu, Y., "Fatigue crack initiation and growth behavior of Ti-6Al-4V under non-proportional multiaxial loading," *International Journal of Fatigue*, vol. 33, no. 7, pp. 842–848, 2011.

[242] Oberwinkler, B., Lettner, A., and Eichlseder, W., "Multiscale fatigue crack observations on Ti-6Al-4V," *International Journal of Fatigue*, vol. 33, no. 5, pp. 710–718, 2011.

[243] Fatemi, A. and Shamsaei, N., "Multiaxial fatigue: An overview and some approximation models for life estimation," *International Journal of Fatigue*, vol. 33, no. 8, pp. 948–958, 2011.

[244] Araújo, J. A. and Nowell, D., "The effect of rapidly varying contact stress fields on fretting fatigue," *International Journal of Fatigue*, vol. 24, no. 7, pp. 763–775, 2002.

[245] Dick, T., Basseville, S., and Cailletaud, G., "Fatigue modelling in fretting contact with a crystal plasticity model," *Computational Materials Science*, vol. 43, no. 1, pp. 36–42, 2008.

[246] Gumbel, E. J., *Statistics of extremes*. Courier Corporation, 2012.

[247] Adams, B. L., Gao, X. C., and Kalidindi, S. R., "Finite approximations to the second-order properties closure in single phase polycrystals," *Acta Materialia*, vol. 53, pp. 3563–3577, Aug. 2005.

[248] Harewood, F. and McHugh, P., "Comparison of the implicit and explicit finite element methods using crystal plasticity," *Computational Materials Science*, vol. 39, pp. 481–494, Apr. 2007.

[249] Lemaitre, J. and Chaboche, J.-L., *Mechanics of solid materials*. Cambridge university press, 1994.

[250] Peters, M., Gysler, A., and Lütjering, G., "Influence of texture on fatigue properties of Ti-6Al-4V," *Metallurgical Transactions A*, vol. 15A, pp. 1597–1605, 1984.

[251] Wang, Y. N. and Huang, J. C., "Texture analysis in hexagonal materials," *Materials Chemistry and Physics*, vol. 81, no. 1, pp. 11–26, 2003.

[252] Groeber, M. A. and Jackson, M., "DREAM. 3D: A digital representation environment for the analysis of microstructure in 3D," *Integrating Materials and Manufacturing Innovation*, vol. 3, pp. 1–17, 2014.

[253] Yin, X., Chen, W., To, A., McVeigh, C., and Liu, W. K., "Statistical volume element method for predicting microstructureconstitutive property relations," *Computer Methods in Applied Mechanics and Engineering*, vol. 197, pp. 3516–3529, Aug. 2008.

[254] Tromans, D., "Elastic anisotropy of HCP metal crystals and polycrystals," *International Journal of Research and Reviews in Applied Science*, vol. 6, no. 4, pp. 462–483, 2011.

[255] Goulding, A. N., *Implementing the materials genome initiative: best practicies for developing meaningful experimental data sets in aluminum-zinc-magnesium-copper alloys*. PhD thesis, Georgia Institute of Technology, Atlanta, May 2016.

[256] Kern, P. C., Priddy, M. W., Ellis, B. D., and McDowell, D. L., "pyDEM: A generalized implementation of the inductive design exploration method," *in preparation*.

[257] MATLAB, *version 8.0.0 (R2012b)*. Natick, Massachusetts: The MathWorks Inc., 2012.

[258] Taylor, G. I., "Plain strain in metals," *Journal of the Institute of Metals*, vol. 62, no. 1, pp. 307–324, 1938.

[259] Van Houtte, P., Li, S., Seefeldt, M., and Delannay, L., "Deformation texture prediction: from the Taylor model to the advanced Lamel model," *International Journal of Plasticity*, vol. 21, no. 3, pp. 589–624, 2005.

[260] Ahzi, S. and MGuil, S., "A new intermediate model for polycrystalline viscoplastic deformation and texture evolution," *Acta Materialia*, vol. 56, no. 19, pp. 5359–5369, 2008.

[261] Beausir, B., Tóth, L. S., and Neale, K. W., "Ideal orientations and persistence characteristics of hexagonal close packed crystals in simple shear," *Acta Materialia*, vol. 55, no. 8, pp. 2695–2705, 2007.

[262] Wang, H., Raeisinia, B., Wu, P., Agnew, S. R., and Tomé, C. N., "Evaluation of self-consistent polycrystal plasticity models for magnesium alloy AZ31B sheet," *International Journal of Solids and Structures*, vol. 47, no. 21, pp. 2905–2917, 2010.

[263] Rajasekaran, R. and Nowell, D., "Fretting fatigue in dovetail blade roots: Experiment and analysis," *Tribology International*, vol. 39, no. 10, pp. 1277–1285, 2006.

[264] Kehagias, T., Komninou, P., Dimitrakopulos, G., Antonopoulos, J., and Karakostas, T., "Slip transfer across low-angle grain boundaries of deformed Titanium," *Scripta Metallurgica et Materialia*, vol. 33, pp. 1883–1888, Dec. 1995.

[265] Werner, E. and Prantl, W., "Slip transfer across grain and phase boundaries," *Acta Metallurgica et Materialia*, vol. 38, pp. 533–537, Mar. 1990.

[266] Abuzaid, W. Z., Sangid, M. D., Carroll, J. D., Sehitoglu, H., and Lambros, J., "Slip transfer and plastic strain accumulation across grain boundaries in Hastelloy X," *Journal of the Mechanics and Physics of Solids*, vol. 60, pp. 1201–1220, June 2012.

VITA

Matthew William Priddy was born in Swindon, England on December 2, 1985. He is the son of Richard William Priddy and Anita Marie Priddy of Columbus, MS. Matthew graduated from Caledonia High School in Caledonia, MS in 2004. He was awarded the degrees of Bachelor of Science in Civil Engineering, Summa Cum Laude, in 2008, and Master of Science in Civil Engineering in 2010, both from Mississippi State University in Starkville, MS. Matthew was the recipient of the Georgia Institute of Technology President's Fellowship from 2010-2013.

Matthew was married to Lauren Edith Beatty in Starkville, MS on December 20, 2008.